

UNIVERSITÀ
DEGLI STUDI
DI PADOVA

Sede Amministrativa: Università degli Studi di Padova

Dipartimento di Geoscienze

CORSO DI DOTTORATO DI RICERCA IN: Scienze della Terra

CICLO: XXXII

**CHROMIUM AND ARSENIC REMOVAL FROM CONTAMINATED
WATER: ENVIRONMENTAL APPLICATION OF MAGHEMITE
NANOPARTICLES (SAMNs)**

Coordinatore: Prof. Claudia Agnini

Supervisore: Prof. Gabriella Salviulo

Co-Supervisore: Prof. Fabio Vianello

Co-Supervisore: Prof. Cristina Carbone

Dottorando: Simone Molinari

CONTENTS

Summary	1
Riassunto	4
Aim of the thesis	7
List of publication	8
1. Introduction	9
1.1 Arsenic	9
1.1.1 Occurrence and environmental problematics	9
1.1.2 Speciation in water	10
1.2 Chromium	11
1.2.1 Occurrence and environmental problematics	11
1.2.2 Speciation in water	12
1.3 Arsenic and chromium remediation methods	13
1.3.1 Conventional physical and chemical methods	13
1.3.2 Nanotechnologies in water treatment	15
1.3.3 Application of iron-based nanomaterial for wastewater remediation	16
2. Material and Methods	19
2.1 Chemicals	19
2.2 Synthesis of maghemite nanoparticles (SAMNs)	19
2.3 Determination of Arsenic	20
2.4 Determination of hexavalent Chromium	21
2.5 Physical and chemical characterisation of Ex-Stoppani groundwater	22
2.6 Characterization of SAMNs and SAMN@metal complexes	22
3. Synthesis of colloidal maghemite nanoparticles with novel and peculiar chemical properties	26
3.1. Abstract	26
3.2 Introduction	26
3.3 Results and discussion	28
3.4 Conclusions	46
4. Naked colloidal maghemite nanoparticles with unique surface properties encode binding specificity toward As^{III} and As^V	48
4.1 Abstract	48
4.2 Introduction	48
4.3 Results	50
4.4 Conclusions	67
5. Chromium remediation from industrial groundwater: the Ex-Stoppani case study	69
5.1 Ex-Stoppani site	69
5.2 Mineralogical, chemical and spectroscopic characterization and time-lapse monitoring of chromite-ore processing residues: the Ex-Stoppani case study	71
5.2.1 Abstract	71
5.2.2 Introduction	73

5.2.3 COPRs samples	75
5.2.4 Results	75
5.2.5 Discussion and conclusions	94
5.3 Colloidal Surface Active Maghemite Nanoparticles for Cr ^{VI} remediation from contaminated industrial groundwater	97
5.3.1 Abstract	97
5.3.2 Introduction	98
5.3.3 Industrial application for Cr ^{VI} in-situ remediation by SAMNs	99
5.3.4 Results of SAMNs application to Ex-Stoppani groundwater	101
5.3.5 Conclusions	105
6. Final discussion and conclusions	107
7. Appendix	112
7.1 Supporting Information to synthesis of colloidal maghemite nanoparticles with novel and peculiar chemical properties	112
7.2 Supporting information for Naked Colloidal Maghemite Nanoparticles with Unique Surface Properties Encode Binding Specificity Toward As ^{III} and As ^V	114
7.3 Paper: Biologically safe colloidal suspensions of naked iron oxide nanoparticles for in situ antibiotic suppression	135
8. References	145

Summary

Among the toxic metals Arsenic($\text{As}^{\text{III-V}}$) and Chromium (Cr^{VI}) are known to be carcinogenic when inhaled or ingested with drinking water, for this reason, they are classified as class A human carcinogens (Holmes et al., 2008; Sun et al., 2015; Smedley and Kinniburgh, 2002). The World Health Organization (WHO) determined guideline values in drinking water of 0.05 mg L^{-1} for total Cr and 0.01 mg L^{-1} for As (WHO, 2017) while in Italy the limit is fixed to 0.01 mg L^{-1} for both As and Cr^{VI} . Metal occurrence in the biosphere is principally due to anthropogenic activities, such as mining activities, coal burning, glass manufacture, wood preservatives, textile, paper, ammunition, pesticides, electroplating, leather tanning, metallurgy, photography, and nuclear power plants, (Smedley and Kinniburgh, 2002; Wang and Mulligan, 2006; Ajmal et al., 2001) even though natural causes like ore minerals alteration and weathering of rocks have been reported (Carraro et al., 2013; Oze et al., 2007).

Many conventional methods are nowadays available to remove As and Cr^{VI} from water, the most used treatments consist in chemical reduction, adsorption and anion exchange even if they present drawback principally related to very high costs, large use of reagents and secondary problems of sludge generation. For all these reasons these methods are often not suitable for application in small-scale industry or natural, non-punctual, pollution sources. Low-cost and sustainable techniques must be identified as alternatives or to implement conventional methods. In this field, nanoparticles are emerging as one of the most promising new technique for soil and water remediation for the opportunity of minimising ex-situ activities, better selectivity, increased subsurface remediation efficiency and supported the growing request of green and sustainable remediation.

In particular, iron-based materials as nanoscale zero-valent iron (Tuček et al., 2017), magnetite (Feng et al., 2012), iron oxy-hydroxides (Müller et al., 2010) were already proposed as appealing options.

The main objective of this PhD thesis is to investigate on the entrapment and removal of As and Cr^{VI} from water by application of magnetic maghemite ($\gamma\text{-Fe}_2\text{O}_3$) nanoparticles called SAMNs (Surface Active Maghemite Nanoparticles) (Magro et al., 2012a) as well as providing a contribution to the knowledge of iron chemistry in water and to propose a new strategy to synthesize maghemite nanoparticles with peculiar chemical and electrochemical properties, which can be easily applicable in many fields.

SAMNs were prepared by a novel synthetic low-cost route, easily upgradable, carried out in water starting from FeCl_3 in the presence of atmospheric oxygen, avoiding any release of toxic waste into the environment (Magro et al., 2012b). They differ from other nanostructured $\gamma\text{-Fe}_2\text{O}_3$ for the excellent colloidal stability in water without needing any coating or superficial modification.

The removal efficiency of As and Cr^{VI} by SAMNs was proved under different testing conditions as concern SAMNs and pollutant concentrations, and solution pH. Moreover, results of kinetic and thermodynamic studies, coupled to a deep structural and chemical characterisation of SAMN@metal complexes substantiated the occurrence of different and complex binding mechanisms, hence revealing a specificity of un-coordinated Fe^{III} sites on SAMNs surface.

Results showed that SAMNs can remediate high concentrations of Cr^{VI} (22 mg L^{-1}) in water with a strong pH dependence. The 99% of removal can be achieved at pH 3.0 in two treatment cycles, while this amount decreased to about 40% at pH 9.0. The optical characterisation of SAMN@ Cr^{VI} complex highlights also the covalent nature of the absorption (Magro et al., 2016).

The results of in-situ application on Ex-Stoppani site (Cogoleto, NW Italy) are showed: the production of sodium dichromate, chromic acid and basic chromium sulphate and subsequent disposal of millions of tons of Chromite Ore Processing Residues (COPRs) resulted in very high pollution of soils and groundwater. COPRs are a strongly alkaline pH waste containing 3-5% of residual total chromium part of that, from 1 to 30%, occurring as toxic Cr^{VI} (Chrysochoou et al., 2010; Matern et al., 2017). COPRs caused long-term problematic of Cr^{VI} leaching due to dissolution and destabilisation of Cr^{VI} rich mineral phases. In fact the instability of deposited COPRs due to weathering and dissolution of Cr^{VI} -bearing minerals coupled with the risk deriving from the high mobility and toxicity of Cr^{VI} in water makes the identification of the mineralogical sources of Cr^{VI} of primary concern (Weng et al., 2001; Farmer et al., 2002; Chrysochoou et al., 2010; Matern et al., 2017). The identification and characterisation of the Cr-bearing phases by a multi-technique approach, the quantification of their role in the release of Cr^{VI} in percolating groundwater in the Ex-Stoppani site represent the first step to understand Cr leaching behaviour and to find the most efficient and sustainable remediation strategy. The identified Cr-bearing phases were sodium chromate and crocoite in younger COPR samples (<25 years) while in more aged and weathered COPRs (~50 years old) ettringite, katoite and hydrotalcite were detected.

The site was characterised by high concentration of Cr^{VI} in the water, wastes and soil. Groundwater showed very high Cr^{VI} ranging from 250,000 to 500,000 µg/L in the plant area and concentrations of total chromium in soils of 15,000 mg kg⁻¹. The in-situ application of SAMNs on 9 wells, at varying pH conditions, confirmed the very high efficiency of SAMNs for Cr^{VI} removal with 99% removal achieved, confirming the very high selectivity for the target metal by the absence of any interfering bound molecule even in complex real groundwater.

For arsenic, besides substantiating the ability of SAMNs to sequester it at completion, a different binding affinity of the two As species (As^{III} and As^V) was observed. Indeed, As^{III} in solution (10 mg L⁻¹) was zeroed at a SAMN concentration of about 3.0 g L⁻¹, while As^V approached the complete removal at 7.0 g L⁻¹ with a two-step binding process, involving very fast adsorption in the first 5 min incubation, followed by a slower binding process. The maximum binding capacity of SAMNs toward As^{III} resulted almost constant in the whole pH range explored, while a rapid decrement with pH was observed for As^V binding, in accordance with Cr behaviour.

The surface of these peculiar iron oxide nanoparticles revealed differences in the binding affinity and stability of SAMN@metal complexes due to the specificity of under-coordinated Fe^{III} sites on SAMN surface resulting in novel and promising features very useful in a wide range of applications comprised large scale water remediation.

The present thesis, enriched the chemistry of iron and the interactions between Cr, As and iron oxides and confirming the possible application of SAMNs as a promising real applicable tool for water remediation by As and Cr, contributes to stimulating the research focused on the development of novel synthetic approaches for known nanomaterials, which still can be object of innovation.

Riassunto

Tra tutti i metalli tossici arsenico ($\text{As}^{\text{III-V}}$) e cromo (Cr^{VI}) sono considerati cancerogeni se inalati o ingeriti attraverso l'acqua; per questa ragione vengono classificati come cancerogeni di classe A (Holmes et al., 2008; Sun et al., 2015; Smedley and Kinniburgh, 2002). L'organizzazione mondiale della sanità (WHO) ha determinato un valore di riferimento di 0.05 mg L^{-1} di Cr^{tot} e 0.01 mg L^{-1} di As come standard di riferimento (WHO, 2017) per le acque potabili; mentre per l'Italia il limite è fissato a 0.01 mg L^{-1} per entrambi i metalli. La presenza di questi metalli nella biosfera è dovuta principalmente ad attività antropiche come ad esempio attività minerarie, combustione di carbone, industria del vetro, trattamenti per il legno, tessuti, carta, munizioni, pesticidi, galvanizzazioni, concia del cuoio, metallurgia, fotografia e centrali nucleari (Ajmal et al., 2001; Smedley and Kinniburgh, 2002; Wang and Mulligan, 2006), anche se elevate concentrazioni sono state descritte per cause naturali in seguito ad alterazione di minerali e dilavamento di rocce (Oze et al., 2007; Carraro et al., 2013).

Molti metodi convenzionali sono disponibili ai giorni nostri per la rimozione di As e Cr^{VI} dalle acque, i trattamenti più utilizzati sono basati su riduzione chimica, adsorbimento e scambio ionico; anche se presentano varie problematiche principalmente legate ad alti costi, grandi quantità di reagenti utilizzati e produzione di fanghi di scarto.

Per i motivi sopracitati questi metodi spesso risultano inadatti all'applicazione per piccole aree industriali o per sorgenti di inquinamento naturali non puntuali. Devono essere quindi identificate tecniche a basso costo e sostenibili come alternative o complemento ai metodi convenzionali. In questo campo, i nanomateriali stanno emergendo come una delle più promettenti tecniche per la bonifica di suoli ed acque, grazie alla possibilità di minimizzare le attività ex-situ, di ottenere una migliore selettività, oltre ad un incremento dell'efficienza per la bonifica sub-superficiale a supporto della crescente richiesta di bonifiche "green" e sostenibili. In particolare, i materiali a base ferrosa come ad esempio nanoparticelle di ferro zero valente (Tuček et al., 2017), magnetite (Feng et al., 2012), ossi(idro)ssidi di ferro (Müller et al., 2010) sono già stati proposti come opzioni interessanti. L'obiettivo principale di questa tesi di dottorato riguarda l'investigazione della possibile applicazione di nanoparticelle magnetiche di maghemite ($\gamma\text{-Fe}_2\text{O}_3$) denominate SAMNs (Surface Active Maghemite Nanoparticles) (Magro et al., 2012a) per la rimozione di As e Cr^{VI} da acque; oltre a fornire un contributo originale alla conoscenza della chimica del ferro in acqua e proporre

una nuova strategia di sintesi di nanoparticelle di maghemite con peculiari proprietà chimiche e elettrochimiche che permettono un'applicazione in vari campi.

Le SAMNs sono preparate attraverso un innovativo metodo di sintesi a basso costo, effettuato in acqua partendo da FeCl_3 in presenza di ossigeno atmosferico evitando qualsiasi rilascio di residui tossici nell'ambiente (Magro et al., 2012b). Differiscono inoltre da qualunque altra nanostrutturata di $\gamma\text{-Fe}_2\text{O}_3$ per l'eccellente stabilità colloidale in acqua senza necessità di alcun ricoprimento e/o modifica superficiale. L'efficacia delle SAMNs nella rimozione di As e Cr^{VI} è stata dimostrata in diversi test variando le condizioni in termini di concentrazione di SAMNs ed inquinante, pH della soluzione. Inoltre, i risultati degli studi cinetici e termodinamici, accoppiati con un'approfondita caratterizzazione strutturale e chimica dei complessi SAMN@metallo ha evidenziato la presenza di diversi e complessi meccanismi di adsorbimento svelando una specificità dei Fe^{III} non-coordinati sulla superficie delle SAMNs. I risultati mostrano che le SAMNs possono rimuovere alte concentrazioni di Cr^{VI} (22 mg L^{-1}) nelle acque con una forte dipendenza dal pH. Il 99% di rimozione è raggiunta a pH 3.0 in due cicli di trattamento mentre la quantità di Cr adsorbita decresce a circa il 40% a pH 9.0. La caratterizzazione ottica dei complessi SAMN@ Cr^{VI} ha inoltre evidenziato la natura covalente dell'adsorbimento (Magro et al., 2016).

I risultati dell'applicazione sul sito Ex-Stoppani (Cogoleto, NW Italy) sono inoltre mostrati: la produzione di cromato di sodio, acido cromico, solfato basico di cromo ed il conseguente stoccaggio di milioni di tonnellate di fanghi residuali di trattamento della cromite (COPRs) hanno provocato fenomeni di elevato inquinamento di suoli ed acque. I COPRs sono un rifiuto fortemente alcalino contenente dal 3 al 5% di cromo residuo; una parte del quale, dall'1 al 30%, come Cr^{VI} tossico (Matern et al., 2017; Chrysochoou et al., 2010). I COPRs possono causare problematiche di rilascio di Cr^{VI} a lungo termine dovute a dissoluzione e destabilizzazione di fasi mineralogiche ricche in Cr^{VI} . Infatti l'instabilità dei COPR, dovuta al dilavamento e dissoluzione di minerali contenenti Cr^{VI} , accoppiata con il rischio derivante dall'elevata mobilità e tossicità del Cr^{VI} , rendono di importanza primaria l'identificazione delle sorgenti mineralogiche coinvolte nel processo (Weng et al., 2001; Chrysochoou et al., 2010; Farmer et al., 2002; Matern et al., 2017).

L'identificazione e caratterizzazione delle fasi a Cromo attraverso un approccio multi-analitico nel sito Ex-Stoppani e la quantificazione del loro ruolo sul rilascio di Cr^{VI} nelle acque percolanti rappresenta il primo step per comprendere i processi di lisciviazione e trovare la più efficiente e sostenibile strategia di bonifica. Le fasi a cromo identificate sono cromato di

sodio e crocoite nei COPR più recenti (<25 anni) mentre nei più vecchi e dilavati (~50 anni) sono state identificate ettringite, katoite ed idrotalcite. Il sito è caratterizzato da alte concentrazioni di Cr^{VI} nelle acque, nei rifiuti e suoli. Le acque mostrano concentrazioni molto elevate di Cr^{VI} comprese tra 250,000 e 500,000 µg L⁻¹ nell'area industriale mentre i suoli di 15,000 mg kg di cromo totale. L'applicazione in situ delle SAMNS su 9 pozzi selezionati, variando le condizioni di pH, ha confermato l'elevata efficienza: con il 99 % di rimozione di Cr^{VI} raggiunta con una selettività molto elevata per il metallo "target" come confermato dall'assenza di ioni interferenti anche in acque industriali particolarmente complesse.

Per l'arsenico, oltre a dimostrare l'abilità delle SAMNs di sequestro fino alla totale rimozione, è stata inoltre riscontrata una differente affinità di legame per le due specie (As^{III} e As^V). In particolare, l'As^{III} in soluzione (10 mg L⁻¹) è stato azzerato con una concentrazione di SAMN di circa 3.0 g L⁻¹ mentre la completa rimozione di As^V è stata raggiunta a circa 7.0 g L⁻¹ con un processo di adsorbimento a due step caratterizzato da una cinetica molto veloce nei primi 5 minuti di incubazione, seguito da un processo di legame più lento.

La massima capacità di adsorbimento per l'As^{III} è inoltre risultata costante in tutto il range di pH investigato mentre per l'As^V è stata riscontrato un rapido decremento della capacità di adsorbimento con l'aumento del pH, in accordo con i risultati per il cromo.

La superficie di queste peculiari nanoparticelle di ossidi di ferro ha rivelato differenze nell'affinità di legame e nella stabilità dei complessi SAMN@metallo dovuto alla specificità dei siti a Fe^{III} non coordinati sulla superficie delle SAMNs risultanti in nuove e promettenti caratteristiche molto utili in un ampio range di applicazioni compresa la bonifica a larga scala.

La presente tesi, oltre ad arricchire la chimica di interazione tra Cr, As e ossidi di ferro e confermare la possibile applicazione delle SAMNs come un promettente strumento per la bonifica di acque inquinate da As e Cr, contribuisce a stimolare la ricerca focalizzata allo sviluppo di nuovi approcci sintetici per nanomateriali già ben conosciuti, ma che possono ancora essere oggetto di innovazione.

Aim of the thesis

The overall aim of this thesis was to study the suitability of specific superparamagnetic maghemite ($\gamma\text{-Fe}_2\text{O}_3$) nanoparticles called SAMNs (Surface Active Maghemite nanoparticles) which stand out, compared to other similar reported material, for the excellent colloidal stability in water without any coating and the unique ability to specifically bind selected molecules, such as arsenic and hexavalent chromium in water.

The first objective of the thesis was to investigate new properties and possible applications of nanostructured uncoated maghemite and of their surface properties, and to deepen the study and characterization of the synthesis protocol. The nanoparticles synthesis, carried out in water, led to unexpected and unpredictable surface properties resulting from solvent and/or ligand interaction, thus the study was aimed at enriching the chemistry of iron oxides and at opening new door for novel synthetic routes and new opportunities for metal oxide nanoparticles.

The second objective was to investigate the adsorption properties of SAMNs for both arsenate and arsenite and to the determination of adsorption mechanism on nanoparticles. It should be noted that our results on the comparative studies of the binding of these two species on iron oxides aimed at remediation purposes represent a novelty as literature studies mainly focused on hydrous ferric oxides. Moreover, As^{III} and As^{V} were used as effective probes for studying the surface characteristics of maghemite nanoparticles as their binding behavior is strictly related to SAMNs defects on the surface structure.

The third objective was the study of the efficiency of SAMNs for Cr^{VI} remediation in water coupled with the possible exploitation in a real complex industrial site, the site of national interest "ex-Stoppani", mimicking a real in situ application.

The compendium of characteristics, from the high colloidal stability, the low toxicity and the high adsorption efficiency, represents a key feature for the exploitation of SAMNs to large scale wastewater remediation.

List of publications

- Massimiliano Magro, Davide Baratella, **Simone Molinari**, Andrea Venerando, Gabriella Salviulo, Giulia Chemello, Ike Olivotto, Giorgio Zoppellaro, Juri Ugolotti, Claudia Aparicio, Jiri Tucek, Anna P. Fifi, Giuseppe Radaelli, Radek Zboril, Fabio Vianello. Biologically safe colloidal suspensions of naked iron oxide nanoparticles for in situ antibiotic suppression, *Colloids and Surfaces B: Biointerfaces* 2019, 181, 102-111 doi:10.1016/j.colsurfb.2019.05.036.

- **Simone Molinari**, Massimiliano Magro, Davide Baratella, Gabriella Salviulo, Juri Ugolotti, Jan Filip, Martin Petr, Jiri Tucek, Giorgio Zoppellaro, Radek Zboril, and Fabio Vianello. Naked colloidal maghemite nanoparticles with unique surface properties encode binding specificity toward AsIII and AsV, submitted to *ACS applied materials and interfaces*.

- Massimiliano Magro, **Simone Molinari**, Andrea Venerando, Davide Baratella, Giorgio Zoppellaro, Juri Ugolotti, Gabriella Salviulo, Radek Zboril, Fabio Vianello. Synthesis of colloidal maghemite nanoparticles with novel and peculiar chemical properties, under finalization.

- **Simone Molinari**, Cristina Carbone, Juri Ugolotti, Massimiliano Magro, Vianello Fabio, Gabriella Salviulo. Mineralogical, chemical and spectroscopic characterization and time-lapse monitoring of Chromite-ore processing residues: the ex-Stoppani case study. under finalization.

- **Simone Molinari**, Massimiliano Magro, Gabriella Salviulo, Cristina Carbone, Davide Baratella, Fabio Vianello Colloidal maghemite nanoparticles for groundwater remediation from contaminated site by Chromite Ore Processing Residues. In preparation.

- Martina Bortoletti, Massimiliano Magro, **Simone Molinari**, Davide Baratella, Luca Fasolato, Juri Ugolotti, Giuseppe Radaelli, Daniela Bertotto, Marco De Liguoro, Radek Zboril, Fabio Vianello. Self-Assembly of Flumequine on γ -Fe₂O₃ Nanoparticles: an Antimicrobial Magnetically Drivable Nanovehicle, in preparation.

- Massimiliano Magro, Davide Baratella, Veronica Colò, Francesca Vallese, Carlo Nicoletto, Paolo Sambo, **Simone Molinari**, Gabriella Salviulo, Andrea Venerando, Fabio Vianello. Electrocatalytic Nanostructured Ferric Tannates as platform for enzyme conjugation: electrochemical determination of phenolic compounds, submitted to Bioelectrochemistry.

- Massimiliano Magro, Davide Baratella, **Simone Molinari**, Andrea Venerando, Giulia Nalotto, Lucio Zennaro, Monica Rossetto, Caroline R. Basso, Valber A. Pedrosa, Gabriella Salviulo, Fabio Vianello. Enzyme-iron oxide nanoparticle conjugation: protein structure modification behind the enhancement of the catalytic activity of xanthine oxidase, under finalization.

1. Introduction

1.1 Arsenic

1.1.1 Occurrence and environmental problematics

The increasing presence of organic and inorganic arsenic in groundwater represents an important threat to human health and the environment. Arsenic is classified by the International Agency of Research on Cancer (IARC) as class I human carcinogen, and chronic exposure can affect human health causing skin lesion, abdominal pain, nausea, cancer, diabetes and many others neurological, respiratory and cardiovascular problems (Ratnaike, 2003; Carlin et al., 2016; Naujokas et al., 2013).

As for chromium, arsenic (As) occurrence in the environment can be due to both natural and anthropogenic causes, and most of the environmental problematics derives from mobilisation under natural conditions. However, important anthropogenic impact can derive from mine wastes, mill tailings, herbicide and glass industry. Natural occurring high As concentrations related to weathering and geochemical reaction, biological activities, as well as volcanic emission, were reported (Mohan and Pittman, 2007; Smedley and Kinniburgh, 2002; Carraro et al., 2015; Angelone et al., 2009). In particular, mineralogy has a key role in As mobility, as this metal is a major constituent of various minerals such as arsenopyrite (FeAsS), realgar (AsS), orpiment (As₂S₃). High As concentration was also reported in

chalcopyrite (CuFeS₂) and galena (PbS) as well as in many Fe-oxyhydroxides as results of As incorporation in their structure and/or surface adsorption, depending on pH and redox speciation (Smedley and Kinniburgh, 2013).

Arsenic concentration in groundwater is variable and depends on various factors such as local conditions and source of contamination (natural or anthropogenic) and represents the greatest worldwide threat to health. Cases of groundwater pollution were reported in Bangladesh and India (Burgess et al., 2010; Chowdhury et al., 2000; Jiang et al., 2013), Taiwan (Liang et al., 2016), Vietnam (Fendorf et al., 2010), China (Zhang et al., 2017), Mexico and Argentina (Navoni et al., 2014; Esteller et al., 2015), USA (Welch et al., 2000; Sorg et al., 2014), Spain (García-Salgado et al., 2012) while high arsenic concentration in Italy were found on the Po and Venetian plain (Carraro et al., 2013; Ungaro et al., 2008; Molinari et al., 2013).

The World Health Organisation provides a guideline value of 10 µg l⁻¹ as a drinking water standard, and the same standard was adopted in European regulation and US EPA, while in some countries the guideline value of 50 µg L⁻¹ it's still adopted (Smedley and Kinniburgh, 2013).

1.1.2 Speciation in water

Arsenic may exist in different valence states (e.g., 3, 0, +3, +5) even if the two major forms found in water are oxyanions of As^{III} and As^V. The toxicity of arsenic depends on its speciation, controlled by redox conditions and pH: under oxidizing condition the two dominant forms in natural water are H₂AsO₄⁻ (at pH values below 6.9) and HAsO₄²⁻ at higher pH, whereas, under reducing conditions, the uncharged As^{III} species H₃AsO₃⁰ (at pH values below 9.2) and H₂AsO₃⁻ at higher pH becomes predominant (Smedley and Kinniburgh, 2002; Lu and Zhu, 2011). The oxidation state and form have a fundamental role in the mobility and toxicity of arsenic in water: the trivalent form is more toxic, mobile and difficult to remove than As^V.

Arsenate and arsenite speciation are given in equations 1 and 2 respectively with the respective pKa (negative logarithm of the equilibrium constant for dissociation) values (Smith et al., 1998; Goldberg and Johnston, 2001).





The relative abundance of As^{III} and As^V in natural water depends on the number of oxidising/reductive agents, such as organic carbon, dissolved oxygen, Mn oxides and microbial activity. As^{III} is the more stable species under anoxic conditions or strongly reducing aquifers, often present as main species in geothermal systems, but tends to easily oxidise when in contact with oxygen-rich surface water or by the action of bacteria (Wilkie and Hering, 1998).

1.2 Chromium

1.2.1 Occurrence and environmental problematics

Chromium (Cr) is one of most strategic metal, due to its wide use in many industries, such as metallurgy, to produce steel and various alloys for plating metals, refractories, pigments and leather manufacturing.

It can be present in water as Cr^{III} and Cr^{VI}, and its origin can be from natural sources, such as weathering of rocks. The ratio between the two main oxidation states is governed by pH, oxic or anoxic conditions, interaction with complexing agents and oxidants/reductants, such as Fe^{II}, dissolved organic matter and hydrogen peroxide (Rai et al., 1989; Pettine and Millero, 1990; Kotaś and Stasicka, 2000).

In soils, the main source of Cr is represented by weathering of parent materials. It is often present often as slightly soluble Cr(OH)₃ or adsorbed on different soil components. In particular, the presence of humic acids leads to complexation of Cr^{III} making it insoluble at acidic conditions (pH<4.5) (Krajnc et al., 1995; James, 2011), while under alkaline conditions (pH>7) the precipitation of Cr(OH)₃ becomes dominant.

Cr^{VI} can also be present in soils in the form of very soluble sodium chromate (Na₂CrO₄) or slightly soluble chromates such as calcium chromate (CaCrO₄), barium chromate (BaCrO₄) and crocoite (PbCrO₄). These phases, undergoing solubilization, release of CrO₄²⁻ and HCrO₄⁻ depending on pH conditions, and are characterised by high toxicity, mobility and elevated persistence, especially in deep soil and groundwater causing important pollution phenomena (James and Bartlett, 1984). Even though, binding phenomena of toxic chromates on iron oxyhydroxides and aluminium oxides due to electrostatic binding

processes are possible (James and Bartlett, 1983; Bartlett and James, 1988; Richard and Bourg, 1991).

1.1.2 Speciation in water

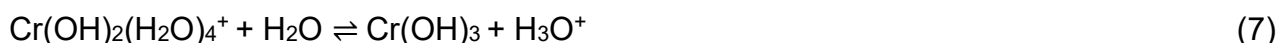
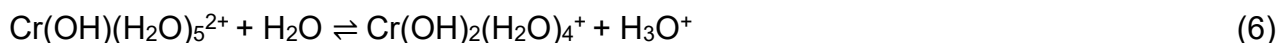
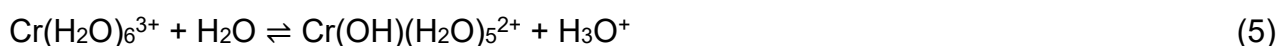
Chromium toxicity depends primarily on its speciation. In fact, it is present in the environment in several oxidation states ranging from 0 to VI, but only the trivalent (Cr^{III}) and the hexavalent forms (Cr^{VI}) are stable enough to occur. Cr^{IV} and Cr^{V} forms give only unstable intermediates under oxidation/reduction reactions between Cr^{III} and Cr^{VI} .

Cr^{III} is the most stable oxidation state, being necessary a considerable amount of energy to convert it to other states. While Cr^{VI} , characterized by high positive redox potential, is a strong oxidizing and undergoes a reduction in the presence of electron donors, depending on pH and relative redox potentials (Eqs. 3-4) (Ball and Nordstrom, 1998; Kotaš and Stasicka, 2000).



Thermodynamically stable aqueous Cr species are ruled by pH and Eh conditions visible in the Pourbaix diagram was used.

In the absence of any other complexing agent, Cr^{III} is expected to be present as different hydroxo-complexes: $\text{Cr}(\text{H}_2\text{O})_6^{3+}$ is the most stable form under acidic conditions ($1 < \text{pH} < \sim 4$) while its deprotonated forms (Eqs. 5, 6, 7) $\text{Cr}(\text{OH})^{2+}$, $\text{Cr}(\text{OH})_2^+$ and $\text{Cr}(\text{OH})_3$ are dominating in the typical range of natural water ($4 < \text{pH} < 10$) (Rai et al., 1987; Ball and Nordstrom, 1998; Kotaš and Stasicka, 2000).



Under high alkaline conditions, $\text{pH} > 11.7$ $\text{Cr}(\text{OH})_3$ transforms into the tetrahydroxo complex $\text{Cr}(\text{OH})_4^-$.

Cr^{VI} forms different species in aqueous solutions and their stability is governed, as well, by pH and Eh (Figure 2): chromic acid (H_2CrO_4) is the prevalent form at very low pH values

(pH < 1), while at pH>1 it deprotonates (Eqs. 8-9) forming HCrO₄⁻ and CrO₄²⁻. The latter represent the predominant Cr^{VI} form in water at pH~7(Kotaś and Stasicka, 2000).



Another important parameter controlling Cr^{VI} speciation is its concentration. In fact, when Cr^{VI} concentration reaches 10⁻² M at pH between 1.0 and 6.0, a condensation of HCrO₄⁻ occurs forming dichromate ion (Cr₂O₇²⁻) (Eqs. 10).



Summarising, under pH conditions expected for natural and industrial groundwater, expected Cr^{VI} forms are CrO₄²⁻, HCrO₄⁻ and Cr₂O₇²⁻ anions, all characterised by high solubility and mobility in the environment.

1.3 Arsenic and chromium remediation methods

1.3.1 Conventional physical and chemical methods

Several methods for the removal of chromium and arsenic are available and principally include precipitation, adsorption, ion exchange, electrochemical reduction, reverse osmosis and nanofiltration (Hu et al., 2004). Additionally, many different sorbents were investigated such as iron, iron oxides (hematite, maghemite and magnetite) and hydroxides, clay minerals, activated carbon and sawdust (Driehaus et al., 1998; Baral et al., 2006; Giménez et al., 2007; Mohapatra et al., 2007; Tuutijaarvi et al., 2009) . Nevertheless, many secondary environmental impacts are associated with these traditional methods, largely related to the specific methodology and the peculiar case of study. It should be mentioned that conventional methods generally suffer from high operational cost, scarce efficiency in complex scenarios and difficult sorbent material preparation.

Physical methodologies comprise many different techniques, such as electrodialysis, membrane filtration, photocatalysis working on physicochemical properties of the pollutants (Jobby et al., 2018 and references therein) while chemical remediation approaches are based on the addition of chemicals (i.e. sulfur dioxide, ferrous sulfate, sodium sulphite) to reduce metals toxicity or mobility by converting them into inactive states.

Filtration techniques were often used as easy method based on the use of sand and/or membrane to trap contaminants in pore spaces of the filter, and methods for removing various pollutants from water were proposed, even if these sole methodologies seem unsuitable for heavy metals removal (Adeleye et al., 2016). However, nowadays ultrafiltration and nanofiltration represent promising technologies for chromium and arsenic retention from groundwater due the low energy consumption and high removal efficiency (Muthukrishnan and Guha, 2008; Nguyen et al., 2009).

Ion-exchange treatments for toxic metal treatment have numerous advantages, such as high volume and removal treatment capacity and low secondary sludge generation (up to 80%) with respect to the above-mentioned conventional methods. These systems are based on cation exchangers, generally of a synthetic resin, and reach the almost total metal removal even if their performances are often affected by various parameters such as pH, metal concentration and contact time (Tiravanti et al., 1997; Rengaraj et al., 2001).

Chemical precipitation represents one of the most used technique for the treatment of large of volumes of polluted wastewater, especially in industrial areas. As previously described, it is based on the reaction between the target metal and a precipitant, leading to an insoluble precipitate easily removable precipitate by filtration or sedimentation from the water media. A simple example consists in the $\text{Cr}^{\text{VI}} \rightarrow \text{Cr}^{\text{III}}$ conversion using ferrous sulfate forming insoluble hydroxides of toxic anions (Evanko et al., 1997; Mirbagheri and Hosseini, 2005). However, the wide utilization of hydroxide precipitation, due to their simplicity and to the possibility to easily separate the metal hydroxide by flocculation and sedimentation, clashes with the amphoteric nature of some toxic metal, especially in complex solution, with the high cost of chemical reagents and with the generation of large volumes of secondary sludges requiring pH adjustment and high-cost special disposal for hazardous materials (Kongsricharoern and Polprasert, 1995).

Biosorption is another attractive “green” option with good performances for metals removal, using largely available, low-cost adsorbent, principally coming from bacteria, fungi, algae and various biomasses such as bark and lignin crab shell. These are particularly useful to treat wastewater with low toxic metal concentrations, in a fast way with high efficiency, especially if applied on very high wastewater volume (Wang and Chen, 2009).

Summarizing, physical and chemical methods are aimed at the large-scale industrial remediation with relatively simple and fast wastewater treatments, but are still suffering from very high operational costs, high-energy consumption and production of a large amount of

secondary sludge and pollutants. Moreover, their performances are dependent on the presence of high metal concentrations and look not so efficient towards new emerging pollutants (i.e. PFAS, pharmaceuticals and cosmetics) and not meeting requirements to reach the increasingly research for more green and sustainable remediation processes (Cundy et al., 2008).

1.3.2 Nano-adsorbents in groundwater treatment

Nanotechnologies stand out as promising and efficient solution and/or alternative to improve environmental remediation processes due to their wide application opportunities. Their application is based on the unique properties of nanomaterials, such as very small size, high surface area and high reactivity, as well as environmentally friendly and cost-effective (Xu et al., 2012).

The application of nanomaterial in water treatments is characterised by a very wide diversity with differences in terms of types of sorbent, properties and usages. In the last years many efforts were carried out for deepening the study of the binding efficiency of nano-adsorbent for pollutants removal from wastewater (Manceau and Charlet, 1994; Kanel et al., 2005; Ren et al., 2011; Zhang et al., 2014; Magro et al., 2016).

The applications and characteristics of nanomaterials can be distinguished in three main categories: nano-sorbents, nano-catalysts and nano-membranes (Tesh and Scott, 2014).

Nowadays, nano-sorption represents one of the most used and efficient process for the abatement of inorganic pollutants, especially for heavy metals, from water because of their large surface area and adsorption sites availability on the nanomaterial. Compared to their macro counterparts, nano-sorbents benefits of less waste generated (Sharma et al., 2009). In the aqueous environment, many factors should be taken into account to achieve competitive remediation results. In particular, main advantages are the high surface area, low synthesis costs, adsorption activity, colloidal stability, non-toxicity, as well as high adsorption performances for low concentration (order of part per billion (ppb)) pollutants coupled to the possibility to easily recover the bound target from the nano-sorbent surface by specific treatment and its recycling (Cloete et al., 2010).

Nano-sorbents can be further divided into various categories: carbon, iron and metal and non-metal oxide-based nanomaterials. Carbon based nanomaterials are principally represented by carbon nanotubes (single wall or multi-wall), nanofibers and graphene,

showing very high surface area, elevate adsorption ability and fast binding kinetics with both organic and inorganic pollutants due to the presence of surface functional groups, such as hydroxyl, carboxyl and phenols. In particular, carbon nanotubes formed by graphene sheets with cylindrical shape, have been explored as possible sorbents for As and Cr^{VI} removal (Di et al., 2006; Pillay et al., 2009; Vadahanambi et al., 2013; Lofrano et al., 2017). However, despite their high adsorption ability and broad applicability, these materials still suffer from high production costs due to the use of catalysts and precursors, restricting their possible large-scale application. On the contrary the use of graphene oxide, characterised by a 2D structure produced by oxidation of graphite layers, is deserving attention as nano-sorbent for several environmental application due to its high surface area and high maximum adsorption capacity. Its main advantage rely on the double basal planes available, the chemical stability, as well as the simple synthetic process (Santhosh et al., 2016).

The last category of nano-adsorbents is represented by oxide-based nanoparticles synthesised by both metals and non-metals. These include a wide range of materials, such as titanium, zinc, manganese and magnesium oxides. These materials are already largely applied for the removal of toxic metal from wastewater due high surface area, high adsorption ability and very low secondary toxicity due to their low solubility (Anjum et al., 2016, and references therein).

The unique properties of nanomaterials, here outlined, make nano-sorbents an encouraging way, readily integrable into existing remediation processes, to overcome high operational costs and public health problems. Moreover, the possibility to recycle nanomaterials represent an interesting option from the economical point of view due to the reduction of secondary waste production, as well as the recovery of bound metals.

1.3.3 Application of Iron-based nanomaterial for wastewater remediation

In the last 20 years, nanoscale iron-based materials were proposed as continuously evolving remediation processes, providing new sustainable solutions for environmental clean-up issues, thank to the low toxicity and low cost of iron. Moreover, these small size (1-100 nm) nanomaterials offer the opportunity of flexible application both in-situ and ex-situ (i.e. directly in contaminated soils, in slurry reactors, in solid matrixes for flowing wastewater and gas treatments), and can represent important systems to overcome remediation challenges and cost abatement (Zhang, 2003).

In the last decades, a wide body of research was focused on the application of nanoscale zero-valent iron (nZVI) being non-toxic, very cheap and easy to produce. Furthermore, its high reactivity under environmental conditions makes it an effective reductant, thanks to its reduction potential of -0.447 V , toward oxidised toxic metals, such as Cr^{VI} , (Sasaki et al., 2009; Fu et al., 2014). Several studies demonstrated that the performances of nZVI for the remediation of groundwater contaminated by toxic metals, in particular by arsenic (Nikolaidis et al., 2003; Kanel et al., 2005; Ramos et al., 2009; Tuček et al., 2017) and Cr^{VI} (Shi et al., 2011; Gheju, 2011; Mitra et al., 2011). The main driving mechanism for arsenic removal is complex and characterised by both adsorption and redox processes on nZVI surface, leading to As blocking and to the precipitation of iron (hydr)oxides on the surface (Mak et al., 2009; Tuček et al., 2017).

A similar mechanism was reported for Cr^{VI} adsorption followed by reduction to less toxic Cr^{III} with the concomitant oxidation of Fe^0 to Fe^{III} of nZVI and subsequent coprecipitation in the form of iron hydroxides (Fu et al., 2014). It should be noted that exploitation of nZVI suffer from some limitation due to its low stability and to the difficulties of nZVI recovery after complexation from the solution. For this reason, it is often necessary to support ZVI on different materials, such as zeolite, kaolinite, bentonite and activated carbon (Fu et al., 2014) thus significantly increasing production costs.

Another efficient class of iron-based material applied in the environmental field is represented by iron oxides. In particular, nanoscale iron oxides, are considered efficient and low cost sorbents. Due to the presence of a large number of available sorption sites on their surface, they have a very high adsorption capacity and are able to remediate highly polluted groundwater (Qu et al., 2013).

Different nano iron-based oxide were applied for the removal of toxic metals from wastewater, such as hematite ($\alpha\text{-Fe}_2\text{O}_3$) (Chen and Li, 2010), maghemite ($\gamma\text{-Fe}_2\text{O}_3$) (Hu et al., 2005; Magro et al., 2016), goethite ($\alpha\text{-FeOOH}$) (Grossl et al., 1994) and magnetite (Fe_3O_4) (Giraldo et al., 2013).

For these materials, the size control during the synthesis is a key factor for controlling their colloidal stability and maximum adsorption capacity, and their exploitation in large-scale environmental fields. In particular, it was found that the decrease of nanomaterial size leads to a change in the nanoparticles surface structure, with the creation of new available binding sites and resulting in a consequent increase in the adsorption capacity (Qu et al., 2013). Yean et al. (2005) reported on an increase of 100 times in arsenic adsorption ability by

magnetite nanoparticles when their size is decreased from 300 nm to 11 nm, due to the increase in the specific surface area (Yean et al., 2005). The size dependent adsorption behaviour of nanomaterials becomes evident comparing adsorption capacity and specific surface area. Auffan et al., (2008, 2009) suggested the so-called “nanoscale effect”, and reported on a similar adsorption capacity (~ 3.6 atoms per nm^2) of nanoparticles size from 300 to 20 nm. While three times As adsorption can be achieved decreasing again the size to 11 nm (~ 11 atoms per nm^2) as results of formation of new vacancies on nanoparticles surface. Synthesis methods and possible surface coating represent the main factors controlling, beside size distribution, all the properties (magnetism, morphologies and surface chemistry) needed for any application (Machala et al., 2007).

The property of magnetism of nano-maghemite ($\gamma\text{-Fe}_2\text{O}_3$) is of particular interest for environmental applications of iron oxide nanoparticles, resulting in an effective and easy possibility of separation from the aqueous solution by means of a simple external magnetic field (Gutierrez et al., 2017). In particular, if maghemite nanoparticles are small enough (in the order of 10-20 nm), they are superparamagnetic, resulting the possibility of magnetic driving and re-dispersion after magnetic field removal. This property is particularly convenient for the treatment of large volumes of polluted wastewater, such as in industrial-scale applications (Hu et al., 2010), in which magnetic nanoparticles emerge as one of the most promising material. To enhance the colloidal stability, as well as to improve metal binding selectivity, surface modifications of nanomaterials by organic polymers or inorganic shells can be an option (Xu et al., 2012). It should be noted that coating processes are often expensive and cumbersome, resulting in a reduction of magnetic properties due to the introduction of a diamagnetic shell on nanoparticles surface (Thorek et al., 2006; Mackay et al., 2006). The main advantages of the application of $\gamma\text{-Fe}_2\text{O}_3$ nanoparticles rely on the very high adsorption capacity towards toxic metals (i.e. Cr^{VI} and As), the simple and rapid separation from aqueous solution by external magnetic fields, avoiding the production of secondary pollutants (Tuutijärvi et al., 2009). The possibility to synthesise the maghemite nanoparticles in water, without any harmful solvent, represent a key feature for producing non-toxic nanomaterials for in situ applications (Magro et al., 2012a).

Finally, it was also demonstrated that maghemite nanoparticles can be successfully magnetically recovered, regenerated and recycled for reuse without losing their adsorption efficiency, while the target can be concentrated, thus representing an attractive option from the economic point of view (Hu et al., 2005; Magro et al., 2016).

2. Material and Methods

2.1. Chemicals

Chemicals were purchased at the highest commercially available purity and were used without further treatments. Iron(III) chloride hexahydrate (97%), sodium borohydride (NaBH₄), tetramethylammonium hydroxide, perchloric acid, ammonia solution (35% in water), 1,5-diphenylcarbazine were obtained from Aldrich (Sigma-Aldrich, Italy). Standard solutions of Cr^{VI} were prepared using potassium dichromate (K₂Cr₂O₇).

For arsenic binding experiments, stock solutions of arsenate and arsenite (1000 mg L⁻¹) were prepared using Na₂HAsO₄ · 7H₂O (99.995%, Sigma-Aldrich) and NaAsO₂ (>90.0%, Sigma Aldrich), respectively. As₂O₃ (99.995%, Sigma Aldrich) was used as a calibration standard for atomic absorption spectroscopy (AAS). All the solutions were prepared with deionized water (18 MΩ cm⁻¹, Milli-Q, Merck KGaA, Germany).

A series of Nd-Fe-B magnets (N35, 263-287 kJ/m³ BH, 1170-1210 mT flux density by Powermagnet - Germany) was used for the nanoparticles control (magnetic driving and separation).

2.2 Synthesis of maghemite nanoparticles (SAMNs)

The synthesis method involves several steps (Magro et al., 2012): 10 g of FeCl₃ · H₂O was dissolved in 800 mL of MilliQ grade water at room temperature under vigorous stirring. A NaBH₄ solution 2 g in ammonia (3.5%, 100 mL, 4.86 mol/mol Fe) was then added to the mixture quickly turning the system immediately to a black colour. After the reduction reaction occurred, the temperature of the system was increased to 100 °C and kept constant for 2 hours. The product prepared at this temperature shows high stability and superparamagnetic behaviour with a strong magnetic response. After ageing at room temperature for 2 hours, the resulting magnetic product was separated through the application of an external magnet and washed several times with water. After that, it was thermally treated for 2 hours at 400 °C. The final product is a pure stoichiometrically maghemite characterized by 10 to 12 nm nanoparticles with a polydispersity index comprised from 1.02 to 1.05 and a specific chemical behaviour resulting in the ability to reversibly bind organic and biological molecules (Magro et al., 2012; Magro et al., 2014;

Bonaiuto et al., 2016; Magro et al., 2016; Magro et al., 2017; Magro et al., 2018; Magro et al., 2019). Under these conditions, at the end of the process, 2 g of maghemite nanoparticles were produced with a yield of 68%. Successively, nanoparticles were dispersed in 3.5 L of MilliQ grade water through ultrasonic bath treatment (48 kHz, 50 W) for 3 hours, giving a stable colloidal suspension up to six months.

The synthesis method, carried out totally in water without the use of toxic reagents, is protected by an international patent (Magro et al., 2010).

2.3 Determination of Arsenic

Arsenic concentration in solution was determined by electrothermal atomization-atomic absorption spectroscopy (ETA-AAS), using a graphite furnace (ContrAA 600; Analytik Jena AG, Germany), equipped with a high-resolution Echelle double monochromator (spectral bandwidth of 2 pm at 200 nm) (Figure 1).

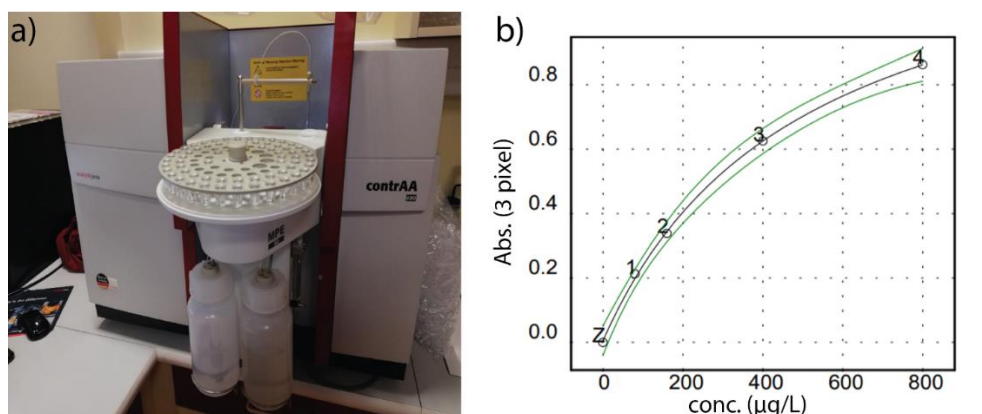


Figure 1. a) ETA-Atomic Absorption Spectrometer; b) calibration curve with standard As solution (TraceCERT) between 0.01 mg L^{-1} and 0.8 mg L^{-1}

A xenon lamp was used as a continuum radiation source, and an absorption line for As, corresponding to a wavelength of 193.696 nm, was used for the analysis. The calibration curve (Figure 1,b) was built with standard solutions of As for atomic absorption spectroscopy (AAS) measurements using TraceCERT commercial standards (with a concentration of 1000 mg L^{-1} of an element in nitric acid) purchased from Fluka Inc. The detection limit of the ETA-AAS technique was 10 ppb.

2.4 Determination of hexavalent Chromium

Cr^{VI} was detected by the diphenylcarbazide method (American Public Health Association, 1975; Petala et al., 2013). In the presence of Cr^{VI} ions, 1,5-diphenylcarbazide form a pink complex in a 12 mM phosphoric acid aqueous solution. The concentration of Cr^{VI} was calculated from the absorbance at 542 nm by spectrophotometry after 10 min incubation. For concentrations higher than 30 mg L⁻¹, Cr^{VI} was also determined by measuring the disappearance of its absorbance at 339 nm ($\epsilon_{339\text{nm}} = 1.48 \times 10^3 \text{ M}^{-1} \text{ cm}^{-1} \text{ Cr}^{\text{VI}}$) (Xia et al., 2002).

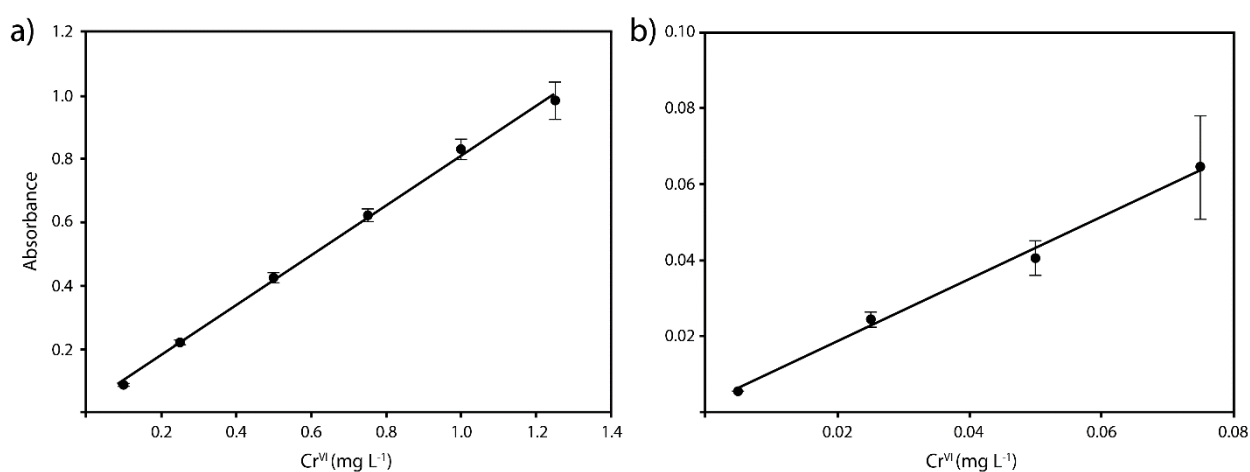


Figure 2. Calibration line with standard Cr^{VI} solutions: a) Cr^{VI} concentration between 0.1-1.2 mg L⁻¹; b) Cr^{VI} concentration between 0.005-0.075 mg L⁻¹

The linearity of the method for determining Cr^{VI} concentrations was tested for concentration ranging from 0.1 mg L⁻¹ to 1.2 mg L⁻¹ and 5 $\mu\text{g L}^{-1}$ to 75 $\mu\text{g L}^{-1}$ (Figure 2a-b respectively) giving very good linearity ($R^2=0.998$ and 0.994 respectively) allowing to detect Cr^{VI} presence down to the legal limit in groundwater.

Hereafter are reported the two equations (Eqs.11-12) to convert absorbance value to Cr^{VI} concentrations for the two ranges.

$$[\text{Cr}^{\text{VI}}] (\text{mg L}^{-1}) = [(\text{Abs}_{540\text{nm}} - 0.01992) / 0.7873] * 10 \quad (11)$$

$$[\text{Cr}^{\text{VI}}] (\text{mg L}^{-1}) = [(\text{Abs}_{540\text{nm}} - 2.035 * 10^{-3}) / 0.8201] * 10 \quad (12)$$

2.5 Physical and chemical characterisation of Ex-Stoppani groundwater

All the elements were measured by using inductively coupled plasma coupled to a mass spectrometer (ICP-MS) Agilent Technologies 7700ICP-MS system (Agilent Technologies International, Japan, Ltd., Tokyo, Japan). Cr^{VI} was measured spectrophotometrically according to dyphenilcarbazine method (see paragraph 2.4).

HCO₃⁻, F⁻, Cl⁻, NO₃⁻, SO₄⁻ were determined through Chromatographic analysis performed with an ion chromatograph, model DX-600 (Dionex, Sunnyvale, CA, USA) that included a gradient pump GP40. Groundwater pH was measured after daily calibration using a crison basic 20 pH meter after addition of 0.5M KCl to the solution.

2.6 Characterization of SAMNs, SAMN@metal complexes and Stoppani COPRs

A wide multi-technique approach was necessary for a deeper characterisation of the investigated material, for simplicity, the list of principals employed techniques and their purposes are summarized in Table 1.

Zeta-potentials and size-distribution of SAMNs and SAMN@metal complexes were measured in water solutions on a Zetasizer Nanoparticle analyser ZEN3600 (Malvern Instruments, UK) at T= 298 K. Triplicate experiments were performed. Statistical analysis on the size-distribution was obtained by using the LogNormal-function. FTIR analyses were performed using a Fourier Transform Infrared (FT-IR) spectrometer (Thermo Scientific Nicolet iS5). ATR-FTIR spectra of samples were obtained with a ZnSe window. Each spectrum was recorded in the 4000-500 cm⁻¹ wavenumber range with 50 scans at a resolution of 2 cm⁻¹. X-ray photoelectron spectroscopy (XPS) measurements were carried out by a PHI 5000 VersaProbe II XPS system (Physical Electronics) with monochromatic Al-K_α source (15 kV, 50 W) and photon energy of 1486.7 eV. All the spectra were measured in the vacuum at 1.3 x 10⁻⁷ Pa and room temperature (21 °C). The analysed area of each sample was a spot of 100 μm in diameter. The survey spectra were measured with a pass energy of 187.850 eV and energy step of 0.8 eV, while for the high-resolution spectra pass energy of 23.500 eV was used and an energy step of 0.2 eV. Dual-beam charge compensation was used for all measurements. The spectra were evaluated with the MultiPak (Ulvac - PHI, Inc.) software. All binding energy (BE) values were referenced to the C1s carbon peak at 284.80 eV.

Table 1. Analytical techniques employed and their purposes

Analytical Technique	Analyzed sample	Investigation purpose
Dynamic Light Scattering (DLS)	SAMNs, SAMN@Cr, SAMN@As	hydrodynamic size measurement
		Zeta potential (surface charge)
Fourier Transform Infrared Spectroscopy (FTIR)	SAMNs, SAMN@As	As and Cr surface complexation
	COPRs	Cr ^{VI} -bearing phases characterization
X-Ray photoelectron spectroscopy (XPS)	SAMNs, SAMN@Cr, SAMN@As	Elemental composition and electronic state
High Resolution Transmission Electron Microscopy (HRTEM)	SAMNs, SAMN@Cr, SAMN@As	Morphological organization
		Chemical mapping
X-Ray Powder Diffraction (XRPD)	SAMNs, SAMN@As	Bulk mineralogical characterization and phase identification
	COPRs	
Transmission ⁵⁷ Fe Mössbauer spectroscopy	SAMNs, SAMN@Cr, SAMN@As	Phase composition and nature of iron oxide
Environmental Scanning Electron Microscope (ESEM)	COPRs	Morphological and Chemical characterization of Cr ^{VI} -bearing phases
Micro-Raman spectroscopy (μ -Raman)	SAMNs, SAMN@Cr	Cr ^{VI} surface complexation
	COPRs	Identification of soluble Cr ^{VI} phases

Transmission electron microscopy (TEM) images were taken on a JEOL JEM-2010 transmission electron microscope equipped with a LaB₆ cathode operated at an accelerating voltage of 160 kV with a point-to-point resolution of 0.194 nm. A drop containing the sample dispersed in high-purity distilled water was placed onto a holey carbon film supported on a copper-mesh TEM grid (SPI Supplies, USA) and air-dried at room temperature. High-resolution transmission electron microscopy (HRTEM) images were obtained using an HRTEM TITAN 60-300 microscope with an X-FEG type emission gun, operating at 80 kV, equipped with a Cs image corrector and a detector providing scanning transmission electron microscope/high angle annular dark-field imaging (STEM/HAADF) option. Elemental chemical mappings were obtained by combining STEM and EDS technique. For HRTEM, STEM/HAADF, and STEM/EDS analyses, powder samples were dispersed in ethanol and ultrasonicated for 5 min. One drop of the resulting suspension was then placed on a copper grid covered with a holey carbon film and allowed to dry at room temperature. X-ray powder diffraction (XRPD) patterns were acquired at room temperature on an X'Pert PRO MPD

(PANalytical, The Netherlands) instrument in Bragg–Brentano geometry with iron-filtered Co-K α radiation (40 kV, 40 mA, $\lambda = 0.1789$ nm), equipped with an X'Celerator detector. The powder sample was placed onto a rotating zero-background Si slide; the angular range was set as $2\theta = 3 - 85^\circ$, with a step size of 0.017° and a scan speed of $0.0061^\circ \text{ s}^{-1}$. The identification of the crystalline phases in the experimental XRD pattern was obtained using the X'Pert High Score Plus software that includes a PDF-2, Pan-ICSD and COD (Crystallography Open Database) databases.

Transmission ^{57}Fe Mössbauer spectra were collected by a home-made Mössbauer spectrometer, operating in a constant acceleration regime and equipped with 50 mCi $^{57}\text{Co}(\text{Rh})$ radioactive source. To fit the recorded ^{57}Fe Mössbauer spectra, the MossWinn software package was used. The isomer shift values were referenced to α -Fe foil at room temperature.

The X-ray Photoelectron Spectroscopy (XPS) measurements were carried out with the PHI 5000 VersaProbe II XPS system (Physical Electronics) with monochromatic Al-K α source (15 kV, 50 W) and photon energy of 1486.7 eV. All the spectra were measured in the vacuum at 1.3×10^{-7} Pa and room temperature (21°C). The analysed area of each sample was a spot of 100 μm in diameter. The survey spectra were measured with a pass energy of 187.850 eV and energy step of 0.8 eV, while for the high-resolution spectra pass energy of 23.500 eV was used and an energy step of 0.2 eV. Dual-beam charge compensation was used for all measurements. The spectra were evaluated with the MultiPak (Ulvac - PHI, Inc.) software. All binding energy (BE) values were referenced to the carbon peak C1s at 284.80 eV.

Raman spectra were acquired using the Thermo Scientific DXR Raman microscope (Thermo Electron, U.S.A.) equipped with a laser operating at 532 nm. The laser power on the sample was set to 10 mW. Exposition time was set to 5 s with three expositions per spectrum. Sixteen spectra were averaged to get one experimental data point.

The bulk-element composition (major, minor, and trace elements) of the seven COPR samples was performed through ICP-OES, ICP-MS (trace elements) and Aqua Regia ICP-AES/MS methods; the total S and C were determined by Leco analysis (ACME Laboratory, Bureau Veritas, Vancouver, Canada).

Scanning electron microprobe analyses were performed with an "SEM VEGA3 TESCAN" (DISTAV, Genova University) operated at 20 kV and equipped with an "EDAX-APOLLO_X SDD" energy-dispersive (EDS) X-ray spectrometer. 1.2 nA beam current, and 5-10 μm

beam diameter. COPRs samples were embedded in epoxy resin, polished to produce a smooth, flat surface, and coated with a thin layer (20 nm) of vacuum-evaporated carbon. Pristine material and dry polished thin sections for characterisation of soluble Cr^{VI}-bearing phases were analysed with Environmental Scanning Electron Microscope FEI ESEM Quanta 200 in low vacuum operating at 20 kV coupled with EDS, with Dual BSD detector.

3. Synthesis of colloidal maghemite nanoparticles with novel and peculiar chemical properties

3.1. Abstract

Among nanosized iron oxides, peculiar maghemite nanoparticles, called surface active maghemite nanoparticles (SAMNs), stand out for the excellent colloidal stability in water without any coating and the unique ability to specifically bind selected molecules. Herein, the wet synthesis of SAMNs was described along with their evolution into maghemite nanocrystals by characterising the crucial intermediates by High-Resolution Transmission Electron Microscopy (HR-TEM), High-Angle Annular Dark-Field Scanning Transmission Electron Microscopy (STEM-HAADF), X-Ray Powder diffraction (XRPD), Fourier Transform infrared spectroscopy (FTIR) and Mössbauer spectroscopy. Moreover, the surface of the final nanomaterial was probed with As^{III} and As^V by x-ray photoelectron spectroscopy. SAMN's selectivity toward As^{III} and As^V is strictly correlated with the ability of ligands of restructuring the nanomaterial at the crystal truncation. In particular, the integration of oxygen atoms provided by arsenite and arsenate into the maghemite lattice leads to the restoration of the Fe^{III} dangling bonds at the nanoparticle surface. The present study, besides enriching the chemistry of iron oxides, stimulates novel synthetic routes for classical materials and evidence novel and unpredictable properties at the boundary with the solvent.

3.2 Introduction

Magnetic nanoparticles constituted of iron oxides, namely maghemite (γ -Fe₂O₃) and magnetite (Fe₃O₄), play an important role in recent applications of nanotechnology in biomedicine and biotechnology (Magro et al., 2017). In fact, among magnetic materials, nanosized iron oxides possess several superior properties, including magnetic (e.g. superparamagnetism, high values of saturation magnetization, easy control by small magnetic fields) and biochemical (e.g. non-toxicity, biodegradability, biocompatibility), which empower their applications in different fields of medicine (Petros and Desimone, 2010; Meyers et al., 1963) and biotechnology (Hola et al., 2015). Indeed, particles, such as cross-linked iron oxide (Schellenberger et al., 2002; Wunderbaldinger et al., 2002), ultrasmall

superparamagnetic iron oxide (Saito et al., 2012) and monocrystalline iron oxide nanoparticles (Wang et al., 2012) have all been developed as imaging contrast agents in magnetic resonance imaging (MRI), drug delivery carriers (Wang et al., 2013; Magro et al., 2019) and magnetofection devices (Schillinger et al., 2005; Heiligtag and Niederberger, 2013; Estelrich et al., 2015).

Most of the proposed procedures aimed at the synthesis of iron oxide nanoparticles involve solid-state decomposition of iron complexes (Ali et al., 2016), or the utilization of high purity organic solvents (Wu et al., 2016) and/or an oxygen-free environments (Bandhu et al., 2009), expensive surfactants (Gupta and Gupta, 2005) or costly instrumentation (Santillán et al., 2017) as reviewed by Wu (Wu et al., 2015). Moreover, the surface of these magnetic nanoparticles is generally coated with compounds, mostly of organic nature, for allowing their dispersibility in water and favoring specific interactions with biological macromolecules (Reddy et al., 2012).

A synthetic route for maghemite nanoparticles carried out in aqueous ammonia starting from FeCl_3 , and a reductant (NaBH_4) in the presence of atmospheric oxygen was already developed by the research group (Magro et al., 2012b). The synthetic reaction is low cost, easily upgradable and does not require any organic solvent. The final synthetic product is composed of spherical maghemite nanoparticles, characterised by a mean diameter of about 10 nm, which form very stable colloidal suspensions in water without any surface coating. As prepared nanoparticles are characterized by the ability to reversibly bind specific molecules on their bare iron oxide surface in water by self-assembly (Sinigaglia et al., 2012; Magro et al., 2015), and the presence of solvent accessible under-coordinated iron(III) sites on nanoparticle surface was demonstrated (Magro et al., 2014). Due to the peculiar surface chemistry, this nanomaterial was called SAMNs (surface active maghemite nanoparticles), and was used for different biotechnological applications for biomolecule purification and biosensing (Sinigaglia et al., 2012; Magro et al., 2013; Baratella et al., 2013), and for water remediation from toxic metals (Magro et al., 2016). However, the features leading to the unique and multifaceted surface chemistry of these nanoparticles are not fully understood. Herein, the synthetic process of the nanomaterial was examined by characterising the crucial intermediates, and the surface structure of the final product were explored by studying the binding of As^{V} and As^{III} as probes by x-ray photoelectron spectroscopy (XPS). Noteworthy, As^{III} emerged as an elective probe leading to a substantial restoration of the nanocrystal surface.

Besides providing a contribution to the knowledge of iron chemistry in water, the present study proposes a new strategy to synthesise maghemite nanoparticles with peculiar chemical properties, and with favourable features for their easy applications in many fields.

3.3 Results and Discussion

A complex multicomponent system is formed during the wet reaction (S0 sample), which turns into monodispersed nanostructured maghemite particles by simple ageing in water (S1 sample). These nanoparticles are partially amorphous, but already display a spherical shape and a diameter around 10 nm, comparable with the morphology of the final product (S2 sample, SAMNs). Most importantly, S1 is the sole material after the wet reaction, and no trace of iron-based byproducts can be found at the accomplishment of the ageing period in water. The curing step at 400° C confers the ultimate crystallinity to nanoparticles leading to stoichiometric maghemite (S2). Thus, to describe the synthetic process, the structural and morphological transformations at the beginning and the end of the wet reaction were investigated. Indeed, this reaction period represents the crucial step of the synthetic process. In particular, to rationalise the fundamental role of the prolonged incubation in water during the development of the nanostructured iron oxide, samples were collected after 90 min from the NaBH₄ addition (S0 sample), and after the 24 hours ageing period at RT (S1 sample). Moreover, the effects of the curing at 400°C were described, and the surface properties of the obtained nanomaterial (S2 sample) were studied by analysing the interaction with arsenite and arsenate ions, which were used as probes to gather insights on the properties of surface under-coordinated Fe^{III} in the presence of ligands.

Chemical and structural transformations during the wet reaction

Zero-field ⁵⁷Fe Mössbauer spectroscopy was used to study the composition and structure of iron species during the synthetic process. The Mössbauer spectrum of the S0 sample is presented in Figure 3a and can be interpreted as the sum of the contributions of several iron species. Such a complex spectral profile can be fitted with two sextets. According to the low value of the internal field, one sextet can be ascribed to metallic iron (component 2 in Figure 3a and Table S1). The presence of zero-valent iron in this initial step is not surprising as it is the expected product from the FeCl₃ reduction by NaBH₄ (Martin et al., 2008). The other sextet is due to an oxidic Fe^{III} compound, whose parameters are compatible with

maghemite. Thus, it is worth to note that $\gamma\text{-Fe}_2\text{O}_3$ was already present at this stage, exceeding zero-valent iron in the sample (Table S1).

Furthermore, the most relevant spectral component (54 %) underwent a fast-magnetic relaxation not blocked even at 12 K (not shown). The material producing this broad and unfittable component can be assumed an amorphous Fe^{III} phase. The remaining Mössbauer absorption was attributed to a paramagnetic Fe^{III} compound, not easily identifiable.

Differently from the variety of spectral features of the S0 sample, the Mössbauer profile of the S1 sample was characterised by a single sextet (Figure 3b). The external components of the spectrum were slightly asymmetric and can be fitted with two magnetic sextets, with typical hyperfine parameters of maghemite (Table S1). As an alternative, the spectrum can be fitted with a distribution of internal field values and, again, the average parameters are compatible with those of maghemite. In any case, the asymmetry may be ascribed either to the strong interparticle interactions due to a high fraction of interfacial Fe^{III} with relaxing magnetic hyperfine fields or to a very low crystallinity. Noteworthy, while maghemite represented a minor component (22 %) at the end of the reduction step (sample S0), it was the sole species at the end of the prolonged incubation in the water at RT (sample S1).

Therefore, as the ageing period in water led to the complete disappearance of the prevalent unknown Fe^{III} component, of metallic iron and, as well, of the minor paramagnetic iron phase, it can be assumed that the wet reaction involves the spontaneous transformation of all different iron species of S0 into $\gamma\text{-Fe}_2\text{O}_3$.

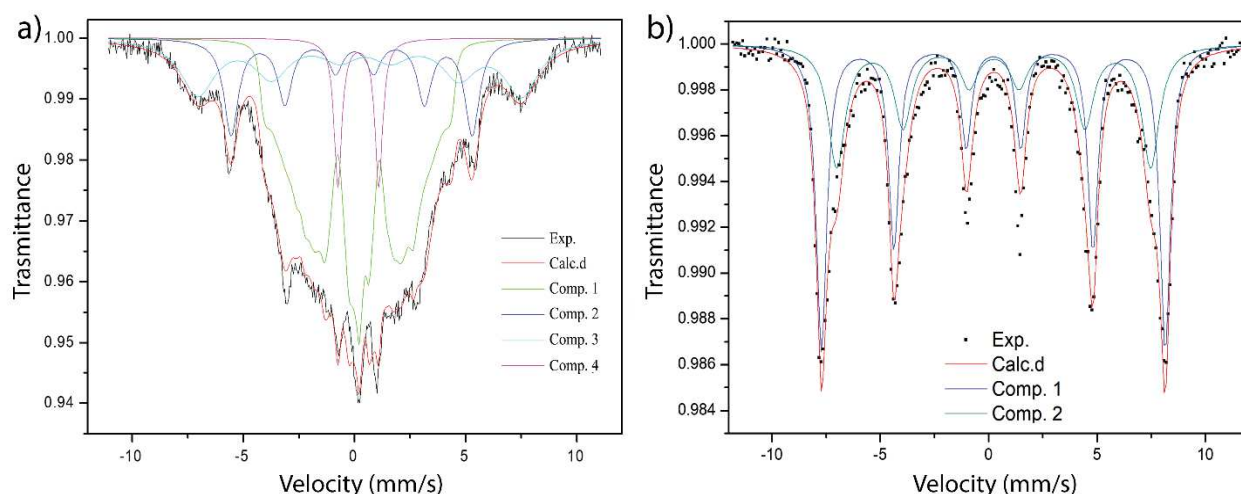


Figure 3. Mössbauer spectra of a) S0 and the b) S1 samples at room temperature.

The XRPD characterisation of the S0 and S1 samples was carried out at room temperature (Figure 4A and 5A). S0 displays a high background and broad, low-intensity diffraction maxima attributable to metallic iron and maghemite or magnetite (magnetite can be excluded by Mössbauer spectroscopy) (Figure 3a). The high background is related to a considerable amount of amorphous materials, which is plausibly due to the contribution of the most abundant Fe^{III} component recorded by Mössbauer spectroscopy (Table S1). XRPD analysis of the S1 sample showed a reduction of the background XRPD signal, the disappearance of the Fe⁰ line and the appearance of a broad maghemite line, further confirming Mössbauer analysis. The only other phase in the S1 sample was sodium chloride (NaCl), representing a residual product of the synthesis (Figure 5A).

The thermally induced phase transformations and crystalline size of S0 and S1 samples were investigated by in situ x-ray powder diffraction (XRPD) in the 25°C to 700°C temperature range. Samples for thermal treatment were mounted on flat sample stage (in black), and HTK16 temperature camera (in red) differ only for the presence of Pt heating filament lines (Pt) (Figure 4A). Modifications of the diffraction patterns of the S0 sample were evidenced between T = 350°C and T = 500°C (Figure 4B) with the Fe (110) line ($2\theta = 44.83^\circ$) fading out while the intensity of the hematite (104) line at $2\theta = 33.05^\circ$ line increased.

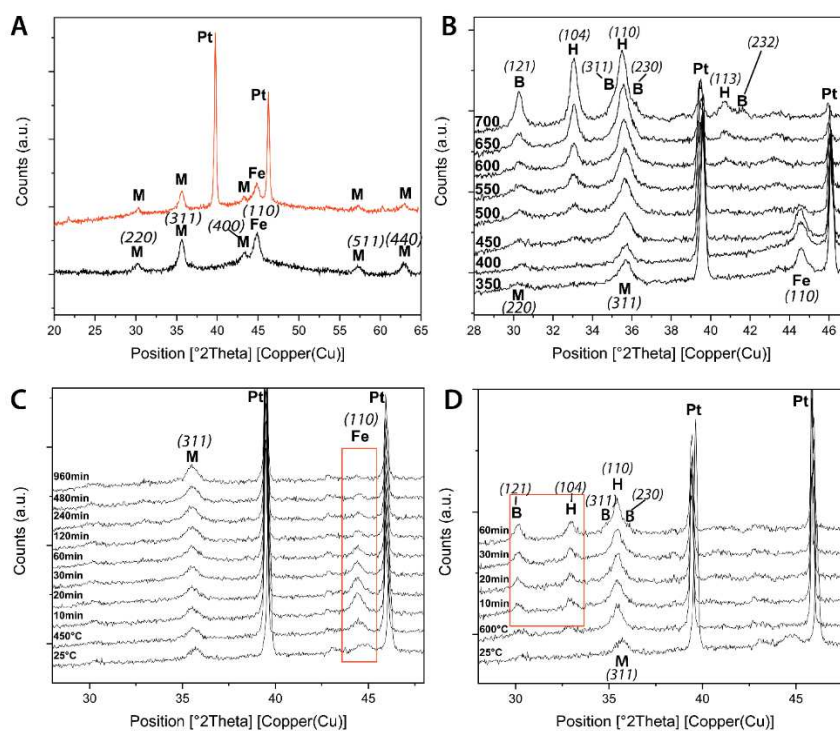


Figure 4. In situ x-ray powder diffraction of the S0 sample. A) X-ray diffraction patterns for S0 sample at room temperature mounted on flat sample stage (in black) and HTK16 temperature camera (in red). B) Evolution of S0 sample during the Fe^0 - $\gamma\text{-Fe}_2\text{O}_3$ - $\alpha\text{-Fe}_2\text{O}_3$ phase transformation $350^\circ\text{C} < T < 700^\circ\text{C}$; C) Evolution of Fe (110) line (red box) at $T = 450^\circ\text{C}$; D) kinetic of $\gamma\text{-Fe}_2\text{O}_3$ to $\alpha\text{-Fe}_2\text{O}_3/\text{Fe}_3\text{BO}_6$ transformation at $T = 600^\circ\text{C}$. M = maghemite ($\gamma\text{-Fe}_2\text{O}_3$); H = hematite ($\alpha\text{-Fe}_2\text{O}_3$); B = Fe_3BO_6 ; Pt = Platinum. Numbers in parenthesis indicate (hkl) indexes

Differently, X-ray diffraction patterns of the S1 sample showed no significant changes up to $T = 500^\circ\text{C}$ (not shown). At $T = 550^\circ\text{C}$, hematite (104) line at $2\theta = 33.05^\circ$ appeared and at $T = 600^\circ\text{C}$ hematite (012) line appeared at $2\theta = 24.19^\circ$ as maghemite (220) line ($2\theta = 30.35^\circ$) faded out (Figure 5C). The complete phase transformation from maghemite to hematite occurred during the thermal treatment.

On these bases, the kinetics of polymorphous transitions of S0 and S1 samples were studied by *in situ* X-ray diffraction in the already described temperature range. More specifically, in order to kinetically characterise the modifications of the S0 system, a punctual investigation was carried out and the isothermal evolution was monitored over 960 min at four temperature values (350°C , 400°C , 450°C and 600°C). No significant modifications of XRPD signals were observed at $T = 350^\circ\text{C}$ and 400°C (Figure S1A and S1B), while at $T = 450^\circ\text{C}$, significant variations of the Fe (110) line at $2\theta = 44.83^\circ$ occurred (Figure 4C). Specifically, the Fe (110) line intensity after an initial increase (within 10 min), progressively faded out after 480 min. After this point, only the background signal was found. The initial intensity increase of the Fe (110) line was probably related to a transitory increase of crystallite size of zero-valent iron. During the same period, no significant variations of the maghemite (311) line at $2\theta = 35.61^\circ$ were observed (Figure 4C). At 600°C , the hematite (104) line gradually grow up (Figure 4D). The thermal treatment of the S0 sample highlighted progressive oxidation of the iron cores along with the formation of maghemite and the subsequent progressive transformation into $\alpha\text{-Fe}_2\text{O}_3$. Most importantly, a new peak at $2\theta = 24.3^\circ$, unequivocally matching the (121) of Fe_3BO_6 appeared (Figure 4D). Unfortunately, the (311) and (230) lines of Fe_3BO_6 overlapped in the (110) lines of hematite and maghemite. The detailed study of the kinetics of S0 evolution at 600°C (see Figure 4D) showed a very fast formation of Fe_3BO_6 , which was already visible after 10 min.

The S1 sample evolution during the maghemite to hematite phase transformation at 600°C was monitored, and quantitative measurements of phase transitions were obtained by comparing diffraction intensities and phase chemical compositions (see Figure 5D). The

mass absorption coefficients for maghemite and hematite are the same ($\mu = 54.18 \text{ cm}^2\text{g}^{-1}$), allowing a direct quantification from the area of diffraction lines. However, the most intense peak of maghemite (311) is unfortunately overlapped in the (110) of hematite. To avoid overlapping, the hematite (104) peak and the maghemite (220) peak were used for the quantitative analysis, according to Belin et al., (2007). Two aspects outlined by the overall XRPD study deserve particular attention. Firstly, the thermal treatment of the S0 sample led to the crystallisation of iron borates, which disappeared as a consequence of the ageing in water for the formation of the S1 intermediate. Possibly, the iron-boron interactions characterising the S0 sample were, to some extent, labile. Indeed, in the absence of the prolonged incubation in water, the transformation of a significant fraction of S0 into maghemite was not allowed, and the material turned into crystalline Fe_3BO_6 upon heat treatment. Up to authors knowledge, the observed formation of iron oxyborate stands out as it occurred at a relatively low temperature with respect to already described analogous processes and followed the fastest reported kinetics for Fe_3BO_6 crystallization (Nurmi et al., 2005; Biryukov et al., 2016; Ozer and Icten, 2019; Çam, İ. and Timuçin, M., 2004; Diehl and Friedrich, 1976; Rowsell et al., 2001). Indeed, $\text{Fe}_2\text{O}_3\text{-B}_2\text{O}_3$ systems generally crystallise at around 900 °C during several tenths of hours (Biryukov et al., 2016; Ozer and Icten, 2019; Diehl and Friedrich, 1976).

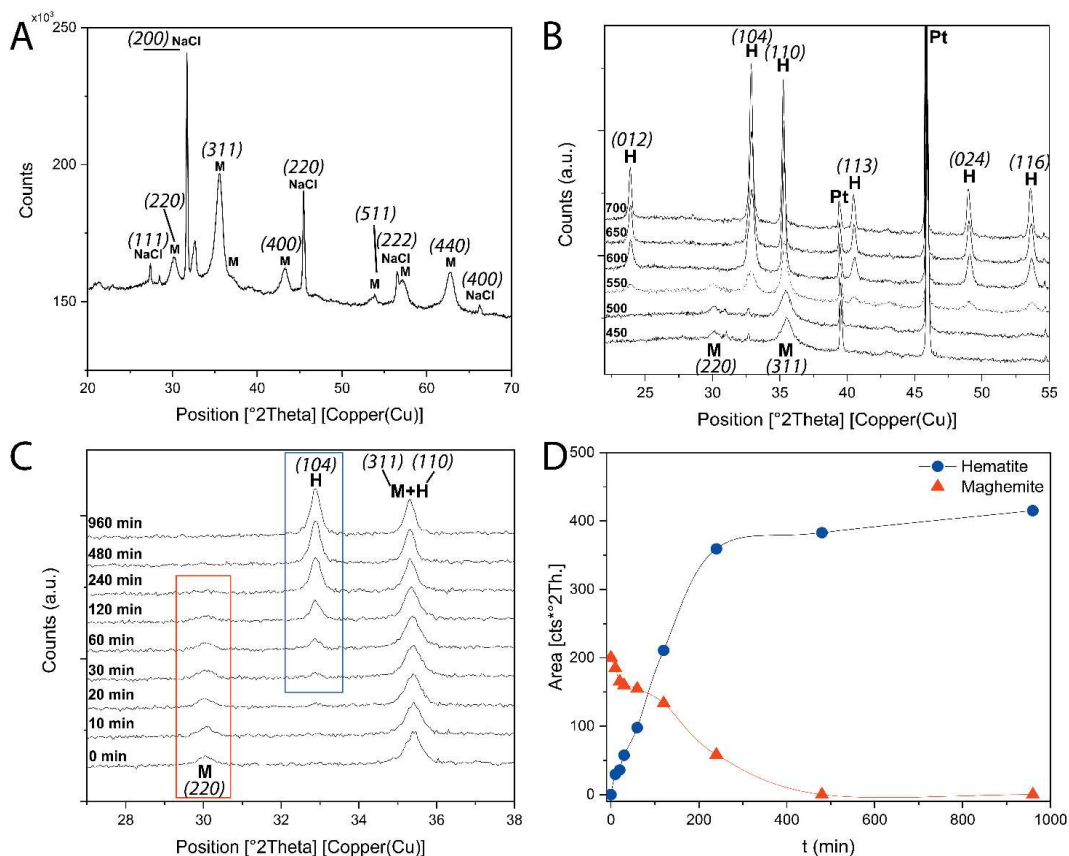


Figure 5. A) X-ray diffraction pattern of S1 sample at $T = 25^{\circ}\text{C}$; B) Evolution of S1 sample during $\gamma\text{-Fe}_2\text{O}_3 - \alpha\text{-Fe}_2\text{O}_3$ phase transformation; C) Kinetic of $\gamma\text{-Fe}_2\text{O}_3 - \alpha\text{-Fe}_2\text{O}_3$ phase transformation at $T = 600^{\circ}\text{C}$; D) Variations of area of (104) line of hematite and (220) line of maghemite and relative amount of the two phases with time at $T=600^{\circ}\text{C}$

Uncommonly, the Fe_3BO_6 lattice was produced at 700°C in about 60 min (Çam and Timuçin, 2004) or at 600°C using 5 nm $\alpha\text{-Fe}_2\text{O}_3$ nanoparticles as precursor over two days curing (Rowell et al., 2001). Plausibly, the here reported results reflect the presence of unprecedented iron borate phases as starting material. Hence, the appearance of the Fe_3BO_6 crystalline phase indicated that boron was not merely physical adsorbed on the polyphasic S0 system.

On the contrary, boron should be necessarily involved in the chemical interactions with one or more of the iron mentioned above species identified by Mössbauer spectroscopy in the S0 sample (Table S1).

It should be noted that Fe_3BO_6 crystallisation occurred with the same time evolution of the maghemite to hematite phase transformation. In particular, the line at $2\theta = 30.28^{\circ}$ of Fe_3BO_6 (121) and the line at $2\theta = 33.03^{\circ}$ of hematite grew up coherently (Figure 4D), suggesting a

strong relationship among the different components of the S0 sample. In this view, it should be recalled that S1 sample was exclusively composed of maghemite, and no trace of Fe_3BO_6 was recorded upon the thermal treatment, indicating that borates interact with other iron compounds of the S0 sample, but not with maghemite.

The presence of borate on the surface of zero-valent metal nanoparticles was already described (Bönnemann et al., 1994; Sardar et al., 2007; Nurmi et al., 2005). Turabik and Simsek demonstrated that NaBH_4 was important not only as a reductive agent but played a role in the control of particles size and consequently, nanoparticle properties (Turabik and Simsek, 2017). It is generally assumed that zero-valent iron nanoparticles present a core-shell morphology, in which zero-valent iron is the core and iron oxide/hydroxide constitute the shell. The interaction of boron with hydrous ferric oxides, as boric acid (trigonal molecular structure) or borate (tetrahedral molecular structure), was documented (Su and Suarez, 2007). Interestingly, the fraction of the Fe_3BO_6 phase developed upon the thermal treatment of the S0 sample was similar to the content of the amorphous Fe^{III} material estimated by Mössbauer spectroscopy. Taking into account that the amorphous Fe^{III} phase is probably the oxygen-rich wide lamellar morphology observed by electron microscopy (see hereafter) and can be interpreted as the amorphous ferrihydrite product of zero-valent corrosion, borate can be involved in the interaction with this precursor.

Secondly, the temperature of maghemite to hematite phase transformation of the S1 sample occurred at the higher temperature (600 °C) than that reported by Belin et al., (2007) and Machala et al., (2011). Indeed, the $\gamma\text{-Fe}_2\text{O}_3$ to $\alpha\text{-Fe}_2\text{O}_3$ transformation was reported to occur between 500 °C and 600 °C for bulk materials, while it decreases to about 200-500 °C for nanomaterials (Ennas et al., 2002). This transition was reported in the 370-600 °C range depending on the material size due to the lowering of activation energy for nanometric maghemite (Gnanaprakash et al., 2006; Belin et al., 2007). It should be taken into account that during the thermal process at 400 °C, the heterogeneous and partially amorphous nanometric maghemite of the S1 sample led to the formation of stoichiometric maghemite nanoparticles (S2, SAMNs). Very likely, the latter is endowed of an unusual high structural stability, justifying the bulk-like temperature of the γ - to the $\alpha\text{-Fe}_2\text{O}_3$ phase transition.

The S0 and S1 samples were further characterised by infrared spectroscopy (FTIR), and representative spectra are presented in Figure 6a,b. The FTIR spectrum of the S0 sample (Figure 6a) showed a band at $\approx 585\text{ cm}^{-1}$ assigned to stretching vibration of Fe-O bonds

(Multari et al., 2019); while the peaks at $\approx 1635\text{ cm}^{-1}$ and $\approx 3400\text{ cm}^{-1}$ were assigned to O-H bending and stretching vibrations respectively.

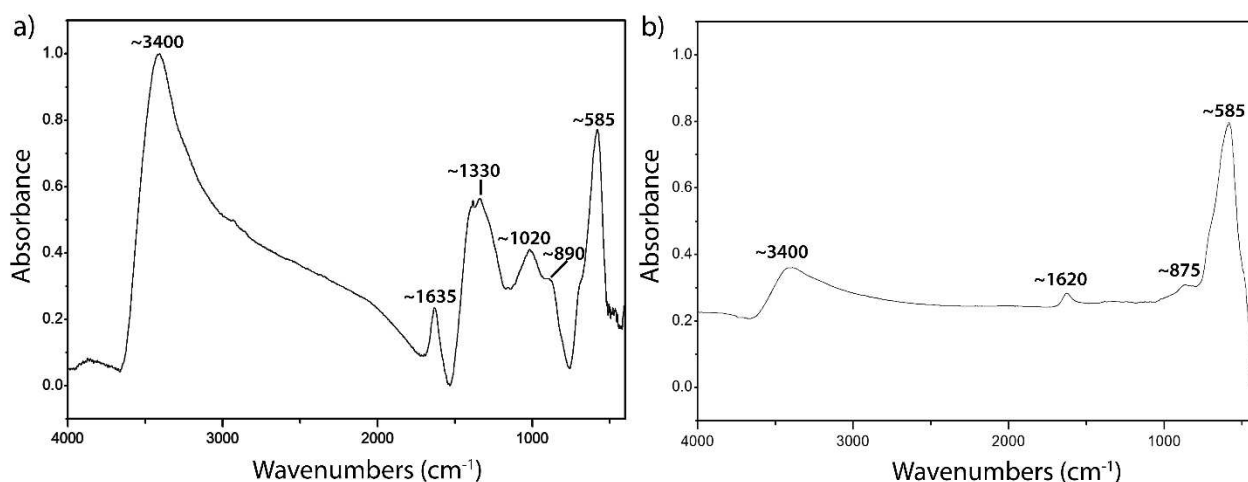


Figure 6. FTIR spectra of S0 and S1 intermediates. a) S0 intermediate; b) S1 intermediate.

The overlapping absorbances of the FTIR spectrum in the $700\text{--}1500\text{ cm}^{-1}$ region showed in Figure 6a can be assigned to the combination of trigonal and tetrahedral boron, such as B-O-H bending, trigonal B-O stretching, and tetrahedral B-O stretching. Peaks identification resulted in problematic due to peak broadness, representative of multiple overlapping. According to Peak et al., (2003), the symmetric (ν_1) and asymmetric (ν_3) B-O stretching vibrations of borate interacting with iron oxyhydroxides are evidenced at $\approx 1020\text{ cm}^{-1}$ and $\approx 1330\text{ cm}^{-1}$, respectively. In particular, the latter was attributed to an inner sphere complex between the anion and the metal oxyhydroxide.

The FTIR spectrum of S1 sample after ageing in water, in comparison with the S0 intermediate, showed the disappearance of the signals due to the B-O vibrational modes (Figure 6b). At the same time, three main iron oxide bands were preserved. Interestingly, a new feature characterised by a shoulder at 875 cm^{-1} is well visible in the FTIR spectrum and may be due to vibrations of Fe-OH bonds (Karpushenkov et al., 2010). This confirms that the evolution of the heterogeneous S0 system to maghemite (S1) involved the elimination of boron compounds and was correlated to the concomitant hydration of the material.

Finally, S0 and S1 samples were analysed by differential scanning calorimetry (DSC) in the air (see Figure 7a,b).

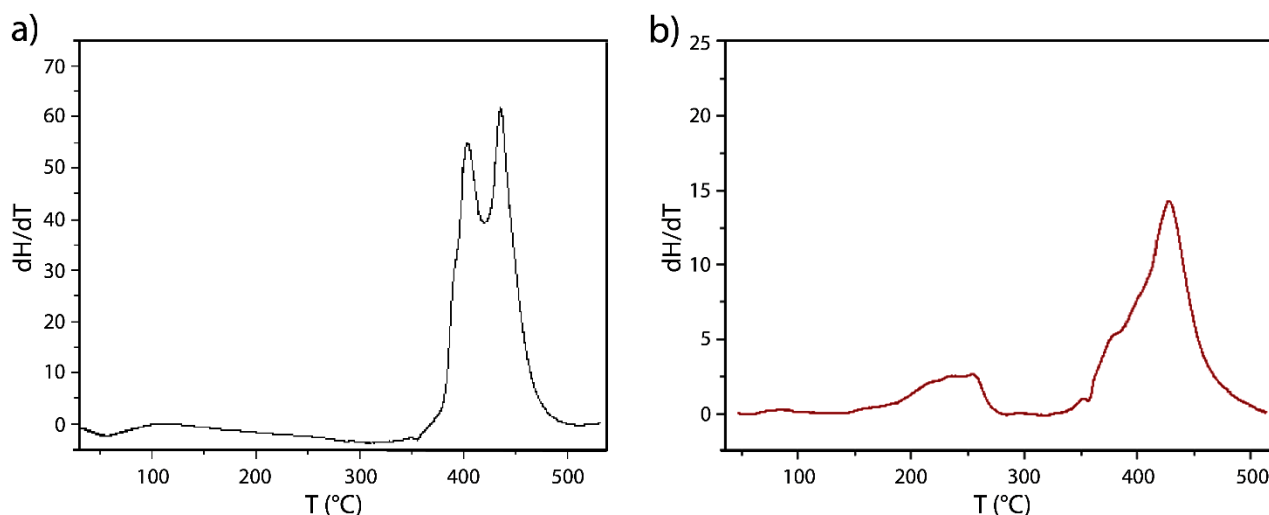


Figure 7. Differential scanning calorimetry of the S0 and S1 samples. a) S0 intermediate; b) S1 intermediate.

The DSC measurements of the S0 sample presented a hardly interpretable profile with two transitions between 400-500 °C, which can be related to a complex crystalline modification where the transition attributed to material dehydration was absent (see Figure 5a). The DSC profile of the S1 sample revealed two broad peaks related to the phase transitions at 250 and 440 °C (Figure 7b). The first can be attributed to the elimination of surface-bound water and the second to the maghemite to hematite phase transition, in agreement with XRPD findings. DSC results substantiated the FTIR observations and the role of water in the hydration of the polymorphous S0 material to form the S1 intermediate.

Summarising, the formation of maghemite, as sole species in the S1 intermediate, spontaneously took place in an ammonia containing water starting from a complex mixture of iron species (S0 intermediate). XRPD and FTIR evidenced the interactions between the different iron phases of the S0 sample and borate produced from the NaBH_4 oxidation. As a consequence, borate could be involved in the formation of complexes with amorphous oxyhydroxide phase, which were revealed by Mössbauer spectroscopy. These iron-boron compounds led upon thermal treatment to crystalline Fe_3BO_6 , and the process occurred at the lowest temperature (600 °C). Hence, borate appeared to play a role in the complex scenario of the synthetic route to colloidal naked nanosized maghemite. Furthermore, differently from already described maghemite nanoparticles, the transition of maghemite to hematite of the S1 sample took place at a significantly higher temperature evidencing the structural stability of the nanomaterial.

In order to shed light into the evolution of iron species of the isolated intermediates, a morphological characterization of the S0 and S1 samples was carried out by transmission electron microscopy (TEM), scanning transmission electron microscopy (STEM) with energy-dispersive X-ray spectroscopy (EDX) and scanning transmission electron microscopy equipped with annular dark-field imaging (STEM-HAADF).

Morphologic transformations during the wet reaction

The previously described S0 and S1 samples were further morphologically investigated. Figure 8 shows a typical STEM image of the S0 sample. In agreement with the chemical and structural studies reported in the previous paragraph, S0 is characterised by the coexistence of different iron species, distinguishable for their different morphologies, which were identified and described (see Figure 9A). Specifically, submicron (200-500 nm) electron-dense particles (Figure 9A,a), wide (0.5 – 1 μm) lamellar structures (Figure 9A,b) and extended aggregates of nanoparticles (10-20 nm) (Figure 9A,c) were observed. The radial intensity distribution of the diffraction pattern and the diffraction pattern of the S0 sample, where arrows mark the intensity peak barycenter, are presented in Figure 10B, C.

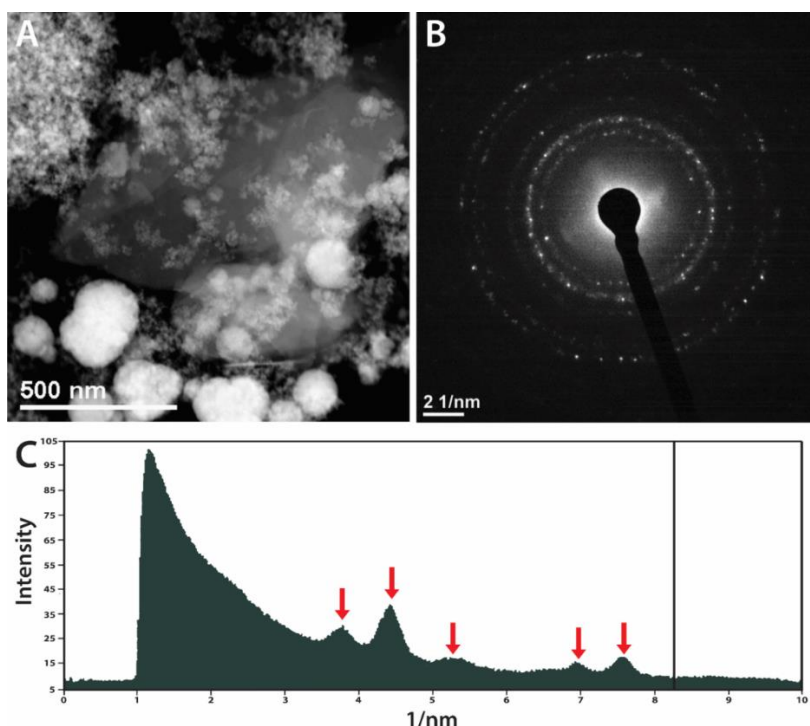


Figure 8. Scanning transmission electron microscope (STEM) images of the S0 sample.

A) STEM image of S0 sample; B) Radial intensity distribution of the diffraction pattern; C) diffraction pattern of the S0 sample.

High-resolution transmission electron microscopy (HR-TEM) and scanning transmission electron microscope equipped with annular dark-field imaging (STEM-HAADF) were carried out in the previously described iron species regions. The elemental mapping of the intensities of iron and oxygen k-alpha peaks (Figure 9, panels B and C) showed different compositions in terms of the content of iron and oxygen. Iron is highly concentrated in the large electron-dense particles and considerably less represented in nanoparticles and 2D structures. Conversely, the relatively low oxygen content was observed in large particles and higher content in the rest of the sample. The overlapping of the two k-alpha peaks intensities distribution was reported in Figure 8, panel C. The atomic fraction of iron and oxygen in the three different morphologies is reported in Table S2.

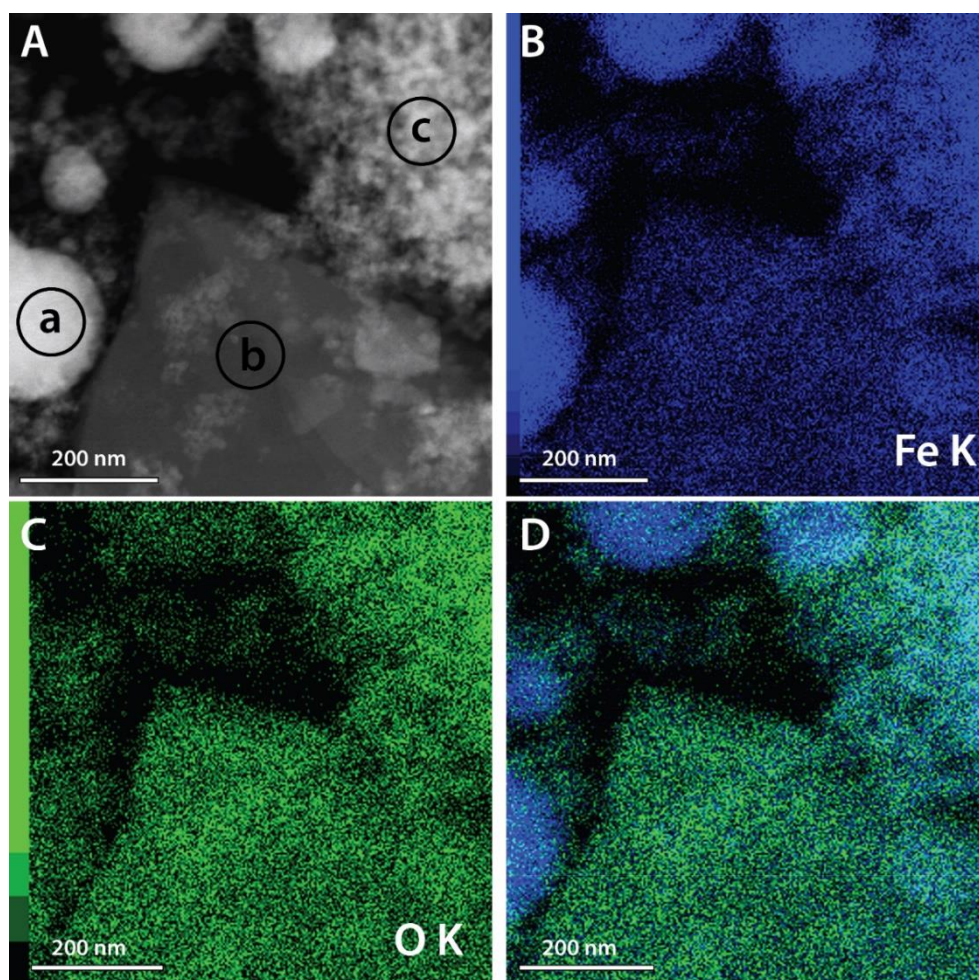


Figure 9. High-resolution transmission electron microscopy (HR-TEM) and scanning transmission electron microscope equipped with annular dark-field imaging (STEM-HAADF) of the S0 intermediate. Panel A shows the high-resolution transmission electron microscopy (HRTEM) images of S0 together with the elemental mapping (EDS) performed by electron dispersive spectroscopy (B, elemental Iron; C, elemental Oxygen; D, overlay of Fe/O).

The electron-dense particles with diameters ranging from 100 to 500 nm (Figure 9A, a) were mainly composed of metallic iron, as previously identified by Mössbauer and XRPD, comprising 87% iron and 13% oxygen. The oxygen content of the structures can be likely attributed to the surface oxidation of zero-valent iron. These large metallic structures appeared as wrapped into extended 2D structures, which can be distinguished from zero-valent iron particles (2D structures in Figure 9A,b) and were composed of 12% iron and 77% oxygen, probably oxyhydroxides layers. These planar structures, several hundred square nanometers wide, resulted non-crystalline and were characterised by TEM (Figure 10C,E). Possibly, they were due to the exfoliation of the surface of zero-valent iron particles (Figure 9A,a). These extended oxygen-rich 2D structures represent the amorphous component observed by Mössbauer spectroscopy and XRPD. Plausibly, under the reaction conditions, these 2D oxyhydroxides structures tended to crumple (Figure 10D), envisaging the formation of spherical nanoparticles in the wrinkles. Alternatively, the 2D structures could roll up forming tubular objects, roughly nanotubes (Figure 10E).

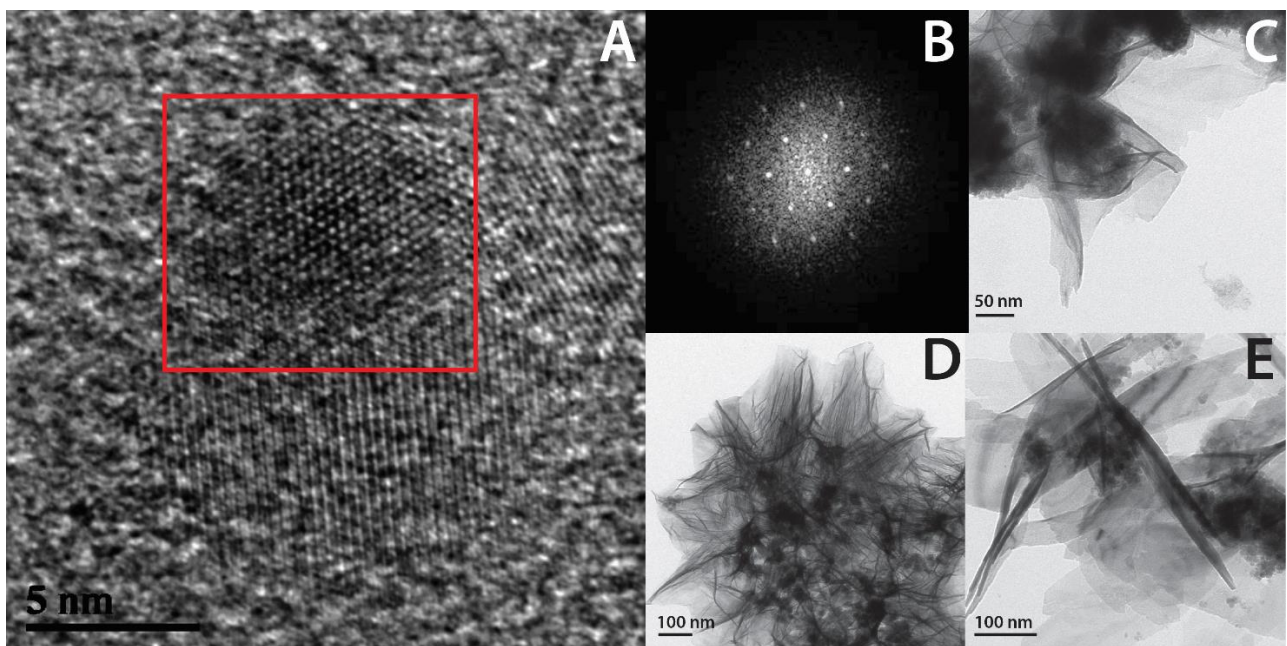


Figure 10. HR-TEM images of nanoparticle and 2D structures in the S0 sample. A) Nanoparticle; B) diffraction pattern of nanoparticles of the S0 sample; C) 2D structures of the S0 sample.

As well, the nanoparticulated material (Figure 9A,c) was analysed and resulted constituted of 61 % iron and 39 % oxygen, compatible with maghemite ($\gamma\text{-Fe}_2\text{O}_3$) or hematite ($\alpha\text{-Fe}_2\text{O}_3$). The high-resolution TEM (HR-TEM) image of the nanostructure is reported in panel A of

Figure 10, while in Figure 10B is shown the corresponding diffraction pattern. Thus, as substantiated in the previous paragraph, maghemite is present in the S0 sample and the morphological analysis evidenced monodisperse nanoparticles with a diameter of about 10 nm, hence already compatible with the nanoparticulate constituting the S1 sample, as well as with the size of SAMNs (see hereafter).

Indeed, the characterisation of the S1 sample by transmission electron microscopy (TEM) obtained after 24 hrs ageing in the water of the S0 intermediate showed only spherical nanoparticles (average diameter of about 10 nm), and a representative image is presented in Figure 11.

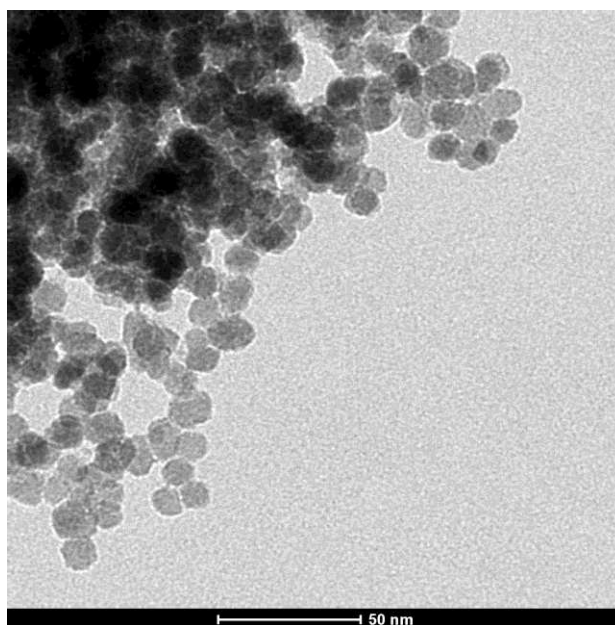


Figure 11. TEM image of the S1 sample.

Noteworthy, TEM micrographs of the S1 sample revealed the complete disappearance of the large electron-dense particles as well as of the 2D structures observed in the S0 sample, suggesting that these two species evolved into nanoparticles. Thus, the hypothesis is that zero-valent iron (submicron electron-dense particles), Fe^{III} oxyhydroxide 2D structures and the paramagnetic iron component observed by HR-TEM, STEM-HAADF and Mössbauer spectroscopy represent different moments of a system spontaneously evolving into maghemite. Considering a large amount of zero-valent iron generated during the reductive phase of the reaction in the presence of NaBH₄, as well as its known instability in water, we suggest that this component is the precursor of the Fe^{III} oxyhydroxide 2D phase, that eventually leads by crumpling to maghemite nanoparticles. Accordingly, studies on zero-

valent iron nanoparticles evidenced core-shell structures characterised by iron hydroxide - oxide coatings, and oxide shells were claimed for the protection of the metallic iron core from the rapid oxidation (Nurmi et al., 2005; Li and Zhang, 2006; Martin et al., 2008). Furthermore, the Fe^{III} oxyhydroxide 2D structures can reasonably be responsible for the interaction with borate anion.

Characterisation of the final synthesis product (S2)

Finally, the curing treatment at 400°C of the S1 sample produced a characteristic crystalline structure already observed in the S2 sample (SAMNs) (Magro et al., 2012). Briefly, during the heat treatment, the nanoparticulate S1 sample turned from partially amorphous to stoichiometric crystalline maghemite. In contrast with already reported nanostructured iron oxides (Boyer et al., 2010), these maghemite nanoparticles display high colloidal stability in water without any superficial modification or coating derivatisation. Indeed, the unusual colloidal behaviour can be substantiated by the high value of zeta potential at neutral pH ($\zeta > + 30$ mV) (Magro et al., 2017). Differently, reported maghemite nanomaterials to approach the value of zero-charge at neutral pH, explaining their very low colloidal stability in water (Lucas et al., 2007; Patel and Agrawal, 2011).

Insights on the characteristics of the surface of these maghemite nanoparticles were already provided by incubation in the presence of Fe(CN)₆K₄, and evidencing the formation of a coating of Prussian blue (Magro et al., 2014). The presence of surface under-coordinated Fe^{III} explains their unusual colloidal behaviour in water. Indeed, water molecules can act as coordinating ligands for surface Fe^{III} sites, recalling hydrous ferric oxides bearing positively charged labile OH₂^{+0.5} groups on their surface (Gu and Karthikeyan, 2005). The role played by surface under-coordinated Fe^{III} was evident as colloidal stability of SAMNs is higher in dimethyl sulfoxide (DMSO) than in water. DMSO is known to be, at the same time, a solvent and a surface stabiliser via metal ion coordination (Meek et al., 1960; Duggan et al., 2013; Magro et al., 2019).

Furthermore, SAMNs showed an unusual proclivity to selectively bind biomolecules, such as DNA resulting in an electrically conductive metamaterial (Magro et al., 2015), and bioconjugates (Magro et al., 2019). This last property was attributed to the surface topography of under-coordinated Fe^{III} sites.

Nevertheless, the comprehension of the reactivity of surface Fe^{III} sites, considered individually and not as a surface distribution, is a crucial task. Arsenic oxyacids were chosen

as small molecular probes, namely as species which cannot develop extended multiple binding, to test the specificity of under-coordinated Fe^{III} sites on nanoparticle surface. In fact, besides the interest in remediation issues, arsenic emerged as an elective probe for studying the surface structure of maghemite nanoparticles (Auffan et al., 2008). On these bases, henceforward the surface characteristics of maghemite nanoparticles were investigated by studying the binding behaviour of arsenite (As^{III}) and arsenate (As^V) in water. It should be mentioned that comparative studies on these two arsenic species and iron oxides are rare, in particular concerning maghemite. Previous studies mainly focused on hydrous ferric oxides for environmental remediation (Wilkie and Hering, 1996); but no detailed investigation of superficial processes leading to specific adsorption mechanisms onto nanoparticles surfaces were performed.

As^{III} and As^V binding to the nanoparticle surface

Arsenic may exist in different oxidation states (e.g., -3, 0, +3, +5) even if the two common forms in water are oxyacids (or their salts) of As^{III} (H₃AsO₃) and As^V (H₃AsO₄), and both lead to different complexes with iron oxide nanostructured materials. The binding efficiency of arsenate and arsenite to SAMNs surface was investigated as a function of pH (Figure 12a). The absorption of the two As oxyacids follows two completely different trends: for arsenate, the maximum binding efficiency was found at pH = 3.0 (32.5 mg g⁻¹), and it linearly decreased with pH reaching 20% of the maximum binding at pH 11. Differently, the binding efficiency of arsenite on SAMNs was almost constant in the 3.0-9.0 pH range (20.0 mg g⁻¹), and decreased at higher pH values, reaching 60 % of the maximum value at pH 11 (Figure 12a).

Intriguingly, the binding behaviors of As^{III} and As^V were superimposable with the results reported on goethite nanoparticles (Manning et al., 1998) and drastically diverged from those on nanostructured maghemite (Lin et al., 2012; Liu et al., 2016) substantiating an analogy between the surface chemistry of SAMNs and oxyhydroxides. Therefore, the structure of SAMNs can be unequivocally attributed to maghemite nanocrystals, while their surface resembles the behaviour of ferric oxy-hydroxides and is different from other maghemite nanostructures.

To appreciate the elemental composition and the chemical oxidation state of surface species on SAMNs, X-Ray Photoelectron Spectroscopy (XPS) was used. XPS wide scans of bare

SAMNs, SAMN@As^V and SAMN@As^{III} complexes are illustrated in Figure 12 (b,c,d respectively).

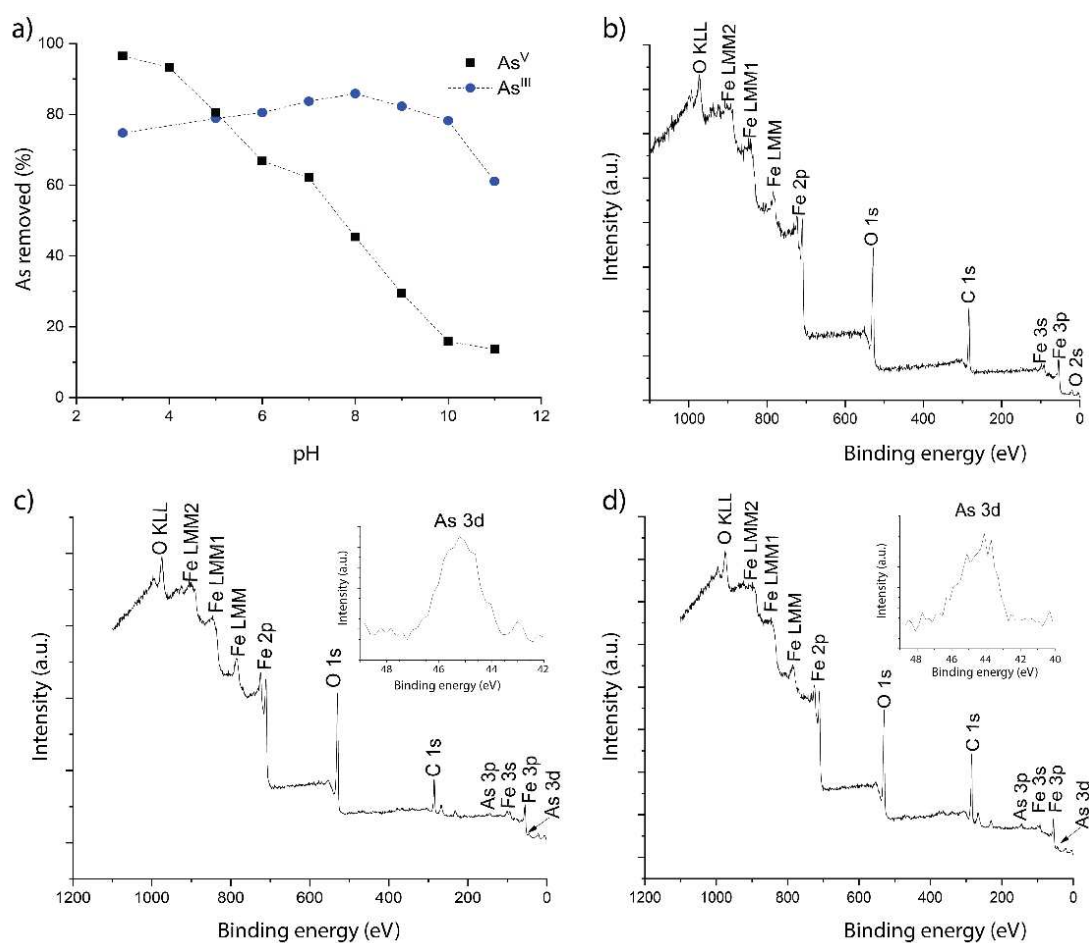


Figure 12. Binding efficiency of arsenate and arsenite to SAMNs as a function of pH and XPS wide scan spectra of bare SAMNs and of SAMN@As^V and SAMN@As^{III} complexes. a) Binding efficiency of arsenate and arsenite to SAMNs as a function of pH (arsenite, blue circles; arsenate, black squares); b) XPS wide scan spectrum of bare SAMNs; c) XPS wide scan spectrum of SAMN@As^V, d) XPS wide scan spectrum of SAMN@As^{III}. Complexes were prepared with 1 g L⁻¹ SAMN and 10 mg L⁻¹ As.

Three major peaks were observed in all samples at 284.8, 529.7, and 710.5 eV binding energies corresponding to C 1s, O 1s and Fe 2p peaks, respectively. Noteworthy, the appearance of a new peak at a binding energy of about 43 – 47 eV, corresponding to As3d peak (Figure 12c,d and insets) was observed in SAMN@As complexes, confirming the adsorption occurrence. Atomic weight fractions of elements are reported in Table S3.

The analysis of the XPS spectra was carried out even on the oxygen O1s region, and Figure 13a,c) reports on the O 1s peaks of bare SAMNs, SAMN@As^V and SAMN@As^{III} complexes. As shown in Figure 13a, the O1s spectrum of bare SAMNs is composed of three overlapped peaks: the first at 529 eV, representing O²⁻ peak (Fe-O lattice oxygen of maghemite), the other two at 531.4 and 533 eV the surface hydroxyl group (OH⁻) and adsorbed H₂O, respectively.

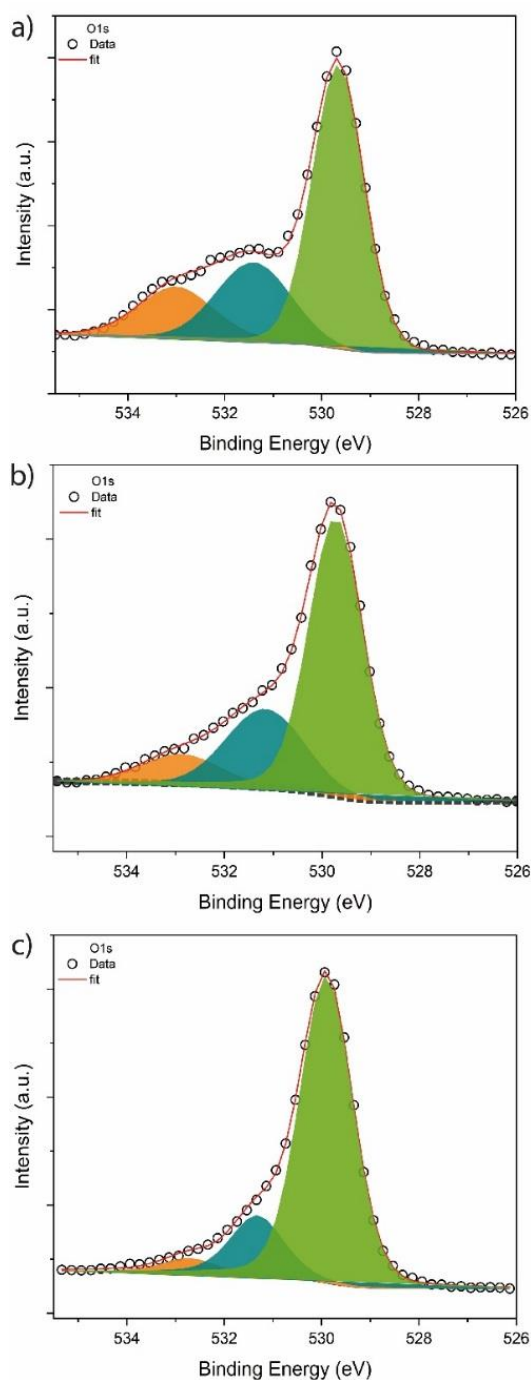


Figure 13. X-ray photoelectron spectroscopy of O 1s region of bare SAMNs, and the SAMNs@As^V and SAMN@As^{III} complexes with their curve fitting. a) Bare SAMNs, b) SAMNs@As^V complex, c) SAMN@As^{III} complex. Complexes were prepared using 1 g L⁻¹SAMN and 50 mg L⁻¹ As, pH 3.0.

Compared to bare SAMNs, the O1s peak areas of the two SAMN@As complexes evidenced that the content of lattice oxygen increased from 60% for pristine maghemite nanoparticles to 73% and 79% for As^V and As^{III} core-shell nanostructures, respectively. At the same time, surface hydroxyl groups decreased from 23% of naked SAMNs to 16% and 17% of SAMN@As^V and SAMN@As^{III} complexes, respectively, coupled to a visible change of the curve shape. Moreover, coordinated water lowered from 16% of SAMNs to 10% and 4% of SAMN@As^V and SAMN@As^{III} complexes, respectively. These findings suggested that, upon As binding, oxygen atoms provided by arsenite and arsenate were integrated into the maghemite lattice restoring the Fe^{III} dangling bonds at the nanoparticle surface.

Moreover, the loss of the hydroxyl group (OH⁻) in SAMN@As^V and SAMN@As^{III} complexes and adsorbed H₂O was perfectly balanced by the increase of lattice oxygen thus revealing that the binding of arsenite and arsenate occurs via ligand exchange mechanism. More specifically, notwithstanding arsenite loading on SAMN was lower than for arsenate (20 mg As^{III} g⁻¹ SAMNs vs. 32 mg As^V g⁻¹ SAMN), the binding of the As^{III} oxyacid to nanoparticles led to a higher content of lattice oxygen and, as a consequence, a more relevant displacement of surface -OH⁻ and H₂O groups with respect to As^V.

The morphological organisation and the elemental composition of SAMN@As^V and SAMN@As^{III} complexes was investigated by high resolution-transmission electron microscopy (HR-TEM) and chemical mapping by scanning transmission electron microscopy coupled to energy-dispersive x-ray spectroscopy (STEM/EDS) (Figure 14a,h). The presence of As peaks by EDS in the STEM image confirmed the As adsorption on nanoparticle surfaces (Figure 14g,h). Moreover, the chemical mappings of As, Fe and O by STEM-EDS of the two SAMN@As complexes are shown in Figure 14e,f. The comparison of As^{III} and As^V distributions in the SAMN@As complexes indicated a higher concentration of bound As^V compared to As^{III} (Figure 14e,f) under the investigated conditions (i.e. pH 3.0) in agreement with the binding efficiency measurements.

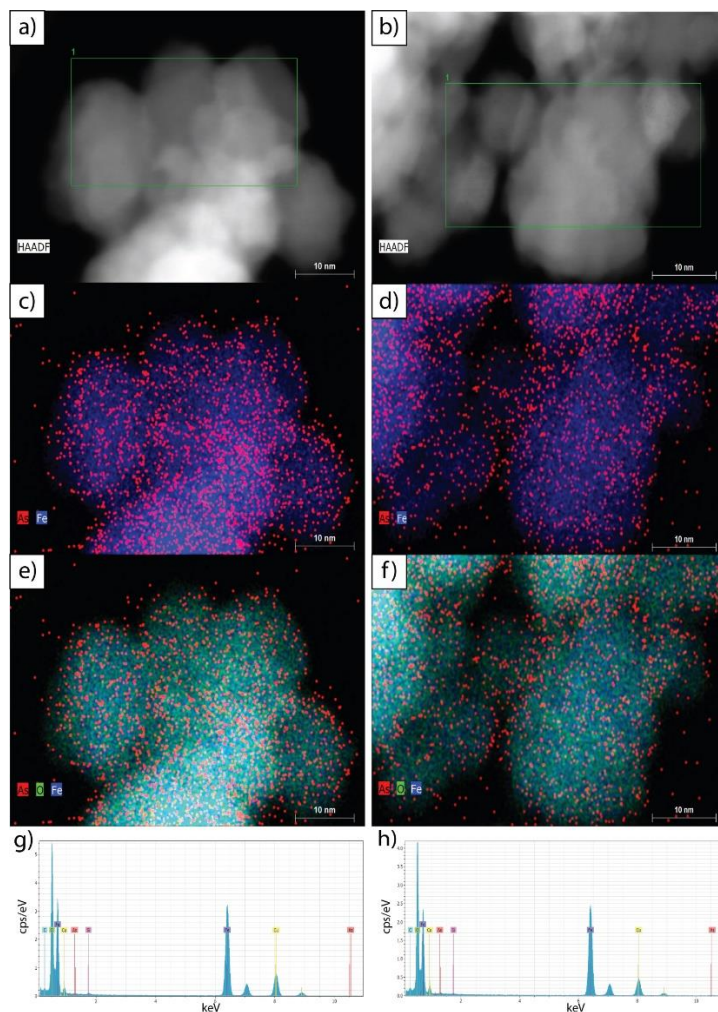


Figure 14. HR-TEM and HAADF–STEM images of SAMN@As^{III} and SAMN@As^V complexes. a,b) HAADF–STEM images of SAMN@As^{III} and SAMN@As^V complexes, respectively showing the mapping areas (green rectangle); c,d) EDS chemical mapping of the SAMN@As^{III} and SAMN@As^V complexes, respectively, showing Fe and bound As; e,f) EDS chemical mapping of the SAMN@As^{III} and SAMN@As^V complexes, respectively, showing Fe, O and As; g,h) representative energy-dispersive x-ray spectroscopy mappings of SAMN@As^{III} and SAMN@As^V complexes, respectively, showing the dominant peaks from Fe, O and bound As. Peaks belonging to C, Cu and Si originate from the copper grid and holey carbon.

3.4 Conclusions

The synthetic process of the formation of maghemite nanoparticles characterised by peculiar surface chemistry (SAMNs) was organised into the main steps, which were fully characterised. The first sample (S0), obtained by incubating FeCl₃ in the presence of NaBH₄ in ammonia containing water at 100°C, was heterogeneous, being constituted of submicron electron-dense particles, wide 2D oxyhydroxide structures and iron oxide nanoparticles. The submicron electron-dense particles, being constituted of zero-valent iron, were supposed to

be the first compound originated by FeCl_3 reduction by NaBH_4 , and appeared the precursors of other morphologies. Oxyhydroxyde 2D structures, possibly originating from the exfoliation of zero-valent iron particles in water, were observed at various stages of crumpling. We hypothesise that the latter process led to partially amorphous maghemite nanoparticles (S1 intermediate), already in size range of the final product. The study of the interaction of SAMNs with arsenite and arsenate by XPS revealed a correlation between the binding specificity, the modification of lattice oxygen and the restoration of surface crystallinity. Thus, the properties of SAMNs, such as the high colloidal stability, the ligand-binding selectivity, the magnetic behaviour, and chemical inertness, are the result of a robust core of stoichiometric maghemite combined to a defected surface, possibly exposing tetrahedral vacancies. The present study, besides enriching the knowledge on iron oxides, opens the door to new synthetic approaches to investigate new opportunities from metal oxide materials.

4. Naked Colloidal Maghemite Nanoparticles with Unique Surface Properties Encode Binding Specificity Toward As^{III} and As^V

4.1 Abstract

A peculiar category of pristine iron oxide nanoparticles (SAMNs) displays high colloidal stability and the ability to bind selectively macromolecules. This property is due to the topography of undercoordinated Fe^{III} sites on SAMNs surface. Herein, As^V and As^{III} oxyacids were used as small molecular probes, not able to develop multiple point bindings, to deepen into the specificity of this surface. Thermodynamic and kinetic studies, along with the chemical and structural characterisation of the SAMN@As complexes, substantiated the occurrence of two binding mechanisms. Arsenite, compared to arsenate, emerged as an elective ligand, displaying a specific modality of binding. Conversely, arsenate adsorption on SAMNs was significantly more labile, pH-dependent and ruled by different binding possibilities. The present report, besides enriching the chemistry of the interactions between iron oxides and arsenic, contributes to stimulating the research focused on the development of novel synthetic approaches for known nanomaterials, which can still be an object of innovation.

4.2 Introduction

Among different magnetic nanosized materials, iron oxide nanoparticles, such as maghemite (γ -Fe₂O₃) and magnetite (Fe₃O₄), possess several superior properties, including magnetic (e.g. superparamagnetism, high values of saturation magnetization, easy control by small magnetic fields) and biochemical (e.g. non-toxicity, biodegradability, biocompatibility) characteristics that empower their prominent position in diverse fields of medicine (Meyers et al., 1963; Petros and Desimone, 2010) and biotechnology (Hola et al., 2015) Physical and chemical properties, such as size and surface charge and chemistry, have been identified as essential parameters to determine the mode of action of nanomaterials in a given environment (water, buffer, biological fluid, etc.), through different surface interactions. In this view, the characterisation of nanomaterials surface is still incomplete, and data are needed for reproducing and validating experimental findings for

applications in environmental, biomedical and biotechnological fields. Among important issues, arsenic contamination represents an environmental concern worldwide (Singh et al., 2015) and many different sorbents were studied aiming at its removals, such as mesoporous alumina (Kim et al., 2004), red mud (Soner Altundoğan et al., 2000), titanium dioxide (Pena et al., 2006) and activated carbon (Chen et al., 2007). In this context, iron-based materials, such as nanoscale zero-valent iron (Tuček et al., 2017), magnetite (Feng et al., 2012), iron oxy-hydroxides (Müller et al., 2010) were proposed as appealing options. Besides, the interest in remediation issues, arsenic emerged as an elective probe for studying the surface structure of maghemite nanoparticles and the specificity of arsenite for a class of crystalline vacancies on the oxide boundary with solvent was proposed (Auffan et al., 2008).

On these bases, the present work investigates on the characteristics of the surface of a peculiar category of synthetic maghemite nanoparticles, called SAMNs (Surface Active Maghemite Nanoparticles) by studying the binding behaviour of both arsenite (As^{III}) and arsenate (As^{V}). It should be mentioned that comparative studies on the absorption of these two species and iron oxides were mostly dedicated to hydrous ferric oxides for environmental remediation purposes (Wilkie and Hering, 1996; Kanematsu et al., 2013). Only a few studies were focused on maghemite (Lin et al., 2012; Liu et al., 2016) and noteworthy, no specificity was reported in the binding of arsenite or arsenate.

SAMNs used in the present work stand out among other nanostructured $\gamma\text{-Fe}_2\text{O}_3$ for their excellent colloidal stability in water without any coating or superficial modification (Magro et al., 2015). It was demonstrated that the peculiar surface behaviour allowed the conjugation of different molecules with applications in different biotechnological fields (Venerando et al., 2013; Magro et al., 2015). Moreover, SAMNs were already applied as efficient sorbent nanomaterial for eliminating toxic metals in water (Magro et al., 2016). To note that most of the reported syntheses of magnetic nanoparticles involve the use of organic solvents or toxic substances, which lead to high costs, heavy environmental impact and difficult scalability, hampering their application at an industrial level. In addition, to avoid self-aggregation and meet long-term stability, pH and electrolyte tolerance, and specific surface chemistry, magnetic nanoparticles need to be modified by proper coatings. Coating processes represent a further obstacle for large scale production of nanomaterials as well as a source of pollutants (Magro et al., 2016). Thus, the use of nanomaterials aiming to solve environmental issues could become a paradox.

As a further distinctive tract, SAMNs can selectively bind biomolecules of great biotechnological interest, such as proteins (Magro et al., 2019) and DNA (Magro et al., 2015). This property was correlated to the surface topography of under-coordinated Fe^{III} sites determined by the interruption of the crystal at SAMN surface, which represents the physical boundary of the nanomaterial. The reactivity of these sites was highlighted by an electron transfer from DNA to iron oxide, leading to an electrically conductive hybrid metamaterial and the appearance of Fe^{II} on the surface of maghemite (Magro et al., 2015). Nevertheless, the comprehension of properties of surface Fe^{III} sites, considered individually and not as a surface distribution, is an open problem. Herein, arsenic oxyacids were chosen as small molecular probes, namely as species which cannot be involved in extended multiple binding, to test the specificity of under-coordinated Fe^{III} sites on SAMN surface. Thus, their binding behaviour to SAMNs was investigated under various experimental conditions. A deep characterization of the SAMN@As complexes was performed by High-Resolution transmission electron microscopy coupled to energy-dispersive X-ray spectroscopy (HRTEM-EDS), X-ray powder diffraction (XRPD), dynamic light scattering (DLS), hysteresis loops and ZFC/FC magnetization measurements, Mössbauer spectroscopy at room temperature and at 5 K, FTIR spectroscopy and X-ray Photoelectron Spectroscopy (XPS), further complemented by density functional theory (DFT) using model systems mimicking the binding of arsenite and arsenate onto surface-exposed Fe^{III} sites of SAMNs. Noteworthy, besides substantiating the efficiency of SAMNs as a competitive option for As removal, the presented results unveil unexpected ability of the nanomaterial to discriminate among arsenite and arsenate.

The current study stimulates the investigation of novel pristine nanostructured metal oxides as their surfaces can be a source of new properties and applications.

4.3 Results

Kinetics of the arsenate and arsenite binding on SAMNs

Auffan et al., (2008) theorised the presence of specific arsenite adsorption sites on the surface of nanostructured maghemite. Their study interpreted the binding of arsenite to maghemite in terms of complementarity between the oxyacid and lattice vacancies due to crystal truncation at the boundary with solvent. These vacancies were attributed to the deficiency of tetrahedral polyhedra and arsenite, displaying the same charge and Pauli

radius, was considered isomorphic to the polyhedra. Hence, it is physically able to occupy the free crystal positions recalling a key-lock fitting (Auffan et al., 2008). In the present study, the binding specificity of maghemite was tested by comparing two ligands: arsenite and arsenate. Here, the two oxyacids were used as probes for gathering insights on the structural features responsible for the peculiar surface chemistry of SAMNs. On these bases, the occurrence of different binding mechanisms, as a consequence of the presence of specific sites on the nanomaterial surface, was hypothesised.

Firstly, the kinetics of the binding process of arsenite and arsenate to SAMNs was followed in the 2 - 1440 min (24 hrs) time range, using 1.0 g L⁻¹ SAMNs and 15 mg L⁻¹ arsenic (as As) at pH 7.0 (Figure 15a,b). After 300 min, the adsorption process was at completion for both the arsenic oxidation states, corresponding to the binding of 62.1 % and 49.6 % of arsenite and arsenate, respectively. The residual As concentrations in solution remained constant until the end of the experiment. Thus, 300 min was chosen as the time for the accomplishment of the adsorption equilibrium.

The As binding phenomenon followed a two-step process, involving very fast adsorption in the first 5 min incubation, followed by a slower binding process. The experimental data were well described ($R^2 > 0.99$) by a pseudo-second-order equation: the non-linear and linear forms are given as Eqs. 13 and 14, respectively (Ho et al., 2000; Lin and Wang, 2009):

$$q_t = \frac{kq_e^2 t}{1+kq_e t} \quad (13)$$

$$\frac{t}{q_t} = \frac{1}{kq_e^2} + \frac{1}{q_e} t \quad (14)$$

Where q_t and q_e (mg As g⁻¹ SAMNs) are the amounts of As adsorbed at time t and equilibrium, respectively, and k is the rate constant of the pseudo-second-order adsorption (mg As g⁻¹ SAMNs min⁻¹).

Interestingly, considering the fast phase of the binding process, a remarkable difference of the binding rates to SAMNs for the two arsenic species was observed: the binding rate of arsenite was faster (1.82 mg As g⁻¹ SAMNs min⁻¹) than of arsenate (0.87 mg As g⁻¹ SAMNs min⁻¹).

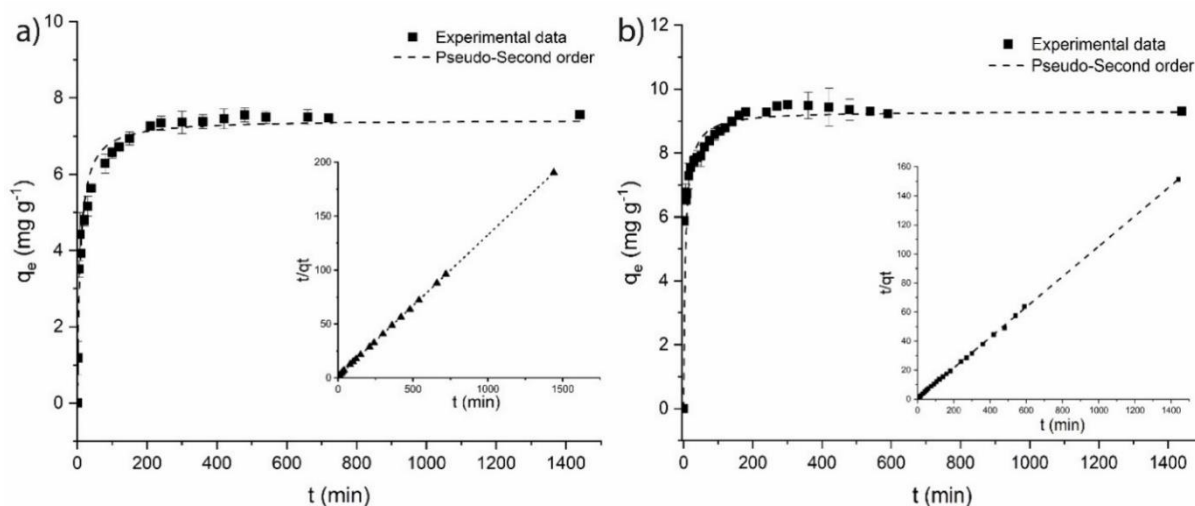


Figure 15. Binding kinetics of As^{V} and As^{III} (as arsenate and arsenite) to SAMNs. a) As^{V} ; b) As^{III} . Initial arsenic concentration 15 mg L^{-1} (as As). Experiments were carried out at pH 7.0 and SAMN concentration 1 g L^{-1} . **Insets:** Data linearizations. Dot lines represent the fitting with a pseudo-second-order kinetic model.

A useful hint can be prompted by an earlier study on the As absorption by mixed magnetite-maghemite nanoparticles, where the initial fast arsenic (both as arsenite and arsenate) absorption was due to the active adsorption sites readily accessible on the nanomaterial surface (Chowdhury and Yanful, 2010). In this view, results of the present paper confirm the hypothesis that the binding process of two oxyacids onto SAMNs is related to two different binding behaviors.

The binding of As^{III} and As^{V} to SAMNs

The binding efficiency at the equilibrium of As^{III} and As^{V} on SAMNs was studied at a constant concentration of arsenite and arsenate (10 mg L^{-1} , as As) as a function of SAMNs concentration in the $0.1 - 10.0 \text{ g L}^{-1}$ range. The binding phenomenon was followed at pH 7.0 and is depicted in Figure 16a, by plotting the values of As species bound to SAMNs vs SAMNs concentration. Bound arsenic species to SAMNs increased, in both cases, up to the complete As removal from the solution. The obtained curves, besides substantiating the ability of SAMNs to sequester As to completion, further provided a demonstration of a different binding affinity of the two As species. Indeed, As^{III} in solution was zeroed at a SAMNs concentration of about 2.0 g L^{-1} , while As^{V} approached the complete removal at $\sim 7.0 \text{ g L}^{-1}$ SAMN (Figure 16a).

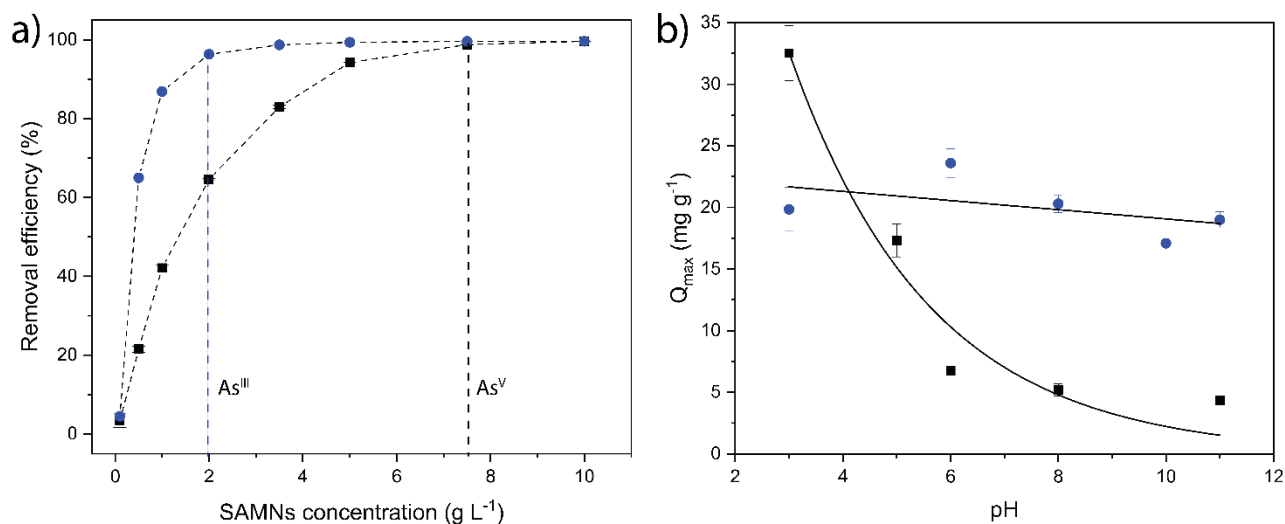


Figure 16. Binding efficiency and maximum adsorption capacity of As^{III} and As^V to SAMNs as a function of pH. a) Binding efficiency of As^{III} (blue circles) and As^V (black squares) as a function of SAMN concentration (pH = 7.0 and 10 mg L⁻¹ arsenic (as As)); b) Maximum adsorption capacity (q_m) of As^{III} (blue circles) and As^V (black squares) to SAMNs as a function of pH.

The binding behaviour of As^{III} and As^V to naked SAMNs was studied at equilibrium according to Langmuir (Langmuir, 1918) and Freundlich (Freundlich, 2017) isotherm models as a function of pH. Freundlich isotherm model failed to outline accurately the As^{III} and As^V binding process to SAMNs as indicated by the low regression coefficient of the fittings (Table S7). Conversely, experimental data well fitted the Langmuir model for both the As species, and a saturation binding behaviour on SAMNs surface was observed. The analysis, according to the Langmuir model, assumes that each binding site on nanoparticle surface acts independently of other sites (Table S7). Thus, the adsorption phenomenon can be considered compatible with the formation of a single molecular layer on SAMNs. The Langmuir equation was applied in the following form (Eq. 15):

$$\frac{C_e}{Q_e} = \frac{1}{q_m K_L} + \frac{C_e}{q_m} \quad (15)$$

Where C_e is the equilibrium concentration of soluble As, q_m is the amount of As bound at the full monolayer coverage, and K_L is the apparent stability constant, and the values of q_m and K_L were determined from the slope and the intercept of the linear plot of C_e/Q_e vs C_e . In the pH range explored, the calculated K_L values for As^{III} binding on SAMNs were higher than those of As^V, confirming two different binding behaviours. As examples, at pH 3.0 the stability constant for the As^{III} binding on SAMNs was 3.82×10^3 L g⁻¹ and 0.56×10^3 L g⁻¹

for As^V, while at pH 11.0, the stability constants were $1.2 \times 10^4 \text{ L g}^{-1}$ and $6.6 \times 10^3 \text{ L g}^{-1}$ for As^{III} and As^V, respectively. Again, different binding behaviours were observed regarding the maximum binding capacity of As^{III} and As^V on SAMNs as a function of pH (Figure 16b). The maximum binding capacity of SAMNs toward As^{III} resulted almost constant in the whole pH range explored, while for As^V binding, the q_m values rapidly decreased with pH. The maximum q_m value observed for As^V binding was 32.5 mg g^{-1} SAMNs at pH 3.0, while the q_m value for As^{III} was around 20 mg g^{-1} SAMNs in the whole pH range explored (Figure 16b). For both the As species, the calculated q_m values were in agreement with those previously reported for other adsorbates on SAMNs displaying comparable size, hence further substantiating the development of a monolayer (Magro et al., 2016). According to the calculated q_m values for As^{III} and As^V binding and the total surface area of SAMNs by Brunauer–Emmett–Teller (BET) analysis (Magro et al., 2014), the surface density of bound As^{III} and As^V on SAMNs corresponded to 3.5 and 5.6 As atoms per nm^2 , respectively. For comparison, the surface density of iron atoms on SAMNs surface was calculated by considering the nanomaterial surface thickness (0.35 nm according to Kachkachi (Kachkachi et al., 2000)), maghemite density (4.86 g cm^3), and Fe₂O₃ molar mass (160 g mole^{-1}). According to these considerations, surface iron atoms resulted in 12.8 per square nanometer. Among superficial iron atoms of maghemite nanoparticles, SAMNs surface is characterized by the presence of under-coordinated solvent-exposed Fe^{III} sites (Magro et al., 2014), which are located at the nodes of a square grid with side length of $0.39 \pm 0.09 \text{ nm}$ (Magro et al., 2016; Magro et al., 2017; Magro et al., 2018), defining a homogenous distribution of about 4 Fe^{III} sites per nm^2 . Hence, fully coordinated iron atoms on SAMN surface should be about two times the number of under-coordinated Fe^{III} sites. Thus, the calculated value of the surface density of bound As^{III} nearly approached the amount of undercoordinated Fe^{III} atoms available on the SAMNs surface. Differently, at least at pH 3.0, the adsorption of As^V exceeded this value and resulted about half the amount of the total iron atoms on SAMNs surface. This further substantiated the occurrence of two different binding mechanisms for arsenite and arsenate on SAMNs. In this view, some useful hints can be provided by literature describing arsenate adsorption on corundum and hematite (Catalano et al., 2008). Indeed, in the case of arsenate, the coexistence of outer-sphere and inner-sphere complexes was also considered. In the present context, inner-sphere complexes could involve the direct As binding to under-coordinated Fe^{III} through actual coordination chemistry. This, independently of the strength and specificity of the binding,

can be common for both As^{III} and As^V oxyacids. Differently, outer-sphere complexes, not presenting a direct chemical bond with the iron oxide surface, should involve other mechanisms, such as electrostatic contributions. Taking into account that hydroxyls groups on iron atoms are protonated at pH = 3.0, leading to positively charged Fe-OH₂⁺ groups (Cornell and Schwertmann, 2003), they can interact with negatively charged species. From an electrostatic standpoint, it is important to consider the speciation of arsenic and arsenous acids in the explored pH range, which can be described by the following equations (Eqs. 16-19) (Nordstrom et al., 2014):



According to Eqs. 16, 17 and 18, arsenate is in the forms of H₂AsO₄⁻ and HAsO₄²⁻ in the explored pH range, and the divalent form increases with pH. Conversely, arsenite is predominantly present in water as neutral arsenous acid (H₃AsO₃) at pH values below 9.2 (Eq. 19). At higher pH values, the anionic form (H₂AsO₃⁻) becomes the dominant species. Therefore, under acidic conditions, arsenate and SAMNs present opposite charge and electrostatics could play a role in the binding. Increasing the pH, a decrease of the charge of SAMNs occurred, leading to a reduction of the electrostatic contribution as suggested by the reduction of the q_m values of arsenate. Differently, As^{III} should mainly bind to SAMNs by surface complexation, and the as-obtained complex is significantly more stable than that involving As^V, as observed in the binding equilibrium experiments according to the Langmuir model (Figure 16b). In this view, studies on soils evidenced a more specific adsorption behaviour of As^{III} in comparison to As^V on Fe^{III} hydroxides (Tufano and Fendorf, 2008).

Possibly, the correspondence between the maximum As^{III} adsorption and the distribution of under-coordinated Fe^{III} sites on SAMNs indicates that these latter surface chemistries can be interpreted as tetrahedral vacancies as suggested by Auffan et al., (2008). Nevertheless, considering the structural similarity of As^{III} and As^V oxyacids, the specificity of arsenite for these sites must necessarily involve different requisites than the mere molecular geometry.

Spectroscopic characterisation of the SAMN@As complexes

The two SAMN@As complexes were fully characterized by x-ray powder diffraction (XRPD), dynamic light scattering (DLS), hysteresis loops and ZFC/FC magnetization measurements, Mössbauer spectroscopy at room temperature and at 5 K. All these techniques evidenced that the maghemite core, in terms of structural and magnetic characteristics, was well preserved upon As oxyacids binding. The X-ray diffraction patterns of SAMN@As^{III} and SAMN@As^V are showed in Figure 17; the two patterns are perfectly superimposable and highlight that the systems consisted of crystalline maghemite, with hematite as minor phase (< 5%), possibly located on SAMNs surface.

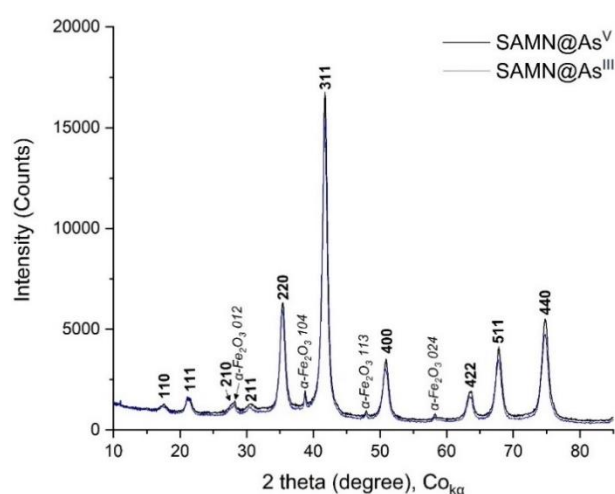


Figure 17. X-ray diffraction patterns of SAMN@As^{III} and SAMN@As^V. Numbers are the miller indices for maghemite (bold) and hematite (Italic).

The SAMN@As^{III} and SAMN@As^V complexes were further characterised by dynamic light scattering (DLS) in water (Figure 18a,b,c).

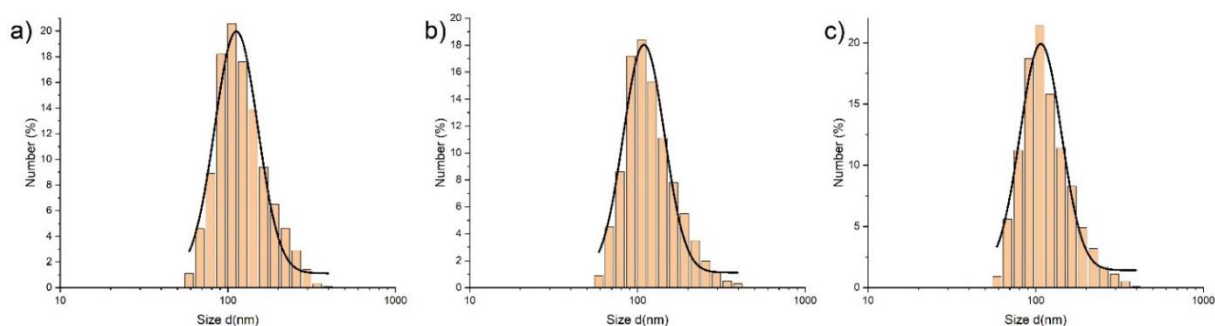


Figure 18. The hydrodynamic size of naked SAMN and the SAMN@As^V and SAMN@As^{III} complexes by DLS analysis. a) SAMN; b) SAMN@As^V; c) SAMN@As^{III}. Bold lines represent the statistical-fit (LogNormal-function); measurements were carried out in triplicate.

The analysis showed a small change in the mean size of nanoparticles, expressed in terms hydrodynamic size (nm), from naked SAMNs sample ($d_{\text{mean}} = 118.4 \pm 2.8$ nm) to the SAMN@As^{III} obtained at pH 3.0 (best adsorption condition) ($d_{\text{mean}} = 124.4 \pm 2.7$ nm) and the SAMN@As^V ($d_{\text{mean}} = 116.4 \pm 1.6$ nm).

Measurement of zeta potentials (ζ) at pH 3.0 before and after arsenic adsorption showed a decrease of ζ values from $+31.1 \pm 5.5$ mV for naked SAMNs (conductivity 0.0116 mS cm⁻¹ in water at 22°C) to $+26.6 \pm 4.8$ mV for the SAMN@As^{III} complex (conductivity 0.0195 mS cm⁻¹) and $+25.8 \pm 4.1$ mV for SAMN@As^V complex (conductivity 0.0184 mS cm⁻¹).

It should be considered that metal chelation can induce the degradation of metal oxides by a process known as “ligand promoted dissolution”(Gu and Karthikeyan, 2005). Thus, to verify that no structural alteration affected SAMNs upon incubation with arsenite and arsenate at pH 3.0, the magnetic properties of the two SAMN@As complexes were analysed by acquiring hysteresis loops (Figure 19a,b) and ZFC/FC magnetisation measurement (Figure 19c,d). From the hysteresis loops, it is evident that both SAMN@As complexes showed coercivity and remanence values at 5 K reflecting that the systems were in a blocking state below the transition temperature (Tuček et al., 2006). Moreover, the loop profiles of both SAMN@As complexes were almost symmetric around the origin, reaching the magnetic saturation under very small induced magnetic field (10 kOe). The maximum magnetisation values at 50 kOe were slightly different for the measured samples (Table S5). In particular, the values for SAMN@As^V was slightly lower ($M_{\text{max}+} = 69.38$ and 59.51 emu/g at $T = 300$ and 5 K, respectively) than those measured for SAMN@As^{III} ($M_{\text{max}+} = 72.32$ and 60.20 emu/g at $T = 300$ and 5 K, respectively), confirming the adsorption of different amount of diamagnetic arsenite and arsenate on SAMNs, in agreement with experiments on As binding at equilibrium. The absorption of different amount of As^{III} and As^V onto the surface of SAMNs was also visible from the shift of coercivity values at 5 K along with the variation of the orientation of the external magnetic field. The behaviour is known as “exchange bias” and confirms the different magnetic behaviour of the core (iron oxide nanoparticles) and the shell (absorbed component onto the surface) (Nogués and Schuller, 1999).

This represents a crucial factor for the real applicability of magnetic nanomaterials for environmental issues. Furthermore, interesting minor differences emerged between the SAMN@As samples, in particular for the magnetic and hydrodynamic properties.

Moreover, the remanence and coercivity values at 300 K of the two SAMN@As complexes were significantly lower than those measured at 5 K (Figure 19a,b), confirming the

superparamagnetic state of all samples with the spins of all the magnetic nanoparticles fluctuating between the orientations of the easy axis of magnetisation.

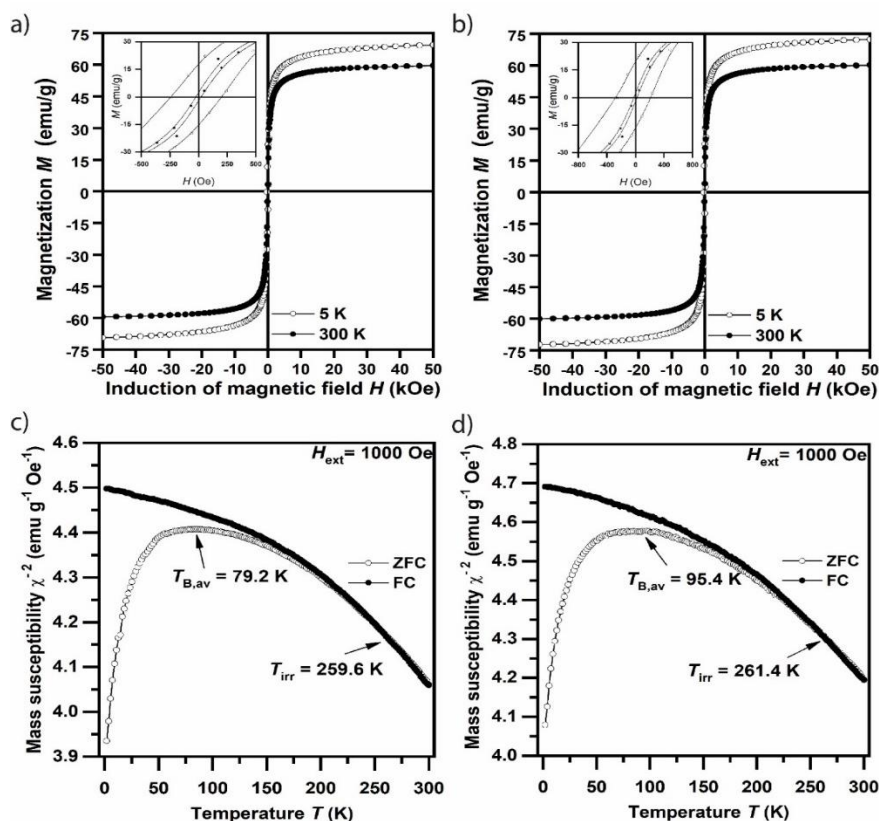


Figure 19. The hysteresis loops of a) SAMN@As^V and b) SAMN@As^{III} recorded at 5 K and 300 K. Panel c) and d) show the ZFC/FC magnetisation measurement of SAMN@As^V and SAMN@As^{III}, respectively, in the presence of external magnetic field (1000 Oe). All reported data are measured for the SAMN@As complexes obtained at pH 3.

The superparamagnetic state was also supported by all ZFC/FC magnetisation curves (Figure 19c,d). Decreasing the temperature, the spins of all magnetic nanoparticles subsequently freeze in the magnetically blocked regime. The temperature at which the transition to the magnetically blocked state occurred is represented by a maximum of the ZFC magnetisation curve and represents the blocking temperature (T_B), where the average size nanoparticles are magnetically blocked ($T_{B,av}$). The separation of the ZFC and FC magnetisation curves is known as irreversibility temperature (T_{irr}), which marks the beginning of the blocking mechanism of the superspin linked to the largest nanoparticles in the system. The differences between T_{irr} and $T_{B,av}$ can be thus described as a quantitative measurement of the particle size distribution: The different values of the blocking and irreversible temperatures for SAMN@As^{III} ($T_B = 95.4$ K and $T_{irr} = 261.4$ K) and for

SAMN@As^V ($T_B = 79.2$ K and $T_{irr} = 259.6$ K) reflected a different size distribution of the systems. Moreover, the lower T_B value for the SAMN@As^V complex compared to SAMN@As^{III} is indicative of a smaller complex size in agreement with DLS results (Figure 18b,c).

Mössbauer spectroscopy at room temperature and 5 K was used to investigate more in detail the phase composition and nature of the SAMNs after As loading. As it is evident from the two spectra recorded at room temperature (Figure 20a,b), the resonant lines are not of Lorentzian character, a distribution of hyperfine magnetic field (B_{hf}) was used to correctly fit the room-temperature ⁵⁷Fe Mössbauer spectrum of both samples; values of Mössbauer hyperfine parameters are given in Table S2. The value of the isomer shift (δ) is typical for Fe³⁺ in a high-spin state (i.e., $S = 5/2$) and lies exactly in the middle of the δ -values frequently reported for tetrahedral (i.e., $\delta = 0.25$ mm/s) and octahedral (i.e., $\delta = 0.37$ mm/s) sites of γ -Fe₂O₃ crystal structure. In addition, the zero value of the quadrupole splitting parameter (ΔE_Q) is also typical for γ -Fe₂O₃ due to its inverse spinel cubic crystal structure and hence symmetric electric field, surrounding the probed Fe³⁺ nucleus. Both samples differ slightly only in the value of B_{hf} , which can be explained by the different particle size distribution of the two complexes (Figure 20a,b). No sign of other Fe species (i.e., no trace of Fe²⁺) was observed for both samples.

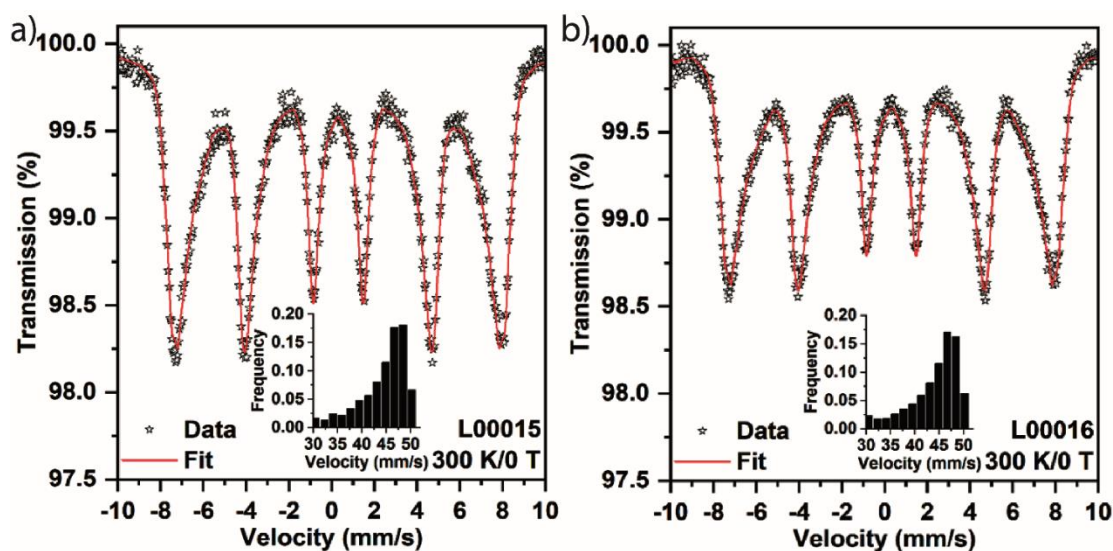


Figure 20. ⁵⁷Fe Mössbauer spectrum of a) SAMN@As^{III} sample and b) SAMN@As^V sample, recorded at room temperature and without an external magnetic field.

The morphological organisation, as well as the elemental composition of SAMNs@As complexes, were investigated by high resolution-transmission electron microscopy (HR-TEM) and chemical mapping by scanning transmission electron microscopy coupled to energy-dispersive x-ray spectroscopy (STEM/EDS) (Figure 21a-h).

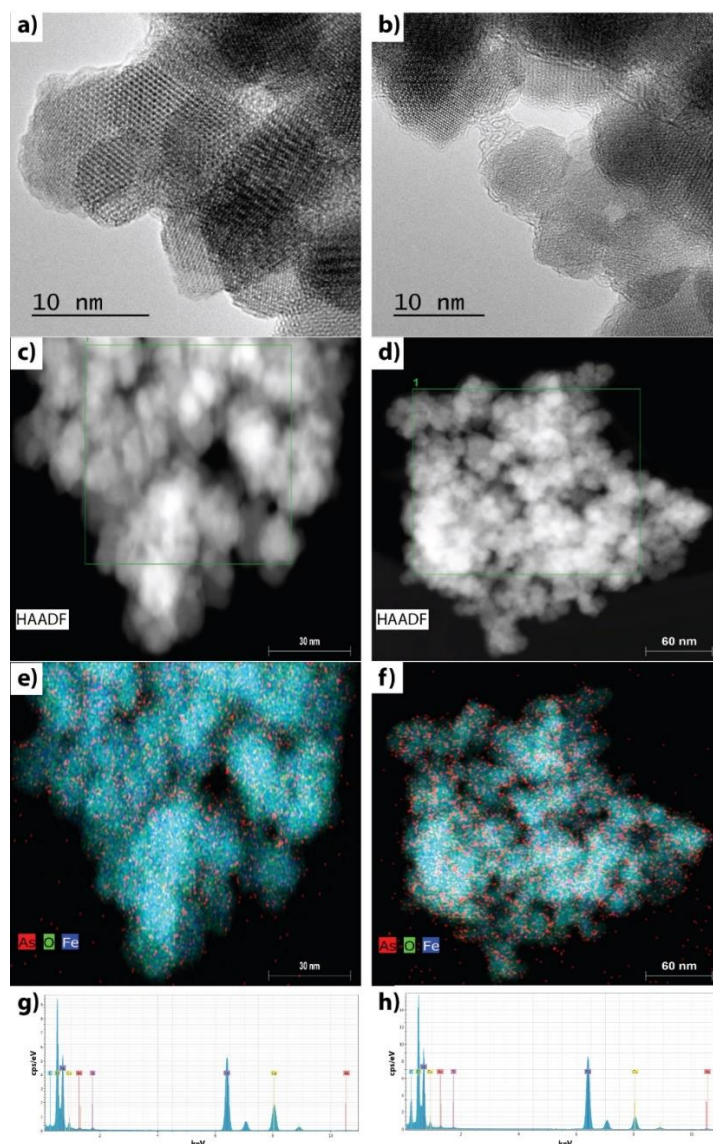


Figure 21. HR-TEM and HAADF–STEM images of SAMN@As^{III} and SAMN@As^V complexes. a,b) representative HR-TEM image of SAMN@As^{III} and SAMN@As^V complexes, respectively, in which diffraction fringes of the crystalline planes of γ -Fe₂O₃ phase are visible; c,d) HAADF–STEM images of SAMN@As^{III} and SAMN@As^V complexes, respectively showing the mapping areas (green rectangle); e,f) EDS chemical mapping of the SAMN@As^{III} and SAMN@As^V complexes, respectively, showing As bound to the SAMN surface; g,h) representative energy-dispersive x-ray spectroscopy mappings of SAMN@As^{III} and SAMN@As^V complexes, respectively, showing the dominant peaks from Fe, O and bound As. Peaks belonging to C, Cu and Si originate from the copper grid and holey carbon.

The presence of As peaks by EDS in the STEM image confirmed the As adsorption on SAMNs surfaces (Figure 21g,h). Moreover, the chemical mappings of As, Fe and O by STEM-EDS of the two SAMN@As complexes are shown in Figure 21e,f. The comparison of As^{III} and As^V distributions in the SAMN@As complexes indicates a higher concentration of bound As^V compared to As^{III} (Figure 21e,f) under the investigated conditions (i.e. pH 3.0) in agreement with the previously described measurements.

To appreciate the elemental composition and chemical oxidation state of species bound to SAMNs surface, x-ray photoelectron spectroscopy (XPS) was used. XPS wide scans of SAMN@As^{III} and SAMN@As^V complexes are illustrated in Figure 22a,c. Three major peaks were observed in all samples at 284.8, 529.7, and 710.5 eV binding energies corresponding to C1s, O1s and Fe2p peaks, respectively. Noteworthy, the appearance of a new peak at a binding energy of about 43 – 47 eV, corresponding to As3d peak (Figure 22b,d) was observed in SAMN@As complexes, confirming the adsorption occurrence. Atomic weight percentages of elements are reported in Table S9.

Figure 22a,b shows the XPS spectra of the As3d peak of SAMN@As^{III} and SAMN@As^V complexes. No arsenic was detected on bare SAMNs, as confirmed by elemental composition analysis (Table S9). Curve fitting of the As3d peaks of SAMN@As complexes involved two unresolved curves, due to spin-orbit splitting, corresponding to As3d_{3/2} and As3d_{5/2} peaks, which were separated by 0.7 eV (Figure 22). Commonly, As3d_{5/2} peak position is in the 43.5-44.5 and 44.8-46.0 range for As^{III} and As^V, respectively (Ramos et al., 2009; Chowdhury and Yanful, 2010; Yan et al., 2010; Sudhakar et al., 2018).

The XPS spectra of the SAMN@As^V complex showed the presence of the sole As^V peak, consistently with previous studies reporting on As^V sorption on oxyhydroxides (Sudhakar et al., 2018). Differently, the SAMN@As^{III} complex generated a broader As3d peak, as shown in Figure 22b. Two mains As3d_{5/2} peaks at 44.0 and 45.2 eV binding energies can be assigned to bound As^{III} and As^V, respectively. The quantitative analysis suggests that 71% arsenic is present as arsenite, while the remaining 29% as arsenate. Oxidation phenomena of As^{III} were already reported for arsenite sorption on other iron oxides (Yan et al., 2010), such as Fe^{II}-activated goethite (Amstaetter et al., 2010) and mixed magnetite-maghemite (Chowdhury et al., 2011). Noteworthy, the recorded oxidised fraction of bound As^{III} was consistent with the results reported by Auffan et al., (2008). According to the authors, the phenomenon is due to the strength of the arsenite binding to specific sites of maghemite

surface, resulting in a high reactivity of bound arsenite toward oxidation. To note that no trace of iron^{II} on SAMN@As^{III} was evidenced by Mössbauer spectroscopy even at 5 K.

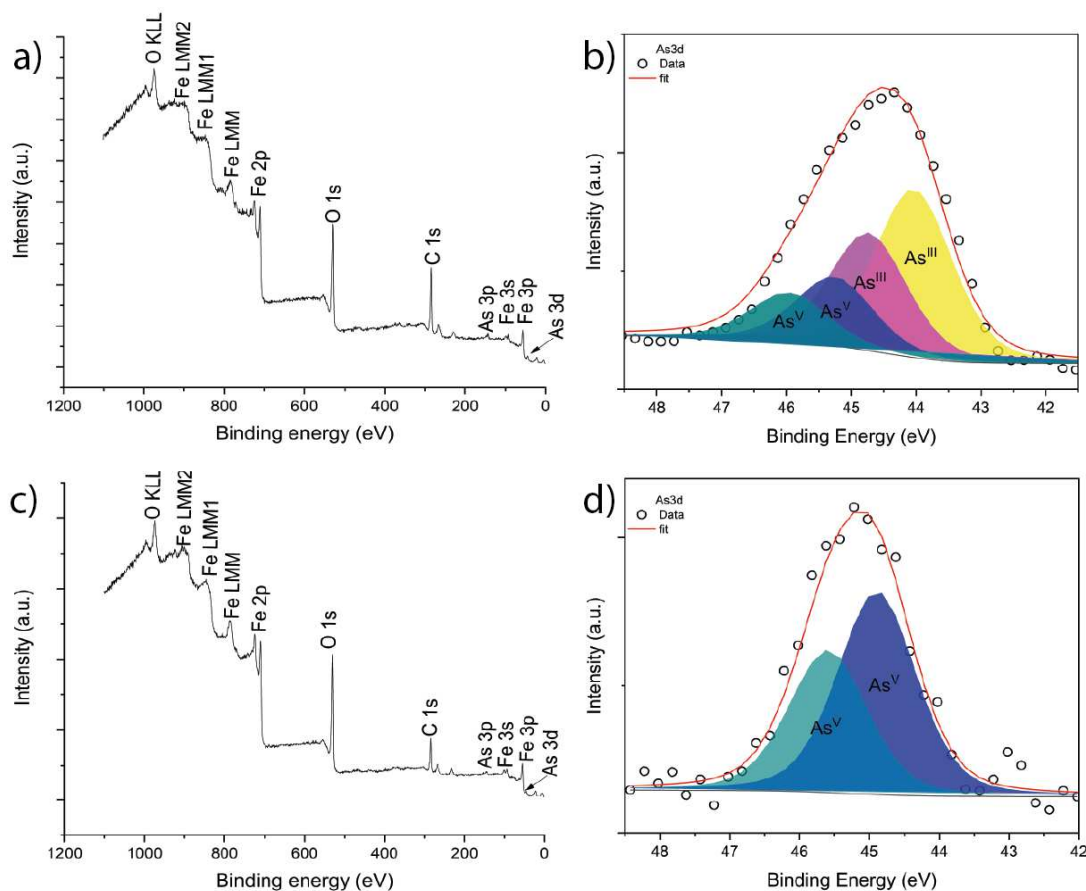


Figure 22. X-ray photoelectron spectroscopy of SAMN@As^{III} and SAMNs@As^V complexes. a) survey XPS spectrum of SAMNs@As^{III}; b) As3d peak of SAMN@As^{III}, c) survey XPS spectrum of SAMNs@As^V, d) As3d peak of SAMN@As^V. SAMN@As complexes were prepared using 1 g L⁻¹ SAMN and 50 mg L⁻¹ As, pH 3.0. For the deconvolution, the intensity ratio of the doublet was kept constant at 3:2 and, a mixture of Gaussian-Lorentzian functions was used.

To investigate more in detail the different binding behaviour of As^{III} and As^V to SAMNs, FT-IR was used as an informative technique. The IR spectra of bare SAMNs and of the SAMN@As^{III} and SAMN@As^V complexes are reported in Figure 23a,b,c. The infrared profiles in the region between 500 and 700 cm⁻¹ showed the typical maghemite adsorption bands at 550, 630, 690 cm⁻¹, which can be assigned to the Fe-O stretching vibrations (Namduri and Nasrazadani, 2008). The weak peak at 1640 cm⁻¹ can be attributed to O-H bending mode, while the broadband at 3400 cm⁻¹ represents the O-H stretching vibration. These features, compatible with the parent γ -Fe₂O₃ particles, witnessed the presence of a

preserved maghemite phase. Noteworthy, the presence of broadband in the region between 750 and 900 cm^{-1} was observed in both the SAMN@As complexes.

According to Goldberg and Johnston (2001), this broadband is related to the presence of Fe-O-As groups. The difference plot between the naked nanoparticles and As bound samples allowed to remove the contribution of iron oxide and provided additional vibrational features as well as a precise peak position (Figure 23, inset). For adsorbed As^{V} , three bands at 790, 834, 878 cm^{-1} were obtained by peak fitting. These values were in agreement with those reported by Müller et al. (2010) for As^{V} adsorption onto poorly crystalline iron oxy-hydroxide and hematite (Müller et al., 2010), and identified as t_d to c_{3v} symmetry reduction due to the formation of an inner sphere bidentate complex. An et al. (2011) reported on a similar broad peak using starch-bridged magnetite nanoparticles for the removal of As^{V} . This binding mechanism was also supported by Goldberg and Johnston (2001) and An et al., (2011) on arsenic sorption to amorphous iron oxides. These authors reported on two different bands at 817, and 824 cm^{-1} described as surface complexed and non-surface complexed As-O groups. The spectrum of adsorbed As^{III} showed two different bands centred at 870 and 794 cm^{-1} (Figure 23c). These bands exhibited a neat split explainable as a change in symmetry from C_{3v} to C_s due to the formation of an inner-sphere surface complex (Müller et al., 2010). Thus, according to FTIR measurements, independently of the strength and specificity of the binding, an inner sphere complexation plausibly emerged as the binding mechanism for both the As species. In this view, it is important to mention that FTIR did not allow to distinguish the spectral contribution from the outer sphere complexation of As^{V} .

Literature reported on different surface structures for As^{III} adsorption on iron oxides on the basis of the interatomic Fe-As distance: a bidentate mononuclear complex for ferrihydrite (Gao et al., 2013), a bidentate binuclear complex for goethite (Manning et al., 1998), a bidentate mononuclear and binuclear complex on ferrihydrite and hematite (Ona-Nguema et al., 2005). More recently, a close distribution of monodentate and bidentate complexes for arsenite adsorbed onto biogenic iron oxy-hydroxides was reported (Sowers et al., 2017). Theoretical Calculations (DFT/BP86/ using the 6-31G* or the 6-31+G* basis set depending on the molecule charges) have been carried out on model systems, which can mimic the interaction of $\text{As}^{\text{V}}/\text{As}^{\text{III}}$ species with the surface exposed Fe sites of SAMNs.

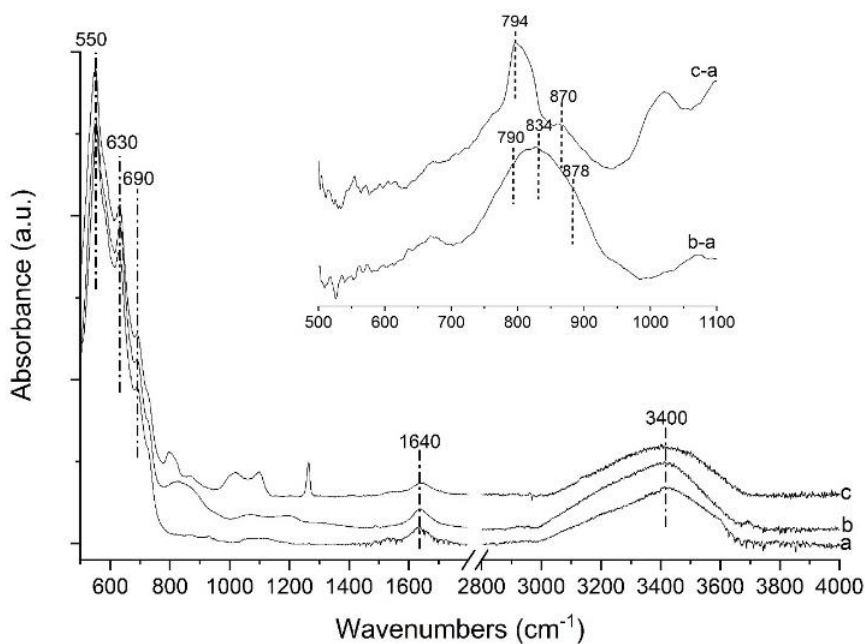


Figure 23. Fourier Transform IR spectra of naked SAMNs and the SAMN@As^V and SAMN@As^{III} complexes. a) naked SAMNs, b) SAMN@As^V, c) SAMN@As^{III}. The inset shows the difference spectra built by subtracting the SAMN contribution from SAMN@As^V (b-a) and SAMN@As^{III} (c-a) in the 500-1110 cm⁻¹ range. Complexes were prepared at pH 3.0.

The theoretically derived IR spectra are collected together in Figure 24 and further details given in the appendix B. For adsorbed As^{III} species onto SAMNs two different bands emerged in the calculated spectrum for the neutral species, at 909 cm⁻¹ and at 798 cm⁻¹ (Figure 24c), which are fairly consistent, in energy position and relative intensity, with those experimentally observed (at 870 and at 794 cm⁻¹, see Figure 24 inset, trace c-a). On the contrary, the spectrum obtained for the negatively charged Fe^{III}-O-As^{III} model (Figure 24d) gives an IR envelope with only one signal falling at 936 cm⁻¹, hence is poorly consistent with that experimentally recorded. The adsorption of As^V is more complex and three models have been tested; (i) a neutral form (Figure 24e) which gives calculated signals at 765 cm⁻¹, 932 cm⁻¹, 968 cm⁻¹, 1047 cm⁻¹, (ii) a negatively charged form (Figure 24f), with calculated signals at 883 cm⁻¹, 1018 cm⁻¹, and (iii) a positively charged species with bidentate As^V binding to the surface exposed Fe^{III} cation (Figure 24g) which gives signals at 757 cm⁻¹, 830 cm⁻¹, 1003 cm⁻¹. Because the difference spectrum is shown in Figure 23 (inset b-a) for the As^V bound to SAMNs is very broad, spreading from ≈700 cm⁻¹ to ≈1000 cm⁻¹, an overlapped contribution coming from all these differently charged species appears highly probable.

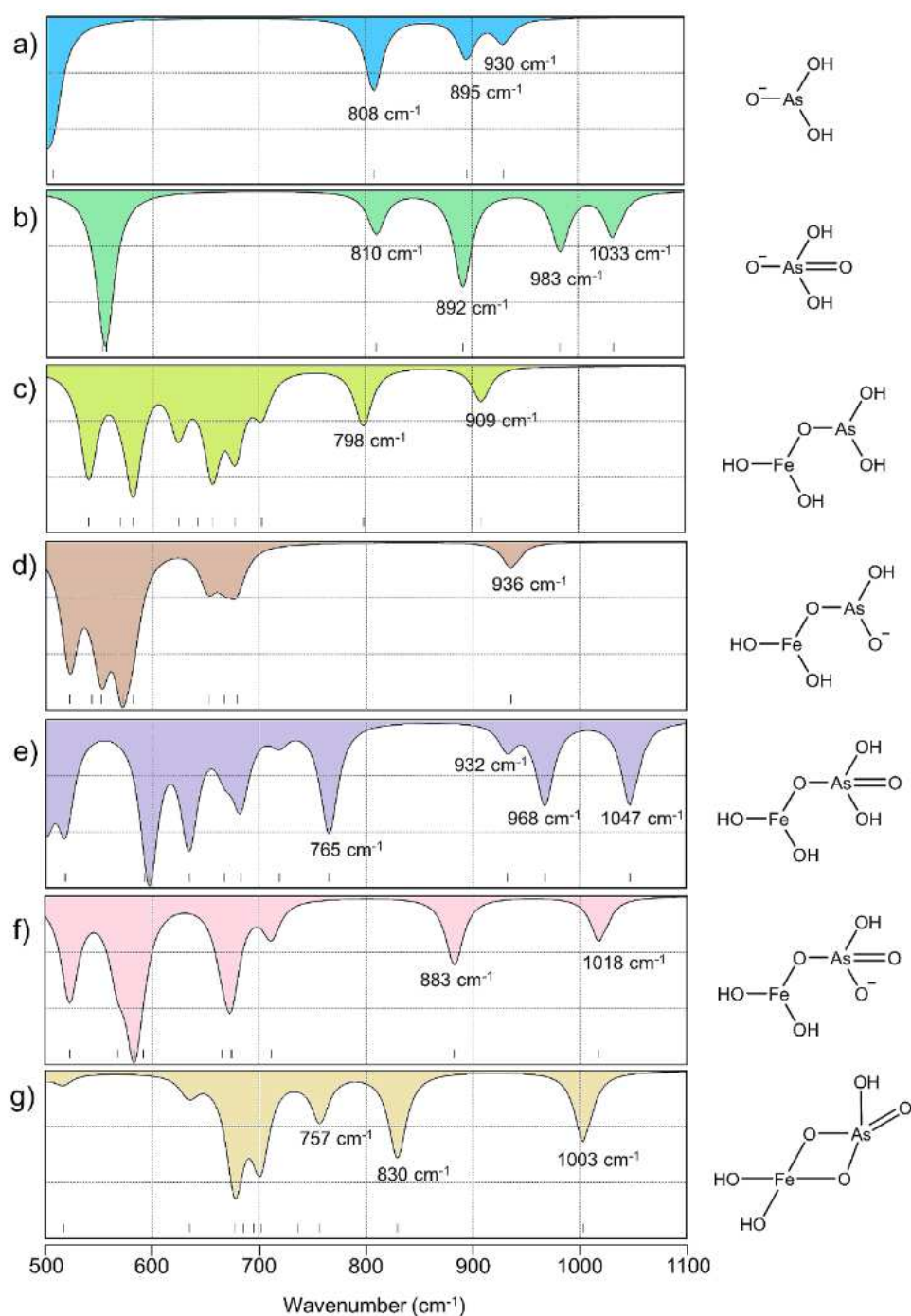


Figure 24. Calculated (BP86/6-31G* or 6-31+G*) IR spectra of model systems for As^{III} (panel a, c, d) and As^V (panel b, e, f, g) either as neatly isolated molecules or bound to surface-exposed Fe^{III} (high spin, $S = 5/2$) sites of SAMNs. Spectra a), b), d), f) are anionic species; c) and e) are neutral species. g) is a cationic species. The calculated energy (E) for the geometry optimized molecules are a) $E = -2462.84892$ a.u.; b) $E = -2538.06676$ a.u.; c) $E = -3878.27286$ a.u., $S^2 = 8.7542$; d) $E = -3877.79188$ a.u., $S^2 = 8.7547$; e) $E = -3953.45294$ a.u., $S^2 = 8.7543$; f) $E = -3953.00230$ a.u., $S^2 = 8.7544$; g) $E = -3952.47993$ a.u., $S^2 = 8.7766$.

At the light of previous results on the different pH pendency of arsenite and arsenate binding to SAMNs, FTIR spectra of both SAMN@As complexes were collected as a function of pH 65

(Figure 25). The infrared profiles were fully in harmony with the observed binding behaviour from the equilibrium measurements, according to Langmuir (Figure 16b). In particular, the FTIR spectra of the SAMN@As^{III} complex highlighted that the As-O band was constant with pH, followed by a slight increase at basic pH values and its complete disappearance at pH 10.0 (Figure 25a, inset). On the contrary, FTIR spectra of the SAMN@As^V complex showed a progressive reduction of the As-O band at around 800 cm⁻¹ with pH, and it completely disappeared at pH 7.0 (Figure 25b, inset). This was consistent with the observed decrease of the As^V loading on SAMNs with pH. Therefore, besides the inner sphere character of the binding of both As species, the interaction with SAMN surface resulted significantly stronger for As^{III} compared to As^V. Intriguingly, in the FTIR spectrum of the SAMN@As^V complex, a new vibrational feature centred at about 1005 cm⁻¹ appeared at neutral pH, suggesting a modification of the As^V binding mechanism, and possible competition with OH⁻ groups.

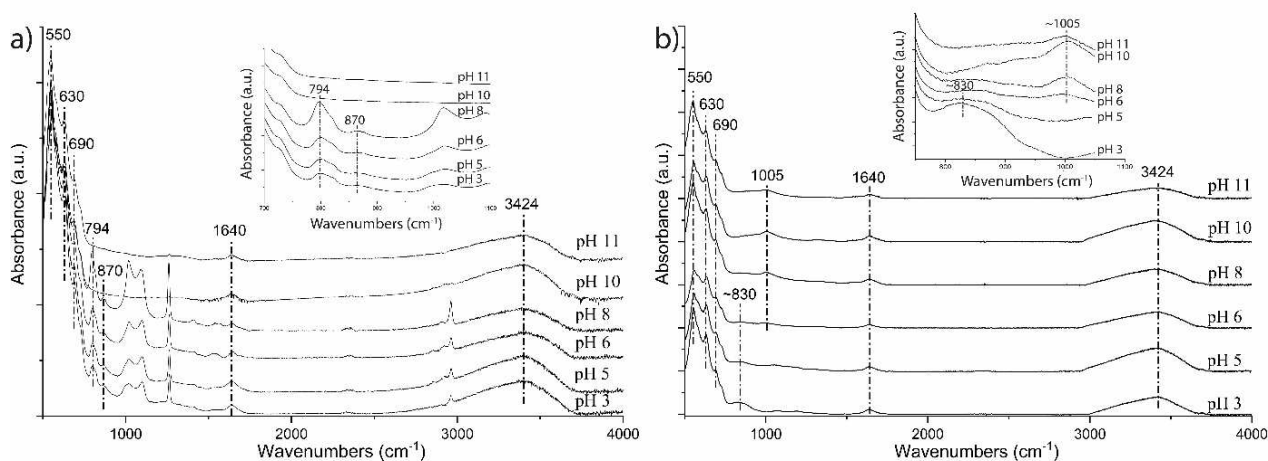


Figure 25. FTIR spectra of SAMN@As complexes as a function of pH. a) SAMN@As^{III}; b) SAMN@As^V.

Insets: magnification of FTIR bands due to As binding onto SAMNs.

Thus, the spectroscopic characterisation of the SAMN@As complexes confirmed the occurrence of two different binding mechanisms for As^{III} and As^V on naked maghemite nanoparticles. Arsenite appears to interact with SAMNs by monodentate inner-sphere coordination, while arsenate binding is characterised by higher degrees of freedom, and, therefore, different binding options. Thus, the higher binding specificity to SAMNs shown by As^{III} compared to As^V substantiated the hypothesis of the existence of specific sites on SAMNs surface. Up to the author's knowledge, only rare examples of comparative studies on the As^{III}-As^V couple were performed on maghemite (Lin et al., 2012; Liu et al., 2016).

However, they did not show any specificity of the adsorption mechanism of the two oxyacids onto the metal oxide. Therefore, the SAMNs here presented to display an unusual chemical behaviour compared to other nanostructured materials sharing the same crystalline composition. This suggests that the difference is correlated with the crystal truncation at the physical boundary of the nanomaterial, hence determining peculiar surface chemistry.

4.4 Conclusions

The present work reports on a category of nanosized maghemite called Surface Active Maghemite Nanoparticles (SAMNs), characterised by excellent colloidal properties in a wide pH range without any coating or surface modification, which stand out among similar nanomaterials for the selective binding of organic and inorganic molecules (Magro et al., 2014; Magro et al., 2015; Magro et al., 2016; Magro et al., 2019). This property, already highlighted with macromolecules, such as proteins and DNA, was tested with As^{III} and As^V oxyacids as molecular probes.

The surface of these peculiar iron oxide nanoparticles revealed differences in the binding affinity and stability constants of arsenate and arsenite. In particular, arsenite binding on SAMNs, with respect to arsenate, was faster, displayed higher stability and a pH-independent binding behaviour. Conversely, arsenate adsorption on SAMNs progressively decreased as a function of pH and appeared more labile. These features can be attributed to the different binding mechanism on the iron oxide surface, hence revealing a specificity of under-coordinated Fe^{III} sites on SAMNs surface. In particular arsenite appears to bind to SAMNs by monodentate complexation, whereas arsenate displays several binding modalities, resulting in the observed lower specificity. Thus, besides the binding selectivity observed with macromolecules due to the surface distribution of under-coordinated Fe^{III} sites, these single binding points display the ability to discriminate among small ligands with a similar structure. Noteworthy, this property was not observed in similar, already reported comparative studies.

The compendium of characteristics, spanning from the synthesis completely carried out in the water, the surface reactivity and specificity and the biocompatibility make these SAMNs an ageing candidate for large scale remediation processes.

Even if nanosized iron oxide were deeply studied, novel syntheses could lead to nanomaterials characterised by smart surfaces, offering novel and promising features which can be very useful for a wide range of applications, from water remediation to biotechnology.

5. Chromium remediation from industrial groundwater: the Ex-Stoppani case study

5.1 The Ex-Stoppani site

The investigated site is the Ex-Stoppani industry (Figure 26) located between the municipalities of Cogoleto and Arenzano (Genova, Italy) and two different COPR disposal sites (Pian Masino area and Molinetto dump) nearby the industrial area. Since 2001 all the area is in the list of Site of national interest for remediation defined with Ministerial decree 468/01.

The activity of the factory began in 1901 with the authorization of Cogoleto municipality; it was based on the transformation of a Cr^{III}-rich mineral (i.e. Chromite ((Mg,Fe)Cr₂O₄)) into a Cr^{VI}-rich product Sodium dichromate (Na₂Cr₂O₇) produced through the so-called high-lime roasting process consisting in a high temperature (~1200 °C) roasting process in excess of lime (CaO) and oxidizing conditions in order to convert the Cr^{III} into Cr^{VI}.

The highly soluble Na₂Cr₂O₇ was then separated from the residual mass and transformed into chromic acid (H₂CrO₄) and basic chromium sulphate (Cr(OH)SO₄) for galvanic processes and tanning industries respectively.

During the over 100 years of production, the discharge of millions of tons of Cr^{VI} rich post-production mud (COPRs) (Cr^{VI} concentrations above 100 µg g⁻¹), in all the area surrounding the factory generated serious problematics of groundwater pollution.

Besides the industrial area (Figure 26b,c) with concentrations of total Cr in soils up to 15,000 mg kg⁻¹ and Cr^{VI} in groundwater ranging from 500 µg L⁻¹ to 150000 µg L⁻¹, all the site is affected by hard Cr^{VI} pollution in groundwater influencing also the Lerone creek and all the coast facing the industrial site. In particular, the discharge of post-production mud, on the beaches and the sea generates a widespread pollution affecting water and sediments as far as 500 m from the coast (Mugnai et al., 2010; Bertolotto et al., 2005).

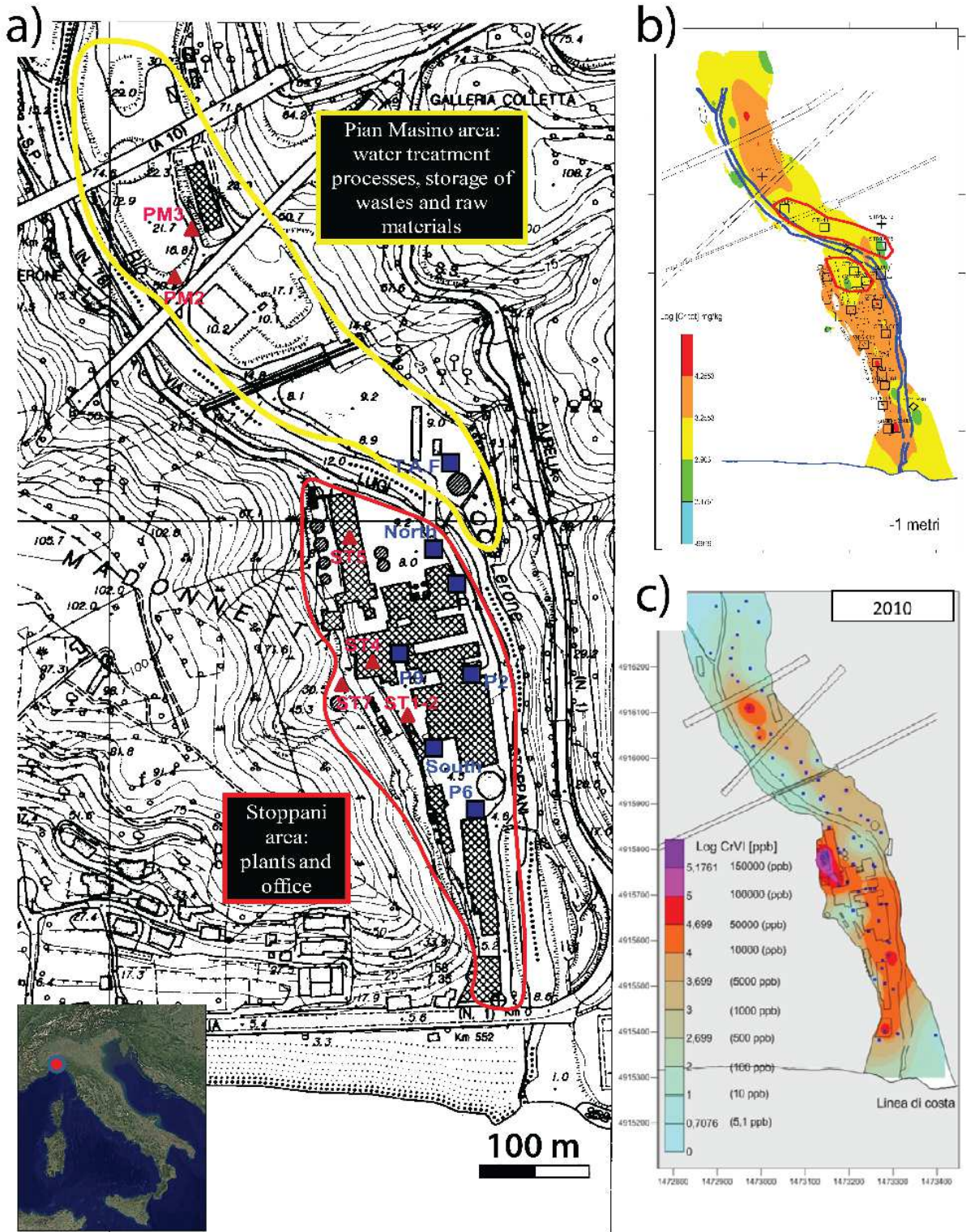


Figure 26. Site of National Interest Ex-Stoppani: a) samples location in Stoppani and Piano Masino dump area: wells (blue squares), COPRs (red triangles); b) total Cr concentration in soils (linear kriging); c) Cr^{VI} concentration in groundwater (linear kriging) (Regional Agency for Environmental Protection and Prevention Liguria)

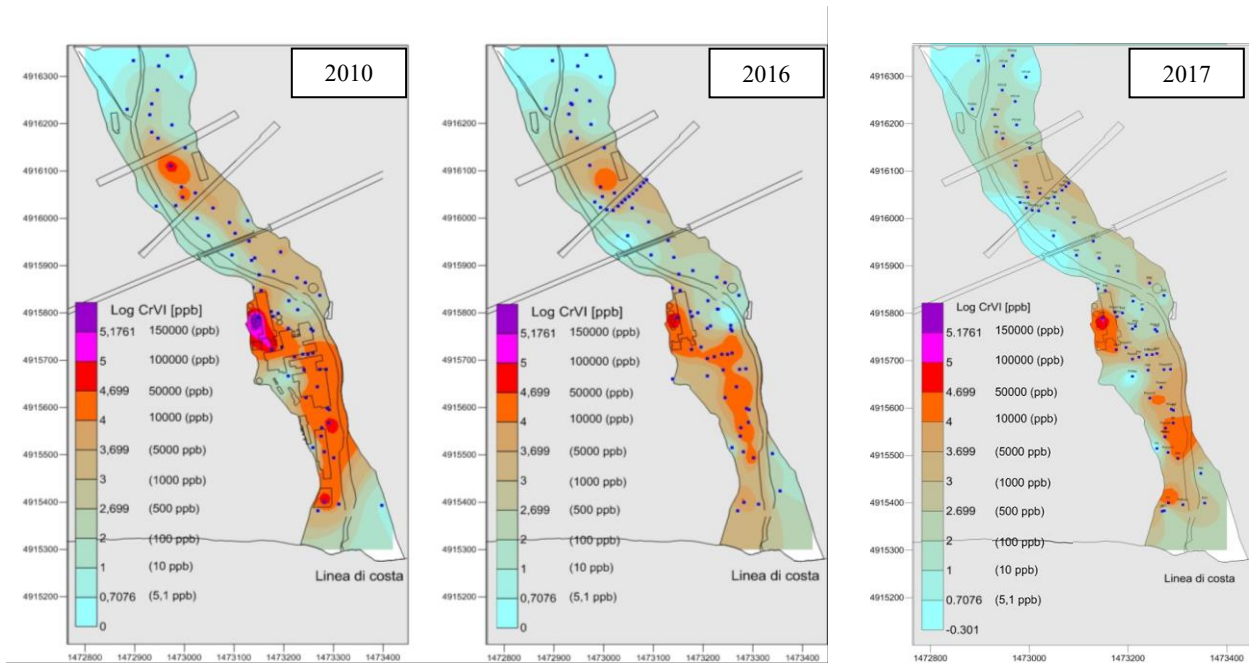


Figure 27. Evolution of Cr^{VI} concentrations in groundwater (Regional Agency for Environmental Protection and Prevention Liguria)

Strictly concerning the groundwater Cr^{VI} concentrations in the Ex-Stoppani site, values as high as 0.15 g L⁻¹ was found in 2010 (Figure 27) with a temporal decrease due to the decommissioning operation and impermeabilization of all the areas. The consequent decrease of Cr^{VI}-rich phases by weathering was observed. Nevertheless, very high Cr^{VI} concentrations are still registered at values higher than 500 ppb, with hotspots characterised by concentrations above 50.000 ppb. Notably, the Italian law limit is 10 ppb for Cr^{VI} in water (Legislative Ordinance 152/2006, Ministerial Ordinance 15/2016).

5.2 Mineralogical, chemical and spectroscopic characterisation and time-lapse monitoring of chromite-ore processing residues: the ex-Stoppani case study.

5.2.1 Abstract

This study presents the results of the mineralogical, chemical and spectroscopic characterization of Chromite Ore Processing Residues (COPRs) from the Ex-Stoppani site

and provides new insights in the evolution and identification of COPR mineralogy and of Cr-bearing mineral phases and reactions of retention and release of Cr^{VI} in groundwater by a wide multi-technique characterization coupled to an innovative sample preparation approach.

COPR is a high pH waste containing elevated residual total Chromium concentrations, up to 30 wt% occurring as toxic Hexavalent Chromium (Cr^{VI}).

Millions of tons of Chromite Ore processing Residue (COPR) were discharged in the area referred as Ex-Stoppani site of national interest, resulting in intense phenomena of Cr^{VI} leaching from COPR and contamination of percolating groundwater. An accurate characterisation of COPRs is necessary to deepen our knowledge on processes controlling retention and release of Cr^{VI} by X-Ray Powder Diffraction (XRPD), Scanning Electron Microscopy (SEM), Energy Dispersive X-ray analysis (EDX) coupled with μ -Raman and Fourier transform infrared (FTIR) spectroscopy and thermogravimetric analysis (TGA). In particular, all the analysis were performed on pristine samples and on dry polishing sections to avoid any Cr-bearing mineral destabilisation during sample preparation that is not taken into account into previous works (Hillier et al., 2003; Chrysochoou et al., 2009, 2010).

Results showed that mineral assemblages in COPRs can be summarised into three main categories: unreacted chromite ore, high-temperature mineral formed during the roasting process (Brownmillerite) and, finally, minerals formed after the in-site disposal under ambient conditions (Calcite, Aragonite, Gypsum, Ettringite, Katoite, Hydrotalcite). Moreover, the opportunity to the study COPRs affected by different weathering degrees in the site (at the beginning of remediation phases) has revealed substantial differences in mineral assemblages concerning the Cr-bearing phases. It should be stressed that the proposed study approach highlighted the presence of highly soluble Na₂CrO₄ in COPR aged less than 15 years. Moreover, μ -Raman analysis of untreated samples also revealed the presence of a never detected Cr-bearing mineral, crocoite (PbCrO₄), found in both low aged and weathered COPRs thus confirming its formation during the manufacturing process. The results of the present study represent the first step at the basis of risk assessment and suggest the development of the best-performing stabilisation/remediation procedure.

Keywords: chromium; Chromite ore processing residue; Mineralogy; Crocoite

5.2.2 Introduction

Chromium (Cr) received important interests in the last century due to its properties and extensive possibilities for many industrial fields such as metal plating, textile dyes, pigments and leather tanning.

Cr is a redox-sensitive metal usually found in nature in two main oxidation states (+3 and +6): the trivalent form (Cr^{III}) is the more stable and is characterised by low solubility and toxicity in trace amounts. Moreover, it is an essential trace element for human and animal health participating at carbohydrate and lipid metabolism (Davis and Vincent, 1997; Kimbrough et al., 1999). The major source of geogenic Cr^{III} is represented by Chromite FeCr_2O_4 , a stable mineral at environmental conditions characterised by low solubility. The hexavalent form (Cr^{VI}), a strong oxidant, is known to be carcinogenic when inhaled or ingested with drinking water (Holmes et al., 2008; Sun et al., 2015) and is usually produced by industrial process..

Due to its toxicity, the World Health Organization determined a guideline value of 0.05 mg L^{-1} for total Cr in drinking water (WHO, 2017) and Italy set a maximum value of Cr^{VI} for groundwater of 10 ug L^{-1} (Legislative Ordinance 152/2006, Ministerial Ordinance 15/2016). The large use of Cr^{VI} salts in many industrial activities (i.e. textile dyes, wood preservation, anti-corrosion products, tanneries, pigments) caused important cases of pollution of soils and groundwater, and, in last years, attention was devoted to pollution phenomena for uncontrolled disposal of Cr^{VI} -rich industrial residues.

Chromite Ore Processing Residue (COPR) is a waste generated by production of sodium chromate (Na_2CrO_4) via high lime process by chromite ore: pulverised chromite is heated at $1200 \text{ }^\circ\text{C}$, and an alkali carbonate (i.e. Na_2CO_3) added to create the oxidising conditions necessary to transform Cr^{III} to the more soluble Cr^{VI} , that is then extracted in water.

This process produces big volumes of sludge, characterised by strong alkalinity ($\text{pH} \sim 12$) containing 3-5% of residual total chromium, where part of it (from 1 to 30%), occurs as toxic Cr^{VI} (Chrysochoou et al., 2010; Matern et al., 2017).

The production of this type of waste was documented in several industrial areas all around the world, such as New Jersey, USA (Weng et al., 1994), Glasgow, Scotland (Hillier et al., 2003) and Uttar Pradesh, India (Matern et al., 2016).

The use of high lime processes was gradually abandoned in Europe and United States in the 60s due to the toxicity of waste residues. However, in many countries such as Russia, China, Pakistan and India it's still used (Farmer et al., 2006; Geelhoed et al., 2003).

Moreover, the use of millions of tons of this waste material as landfill or its improper treatment and disposal caused long-term problematic of Cr^{VI} leaching coming from dissolution and destabilisation of Cr^{VI} mineral phases. The instability of deposited COPR due to weathering and dissolution of Cr^{VI}-bearing minerals, the high risk deriving from the high mobility and toxicity of Cr^{VI} in water, make the identification of its mineralogical sources of primary concern (Weng et al., 2001; Farmer et al., 2002; Chrysochoou et al., 2010; Matern et al., 2017).

The present study is focused on the Ex-Stoppani site (previously described), since 2001 in the list of site of national interest for remediation as defined by the Ministerial Ordinance 468/01, and on two different COPR disposal sites (Pian Masino area and Molinetto dump), nearby the Ex-Stoppani industrial area. COPRs were found in all the areas as berms, foundation materials and backfills, and represent a serious problem due to release of CrVI in percolating groundwater in the proximity to the mouth of Lerone river and the subsequent high impact on the coastline, just in front the industrial area.

Even if the chemical composition, mineralogy, leaching behaviour and geotechnical characteristics have been widely described in the last 20 years in many countries (Weng et al., 2001; Hillier et al., 2003; Chrysochoou and Dermatas, 2006; Dermatas et al., 2006; Farmer et al., 2006; Chrysochoou et al., 2010; Boecher et al., 2012; Matern et al., 2016, 2017), the Ex-Stoppani area, being very recently closed, represent a unique opportunity to follow the evolution of COPR from first stages of the processing of parental material to the oldest (~50 years) deposited material. Recently, Matern et al., (2016) demonstrated that important differences are related to COPR age and geographical localisation due to weathering conditions, deposition technique and chromite ore composition. In particular, they found that the age of the deposit is a key factor for Cr content and presence of reactive mineral phases.

The aim of this study is to identify and characterise the Cr-mineralogical phases in the Ex-Stoppani site and to clarify the role of Cr-bearing phases on the release of Cr^{VI} in percolating groundwater by a multi-technique approach: bulk chemical analyses, X-ray powder diffraction (XRPD), Scanning Electron Microscopy (SEM), μ -Raman spectroscopy, Fourier Transform Infrared spectroscopy (FTIR) and thermogravimetric analyses (TGA).

Moreover, the present study provides the opportunity to follow the evolution of COPR material from low aged (<15 years) roasting material, comparable to Indian COPRs (Matern et al., 2016), up to the oldest, more evolved material, that is comparable to that described in U.S and Glasgow (Hillier et al., 2003; Dermatas et al., 2006). Furthermore, so far available data reported in literature about the pollution of the SINs were focused on superficial sediment pollution far from the coast (Bertolotto et al., 2005; Mugnai et al., 2010), while no in-depth mineralogical studies are available to assess Cr^{VI} rich-phases in the factory area, which are responsible for the long-term pollution of areas surrounding the Ex-Stoppani site.

5.2.3 COPRs samples

COPR materials were sampled from the three sites (see Figure 26): samples from Ex-Stoppani site (labelled ST) are representative of the more recent COPR material: ST1 and ST2 are the more recent (<15 years) roasting material and were preserved from weathering; ST5 was sampled in a waste cumulus and represents another young waste of the manufacturing process. Other ST samples (namely ST4, ST7) are representative of the superficial foundation material of the factory area and were not protected from weathering processes. Finally, Pian Masino and Molinetto dump samples (labelled PM and DM respectively) represent the oldest weathered COPR material (~30 years old).

5.2.4 Results

Mineralogical and chemical characterization

The typical COPR mineral assemblage can be divided into three main categories: i) the unreacted ore represented by chromite; ii) high-temperature minerals formed during the roasting process; iii) all the minerals formed during the subsequent manufacturing process and due to weathering after deposition of COPR at ambient conditions (Hillier et al., 2003). Typically, the pH of COPRs (Table 5) is in general strongly alkaline (pH>9), with the two less aged samples (ST1 and ST2) characterised by the highest pH value (pH = 10.6 and 10.3, respectively). The high pH value can be consistent with the use of lime (CaO, pH = 12.4) during the roasting of the chromite ore (Hausmann, 1990). All the other investigated COPR samples showed slightly lower values pH values, ranging from 8.7 to 10.4. These pH values

are lower than those reported for the U.S. and Indian COPR (Dermatas et al., 2006; Chrysochoou et al., 2010; Matern et al., 2016) and this can be due to the very superficial nature of Ex-Stoppani samples and to the subsequent mixing with other materials and local soils. Similar pH values were found in superficial COPR-soil mixture in four sites in Glasgow (Graham et al., 1999; Farmer et al., 2002), where COPR was used as landfill.

Table 5. Bulk chemistry of young roasting and weathered COPRs

	Young COPRs			Aged and weathered COPRs						
	ST1	ST2	ST5	ST4	ST7	PM2	PM3	DM1	DM2	DM3
pH in CaCl ₂ (-)	10.6	10.3	9.8	9.6	9.1	9.6	9.5	9.2	8.7	9.0
Total C (g kg ⁻¹)	33.3	32.9	2.6	26.0	24.0	17.7	43.1	1.6	1.5	8.0
Inorganic C (g kg ⁻¹)	29.3	28.8	1.8	20.5	20.1	11.4	41.27	1.6	1.5	5.0
Organic C (g kg ⁻¹)	4.0	4.1	0.8	5.5	3.9	6.3	1.83	N.D.	N.D.	3.0
Total S (g kg ⁻¹)	N.D.	N.D.	187.9	10.6	1.8	8.5	1.3	8.3	6.4	45.8
Ca (g kg ⁻¹)	0.79	1.72	8.43	104.06	134.58	94.27	62.61	15.01	13.22	74.62
Al (g kg ⁻¹)	50.60	50.33	4.71	51.87	64.36	61.50	65.20	93.78	97.33	50.49
Fe (g kg ⁻¹)	55.74	61.09	6.82	83.13	47.42	39.94	64.21	122.50	137.68	89.81
Mg (g kg ⁻¹)	36.06	36.60	5.01	60.60	55.00	51.26	45.89	71.40	74.17	46.86
Cr (g kg ⁻¹)	114.29	125.05	14.76	50.97	21.31	18.06	36.16	73.31	79.54	60.38
Si (g kg ⁻¹)	3.37	8.65	7.01	15.52	78.57	127.23	125.60	18.00	19.40	24.68
Mn (g kg ⁻¹)	1.16	1.24	0.15	1.63	1.39	1.08	1.32	2.09	2.48	1.78
K (g kg ⁻¹)	N.D.	0.33	0.66	0.25	8.80	7.39	8.22	0.83	0.91	0.66
Na (g kg ⁻¹)	101.86	107.94	281.53	2.30	2.52	6.16	6.60	5.19	5.42	2.15
V (g kg ⁻¹)	1.29	1.27	0.08	1.11	0.52	0.38	0.61	2.07	1.99	1.12
Ti (g kg ⁻¹)	2.28	2.28	0.24	2.22	2.46	2.46	3.30	4.38	4.26	2.40
Ni (g kg ⁻¹)	0.60	0.62	0.07	0.89	0.66	0.52	0.74	1.13	1.27	0.81

Table 6 showed that a total of 24 mineralogical phases were found in the studied COPRs, and clearly highlights that studied samples can be divided into two groups on the basis of mineralogy. This subdivision is related to the different COPR aging and weathering in (ST1, ST2 and ST5 <15 years; ST4, ST7, PM and DM > 30 years). Thus, a separate discussion is followed in the text.

ST1 and ST2, low aged roasting samples, showed almost the same mineralogical association (Figure 29a), characterised by three main phases: chromite, trona and sodium chromate. Chromite, representing the un-reacted primary ore, was identified as major components in both the two COPR samples and was consistent with the highest Cr values (114.29 and 125.05 g kg⁻¹ for ST1 and ST2, respectively) (Table 5). Peaks broadness in the XRPD spectra highlighted the presence of at least two spinels with different composition.

Chromite is easily recognised as a stand-alone phase, with preserved core and corroded rims, or rimmed by a series of fine-grained crystals forming an alteration halo (Figure 30b,a) as also reported by (Hillier et al., 2003; Matern et al., 2016).

Table 6. Minerals identified in COPR samples and known chromium substitutions

Mineral	PDF	Indicative formulae*	Known Cr substitution	Young COPRs			Aged and weathered COPRs						
				ST1	ST2	ST5	ST4	ST7	PM2	PM3	DM1	DM2	DM3
Chromite	96-900-4950	(Mg,Fe)Cr ₂ O ₄		X	X		X	X		X	X	X	X
Trona	98-006-2200	Na ₃ (CO ₃)(HCO ₃)*2(H ₂ O)		X	X								
Grimaldiite	01-085-1372	Cr(OH)		X									
Sodium Chromate	00-022-1366	Na ₂ CrO ₄		X	X								
Brownmillerite	98-002-7112	Ca ₂ (Al,Fe)O ₅	Cr ³⁺ for Fe, Al (Battle et al., 1991)	X	X								
Gypsum	01-070-0982	Ca(SO ₄)*(H ₂ O) ₂					X		X		X	X	X
Calcite	01-083-1762	CaCO ₃				X	X	X	X	X			
Dolomite	98-010-0416	CaMg(CO ₃) ₂				X							
Aragonite	98-016-9892	CaCO ₃					X						
Etringite	98-015-5395	Ca ₆ Al ₂ (SO ₄) ₃ (OH) ₁₂ *26(H ₂ O)	CrO ₄ ²⁻ for SO ₄ ²⁻ (Hillier et al., 2003)				X	X	X				
Katoite	96-900-1773	Ca ₃ Al ₂ (SiO ₄) ₃ (OH) ₄ , x=1.5-3	Cr ³⁺ for Al, Fe (Kindness et al., 1994) CrO ₄ ²⁻ for OH ⁻ (Hillier et al., 2007)					X	X				
Hydroxalite	01-089-0460	Mg ₆ Al ₂ CO ₃ (OH) ₁₆ *4H ₂ O	CrO ₄ ²⁻ for CO ₃ ²⁻ (Chrysochoou et al., 2009)					X	X				
Thenardite	01-070-1541	Na ₂ SO ₄				X							
Bassanite	98-007-3263	Ca(SO ₄)*0.5H ₂ O					X						
Muscovite	00-006-0263	KAl ₂ (Si ₃ Al)O ₁₀ (OH,F) ₂						X	X	X			
Phengite	96-900-5487	K(Al,Mg) ₂ (OH) ₂ (Si,Al) ₄ O ₁₀					X						
Antigorite	96-901-4626	(Mg,Fe) ₃ Si ₂ O ₅ (OH) ₄					X			X	X	X	X
Lizardite	01-084-1391	(Mg,Fe) ₃ Si ₂ O ₅ (OH) ₄											
Clinocllore	00-007-0076	Mg ₃ Al(AlSi ₃ O ₁₀)(OH) ₈			X		X	X		X			
Quartz	01-079-1910	SiO ₂			X		X	X	X	X			
Biotite	98-009-8157	K(Mg,Fe) ₂ AlSi ₃ O ₁₀ (OH,F) ₂			X								
Pyrophyllite	00-046-1308	Al ₂ Si ₄ O ₁₀ (OH) ₂			X								
Paragonite	00-024-1047	NaAl ₂ (Si ₃ Al)O ₁₀ (OH) ₂						X	X				
Albite	98-010-0337	NaAlSi ₃ O ₈							X	X			

*Indicative formula reported for simplicity (in agreement with Hillier et al., 2003)

Chromite are characterized by a core with high Mg content representing the preserved original feedstock of magnesium chromite ore used in the roasting process. On the contrary, the rim was characterised by an enrichment in Fe^{III} with a composition close to magnesium-ferrites (Figure 28) probably generated as result of roasting process at oxidising conditions for the conversion of the Cr^{III} to Cr^{VI}. Moreover, the bulk Mg content of ST1 and ST2 (36.06 and 36.60 g kg⁻¹, respectively) were similar and slightly lower than those reported for Indian and Glasgow COPRs, thus reflecting a magnesiocromite composition of the original ore.

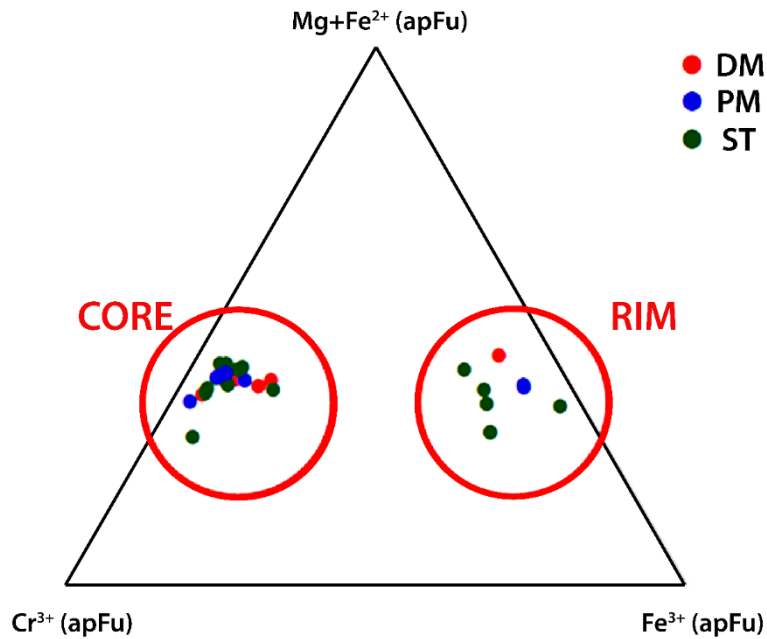


Figure 28. Composition (atom per formula unit (apFu) of chromite in the ternary diagram $\text{Cr}^{3+} - \text{Fe}^{3+} - (\text{Mg} + \text{Fe}^{2+})$

The second more abundant minerals are Trona ($\text{Na}_2(\text{CO}_3)(\text{Na}(\text{HCO}_3))(\text{H}_2\text{O})_2$). Trona, that was not described and detected in other COPRs, was probably used a source of Sodium carbonate for the first step of the manufacturing process, being composed by 46% of sodium carbonate and 36% of Sodium bicarbonate (Cho et al., 2008) and presenting a phase transition to pure Sodium carbonate at 160°C (Gärtner and Witkamp, 2002). It was easily recognized on pristine sample under low vacuum ESEM images (Figure 30C) in well-formed elongated tabular crystals, while it was not found in sections, probably due to its destabilization during sample preparation. Anyway, its presence and participation in manufacturing process was testified by the detection of Na in EDS analysis of alteration halos of chromite (Figure 30b). The high Na content (101.86 and 107.94 g kg^{-1} for ST1 and ST2, respectively), coupled with total carbon content (33.3 and 32.9 g kg^{-1} for ST1 and ST2, respectively) (Table 5) reflected the use of soda (Na_2CO_3) during the first roasting phase. The third component was sodium chromate (Na_2CrO_4), whose preservation, already described by Matern et al., (2016) in pores in Chhwali COPR, is a consequence of solubilisation and evaporation phenomena of Cr^{VI} -rich solutions in matrix pores driven by particular climate conditions or to the impossibility of leaching of the primary sodium

chromate, being the sample stored in regions protected from interaction with water (matrix pores) (James, 1994; Matern et al., 2016).

Other two phases were detected in the ST1 and ST2 samples: Grimaldiite ($\text{CrO}(\text{OH})$) and Brownmillerite ($\text{Ca}_2(\text{Al}, \text{Fe}^{3+})_2\text{O}_5$).

Grimaldiite was firstly described in COPRs by Matern et al., (2016) in Chhwali COPR. The identification in Ex-Stoppani samples was difficult due to XRPD peaks overlapping with Na_2CrO_4 , while SEM identification was unsuccessful due to the very fine grains of minerals. Brownmillerite, a high-temperature mineral formed during roasting process in the first HT phases ($\sim 1200^\circ\text{C}$) of production (Hillier et al., 2003) characterising the alteration halo of chromite (Figure 30a), was also observed. Moreover, EDS analysis showed 6% of Cr content in brownmillerite minerals.

Interestingly ST1 and ST2 samples showed the lowest Ca values (0.79 and 1.72 g kg^{-1} for ST1 and ST2, respectively) with respect other samples. This is apparently contradictory with the roasting process carried out in excess of lime, but can probably reflect a change in the manufacturing process occurred from 1950s when lime was removed to decrease the workers exposure to calcium chromate, and consequently reduce the health risks (Davies et al., 1991).

XRPD spectra of ST4, ST5 and ST7 are reported in Figure 29Ba,b,c respectively, showing a more complex mineralogy compared to ST1 and ST2 samples. Sample ST5 is mainly composed by Thenardite (Na_2SO_4), as highlighted also by the chemical composition of the sample, mainly composed of Na and S (Table 5). Thenardite was in association with crocoite (Figure 30e), and low amounts of calcite (CaCO_3) and dolomite ($\text{CaMg}(\text{CO}_3)_2$). Thenardite was characterised by tabular habit (Figure 30e) with no Cr substitution and was previously described only in Chhiwali COPR as microcrystalline fillings in pores and consequently preserved from leaching (Matern et al., 2016). Crocoite (PbCrO_4) (Figure 30e) was never detected before in COPR phase.

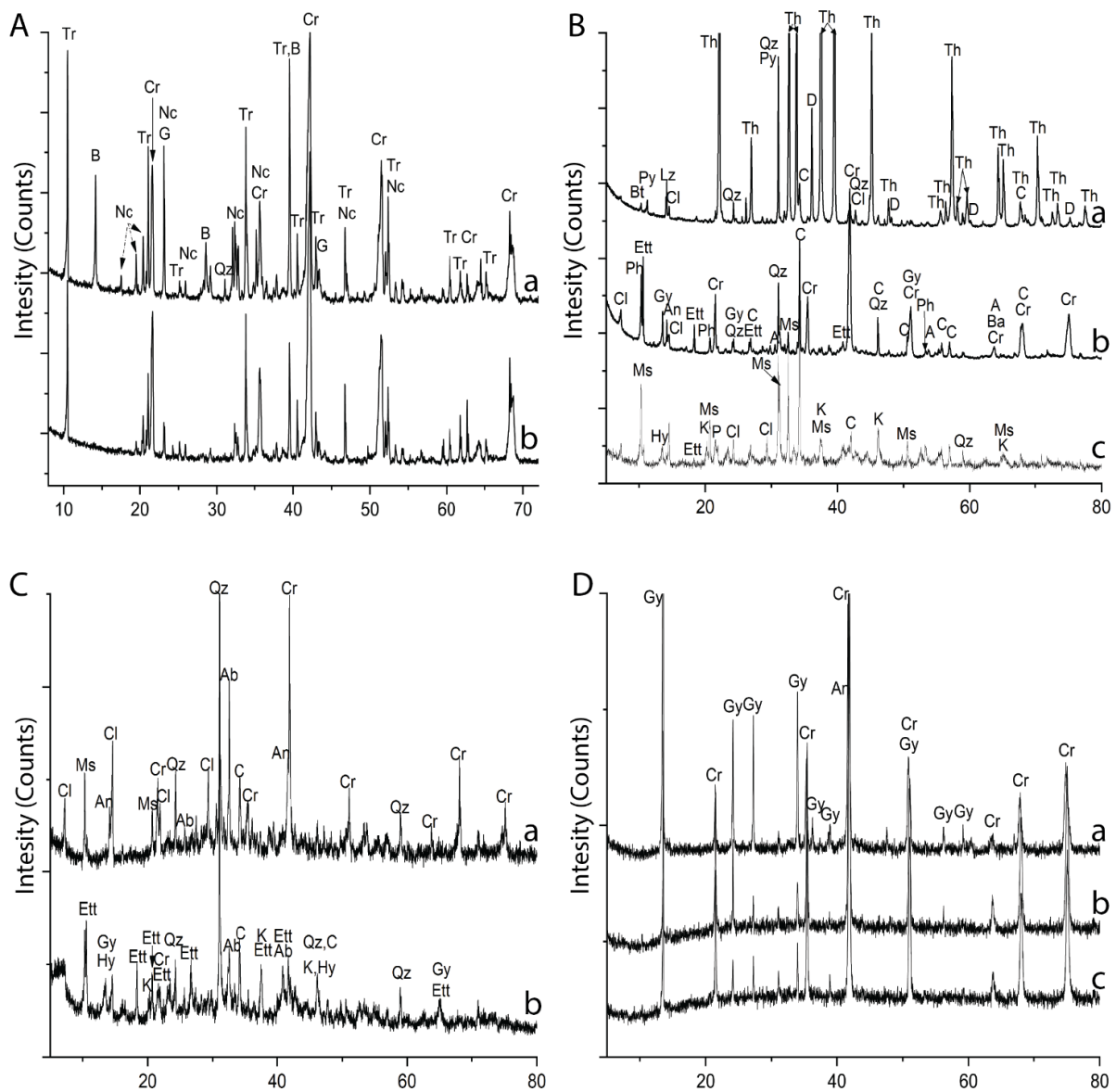


Figure 29. X-ray powder diffraction patterns of COPR: A) young roasting samples from Stoppani site (a. ST1 and b. ST2); B) COPRs from Stoppani site (a. ST5, b. ST4, c. ST7); C) COPRs from Pian Masino area (a. PM3, b. PM2); D) COPRs from Molinetto dump area (a. DM3, b. DM2, c. DM1). Identification of main peaks for the various minerals present is indicated. Patterns are offset for clarity. Tr=Trona; B=Brownmillerite; Nc=Sodium Chromate; G=Grimaldiite; Qz=Quartz; Bt=Biotite; Cl=Clinocllore; Th=Thenardite; Lz=Lizardite; D=Dolomite; Py=Pyrophyllite; C=Calcite; Pc=Crocoite; Ett=Ettringite; Hy=Hydrotalcite; Ph=Phengite; A=Aragonite; Ms=Muscovite; K=Katoite; Gy=Gypsum; Ab=Albite; An=Antigorite; Cr=Chromite; P=Paragonite.

Its identification was unsuccessful by XRPD due to peak overlapping, but was possible by low-vacuum SEM working on pristine samples and dry polished sections. The other two COPR minerals, in low amount were calcite (CaCO_3), and dolomite ($\text{CaMg}(\text{CO}_3)_2$), representing the last carbonation products of COPR reaction with percolating water with the

subsequent sequestration of CO₂ in the solution at high pH conditions by a Ca-rich source (Chrysochoou et al., 2010).

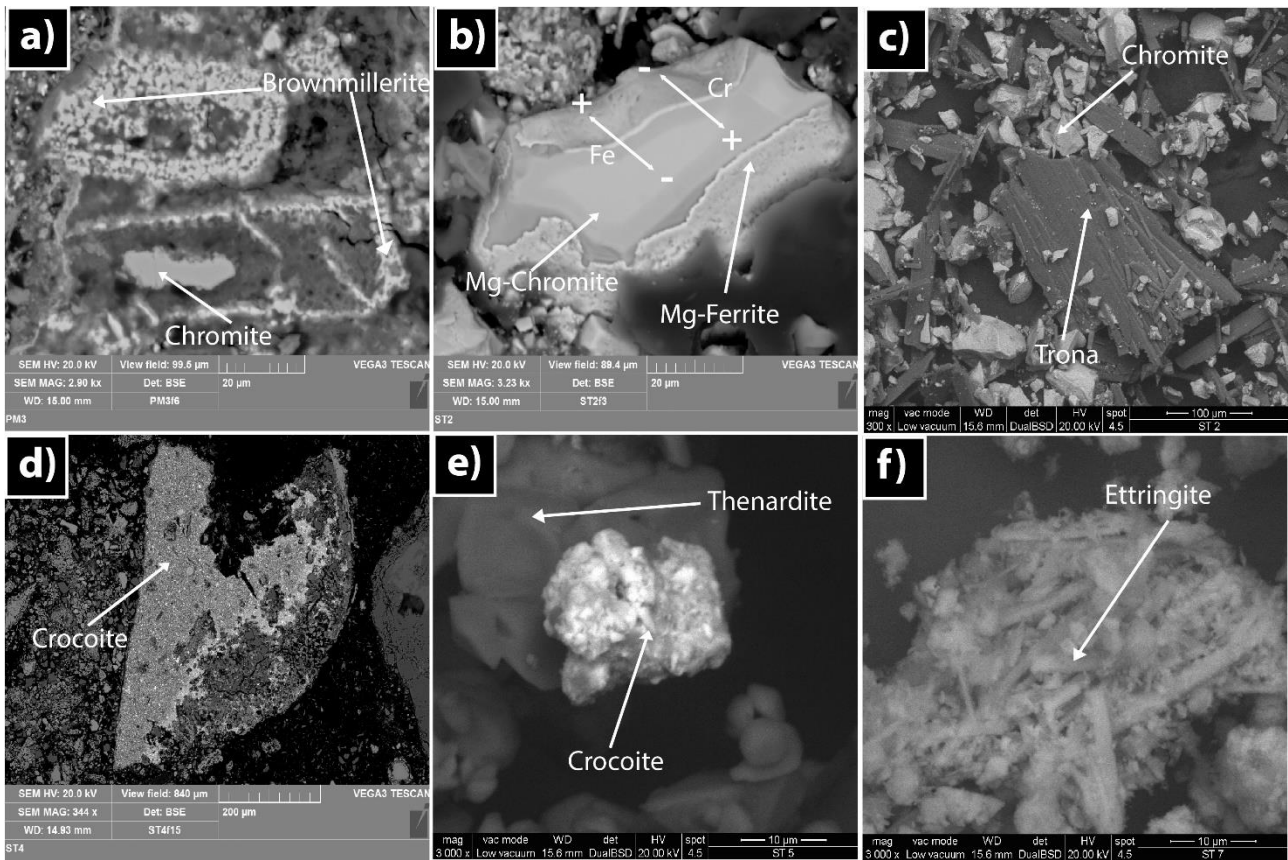


Figure 30. High Vacuum Backscattered electron images of polished sections (a, b, d, f) and Low Vacuum backscattered electron image of pristine (c, e) COPR samples

Sample ST4, ST7, PM2, PM3, characterised by the previously described unreacted feedstock ore, and showed similar composition for Cr, Ca, Al, K, Na and total carbon to US and Glasgow and Indian COPRs except for DM1 and DM2 due to mixing in the dump with recent roasting material. The only chromate detected was crocoite (by SEM) in sample ST4 on dry polished sections. This highlights its persistence during the evolution of COPRs.

All samples showed the presence of a possible Cr^{VI}-bearing phase (Figure 29Bb, c): namely ettringite (Ca₆Al₂(SO₄)₃(OH)₁₂·26(H₂O)), representing one of the brownmillerite hydration products by reaction with sulphate. ESEM analysis on the dry polished section also confirmed that it was characterised by a very long prismatic habit (Figure 30f). Possible sulphate (SO₄²⁻) – chromate (CrO₄²⁻) substitutions in the structure were reported by Hillier et al., (2003) and Matern et al., (2016) while this substitution process was negligible in U.S

samples (Chrysochoou and Dermatas, 2007). EDX analysis of ettringite evidenced a Cr content ranging from 0.6 to 2.8%.

Another Brownmillerite hydration product, katoite ($\text{Ca}_3\text{Al}_2(\text{SiO}_4)_{3-x}(\text{OH})_{4x}$ $x=1.5-3$), was found in ST7 and PM2 samples; its find in COPR is well known and reported in Glasgow, U.S. and Indian COPRs. Katoite represents another possible Cr-bearing mineral that can incorporate Cr inside its structure, both as Cr^{III} in the octahedral sites and Cr^{VI} in the tetrahedral sites (Hillier et al., 2007, 2003). However, in Ex-Stoppani samples the identification by SEM was unsuccessful, making impossible to estimate Cr substitution.

Another potential Cr^{VI} bearing phases is hydrotalcite ($\text{Mg}_6\text{Al}_2\text{CO}_3(\text{OH})_{16} \cdot 4\text{H}_2\text{O}$), found in samples ST4 and PM2, that refers to magnesium aluminium carbonate hydrates, formed from brucite or periclase, as result of brownmillerite destabilisation and Al release (Wazne et al., 2008). Hydrotalcite belongs to the group of double-layered hydroxides (DLHs) and can retain Cr^{VI} inside the interlayer structures as CrO_4^{2-} (Chrysochoou et al., 2009) as well as many other cation substitutions in the octahedral sites (Ca, Mg, Al, Fe).

The last COPR-derived mineral detected in all the aged samples was gypsum. Its presence was reported only in a disposal site in Yima (China) (Li et al., 2017) and can be described as secondary precipitate due to COPR aging and dissolution in the presence of high quantity of Ca^{2+} and SO_4^{2-} in percolating water (Geelhoed et al., 2002). All the analysed samples from Molinetto dump (DM1, DM2 and DM3) showed a very simple mineralogical composition characterised by the unique presence of the original feedstock ore and by gypsum (Figure 29D). No Cr-bearing phases were detected, and, for this reason, these three samples will not be discussed.

Noteworthy, aged samples were characterised by a multitude of non-COPR mineral phases, especially silicates, such as biotite, muscovite clinocllore, pyrophyllite, lizardite and quartz, which cannot be considered as derived from the manufacturing process due to instability at high temperatures during the roasting process (Dermatas et al., 2006). In particular, quartz was an important constituent of all Ex-Stoppani and Pian Masino samples, and even if it derived from mixing with native soils, it represent an important SiO_2 source for crystallisation of amorphous CSH (Calcium silicate hydrates), that was responsible, for a certain extent, to COPRs cementation. This was confirmed by the very high Si content (4 times higher than the COPR from India), especially in PM samples. It should be noted that the massive presence of residual Cr and the concomitant high amount of unreacted feedstock ore demonstrated a marked inefficiency of the roasting process, considering an initial Cr content

of $\sim 400\text{-}420 \text{ g kg}^{-1}$ (data not shown) and an extraction rate between 78%-90%, similar to that reported by (Matern et al., 2016).

Spectroscopic characterisation

Results from XRPD and SEM analysis highlighted that, for a complete COPR characterisation, any phase of sample preparation should be carefully checked and possible destabilisation and leaching of soluble Cr^{VI} -bearing minerals should be minimised. Among the possible characterisation techniques, FTIR and μ -Raman spectroscopies stand out for the quality of the information, low cost compared with more complex techniques, and the possibility of working on pristine materials. FTIR spectra of selected samples are reported in Figure 31A, B, and were divided in two categories: the three low aged COPR samples (ST1, ST2, ST5) (Figure 31A), and other heavy aged COPRs samples (Figure 31B).

All samples, except for ST5, showed a wide band that can be attributed to Cr^{III} -O vibrations of the unreacted feedstock ore in the $500\text{-}650 \text{ cm}^{-1}$ region (Lenglet and Hochu, 1997; Reddy and Frost, 2005). The impossibility to resolve the fundamental (ν_1 and ν_2) frequencies of chromite arose from the core-rim variations in the chemical composition of residual chromites (Figure 30b).

Samples ST1 and ST2 were dominated by stretching vibrations of trona (Figure 31A). In particular, the bands at 850 cm^{-1} and 1455 cm^{-1} , representing the ν_2 out of plane bending and the ν_3 asymmetric stretching vibrations of carbonate, and the two peaks at 3045 , 3448 cm^{-1} and 1680 cm^{-1} attributed to hydroxyls vibration arising from water molecules, were observed (Huang and Kerr, 1960; O'Bannon et al., 2014).

.Interestingly a broad peak in the region $800\text{-}900 \text{ cm}^{-1}$ (a precise peak position cannot be determined due to overlapping by ν_3 carbonate stretching vibration) was visible in the two roasting samples (ST1 and ST2). Nevertheless, this region provided a fast information about the presence of chromate, being characteristic of asymmetric CrO_4^{2-} vibrations (Miller and Wilkins, 1952; Monico et al., 2016).

The FTIR spectrum of sample ST5, as well, was characterised by a series of bands attributable to thenardite, as sole dominant mineralogical phase. Three main bands at 610 , 637 , 1100 cm^{-1} , corresponding to SO_4^{2-} vibrations, and a broad peak centred at $\sim 3300 \text{ cm}^{-1}$ due to OH stretching vibrations, were observed (Maglione and Carn, 1975). The broad band at $\sim 1450 \text{ cm}^{-1}$ attributed to the ν_3 asymmetric CO_3 stretching of calcite and dolomite was also found (Hillier et al., 2003; Gunasekaran et al., 2006).

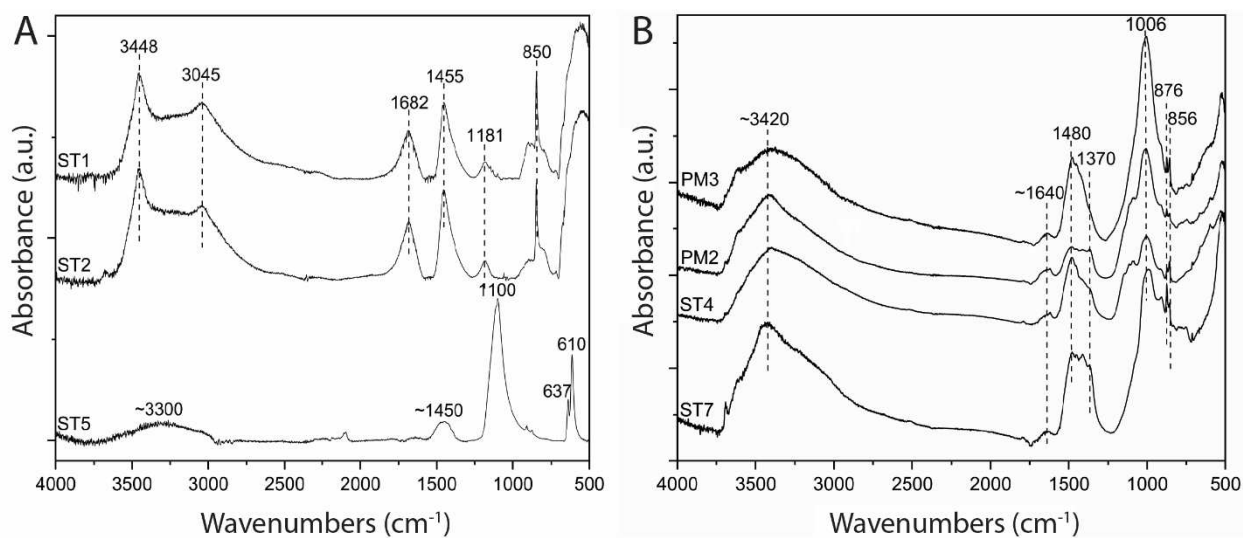


Figure 31. Infrared spectra of samples: A) Young roasting and COPR samples from Stoppani site, B) older COPRs from Stoppani and Pian Masino site. Pattern are offset for clarity

All other more aged COPR (ST4, ST7, PM2 and PM3) displayed very similar infrared spectra (see Figure 31B). In particular, the broad peak between 900-1150 cm^{-1} and the one centred at 1006 cm^{-1} can be described as a series of overlapped peaks arising from gypsum and quartz (Akyuz et al., 2009), even if the resolution of each single contributions was difficult. The bands at 856 cm^{-1} and 1480 cm^{-1} can be attributed to aragonite, while the band at 876 cm^{-1} was related to calcite phases (Hillier et al., 2003; Akyuz et al., 2009). Furthermore, Hillier et al. (2003), reported on the appearance of another band at 1429 cm^{-1} related to calcite. On the other hand, Akyuz et al. (2009) reported on the same band at 1418 cm^{-1} . It is clear that in the studied samples the peak showed a shoulder in the carbonate region between 1370 cm^{-1} and 1500 cm^{-1} that can be attributed to CO_3 vibrations related to calcite and dolomite (Gunasekaran et al., 2006), being the main carbonates found in the samples. However, the very broad peak could unveil the presence of other minor carbonates already described in other COPR, such as vaterite (Chrysochoou et al., 2010).

Except for the two roasting samples (ST1, ST2) no CrO_4^{2-} features can be recognised by FTIR spectroscopy, principally due to mineralogical complexity of samples.

For this reason, μ -Raman spectroscopy was used as a powerful technique allowing the fast and punctual characterisation of Cr^{VI} -phases and their association on pristine samples.

Representative Raman spectra of low aged roasting samples showed the presence of a large amount of sodium chromate (Figure 32Aa), as confirmed by the presence of two

absorption bands at 931 and 898 cm^{-1} , representing its ν_3 vibrational mode. Furthermore, an intense peak at 850 cm^{-1} , representing the ν_1 stretching vibration of chromate, two bands at 405 and 390 cm^{-1} , assigned to the ν_4 vibrational mode and the ν_2 vibration at 350 cm^{-1} , were also observed (Davies and Long, 1971).

As already described for the IR spectra, the main associated phase in studied samples was trona, as confirmed by the Na-O vibrations at 140 and 184 cm^{-1} and the two bands at 698 and 1060 cm^{-1} (Figure 32Ab), representing the ν_4 in plane bending and the ν_1 symmetric stretching vibration, respectively, of the carbonate group (O'Bannon et al., 2014).

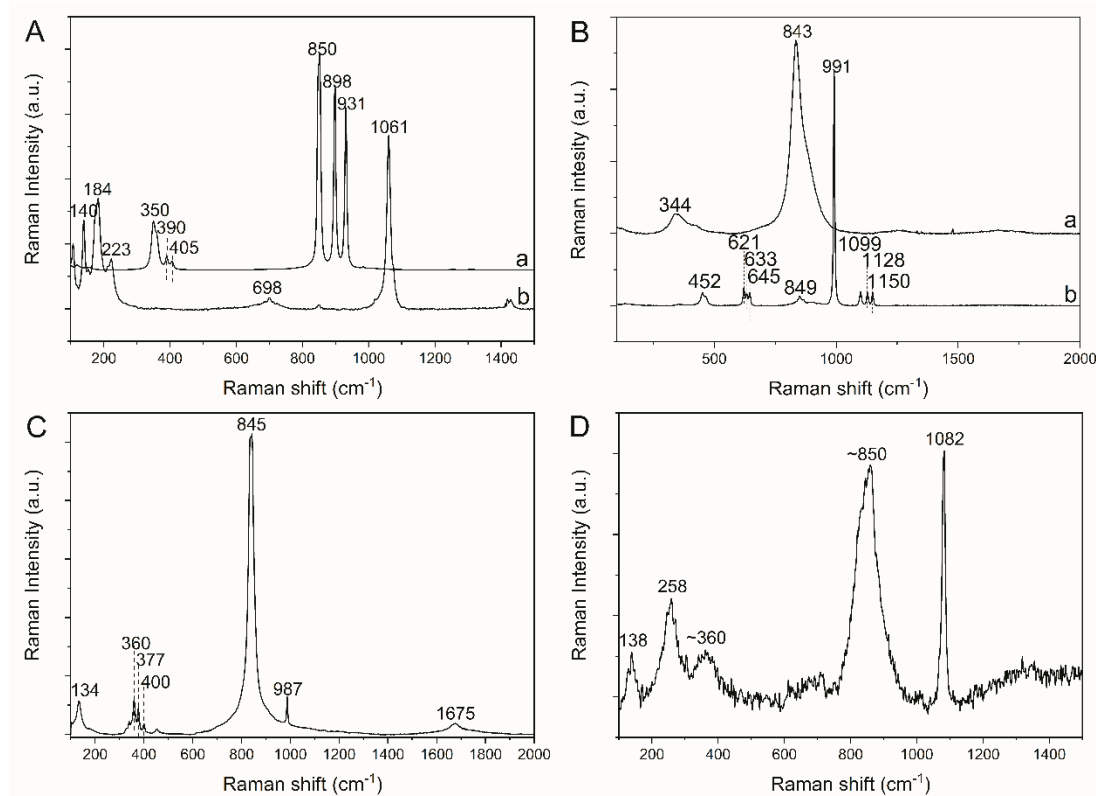


Figure 32. Raman spectra of chromates identified in A) representative young roasting samples (ST2); B) young COPR sample (ST5); C) representative Stoppani COPR (ST4); representative Pian Masino COPR (PM2).

Figure 32Ba show the spectra of thenardite, the most abundant mineral phase of the ST5 sample, characterized by the main band at 991 cm^{-1} representing the S-O symmetric (ν_1) stretching of sulphate, the broad 452 cm^{-1} can be ascribed to ν_2 bending mode of sulphate, the 1099 and 1128 cm^{-1} representing the anti-symmetric stretch ν_3 mode, and the two 621 and 633 cm^{-1} bands of the ν_4 bending modes of sulphate (Hamilton and Menzies, 2010).

The main phase associated with thenardite was crocoite (Figure 32Ba and Figure 30e) characterised by two main broad peaks at 843 and 344 cm^{-1} representing the ν_1 symmetric stretching and the ν_2 bending mode respectively of CrO_4^{2-} anion, respectively (Frost, 2004). Interestingly the presence of a small peak at 849 cm^{-1} in the Raman spectrum of thenardite (Figure 32Bb), representing, as previously described, the most intense symmetric stretching vibration of chromate, indicates a possible substitution of $\text{CrO}_4^{2-}/\text{SO}_4^{2-}$ in the structure. The other two Raman spectra reported in Figure 32C, D represent Crocoites found in both aged Stoppani and Pian Masino COPRs. For ST4 sample (Figure 32C) the mineral resulted very well preserved, allowing the characterization of the low wavenumber vibrations of crocoite, specifically at 367, 377 and 400 cm^{-1} representing the ν_4 bending mode of CrO_4 units (Frost, 2004). In the aged Pian Masino sample (PM2), crocoite resulted more altered and difficult to analyse even at very low laser power (0.1 mW). The quality of the spectra was low, but the features of CrO_4^{2-} of crocoite were still recognizable (Figure 32D). In these aged samples, crocoite was often associated with carbonates, as resulting from the 1082 cm^{-1} band that can be identified as the ν_1 symmetric stretching vibration of CO_3 group of calcite (Gunasekaran et al., 2006).

Thermogravimetric characterisation

Results of TGA analyses for representative low aged samples (ST1) and COPR (ST5) are shown in Figure 33a-b, coupled to evolved gas analyses (EGA) of H_2O and CO_2 evolution during the heating process.

TGA/EGA analysis of ST1 samples produced two different weight changes. The first occurring at $T < 150\text{ }^\circ\text{C}$ (Figure 33a) due to the decomposition of trona, as confirmed by the evolution of H_2O and CO_2 (Figure 33c) and consistent with the calcination process for Na_2CO_3 production for the chromate production (Ekmekyapar et al., 1996). The second decarboxylation took place in the 600-950 $^\circ\text{C}$ range and was described as a weight loss due to the decomposition of Na_2CO_3 and representing the beginning of the reactive process between chromite and sodium carbonate forming sodium chromite ($\text{Na}_2\text{Cr}_2\text{O}_4$) as intermediate phase, that was then oxidized in air to form Na_2CrO_4 (Antony et al., 2001).

The sample ST5 showed very low weight losses in the explored temperature range. The total mass change was $\sim 2\%$, with half of the total degradation registered within 560-650 $^\circ\text{C}$ (see Figure 33c,d) due to the decarboxylation of calcite, being the only carbon-bearing phase identified in the low aged COPR sample (Scrivener et al., 2018).

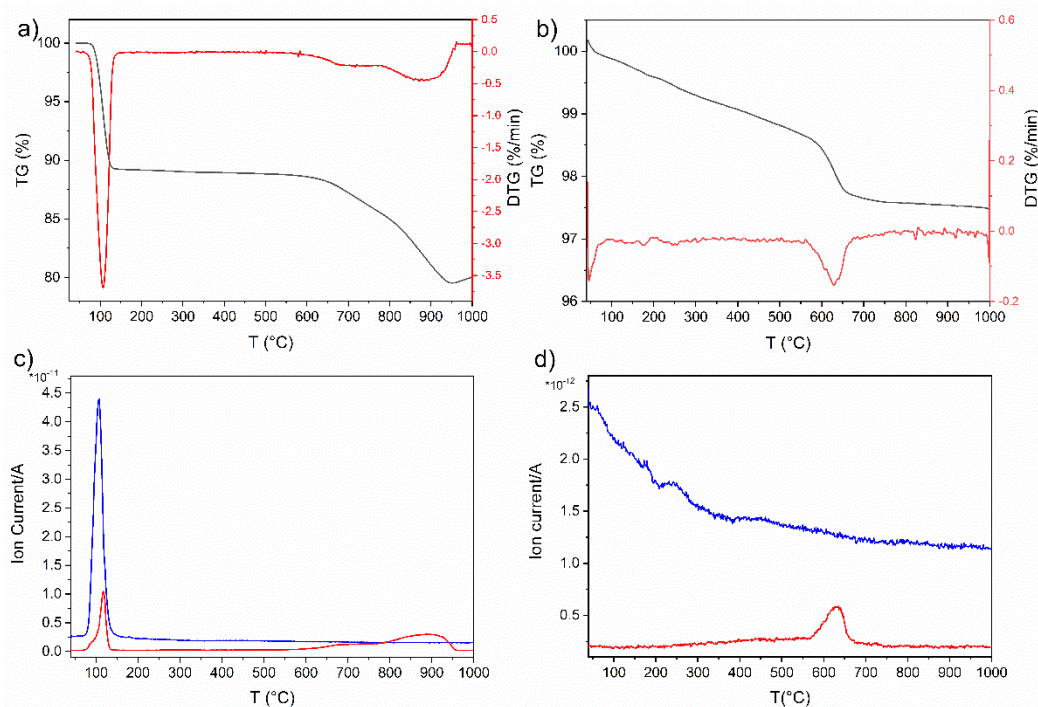


Figure 33. Thermal analysis of young roasting and COPR samples a-b) TGA/DTG of ST1 and ST5 samples; c-d) Evolved gas analysis (EGA) of ST1 and ST5 samples, blue curves represent H₂O (m/z=18) and red curves CO₂ (m/z=44).

Ex-Stoppani and Pian Masino COPRs (ST4, ST7, PM2 and PM3) showed a more complex thermal behaviour, consistent with the mineralogical complexity of the materials. In particular, a series of dehydration processes occurred in the 40-400 °C range, while an important decarboxylation process was clearly visible in all the sample between 650°C and 750 °C (Figure 34,35).

The decarboxylation process occurred in all samples at two distinct temperatures: the first, less evident, close to 400 °C and the second more intense at around 700°C. Calcite was the only phase identified that can account for this weight loss and CO₂ liberation, being aragonite and vaterite (other possible carbonates present in COPRs) recrystallizes to calcite at 450°C without weight loss (Goto et al., 1995; Scrivener et al., 2018). Hydrotalcite or other LDH minerals do not release CO₂ in this range (Boecher et al., 2012; Chmielarz et al., 2003).

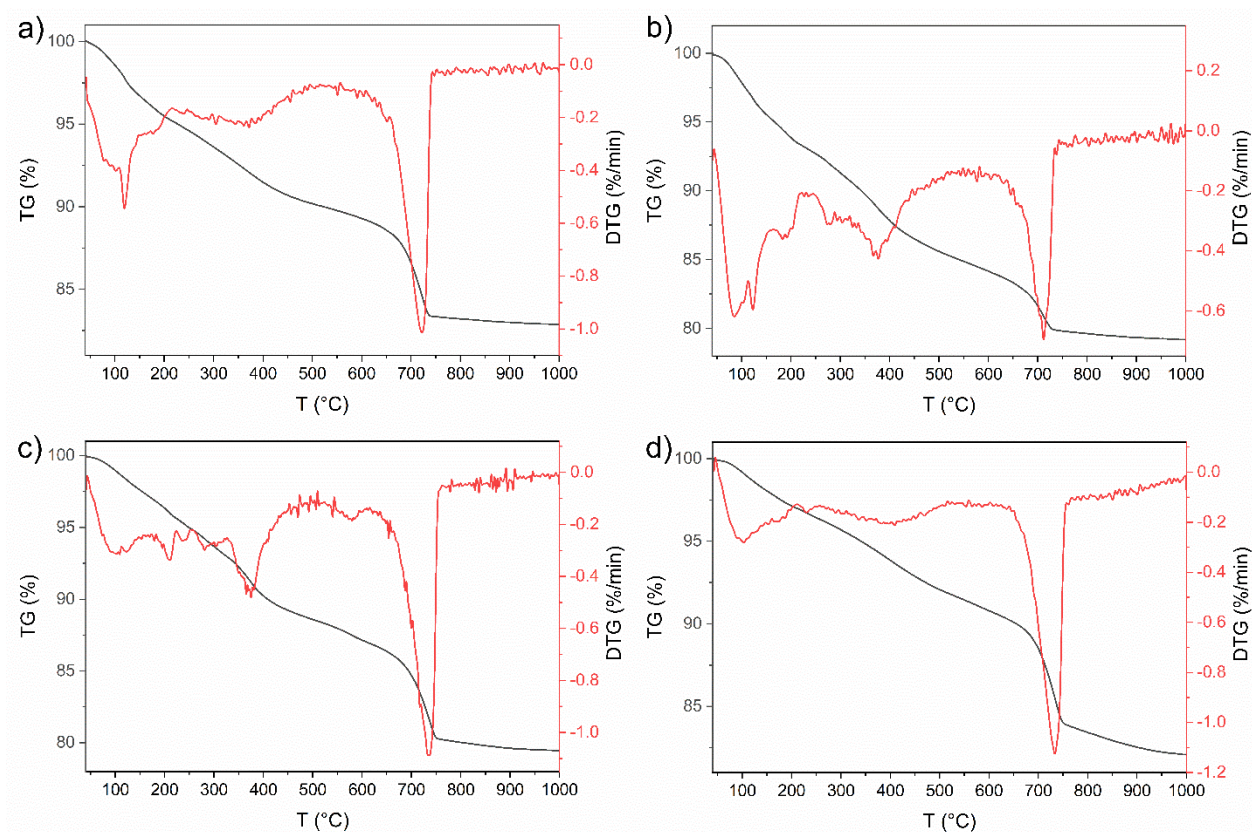


Figure 34. Thermal analysis of COPR samples a-c) TGA/DTG of ST4 and ST7 samples; b-d) TGA/DTG of PM2 and PM3 samples.

All samples showed measurable dehydration process at $T < 100\text{ }^{\circ}\text{C}$ due to pore water and/or dehydration of calcium aluminum chromates (CACs), another brownmillerite weathering product (Boecher et al., 2012), that was not detected by XRPD analysis.

The series of thermal peaks in the $100\text{ }^{\circ}\text{C}$ and $400\text{ }^{\circ}\text{C}$ region were described as degradation of the hydration products, such as LDHs, CACs and Brucite type clays (Boecher et al., 2012; Chmielarz et al., 2003). In particular, the decomposition peak between $300\text{ }^{\circ}\text{C}$ and $400\text{ }^{\circ}\text{C}$ were assumed to be the hydrotalcite decomposition (Wang et al., 1994).

ST4 and PM2 samples showed a well-defined peak within 110 and $125\text{ }^{\circ}\text{C}$ related to a dehydration event (Figure 34-35ab) due to degradation of gypsum (Collier, 2016) that was not present in the other two COPRs, in agreement with XRPD data.

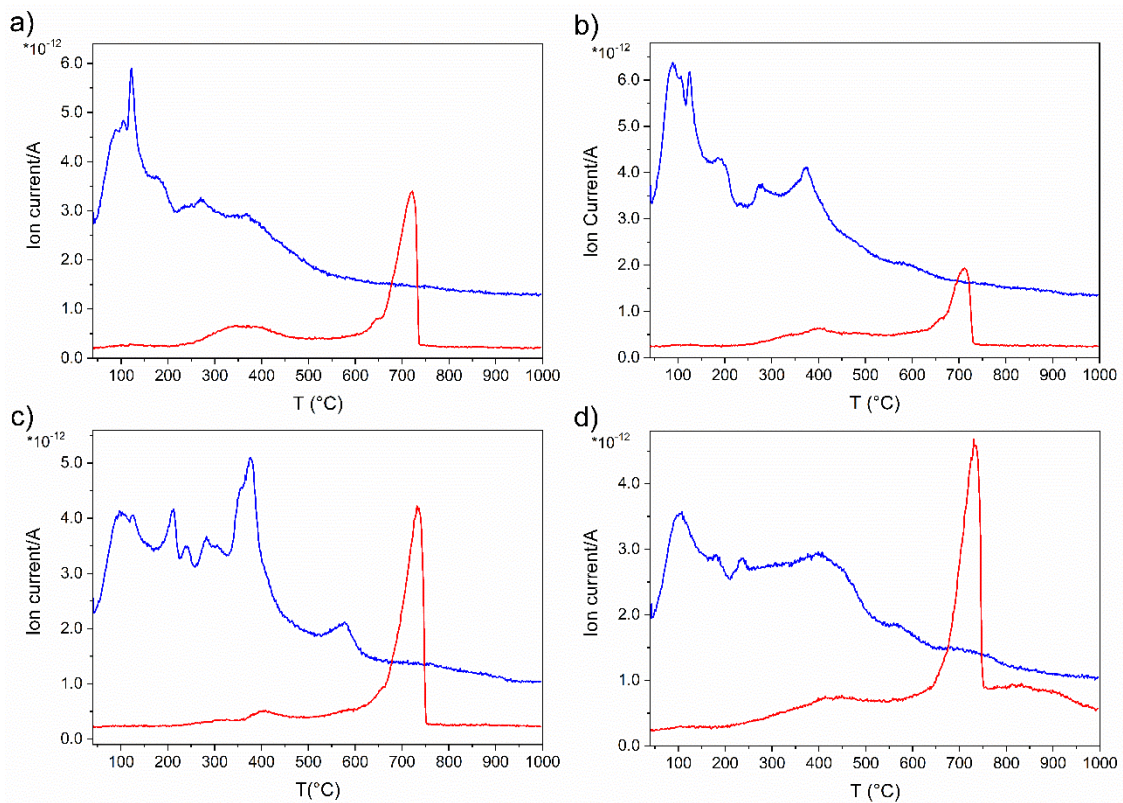


Figure 35. Evolved gas analysis of COPR samples a-c) ST4 and ST7 samples; b-d) PM2 and PM3 samples; blue curves represent H₂O (m/z=18) and red curves CO₂ (m/z=44)

The strong dehydration event occurring within 320-400 °C in ST7 samples (see Figure 35c) was described by Boecher et al., (2012) and attributed to portlandite on the basis of the XRD data. This phase was absent or in negligible amount in Ex-Stoppani COPRs. The only other known mineral phase that dehydrates in this temperature range is katoite, even if an additional minor peak should be present at 450-500 °C and no shown in the TGA/EGA analysis (Collier, 2016). It should be noted that katoite identification was possible only by XRPD, and TGA results provided additional evidences of its presence in Ex-Stoppani COPRs.

Assessment of Cr leaching behaviour in COPRs through BCR sequential extraction procedure

The assessed presence of Cr-bearing minerals in Ex-Stoppani COPRs represents a potential driving mechanism for Cr^{VI} mobilisation, as a result of variation of environmental conditions and consequent dissolution of Cr^{VI} bearing minerals (Chrysochoou et al., 2010; Geelhoed et al., 2002; Elzinga and Cirno, 2010).

Major Cr^{VI} minerals in Ex-Stoppani COPRs were Na₂CrO₄ for low aged samples (ST1 and ST2), while crocoite, katoite, ettringite and hydrotalcite were found in weathered COPRs (Table 6). In addition, Cr^{III} substituted brownmillerite was identified (Figure 30a).

The sequential extraction procedure is widely used to study leaching behaviour of soils (Scheinost et al., 2002; Filgueiras et al., 2002), mining areas (Consani et al., 2019) as well as mash soils deriving from COPRs (Elzinga and Cirmo, 2010) and represents an effective procedure to investigate and quantify the role of Cr-bearing minerals in Cr^{VI} release.

Among the different approaches and method, the sequential extraction procedure by the European Community Bureau of references (BCR), with its modification and improvements, is the most widely applied and standardised (Sahuquillo et al., 1999; Ure et al., 1993; Rauret et al., 1999).

The procedure investigates the metal leaching into three fractions. The first is related to the acid-labile fraction (extraction with solution 0.11M of acetic acid for 16 hours pH=2-3), and is related to the exchangeable and acid extractable fraction. In particular, it is useful for the extraction of metals in carbonates or in mineral phases stable only under high pH conditions (i.e. COPRs minerals). The second and the third steps account for the reducible (extraction by 0.5 M hydroxylamine hydrochloride at pH 1.5 for 16 hours) and oxidizable fraction (extracted by microwave digestion followed by 2 M ammonium acetate for 16 hours), respectively. These two steps account for metals bound to iron (hydro)oxides and sulphides, respectively, and were not performed because out of the aim of the study. In particular, Ex-Stoppani samples, besides COPR related Cr^{VI} minerals, are mainly composed of residual chromite that is considered as almost inert, besides weathering, and for this reason it does not participate at Cr^{VI} leaching processes. In addition to the first step of the BCR, a second step (leaching with ultrapure water pH = 6.6) was performed for investigating in detail on the highly soluble chromates and sulphates present in COPRs and for distinguishing between water soluble and exchangeable fractions.

The accuracy of the extraction procedure was evaluated by comparison with a standardised material (lake sediment CRM BCR 701 from the Orta lake), characterized by serious metal pollution (Pueyo et al., 2001) and with known release values for Cr. Moreover, samples were analysed in triplicates and accompanied with a blank samples.

The results obtained for total chromium extracted from the two steps are reported in Figure 36 as the relative release (%).

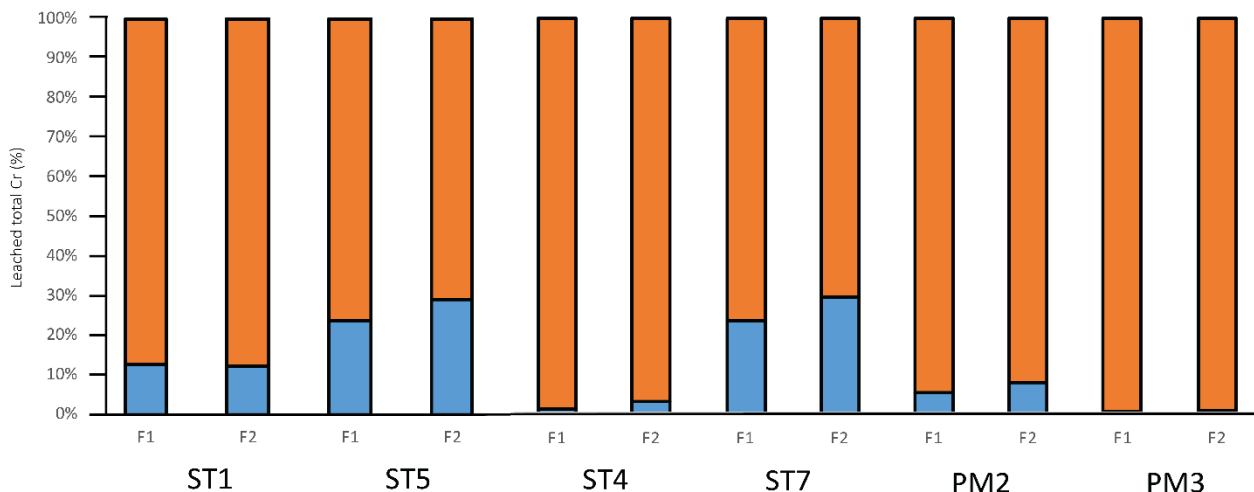


Figure 36. Partitioning of total chromium according to the two extraction steps. Blue column represent the quantity of leached Cr (expressed in %).

As a general consideration, all COPRs showed important amount of Cr leached, from 2% to 23% of total chromium leached by simple treatment with ultrapure water, thus highlighting the high reactivity of COPRs.

ST1 sample (selected as representative for low aged roasting COPRs) showed the highest extracted total chromium among all the studied samples, and almost the same value for the two extraction steps: 375.25 mg Cr L⁻¹ and 381.67 mg Cr L⁻¹ for the first and the second extraction step, respectively (Table 7). The high amount of Cr leached, coupled to the small difference between the two treatment steps, can be explained by analysing the evolution of mineralogy in the different treatments (Figure 37A).

Table 7. Amount of Cr^{VI} leached according to the two extraction steps

Sample	leached Cr ^{VI} (mg L ⁻¹)			
	Step 1 (MilliQ)	std.dev.	Step 2 (HOAc)	std. dev.
ST1	375.25	6.32	381.67	8.75
ST5	100.2	3.26	109.91	3.57
ST4	36.14	1.51	35.03	2.67
ST7	157.28	3.37	180.41	13.94
PM2	23.76	0.85	36.97	2.45
PM3	2.26	0.11	3.67	0.15

XRPD spectra of extracted samples showed that all the mineral phases (Na_2CrO_4 , trona and grimaldiite), except chromite and hematite, underwent total dissolution with both reaction steps. Thus accounting for the same release between the two treatments and also highlighting that the mineralogy is the primary controlling factor for the release of Cr^{VI} . It should be stressed that in the ST1 sample, the only Cr^{VI} containing phase was Na_2CrO_4 , while trona did not show any Cr substitution, as confirmed by SEM analysis.

Sample ST5, on the contrary, showed differences concerning Cr leaching between the two extraction steps (Figure 36), while small differences were shown regarding Cr^{VI} (Table 7).

Mineralogical analysis of the sample (Figure 37B) highlights the differences between step 1 and step 2. In particular, thenardite underwent destabilisation in water, while carbonates (i.e. calcite and dolomite) remained stable after the first step. It is reasonable that carbonates can account for the extracted Cr difference. In fact, it is well known that Cr may co-precipitate with carbonate and highly affected by pH changes (Tessier et al., 1979).

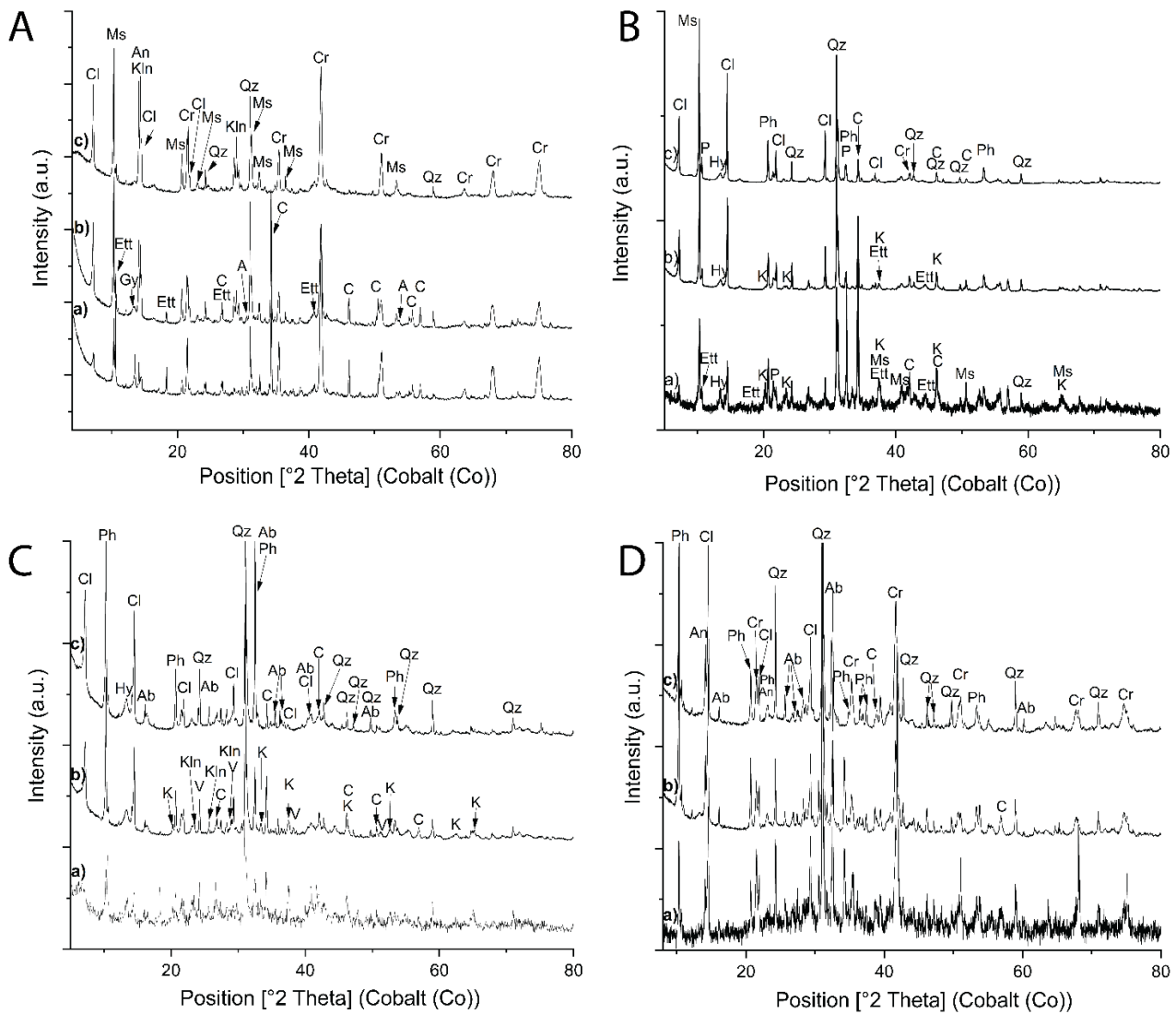


Figure 38. XRPD diagram of sample ST4 (A), ST7 (B), PM2 (C) and PM3: a)pristine sample; b) treated with milliQ water; c) treated with acetic acid 0.11M. Cr=chromite; H=hematite; Cl=chlinochlore; Ph=phengite; Lz=Lizardite; Ab=albite; Qz=quartz; C=calcite; A=aragonite; Gy=gypsum; Ms=moscovite; Ett=ettringite; Hy=hydrotalcite; K=katoite; An=antigortite; V=vaterite.

Heavily aged COPRs, except ST7 sample, showed a remarkable decrease of leachable Cr (Figure 36), consistent with a pronounced weathering at the expense of Cr^{VI} phases. In particular total Cr release accounted for 1 to the 10 % for ST4, PM2, PM3 samples, with the last characterised by the lowest release values. ST7 showed a totally different trend of Cr leaching, showing almost 30% Cr loss.

Noteworthy, all samples showed remarkable differences concerning both total Cr and Cr^{VI} between the two extraction steps (Figure 38). Also for more aged COPR, high Cr^{VI} leached amount were found (Table 7) even by treatment with water: 36.14, 157.28, 23.76, 2.26 mg

L⁻¹ for ST4, ST7, PM2 and PM3 respectively. These amount that increased in acidic conditions to 35.03, 180.41, 36.97 and 3.67 mg Cr^{VI} L⁻¹ for ST4, ST7, PM2 and PM3, respectively. These results highlighted that despite the lack of chromates (except for crocoite representing a minor phase), weathered COPRs still were characterized by high reactivity towards Cr^{VI} release.

The mineralogical analysis of the samples (Figure 38) highlighted differences in composition between the two treatments, thus possibly explaining the different amount of leached Cr.

In particular, katoite, ettringite and hydrotalcite phases, described in the literature as potentially Cr-bearing phases, tended to dissolve only in the second treatment step while were not affected by reaction with ultrapure water. It should be noted that the identification of katoite and hydrotalcite by SEM was unsuccessful, thus making not possible to investigate on the amount of Cr in the structure and subsequently on the quantification of the leaching behaviour of each phase. Anyway, the increase of leached Cr, coupled to the disappearance of these potential Cr-bearing phases, suggested their involvement as controllers of important Cr^{VI}-leaching processes. It should be noted that carbonate bound Cr fraction represents a threat for Cr release for all the studied samples (both low aged and weathered COPRs). In fact, a pH decrease will lead to the destabilization of Cr bearing phases and to the subsequent Cr leaching, that for Ex-Stoppani sample accounts for up to 1- 5% and consisting in 6-23 mg L⁻¹ additional leached Cr^{VI}.

5.2.5 Discussion and Conclusions

The study of differently aged and weathered COPRs by combining whole rock chemical composition, XRPD, ESEM, FTIR, μ -Raman and TGA brought to a deep structural, compositional and morphological characterization for the definition of Cr speciation in COPR samples and of the phases which can potentially retain Cr in the structure, and represents the first stage to assess short and long term Cr leaching behaviour. Matern et al., (2016) pointed out that COPRs, originating in different areas, show different mineralogical association, especially concerning Cr^{VI} host phases due to variation of climatic conditions, pH and age of the COPR deposit. The Ex-Stoppani site provides the unique opportunity to follow the evolution of COPRs from the pristine roasting material to the aged and evolved materials.

The assessed presence of soluble Cr^{VI}-bearing phases, such sodium chromate, ettringite, katoite and hydrotalcite, highlights the necessity of a different approach for minimizing the sample preparation steps and avoiding the use of water.

Sodium chromate (Na₂CrO₄) was identified in low aged samples, in agreement with results from Indian COPRs, and represent a clear short-term hazard leading easily to leachable Cr. For the low aged COPRs of the Ex-Stoppani site, the high amount of pervasive crusts characterising the whole matrix can be considered representative of the conserved frame of the primary industrial oxidation process of the feedstock ore.

Low aged COPRs samples confirmed also the presence of Brownmillerite as the major HT mineral formed during the primary roasting of the material, while other HT minerals, formed during the primary roasting of the material, such as larnite (Ca₂(SiO₄)) (Hillier et al., 2003; Matern et al., 2016), periclase (MgO) and brucite (Mg(OH)₂), were not detected. This can be explained considering the low pH conditions of selected samples (see Table 5) compared with the other reported COPRs. Results are in agreement with Moon et al. (2008) reporting on the total absence of periclase when the pH is lowered from 12.03 to 9.35 and the contemporary decrease of brucite amount from 2.84% to 1.87%.

The Identification of brownmillerite was also important, representing the precursor mineral for the formation of hydrogarnets, in particular, katoite ((CaO)₃Al₂O₃(H₂O)₆), CACs (calcium aluminum chromium oxide hydrates (Ca₄Al₂O₆ (CrO₄)-nH₂O) after deposition at ambient condition. These reaction products represent an environmental concern due to their capacity to sequester Cr^{VI} in their structure (Wazne et al., 2008; Palmer, 2000; Hillier et al., 2007; Matern et al., 2016).

Noteworthy, the identification a new Cr^{VI} host phase, crocoite (PbCrO₄), very important considering its potential impact in Cr^{VI} leaching, was obtained by ESEM and μ-Raman spectroscopy in both low aged and weathered COPRs. It should be stressed that the novelty of the sample preparation approach, totally avoiding classical sample preparation procedures, led to these results.

Moreover, the study of the Cr-bearing phases in COPRs, such as Ettringite, Katoite and hydrotalcite, having a similar structure of so-called CACs (calcium aluminium chromium oxide hydrate) already described in Indian, Glasgow and U.S., allowed the evaluation of the environmental impact of the Ex-Stoppani site, that was very complex due to destabilization processes, especially when the pH is lowered (pH < 12) as in the case of study.

Noteworthy, no CACs and/or Cr^{VI}-hydrocalumite (another hydration product of brownmillerite) (Hillier et al., 2003; Chrysochoou and Dermatas, 2007; Matern et al., 2016) were detected in the Ex-Stoppani samples. It should be stressed that pH conditions strongly affect COPRs mineralogy. In fact, Cr^{VI}-hydrocalumite is stable in the 11.19-12.96 pH range (Chrysochoou and Dermatas, 2006), values sensibly higher than those found in the Ex-Stoppani site and close to previously described COPRs. The absence of CACs and periclase in the Ex-Stoppani sample can be explained by the same destabilisation process due to pH values below 9.0 (Moon et al., 2008). The thermogravimetric analysis was applied as a powerful characterization technique to assess the presence of potentially Cr^{VI}-bearing phases, such as LDHs, CACs and brucite types clays (Chmielarz et al., 2003; Boecher et al., 2012), which were not detected by XRPD and SEM analyses.

The complementary use of different analytical techniques coupled to a proper sample preparation, was fundamental for the complete characterization of COPRs with minimized about Cr^{VI}-bearing minerals (Na₂CrO₄, crocoite, katoite, ettringite and hydrotalcite) preservation, being these minerals, even in low abundance, responsible for the long-term Cr leaching behaviour and for the environmental impact of COPRs.

Sequential extraction experiments highlighted that very high amount of Cr were leached from COPR by simple reaction with ultrapure water (100.2 mg Cr L⁻¹ and 375.25 mg Cr L⁻¹ respectively for ST5 and ST1 samples, respectively), evidencing high reactivity of COPRs towards percolating water. Moreover, Cr^{VI} leaching in low aged COPRs appeared to be driven by highly soluble chromates (Na₂CrO₄ and crocoite), as confirmed by the small differences of Cr^{VI} release between the two extraction steps. Heavily aged COPRs showed a complex behaviour: they were characterized by lower amount of leachable Cr^{VI}, ranging from 2.26 to 36.14 mg Cr L⁻¹, and only the ST7 sample reached 157.25 mg L⁻¹ leached Cr^{VI}. This is consistent with the weathered nature of the samples, leading to the progressive destabilisation of Cr^{VI}-bearing phases. Noteworthy, weathered COPRs showed an increase of Cr leached under acidic conditions. The disappearance of Cr-bearing phases, such as katoite, ettringite and hydrotalcite, under acidic conditions coupled to the increase of leached Cr, suggest their involvement in Cr^{VI}-leaching process.

Moreover, results from sequential extraction processes highlighted that the majority of Cr composing the Ex-Stoppani sample is locked in Chromite, while a considerable fraction is strongly bound into iron oxy(hydroxides) and possibly organic matter (Elzinga and Cirimo, 2010). Thus, it is not readily leachable under environmental conditions. However, the

majority of Cr^{VI} is released by simple reaction with water, thus confirming the primaty role of COPRs in the retention and release of Cr^{VI}.

5.3 Colloidal Surface Active Maghemite Nanoparticles for Cr^{VI} remediation from contaminated industrial groundwater

5.3.1 Abstract

The present study is aimed at the exploration of the application of naked colloidal maghemite (γ -Fe₂O₃) nanoparticles (Surface Active Maghemite Nanoparticles, SAMNs) for the *in-situ* water remediation from Cr^{VI}. SAMNs efficiency for Cr^{VI} binding under laboratory conditions and the extensive characterization of the SAMN@Cr^{VI} complex were reported in a previous work. Considering the affinity and the high removal efficiency of SAMNs for Cr^{VI}, the nanoparticles were exploited in a complex industrial site, mimicking a real *in-situ* application. The Ex-Stoppani area S.p.A, included, with DM n.468/01, into the national program of environmental remediation and restoration was selected. The application of SAMNs on a complex industrial wastewater system confirmed the high adsorption efficiency observed laboratory and the removal of Cr^{VI} above 90% was observed in the investigated wells, either under acidic and *in-situ* conditions.. No interfering anions were found confirming the very high selectivity of SAMNs for the target metal. Moreover, the salinity of the wastewater strongly affected the removal efficiency due to the destabilization of the colloidal nature of the nanoparticle suspensions resulting in a 20% decrease of Cr^{VI} removal. It should be noted that the colloidal properties of SAMNs, along with the binding specificity, represent the key features for the exploitation of SAMNs in large scale Cr^{VI} wastewater remediation.

5.3.2 Introduction

Nowadays, chromium toxicity represents a serious hazard due to its large use in many industrial processes, such as Cr^{VI} salts productions, tannery and metallurgy. Its effects on human health are linked to speciation in water. In fact, chromium can be present in the environment in two oxidation states, namely Cr^{III} and Cr^{VI}. Cr^{III}, generally in trace levels, is an important element affecting carbohydrate, lipid and protein metabolism (Pechova and

Pavlata, 2007). Cr^{VI} is the more soluble form and five resulted times more toxic than the trivalent form (Barceloux, 1999). It is classified as class A carcinogen being a strong oxidant, potentially causing severe health problematics such as liver damage and renal necrosis. Moreover, late tumour occurrence after exposure to Cr^{VI} is documented (Nickens et al., 2010).

Because of its high toxicity, the World Health Organization (WHO) and US-EPA provide a concentration limit in water of 0.050 mg Cr^{VI} L⁻¹ (World Health Organization, 2003; U.S. EPA, 1990); whilst its limit in Italy was stated at 0.010 mg Cr^{VI} L⁻¹ (Legislative Ordinance 152/06, Ministerial Ordinance 15/2016).

High Cr concentrations associated with natural sources are not common even if weathering of mafic and ultramafic rocks can represent a possibility (Paulukat et al., 2015).

Because of the wide use of Cr^{VI} salts and inefficient management of secondary wastes, Cr^{VI} elimination to safe levels is mandatory to reduce pollution problematics. Traditional remediation methods, including chemical reduction and subsequent precipitation as hydroxide, ion exchange or biosorption are commonly used (Cushnie Jr, 1985; Argo, D.G., Culp, 1972; Gunatilake, 2015). These methods are often inefficient, especially for complex industrial scenarios, still suffering from high operational cost, use of high amount of reagents and generation of secondary sludges needing special treatments before the disposal to landfill. Thus, they are hardly sustainable, especially when large areas need to be treated: Alternatively, in the case of biological methods, despite the low sorbent costs, there is the need of proper and continue maintenance (Gunatilake, 2015; Cundy et al., 2008).

Alternative techniques based on low cost technologies, replacing and/or improving traditional technologies represent attractive options in the view of growing awareness on environmental issues. Among the available sorbents, nano metal oxides, including iron oxide nanoparticles, represent one of the most efficient and low cost technique for highly polluted water, due to high selectivity and adsorption capacity (Hua et al., 2012; Pollard et al., 1992). In particular magnetic nanoparticles allow the easy separation under the application of a magnetic field, and represent an interesting system for the rapid and effective application in water remediation (Hua et al., 2012).

The current study investigates the application of synthetic maghemite nanoparticles, called SAMNs (Surface Active Maghemite nanoparticles) for the removal of Cr^{VI} from polluted water *in-situ*. These superparamagnetic nanoparticles present several advantages, such as a cost-effective synthesis protocol totally carried out in water and avoiding any use of organic

solvents, present low toxicity and an excellent colloidal stability without needing any coating or superficial modification. Their peculiar surface behaviour, characterised by the presence of under-coordinated Fe^{III} sites can participate in complex binding reactions, allowing the irreversible binding of different biomolecules and the application in different biotechnological fields (Magro et al., 2015; Venerando et al., 2013). Moreover, their superficial and magnetic behaviour makes them an efficient sorbent material for eliminating toxic metals in water (Magro et al., 2016).

The adsorption capacity of SAMNs toward on Cr^{VI} was already demonstrated in laboratory tests and evidences on Cr^{VI} binding mechanisms were proved (Magro et al., 2016).

Moreover, although many studies report on the application of magnetic nanoparticles for Cr^{VI} remediation at the laboratory scale (Hu et al., 2005; Lin et al., 2012; Badruddoza et al., 2013; Magro et al., 2016), few examples were aimed at moving their application to industrial-scale and to real complex groundwater (Fu et al., 2015; Wang et al., 2019).

The current study investigates removal properties of SAMNs for Cr^{VI} on real polluted industrial water from the Ex-Stoppani site (Cogoleto, Liguria, NW Italy), a site of national interest characterized by high concentration of Cr^{VI} in water, wastes and soil with concentration in groundwater ranging from 250,000 to 500,000 µg L⁻¹ in the plant area. The confirmed adsorption efficiency and the physical and magnetic properties of SAMNs, coupled with the opportunity of recovery of the adsorbed metal and nanoparticle recycling, represent an attractive and economically sustainable option for moving the application to large scale.

5.3.3 Industrial application for Cr^{VI} in situ remediation by SAMNs

The good results obtained in the laboratory studies on the binding efficiency of SAMNs toward Cr^{VI} stimulated their application in real polluted groundwater. The selected area was the Ex-Stoppani industrial site (see Figure 26) located in the area of Cogoleto (Genova, Italy). Total Cr determination was performed through ICP-MS while Cr^{VI} through diphenylcarbazide colorimetric method (see paragraph 2.4 and 2.5).

Sorption studies on Stoppani groundwater were performed following the analytical conditions used in laboratory studies (Magro et al., 2016), in particular SAMNs concentration was fixed at 10 g L⁻¹ while the pH conditions were varied from pH 3.0 (best adsorption conditions) and under the *in-situ* pH conditions. SAMNs were added to the sample solution

and kept in agitation for 12 hours, time necessary to reach the saturation of binding sites on SAMNs surface, as confirmed by previous kinetic studies (Magro et al., 2016). After that SAMN@Cr complexes were separated with a magnet and the residual Cr^{VI} concentration in the supernatant were controlled. Two binding cycles were performed for each Stoppani well (see Figure 26a, blue squares)

Groundwater pH was slightly basic between 7.6-9.7, and is typical of high-lime COPR in the area (Matern et al., 2017). Even if pH conditions don't represent a primary hazard, they are a key factor for SAMNs adsorption properties.

Table 8 shows that the highest total Cr concentrations in groundwater occurred in wells P6 (45.0 mg L⁻¹), South (13.4 mg L⁻¹) and P9 (9.5 mg L⁻¹) predominantly in the form of toxic Cr^{VI} with 42.2%, 100% and 52.6% with respect to total chromium, respectively.

Whereas, the other investigated wells exhibited lower concentrations: North (6.2 mg L⁻¹), T.A.F (5.4 mg L⁻¹), P2 (5.5 mg L⁻¹), and P1 (0.8 mg L⁻¹) with the corresponding Cr^{VI} percentage of 96.7%, 100%, 69.1% and 62.5% respectively. In all the investigated wells, groundwater was highly impacted by COPRs leaching in the area, thus confirming the very strong Cr^{VI} pollution. Concerning other major solutes and anions, they were all below the maximum values for drinking water guidelines (WHO, 2011), thus not subjected to formal actions as they do not represent a hazard for human health. Noteworthy, phosphate, one of the most impactful interfering anion lowering the binding capacity iron oxides, was totally absent in all the Ex-Stoppani groundwater samples (Chowdhury and Yanful, 2010; Zhang et al., 2003).

P2 wells (Table 8) showed a chemical composition very different from the other sampling sites with very high Na, SO₄²⁻, and Cl⁻ values (5316 mg L⁻¹, 15020 mg L⁻¹, and 5181 mg L⁻¹ respectively). Furthermore, this well is characterised by very high salinity, resulting in a very high conductivity (23.35 mS cm⁻¹). These parameters do not represent a risk for human health and conductivity is not considered strictly related to COPR (Matern et al., 2017). However, salinity represents a growing problem already documented in COPRs sites (Matern et al., 2017; Chakraborti et al., 2011) due to the large use of groundwater for irrigation. Notably, this parameter represents an important factor possibly affecting the application of nanoparticles for the influence on binding capacity for the target. It should be reminded that the ionic strength of the medium could strongly affect surface chemistry and colloidal stability of nanoparticles (Wiesner et al., 2009).

Table 8. Physical-chemical characteristic of investigated wells

Wells		North	P6	South	T.A.F	P9	P2	P1
Cr^{tot}	mg L ⁻¹	6.2	45	13.4	5.4	9.5	5.5	0.8
Cr^{VI}	mg L ⁻¹	6.0	19.0	13.4	5.5	5.0	3.8	0.5
pH		8.64	8.88	8.76	8.51	9.16	7.65	9.68
EC	mS cm ⁻¹	N.D.	1.39	0.64	0.49	0.65	23.35	0.37
HCO₃⁻	mg L ⁻¹	98.5	99.2	79.2	70.6	116.2	47.5	91.4
F⁻	mg L ⁻¹	0.05	<D.L.	<D.L.	<D.L.	<D.L.	<D.L.	<D.L.
Cl⁻	mg L ⁻¹	14	7.3	3.6	3.3	7	5181	5.2
NO₃⁻	mg L ⁻¹	6	12.8	6.4	5.8	12.3	<D.L.	9.2
SO₄²⁻	mg L ⁻¹	79	677	223	159	207	15020	74
Na	mg L ⁻¹	37	158	77	59	86	5316	28
Mg	mg L ⁻¹	17	73	25	18	23	511	25
K	mg L ⁻¹	1.6	5.8	2.3	1.6	2.3	23	1.7
P	mg L ⁻¹		0.13	0.07	0.06	0.02	0.12	0.02
Ca	mg L ⁻¹	12	22	2.7	3.7	6	274	13

The knowledge of solute concentrations in groundwater, even if in the specific study not representing a direct hazard for human safety, is fundamental to define groundwater characteristics, possibly affecting nanoparticles/metal interactions, or for the identification of soluble competitors for iron-binding sites onto SAMNs.

5.3.4 Results of SAMNs application to Ex-Stoppani groundwater

Very good Cr^{VI} binding results (Figure 39 and table 9) were obtained for wells P1, P9 and P6 where the total Cr removal was achieved in two incubation cycles, even under high pH conditions (pH 9.7, 9.2 and 8.9 respectively).

Table 9. Cr^{VI} remediation results for Ex-Stoppani investigated wells

Well	initial Cr ^{VI} (mg L ⁻¹)	pH	Cr ^{VI} removed (%)		residual Cr ^{VI} (mg L ⁻¹)
			1 st cycle	2 nd cycle	
P2	3.8	3.0	59.21	80.79	0.73
	3.8	7.6	49.21	70.00	1.14
T.A.F	5.5	3.0	82.91	98.00	0.11
	5.5	8.5	20.00	62.73	2.05
North	6	3.0	91.50	97.83	0.13
	6	8.6	33.50	68.50	1.89
South	13.4	3.0	81.64	97.46	0.30
	13.4	8.8	27.69	60.45	5.30
P1	0.5	3.0	100.00	100.00	<D.L.
	0.5	9.7	100.00	100.00	<D.L.
P9	5	3.0	96.86	100.00	<D.L.
	5	9.2	66.88	100.00	<D.L.
P6	19	3.0	89.23	100.00	<D.L.
	19	8.9	61.22	100.00	<D.L.

It should be noted that, besides P1 well that was characterised by the lowest Cr^{VI} (0.5 mg L⁻¹) concentration and was totally remediated with only one treatment cycle, P6 and P9 wells, characterised by very high Cr^{VI} concentrations (19 mg L⁻¹ and 5 mg L⁻¹ respectively), underwent the total Cr^{VI} removal in two application cycles under both pH conditions. The first application cycle lowered the Cr^{VI} concentration at ~30% of the initial value for both wells. During this first application cycle the binding capacity of SAMNs was strongly dependent on pH.

The same results were obtained on the T.A.F., South and North wells, where small differences in the amount of bound Cr^{VI} following two SAMNs application cycles were observed (98.0%, 97.83% and 97.46% respectively) with a decrease of binding capacity at basic pH (from 36.3% to 29.3 %) consistent with previously described in P6 and P9 wells.

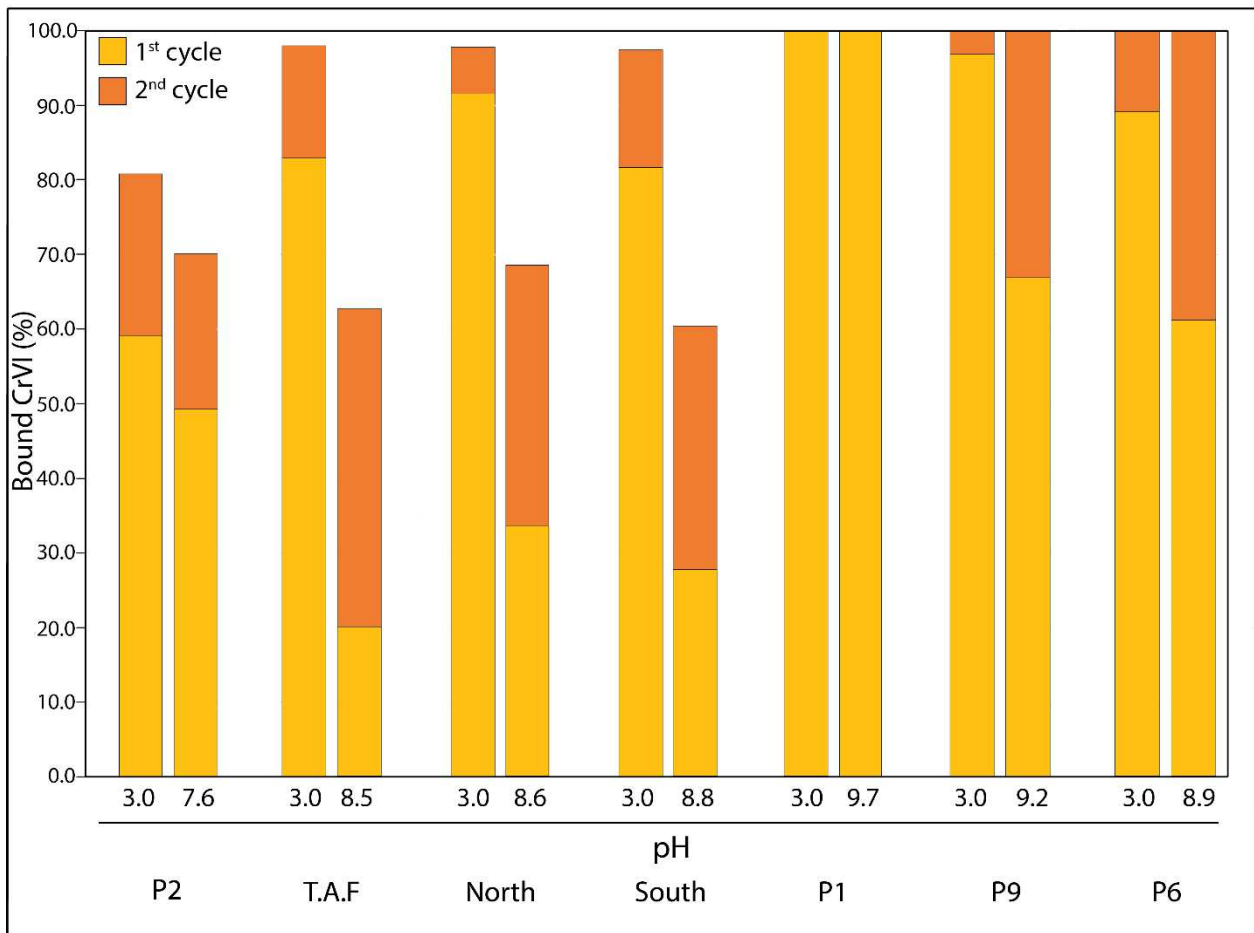


Figure 39. SAMNs application to Ex-Stoppani groundwater; the amount of bound Cr^{VI} vs pH for all investigated wells

It should be noted that relatively poor binding results are obtained on P2 well, where the fraction of Cr^{VI} removed was only 81% under acidic condition after two treatment cycles and a ~10% removal difference was observed between the first and the second application cycle. It should be stressed that this well was not highly polluted compared to the other investigated wells, with Cr^{VI} concentration of 3.8 mg L⁻¹ (Table 8). In this case, pH played a minor role on SAMNs binding properties. As shown in Figure 40 the fraction of bound Cr^{VI}, at pH 3.0 (best condition for binding and colloidal stability of SAMNs) showed that the binding capacity slightly decreases at increasing pollutant concentration. The results on the P2 well deviate from all the other investigated sites, thus revealing an interfering process on SAMNs binding capacity. Anyway, it should be stressed that more than 80 % binding efficiency was obtained for all the wells.

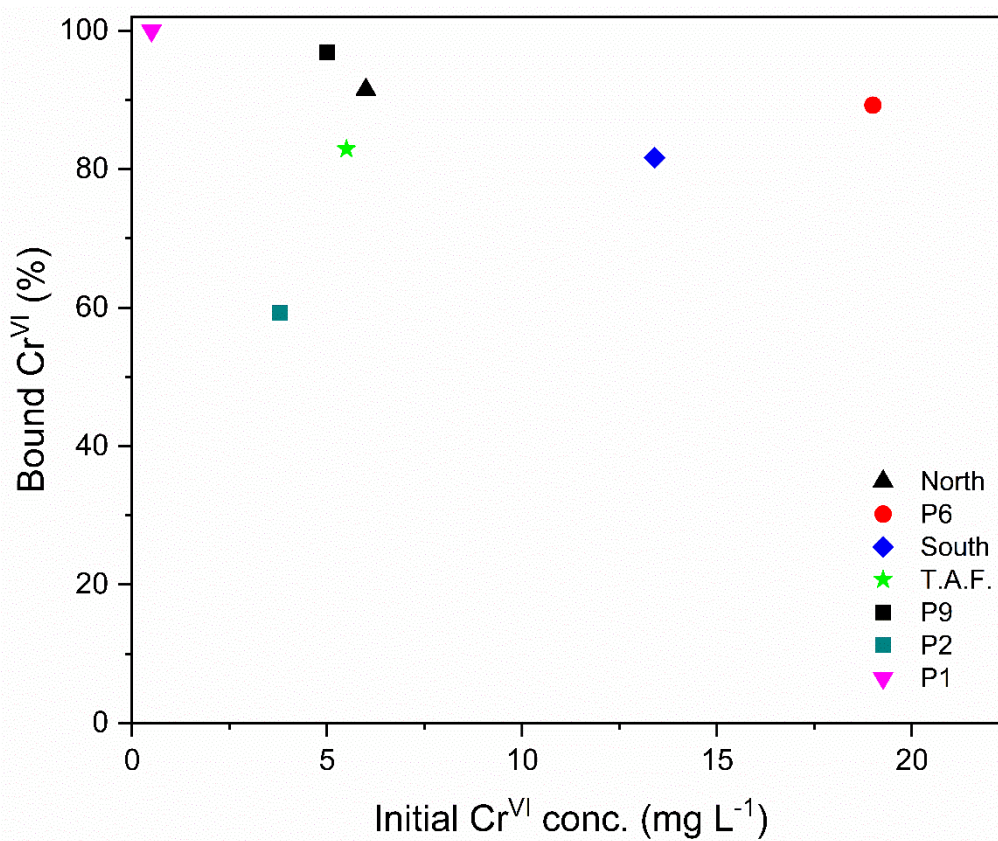


Figure 40. Amount of Cr^{VI} (mg L⁻¹) bound on SAMNs (10 g L⁻¹) vs the initial Cr^{VI} concentration (mg L⁻¹) of the well. pH=3.0

As previously described, P2 wells showed important chemical differences from all the other samples, and the colloidal stability of nanoparticles is governed by the characteristic of the medium (Gao and Zhang, 2001; von der Kammer et al., 2010). Considering that sulphate (15,020 mg L⁻¹ in P2 well) possess very low affinity for maghemite nanoparticles and influence on metal chelation process (Tuutijärvi et al., 2012), the most probable parameter that can contribute to the lowering of the nanoparticle adsorption capacity is the salinity of the solution. Thus, the limited removal efficiency in the P2 well can be explained in terms of colloidal destabilization of SAMNs caused by the salinity of the solution (Magro et al., 2018). In particular, ion concentration can affects the colloidal stability of nanoparticles due to Debye-Hückel screening (Pfeiffer et al., 2014), leading to nanoparticles aggregation or, at last, precipitation can partially or completely decrease their removal efficiency toward a target compound.

At the same time, results in agreement with previous studies, indicate that K, Ca, Mg, sulphate, nitrate and bicarbonate had not a significant impact on metal adsorption onto

SAMNs (Hu et al., 2005; Chowdhury et al., 2011; Tuutijärvi et al., 2012) in the studied wells (data not shown), implying that competition for under-coordinated iron binding sites were negligible and confirming that the selective removal of Cr by SAMNs can be interesting from the economic point of view as it ensures high purity recycled Cr product after NH_4OH treatment (Hu et al., 2005).

Beside bound metal recovery another crucial factor is nanoparticle recycling and reusability (Magro et al. 2016), in order to open the way to the large-scale SAMNs environmental remediation. Bound Cr^{VI} is released upon incubation of $\text{SAMN@Cr}^{\text{VI}}$ in a 2M ammonia solution, obtaining ammonium chromate and naked SAMNs ready to be reutilised (Magro et al. 2016).

Binding reversibility was proved in the 100-3500 mg L^{-1} concentration range, at pH 3.0 using 10 g L^{-1} SAMNs.

In particular it is important to note that at Cr^{VI} concentrations as high as 500 mg L^{-1} , very high concentrations compared to typical industrial pollution scenarios (Brown et al., 2000), the binding reversibility was 90% confirming the reusability of SAMNs for *in-situ* applications.

5.3.5 Conclusions

The application of SAMNs for Cr^{VI} removal showed a great potential for the exploitation to a large-scale industrial level. Results indicate that SAMNs are very promising for real *in-situ* application, considering the high adsorption efficiency even at neutral to basic pH values, typical conditions of groundwater. At the same time, even if no particular interfering anions were found in the studied wells, a decrease in SAMNs binding efficiency occurred when water was characterized by high salinity, possibly due to the destabilization of the colloidal suspensions of nanoparticles leading to aggregation and subsequent decrease of exposed binding sites.

Moreover, another favorable feature for the exploitation of SAMNs in environmental fields is represented by the low synthesis cost of the nanomaterial, occurring completely in water without any hazardous solvent. Thus, the production of SAMNs does not introduce other sources of pollution, and match the need of new sustainable and eco-friendly materials (Magro et al., 2012b).

Moreover, the low toxicity, high colloidal stability and superparamagnetism represent other fundamental properties of SAMNs for environmental remediation issues. Furthermore, for

in-field Cr^{VI} remediation the structural stability of the nanomaterial should be guaranteed as its degradation may represent an environmental hazard. In fact, nanomaterial degradation or its coating deterioration represents a drawback as these phenomena compromise the pollutant binding capability of the material. At the same time, nanomaterials should preserve their magnetic properties after binding, to be easily controlled by an external magnet during the removal process.

Concluding, the capacity of SAMNs to remediate highly polluted water was demonstrated, evidencing that the binding process is strongly affected by pH conditions. Nevertheless, the *ex situ* application of SAMNs highlighted the high adsorption efficiency and the high selectivity for Cr^{VI} remediation, even in very complex media.

6. Final discussion and conclusions

The overall aim of the thesis was to study the synthesis, the properties of specific superparamagnetic maghemite (γ -Fe₂O₃) nanoparticles called SAMNs (Surface Active Maghemite nanoparticles) and their final suitability of as efficient and sustainable sorbent for the removal of As and Cr^{VI}, class A carcinogens, even in groundwater treatments.

The investigation and deeper characterizations of the nanomaterial following each step of the synthesis protocol, that represented the crucial knowledge of any subsequent application, highlighted that SAMNs stand out, compared to other similar nanomaterials, for their superparamagnetic behavior coupled to an excellent colloidal stability in water without any coating and or superficial modification. This makes SAMNs a promising low cost candidate for large scale water treatment. In particular, the structural and morphological characterization from the intermediates of the wet synthesis pointed out that the nanomaterial evolved from a mixture of different iron structures. The S0 intermediate resulted mainly composed of zero valent iron, supposed to be the first compound originated by FeCl₃ reduction by NaBH₄ during the reductive phase of the reaction, and characterized by low stability in water. It was demonstrated that borate played a key role in the complex scenario of the synthetic route to colloidal naked nanosized maghemite, suggesting that its complexation is involved in the exfoliation of the surface of zero valent iron particles leading to the formation of extended oxygen rich 2D structures, probably iron oxy-hydroxides which

represent the amorphous component observed by Mössbauer spectroscopy and XRPD. As the reaction proceeded, the 2D oxyhydroxides structures tended to crumple, envisaging the formation of spherical nanoparticles in the wrinkles, leading to the formation of maghemite nanoparticles. Moreover, an accurate aging period in water of the resulting material followed by a curing period at 400 °C were demonstrated as essential steps for the final formation of stoichiometric maghemite nanoparticles (SAMNs). In particular, the 24 hours aging period in water (S1 intermediate) led to the complete disappearance of the prevalent unknown Fe^{III} component, of metallic iron and, as well, of the minor paramagnetic iron phase of the previous intermediate (S0). In fact, after the thermal process at 400 °C, the heterogeneous and partially amorphous nanometric maghemite of the S1 nanoparticulate sample turned from partially amorphous to stoichiometric crystalline maghemite (S2 intermediate, SAMNs) displaying an unusual high structural stability.

In contrast to other iron oxides (Boyer et al., 2010), SAMNs show a high colloidal stability without any coating or superficial modification, that is substantiated by a very high value of zeta potential at neutral pH ($\zeta > + 30$ mV) (Magro et al., 2017). The assessed presence of surface under-coordinated Fe^{III} explained the unusual colloidal behavior in water as these molecules act as coordinating ligands for surface Fe^{III} sites, recalling the behavior of hydrous ferric oxides bearing positively charged labile OH₂^{+0.5} groups on their surface (Gu and Karthikeyan, 2005). The role played by surface under-coordinated Fe^{III} was evident as the colloidal stability of SAMNs results higher in dimethyl sulfoxide (DMSO) than in water.

The results of the deep structural and morphological characterization of the nanomaterial allowed to acquire information on the surface properties of SAMNs, and opened the door to the possible applications in the environmental field. In particular, the sorption properties of SAMNs towards arsenate and arsenite and the mechanism of sorption mechanism were investigated. It should be noted that the results of the thesis on the comparative studies on As oxyacids and iron oxides represented a novelty, being literature studies mainly focused on hydrous ferric oxides. Only few studies were focused on maghemite (Lin et al., 2012; Liu et al., 2016) and, noteworthy, no specificity was reported for the binding of arsenite or arsenate on other reported iron oxides. SAMNs showed a very high binding for both As oxidation states, even with different binding behaviour and pH dependence. SAMNs sorption of As^{III} resulted almost constant in the whole pH range with a maximum adsorption capacity of around 20 mg g⁻¹ SAMN, while for As^V binding, the nanoparticle adsorption capacity was the highest (32.5 mg g⁻¹ SAMN) at pH 3.0 and rapidly decreased with pH. Moreover, the

kinetics of As binding by SAMNs was investigated and resulted a two-step process, involving a very fast adsorption in the first 5 min incubation, followed by a slower binding process. The experimental data were well described by a pseudo-second-order equation. Considering the fast phase of the binding process, a remarkable difference of the binding rates for the two arsenic species to SAMNs was observed: the binding rate of arsenite was faster ($1.82 \text{ mg As g}^{-1} \text{ SAMN min}^{-1}$) than of arsenate ($0.87 \text{ mg As g}^{-1} \text{ SAMN min}^{-1}$). SAMNs adsorption at equilibrium of both As species was well described by the Langmuir model, thus assuming a saturation binding behaviour on SAMN surface with each binding site on nanoparticle surface acting independently of other sites reaching the formation of a single molecular layer on.

Interestingly, the different binding behaviour of As^{III} and As^{V} was found totally superimposable with the results reported on goethite nanoparticles (Manning et al., 1998) drastically diverging from reports on nanostructured maghemite (Lin et al., 2012; Liu et al., 2016), substantiating an analogy between the surface chemistry of SAMNs and oxyhydroxides. Therefore, the structure of SAMNs can be unequivocally attributed to maghemite nanocrystals, while their surface resembles the behaviour of ferric oxyhydroxides and resulted different from all other reported maghemite nanostructures.

The multi techniques characterization (FITR, HRTEM, hysteresis loops and ZFC/FC magnetization measurement) of SAMN@As complexes showed also that no structural alteration affected SAMNs structure upon the binding of arsenite and arsenate. This is a primary concern for the environmental applications of SAMNs considering that metal chelation can induce the degradation of metal oxides by a process known as “ligand promoted dissolution” (Gu and Karthikeyan, 2005). Moreover, the characterization by infrared spectroscopy and ab initio theoretical calculations of the different binding behaviour of arsenic oxyacids to SAMNs confirmed the occurrence of two different binding mechanisms for As^{III} and As^{V} on the surface of naked maghemite nanoparticles: arsenite appears to interact with SAMNs by a monodentate inner sphere coordination, while arsenate showed different binding options.

Finally, besides remediation purposes, As^{III} and As^{V} were used as effective probe for studying surface characteristics of maghemite nanoparticles being their binding behavior strictly related to defects of the structure of SAMNs surface. In particular, arsenic emerged as an elective probe for studying the surface structure of maghemite nanoparticles and the specificity of As for a class of crystalline vacancies on the oxide boundary with solvent.

XPS analysis highlighted that, upon As binding, oxygen atoms provided by arsenite and arsenate were integrated in the maghemite lattice restoring the Fe^{III} dangling bonds at the nanoparticle surface. Moreover, the loss of hydroxyl group (OH⁻) in SAMN@As^V and SAMN@As^{III} complexes and adsorbed H₂O was perfectly balanced by the increase of lattice oxygen. This suggests that the binding of arsenite and arsenate occurs via ligand exchange mechanism. More specifically, notwithstanding arsenite loading on SAMNs was lower than for arsenate (20 mg As^{III} g⁻¹ SAMNs vs. 32 mg As^V g⁻¹ SAMN), the binding of the As^{III} oxyacid to nanoparticles led to a higher content of lattice oxygen and, as a consequence, a more relevant displacement of surface -OH⁻ and H₂O groups with respect to As^V.

Thus, the higher binding specificity to SAMNs shown by As^{III} with respect to As^V substantiated the hypothesis of the existence of specific sites on SAMN surface. Up to the authors knowledge, only rare examples of comparative studies on the As^{III}-As^V couple were performed on maghemite (Lin et al., 2012; Liu et al., 2016). However, they did not show any specificity of the adsorption mechanism of the two oxyacids onto the metal oxide.

It should be stressed that the compendium of characteristics of SAMNs, such as the high colloidal stability, the low toxicity and the high adsorption efficiency, represents a key feature for SAMNs exploitation to large scale wastewater remediation. Thus, finally, SAMNs efficiency for Cr^{VI} remediation of real industrial groundwater was investigated mimicking a real in situ application. Preliminarily, the removal efficiency of the nanoparticles towards Cr^{VI} was proved with variable testing conditions in terms of SAMNs and pollutant concentrations and pH of the solution. SAMNs removal capacity towards Cr^{VI} was strongly affected by pH conditions, as observed for As^V, and the Cr^{VI} removal showed the highest value at pH 3.0 (99%), with a progressive decrease of the adsorption capacity at the increasing of the solution basicity, down to 40% Cr^{VI} removal at pH 9.0. The maximum absorption capacity considering a monolayer coverage was 44.0 mg Cr^{VI} g⁻¹ SAMNs, coupled to a very high stability of the complex as confirmed by a K_{eq} value of 2.5 L g⁻¹, comparable to other commonly used sorbents such as activated carbon and resins (Huang and Wu, 1977). It should be stressed that no Cr^{VI} release from the SAMN@Cr^{VI} complex was observed after various washing cycles. Moreover, optical characterizations demonstrated the covalent nature of the Cr^{VI} binding to SAMNs, and morphological characterization by HR-TEM excluded any alteration or degradation of SAMNs after the binding.

These results lead to test the SAMNs toward Cr^{VI} binding efficiency on real samples, such as industrially polluted groundwater, namely the Ex-Stoppani site. The chemical

characterization of samples from the Ex-Stoppani wells showed Cr^{VI} concentrations in the 0.5-19 mg L⁻¹ range, confirming the severe pollution affecting groundwater. Moreover, the high Cr^{VI} concentrations found in the Ex-Stoppani wastewater did not follow a trend with time, suggesting an strong Cr^{VI} immobilization in mineral phases produced from chromite ore processing residues (i.e sodium chromate, crocoite, katoite, ettringite). These phases represent a potential source of Cr^{VI} mobilization as a result of variation of environmental conditions leading to the consequent dissolution of Cr^{VI} bearing minerals. Major Cr^{VI} containing minerals in the Ex-Stoppani COPRs were Na₂CrO₄ for low aged samples (ST1 and ST2), while crocoite, katoite, ettringite and hydrotalcite for more weathered COPRs. In addition, Cr^{III} substituted brownmillerite was present.

For analytical purposes, the extraction of chromium from minerals was improved, and performed in two steps: the first with ultrapure water (pH = 6.6) was carried out for investigating in detail on highly soluble chromates and sulphates, while the second was focused on the acid labile fraction and extracted with 0.11 M of acetic acid (pH = 2-3). In fact, results highlighted that an important amount of Cr (2% to 23%) was leached by simple extraction with ultrapure water, simulating COPRs reactivity towards percolating water. In this case, Cr^{VI} leaching in low aged COPRs was driven by highly soluble chromates (Na₂CrO₄ and crocoite). Conversely, aged COPRs, besides showing a remarkable decrease of total leachable Cr, showed a high amount of Cr leached under acidic conditions.

It should be noted that the carbonate bound Cr fraction (both low aged and weathered COPRs) represents a threat for Cr^{VI} release, accounting for 6 to ~23 mg L⁻¹.

Results from sequential extraction demonstrated that the majority of Cr containing in the Ex-Stoppani samples was locked in chromite, while another considerable fraction was firmly bound into iron oxy(hydroxides) and possibly organic matter (Elzinga and Cirimo, 2010). Finally, the primary role of COPRs on the retention/release of Cr^{VI} in percolating groundwater was confirmed, as well as the crucial role of the mineralogical control for any remediation/stabilization attempt. SAMNs application on complex industrial wastewater confirmed the high adsorption efficiency reaching the almost total removal (>90%) of Cr^{VI} either in acidic and basic conditions with two treatment cycles. The application of SAMNs for Cr^{VI} removal showed a great potential for the exploitation to a large-scale industrial level. Results indicate that SAMNs are very promising for real *in-situ* application, considering the high adsorption efficiency even at neutral to basic pH values, typical conditions of groundwater. At the same time, even if no particular interfering anions were found in the

studied wells, a decrease in SAMNs binding efficiency occurred when water was characterized by high salinity, possibly due to the destabilization of the colloidal suspensions of nanoparticles leading to aggregation and subsequent decrease of exposed binding sites.

7. Appendix

7.1 Supporting Information to Synthesis of colloidal maghemite nanoparticles with chiroptical properties

The complexes obtained from the incubation of SAMNs with arsenite and arsenate species, namely SAMNs@As^V and SAMNs@As^{III} complexes, were characterised by zeta potential measurements at pH 7.0. A decrease of ζ values from $+31.7 \pm 0.6$ mV for naked SAMNs to -9.7 ± 0.4 mV for SAMN@As^{III} and -14.1 ± 0.2 mV for SAMN@As^V, was observed. The lowering of the zeta potential upon arsenic binding is consistent with the displacement of coordinated water molecules on the SAMN surface (Gu and Karthikeyan, 2005), already described on ferric oxyhydroxides.

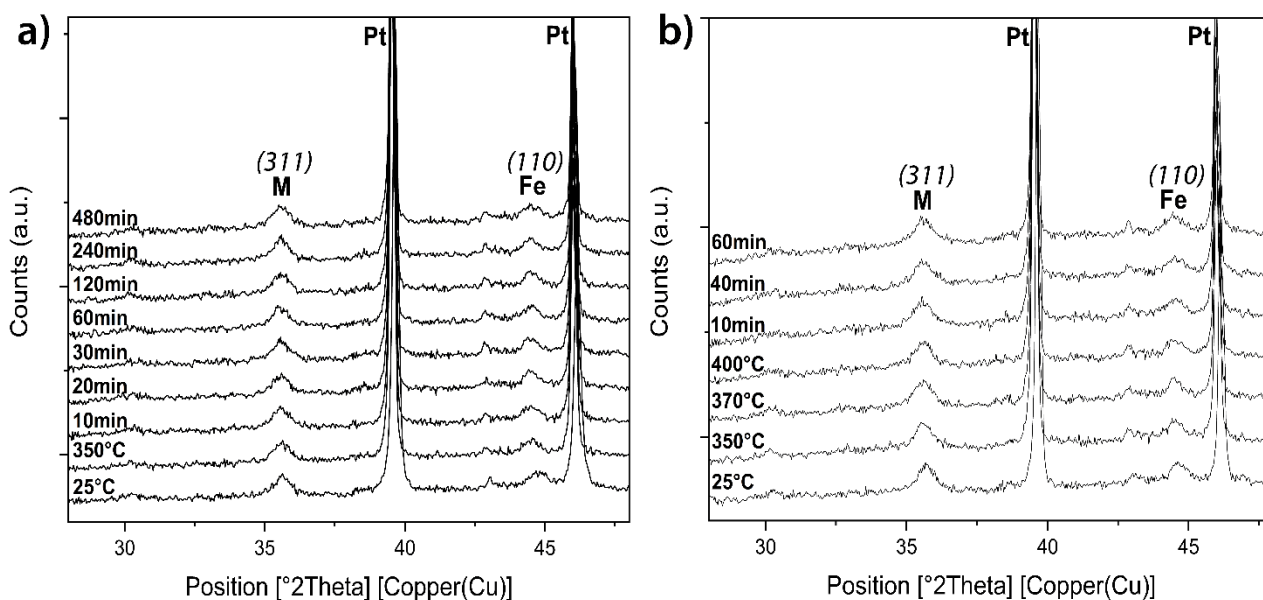


Figure S1. a) Kinetic of structural evolution of S0 at T=350 °C; b) Kinetic of structural evolution of S0 at T=400 °C.

Table S1. Values of the Mössbauer hyperfine parameters, derived from the least-square fitting of the Mössbauer spectra of the S0 and S1 intermediates, where δ is the isomer shift, ΔE_Q is the quadrupole splitting,

Sample	δ mm/s	$\Delta E_Q/\epsilon$ mm/s	H_{int} T	Γ mm/s	A %	component	Attribution
S0	0.27	-0.06	17.1	-	54	1	Relax sp.
	0.10	-0.14	33.6	0.78	16	2	Metallic Fe
	0.47	-0.26	45.1	1.84	22	3	Fe(III) mag.
	0.28	1.84	-	0.42	7	4	Fe(III)
S1	0.33	-0.00	49.2	0.59	60	/	Maghemite
	0.36	-0.02	45.0	0.97	40		Maghemite
S2	0.51	+0.01	50.9		62	/	Maghemite
	0.36	-0.02	50.3		38		Maghemite

Table S2. Elemental content in the region explored by TEM image in Figure 11A.

Region	Oxygen content	Iron content
	%	%
A	12	87
B	77	22
C	61	39

Table S3. Atomic weight fractions of elements obtained by X-Ray Photoelectron Spectroscopy (XPS).

Sample	C 1s	O 1s	Fe 2p	As 3d
SAMN	51.4 at. %	36.1 at. %	12.5 at. %	XXXXX
	32.61 w. %	30.51 w. %	36.88 w. %	XXXXX
SAMN @ As ^{III}	35.2 at. %	45.6 at. %	18.4 at. %	0.8 at. %
	18.88 w. %	32.57 w. %	45.88 w. %	2.68 w. %
SAMN @ As ^V	14.23 at. %	52.35 at. %	31.63 at. %	1.34 at. %
	5.94 w. %	29.13 w. %	61.43 w. %	3.49 w. %

Table S4. Oxygen fraction in pristine SAMNs and SAMN@As^V and SAMN@As^{III} complexes from XPS measurements

Atom	SAMNs (%)	SAMN@As ^V (%)	SAMN@As ^{III} (%)
Lattice Oxygen	60.54	73.41	78.74
-OH groups	23.02	16.31	16.84
Adsorbed H ₂ O	16.44	10.28	4.42

7.2 Supporting information for Naked Colloidal Maghemite Nanoparticles with Unique Surface Properties Encode Binding Specificity Toward As^{III} and As^V

Binding of arsenites and arsenates to SAMNs

The influence of the concentration of SAMNs on the binding of both arsenite and arsenate was studied at pH 7.0, the initial concentration of arsenic was set at 10 mg L⁻¹ (as As), while the concentration of SAMNs varied from 0.1 to 10 g L⁻¹. The effect of pH, in the 3.0-11.0 range, on the binding efficiency of arsenite and arsenate was studied by setting arsenic concentration at 10 mg L⁻¹ and SAMNs at 1 g L⁻¹. In all the experiments, arsenic was added to a 50 mM solution of tetramethylammonium perchlorate, and the proper amount of SAMNs was added in the test tube (2 mL final volume). The pH of the final solution was adjusted by addition of 0.1 M perchloric acid or 0.1 M tetramethylammonium hydroxide. For equilibrium experiments, solutions were mixed in an end-over-end shaker for 12 hours and magnetically separated by an Nd-Fe-B magnet. The supernatants were separated after 3-5 min, depending on SAMNs concentration. The residual arsenic concentration in the supernatants was immediately determined by AAS technique. Kinetic tests for measuring the arsenic sorption rate by SAMNs were carried out. Maghemite nanoparticles were added to 200 mL arsenic solution in the 0.015 - 1.0 g L⁻¹ concentration range (as As), maintaining constant the pH by 0.1 M HClO₄ or 0.1M N(CH₃)₄OH additions, if necessary. The experiments were carried out under agitation. Aliquots (1 mL) were taken at time intervals (from 2 to 1440 min), nanoparticles were magnetically separated, and the residual arsenic concentration in the

supernatants was measured by AAS. The equilibrium adsorption of arsenic on SAMNs was assessed with a series of batch experiments. Known concentrations of arsenic (3-50 mg L⁻¹) were mixed with SAMNs (1.0 g L⁻¹), and the mixture was mixed in an end-over-end shaker for 12 hrs. After equilibrium accomplishment, nanoparticles were magnetically separated, and the residual arsenic concentration in the supernatant was measured by AAS. The following equation was used to calculate the amount of arsenic adsorbed on SAMNs (eq. S1):

$$qe = \frac{(C_0 - C_e) * V}{m} \quad \text{Eq. S1}$$

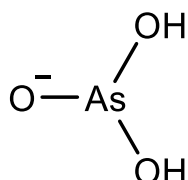
Where q_e (mg g⁻¹) is the amount of adsorbed arsenic at the equilibrium, C_0 and C_e are the initial and final concentration of arsenic (mg L⁻¹) in solution, respectively, V (L) is the volume of the solution, and m (g) is the mass of nanoparticles. Adsorption experiments involving arsenite were carried out in closed 5 mL serum bottles under N₂ atmosphere, and solutions were sparged with nitrogen for 10 min before the addition of arsenite to minimise As^{III} oxidation by dissolved oxygen. The data reproducibility was confirmed by duplicate experimental runs.

Theoretical calculations

The geometry optimisation followed by frequency calculations of the model systems, which have been used for mimicking the binding of As^V or As^{III} to surface-exposed Fe cations in SAMNs, were carried out by density functional theory (DFT) in the gas phase using the BP86 function (Exchange, Becke; correlation, Perdew). The basis set employed were 6-31G* for neutral and cationic species and the 6-31+G* for the anionic species. The Euler-Maclaurin-Lebedev grid (70, 302) has been used for the calculations. The SCF convergence was set to 10⁻⁷ au for the energy change and for the gradient the convergence was set below 10⁻³. Theoretically derived IR spectra have been shown by Lorentzian line using FWHH of 20 cm⁻¹. The detailed list of calculated IR frequencies, including ZPE (kJ mol⁻¹), Enthalpy (kJ mol⁻¹), Entropy (J mol⁻¹ K⁻¹), and Cv (J mol⁻¹ K⁻¹) terms are given in the Supporting material (Figure S2-S22), together with coordinate files

of the optimised structures (mol2 format). The computational package used for the DFT calculations was Wavefunction Inc. Spartan 10 (V.1.1.0).

Figure S2. Optimised structure of As^{III} molecule (drawn below) with coordinates given in mol2 format.



Method: RBP86
Basis set: 6-31+G*
Number of shells: 28
Number of basis functions: 100
Charge : -1
Multiplicity: 1

```
#  
#      File Created by: Spartan '10 Export  
#
```

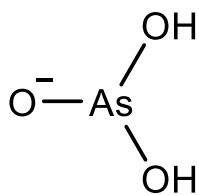
```
@<TRIPOS>MOLECULE  
M0001  
6 5  
SMALL  
MULLIKEN_CHARGES
```

```
@<TRIPOS>ATOM  
1 As1 -0.613308035 -0.100845486 0.000000000 As 1 M0001 0.540786  
2 O2 0.263753277 0.779901600 1.473891958 O.3 1 M0001 -0.773245  
3 O3 0.263753277 0.779901600 -1.473891958 O.3 1 M0001 -0.773247  
4 O4 0.232469557 -1.579357257 0.000000000 O 1 M0001 -0.823522  
5 H5 1.017632487 0.157191098 1.607067608 H 1 M0001 0.414614  
6 H6 1.017632487 0.157191098 -1.607067608 H 1 M0001 0.414614
```

```
@<TRIPOS>BOND  
1 1 2 1  
2 1 3 1  
3 1 4 1  
4 2 5 1  
5 3 6 1
```

This Molecule has 0 Imaginary Frequencies
Zero point vibrational energy: 17.297 kcal/mol

Figure S3. Frequency calculation results.



Standard Thermodynamic quantities at 298.15 K and 1.00 atm

Modifying values for 2 low frequency terms

	Term	ZPE cm-1	Enthalpy kJ/mol	Entropy J/mol.K	Cv J/mol.K	% in Ground IR Int.	
1*	A''	186.786	1.1172	1.2395	8.3144	7.7736	59.40 0.31
2*	A'	193.471	1.1572	1.2395	8.3144	7.7359	60.69 1.42
3	A'	264.971	1.5849	1.2230	6.8148	7.2685	72.16 34.61
4	A''	363.555	2.1745	0.9098	4.6310	6.4738	82.70 54.12
5	A'	418.692	2.5043	0.7656	3.7506	5.9815	86.74 82.25
6	A''	490.172	2.9319	0.6077	2.8583	5.3213	90.61 244.15
7	A'	505.829	3.0255	0.5772	2.6932	5.1759	91.29 139.88
8	A'	807.835	4.8319	0.2000	0.8411	2.6690	97.97 126.21
9	A''	894.930	5.3529	0.1445	0.5961	2.1213	98.67 68.55
10	A'	929.846	5.5617	0.1266	0.5187	1.9269	98.87 41.73
11	A''	3521.617	21.0639	0.0000	0.0000	0.0001	100.00 0.10
12	A'	3521.800	21.0650	0.0000	0.0000	0.0001	100.00 7.02
Total Vibrations		72.3711	7.0333	39.3326	52.4479		
Ideal Gas			2.4789				
Translation			3.7184	168.9548	12.4716		
Rotation			3.7184	106.5047	12.4716		
Totals				89.3202	314.7920	77.3911	
Vibrational(v) Corrections:							
Temp. Correction Hv				89.3202			
Entropy Correction (Hv-TSv)				-4.5351			

Figure S4. IR plot (Lorentzian line, 20 cm⁻¹ FWHH).

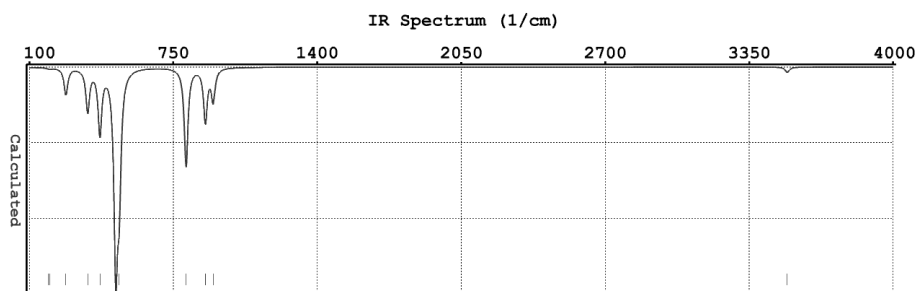
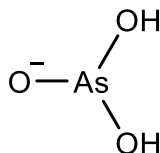
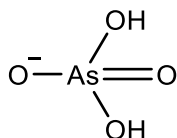


Figure S5. Optimised structure of As^V molecule (reported below) with coordinates given in mol2 format.



Method: RBP86
Basis set: 6-31+G*
Number of shells: 33

Number of basis functions: 119

Charge : -1

Multiplicity: 1

#

File Created by: Spartan '10 Export

#

@<TRIPOS>MOLECULE

M0001

7 6

SMALL

MULLIKEN_CHARGES

@<TRIPOS>ATOM

1	As1	0.072907229	-0.137186736	-0.525668670	As	1	M0001	1.160822
2	O2	0.149740567	-1.377911779	0.856852381	O.3	1	M0001	-0.786368
3	O3	0.914882173	1.321477378	0.262074282	O.3	1	M0001	-0.787140
4	O4	1.038826797	-0.684306560	-1.761982581	O	1	M0001	-0.676228
5	H5	-0.757721280	-1.289019499	1.227408778	H	1	M0001	0.432842
6	H6	0.132263534	1.855759230	0.528136418	H	1	M0001	0.433055
7	O7	-1.550899022	0.311187913	-0.586820555	O.2	1	M0001	-0.776984

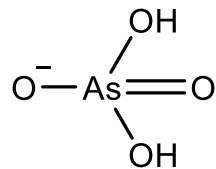
@<TRIPOS>BOND

1	1	2	1
2	1	3	1
3	1	4	1
4	2	5	1
5	3	6	1
6	7	1	2

This Molecule has 0 Imaginary Frequencies

Zero point vibrational energy: 19.859 kcal/mol

Figure S6. Frequency calculation results.



Standard Thermodynamic quantities at 298.15 K and 1.00 atm

Modifying values for 2 low frequency terms

Term	ZPE cm-1	Enthalpy kJ/mol	Entropy J/mol.K	Cv J/mol.K	% in Ground IR Int.
1*	153.804	0.9199	1.2395	8.3144	52.39
2*	211.310	1.2639	1.2395	8.3144	63.93
3	267.916	1.6025	1.2125	6.7345	72.55
4	290.674	1.7386	1.1341	6.1506	75.41
5	294.835	1.7635	1.1202	6.0502	75.90
6	326.204	1.9511	1.0197	5.3505	79.28
7	360.357	2.1554	0.9189	4.6884	82.43
8	552.872	3.3069	0.4932	2.2520	93.06
9	555.779	3.3243	0.4883	2.2272	93.16
10	810.114	4.8456	0.1983	0.8336	97.99
11	891.542	5.3326	0.1464	0.6042	98.65
12	983.328	5.8816	0.1032	0.4186	99.13
13	1033.191	6.1799	0.0850	0.3423	99.32
14	3579.570	21.4106	0.0000	0.0000	100.00
15	3580.390	21.4155	0.0000	0.0000	100.00
Total Vibrations	83.0919	9.3986	52.2808	67.5714	
Ideal Gas		2.4789			
Translation		3.7184	170.4574	12.4716	
Rotation		3.7184	110.0392	12.4716	
Totals		102.4063	332.7774	92.5147	

Vibrational(v) Corrections:
 Temp. Correction Hv 102.4063
 Entropy Correction (Hv-TSv) 3.1887

Figure S7. IR plot (Lorentzian line, 20 cm⁻¹ FWHH).

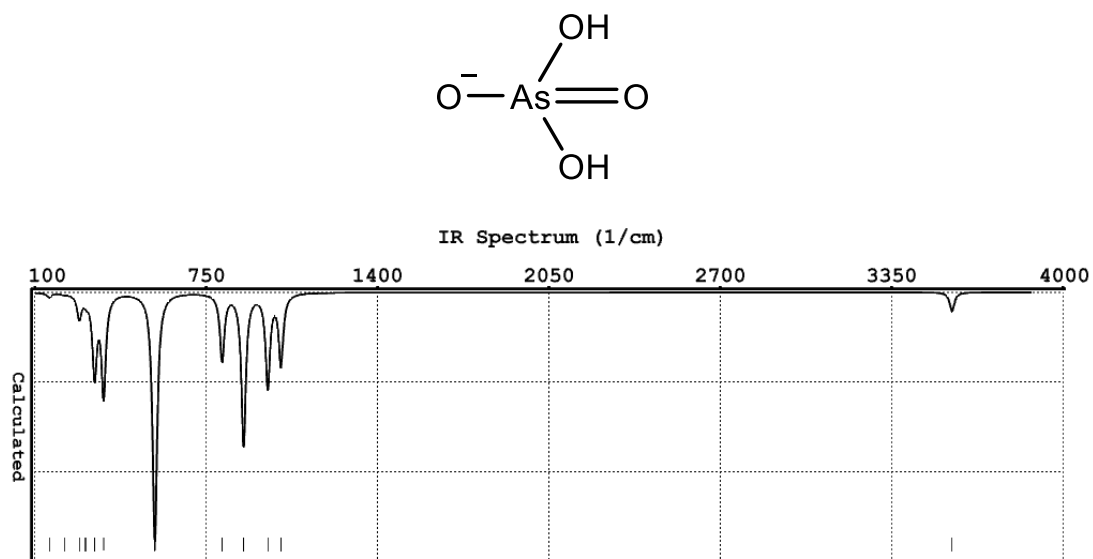
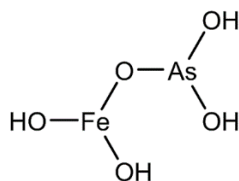


Figure S8. Optimised structure of Fe-O-As^{III} molecule (reported below) with coordinates given in mol2 format.



Method: UBP86
 Basis set: 6-31G(D)
 Number of shells: 43
 Number of basis functions: 147
 Multiplicity: 6

#

File Created by: Spartan '10 Export

#

@<TRIPOS>MOLECULE

M0001

11 10

SMALL

MULLIKEN_CHARGES

@<TRIPOS>ATOM

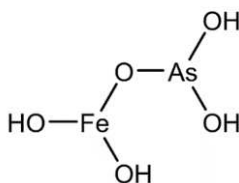
1	As1	-2.075207625	-0.772532788	0.201465640	As	1	M0001	0.848424
2	O2	-1.087909679	-1.629506408	1.430687041	O.3	1	M0001	-0.660310
3	O3	-1.203123535	1.007745636	0.512323469	O.3	1	M0001	-0.726481
4	O4	-1.114544647	-0.825086410	-1.286304576	O.3	1	M0001	-0.653298
5	H5	-0.112487772	-1.449036960	1.222446939	H	1	M0001	0.446060
6	H6	-0.861123965	0.995167293	1.436489813	H	1	M0001	0.428866
7	Fe7	0.289989938	0.362984484	-0.806338126	Fe	1	M0001	1.103818
8	H8	1.739313607	2.096915820	-1.808742126	H	1	M0001	0.415350
9	O9	1.071050219	1.422659608	-2.041935157	O.3	1	M0001	-0.775157
10	O10	1.208667322	-0.467237335	0.588749372	O.3	1	M0001	-0.846584
11	H11	2.145375554	-0.742072886	0.551157869	H	1	M0001	0.419313

@<TRIPOS>BOND

1	1	2	1
2	1	3	1
3	1	4	1
4	2	5	1
5	3	6	1
6	4	7	1
7	8	9	1
8	10	11	1
9	10	7	1
10	7	9	1

This Molecule has 0 Imaginary Frequencies
 Zero point vibrational energy: 35.248 kcal/mol

Figure S9. Frequency calculation results.



Standard Thermodynamic quantities at 298.15 K and 1.00 atm

Modifying values for 8 low frequency terms

	Term cm-1	ZPE kJ/mol	Enthalpy kJ/mol	Entropy J/mol.K	Cv J/mol.K	% in Ground IR Int.	
1*	87.162	0.5213	1.2395	8.3144	8.1929	34.34	16.01
2*	114.216	0.6832	1.2395	8.3144	8.1071	42.37	3.70
3*	140.334	0.8394	1.2395	8.3144	8.0038	49.20	25.68
4*	177.666	1.0627	1.2395	8.3144	7.8233	57.57	56.98
5*	190.963	1.1422	1.2395	8.3144	7.7502	60.21	42.10
6*	204.143	1.2210	1.2395	8.3144	7.6734	62.66	23.57
7*	225.504	1.3488	1.2395	8.0100	7.5403	66.32	50.04
8*	248.914	1.4888	1.2395	7.2728	7.3829	69.92	30.02
9	273.281	1.6346	1.1936	6.5913	7.2074	73.25	49.90
10	320.264	1.9156	1.0382	5.4758	6.8398	78.68	12.57
11	342.021	2.0457	0.9720	5.0321	6.6587	80.80	0.22
12	446.883	2.6730	0.6996	3.3691	5.7227	88.43	85.74
13	539.481	3.2268	0.5159	2.3698	4.8649	92.60	167.95
14	569.596	3.4069	0.4660	2.1129	4.5899	93.60	16.98
15	581.445	3.4778	0.4475	2.0195	4.4829	93.95	186.95
16	623.735	3.7308	0.3869	1.7179	4.1082	95.07	91.52
17	641.868	3.8392	0.3632	1.6024	3.9516	95.48	2.73
18	655.766	3.9224	0.3459	1.5190	3.8335	95.78	153.51
19	677.433	4.0519	0.3205	1.3973	3.6528	96.20	118.97
20	702.266	4.2005	0.2934	1.2694	3.4513	96.63	62.59
21	797.829	4.7721	0.2075	0.8748	2.7377	97.87	93.58
22	908.669	5.4350	0.1372	0.5644	2.0431	98.75	56.60
23	1224.806	7.3260	0.0398	0.1561	0.7916	99.73	108.96
24	3050.381	18.2453	0.0000	0.0001	0.0007	100.00	263.05
25	3571.347	21.3614	0.0000	0.0000	0.0001	100.00	47.35
26	3665.570	21.9250	0.0000	0.0000	0.0001	100.00	65.90
27	3675.127	21.9821	0.0000	0.0000	0.0001	100.00	49.79
Total Vibrations		147.4796	17.3430	101.2411	127.4107		
Ideal Gas			2.4789				
Translation			3.7184	175.7183	12.4716		
Rotation			3.7184	122.8894	12.4716		
Totals			174.7383	399.8488	152.3539		

Vibrational(v) Corrections:

Temp. Correction Hv 174.7383

Entropy Correction (Hv-TSv) 55.5234

Figure S10. IR plot (Lorentzian line, 20 cm⁻¹ FWHH).

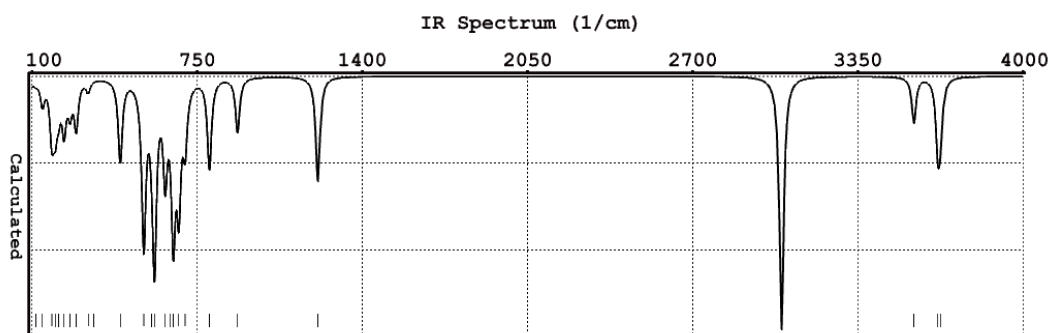
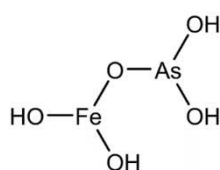
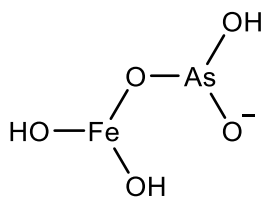


Figure S11. Optimised structure of Fe^{III}-O-As^{III} molecule with coordinates given in mol2 format.



Method: UBP86
Basis set: 6-31+G*
Number of shells: 47
Number of basis functions: 169
Charge : -1
Multiplicity: 6

#

File Created by: Spartan '10 Export

#

@<TRIPOS>MOLECULE
M0001
10 9
SMALL
MULLIKEN_CHARGES

@<TRIPOS>ATOM

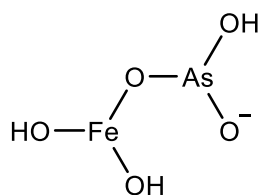
1	As1	2.132396398	0.089209043	-0.394181460	As	1	M0001	0.690693
2	O2	1.176708498	0.643197416	1.030682667	O	1	M0001	-0.747234
3	O3	2.266655828	-1.740826764	0.025527751	O.3	1	M0001	-0.737620
4	O4	0.662264053	0.171399774	-1.457798894	O.3	1	M0001	-0.736728
5	H5	1.475323781	-1.916956788	0.587026620	H	1	M0001	0.431442
6	Fe6	-0.503777339	0.658446360	0.017255224	Fe	1	M0001	1.209583
7	H7	-1.601745228	-1.532807995	-0.241921190	H	1	M0001	0.425626
8	O8	-1.689291310	-0.771601119	0.368327693	O.3	1	M0001	-0.999133
9	O9	-1.475945771	2.265408117	-0.011728350	O.3	1	M0001	-0.958082
10	H10	-2.442588911	2.134532009	0.076809885	H	1	M0001	0.421453

@<TRIPOS>BOND

1	1	2	1
2	1	3	1
3	1	4	1
4	3	5	1
5	4	6	1
6	7	8	1
7	9	10	1
8	9	6	1
9	6	8	1

This Molecule has 0 Imaginary Frequencies
Zero-point vibrational energy: 27.259 kcal/mol

Figure S12. Frequency calculation results.



Standard Thermodynamic quantities at 298.15 K and 1.00 atm

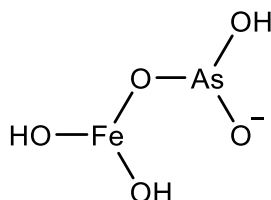
Modifying values for 7 low frequency terms

	Term cm-1	ZPE kJ/mol	Enthalpy kJ/mol	Entropy J/mol.K	Cv J/mol.K	% in Ground IR Int.	
1*	35.781	0.2140	1.2395	8.3144	8.2938	15.86	0.54
2*	94.555	0.5656	1.2395	8.3144	8.1716	36.64	2.76
3*	126.970	0.7594	1.2395	8.3144	8.0591	45.81	11.71
4*	129.242	0.7730	1.2395	8.3144	8.0501	46.40	2.50
5*	155.430	0.9297	1.2395	8.3144	7.9353	52.77	5.37
6*	162.099	0.9696	1.2395	8.3144	7.9031	54.26	20.23
7*	247.137	1.4782	1.2395	7.3257	7.3952	69.66	21.32
8	260.520	1.5583	1.2389	6.9382	7.3007	71.55	2.95
9	277.694	1.6610	1.1783	6.4761	7.1744	73.82	112.75
10	296.687	1.7746	1.1140	6.0062	7.0287	76.11	49.49
11	347.194	2.0767	0.9567	4.9324	6.6147	81.28	14.75
12	406.929	2.4340	0.7947	3.9226	6.0884	85.97	50.05
13	522.472	3.1251	0.5461	2.5282	5.0217	91.96	256.30
14	542.983	3.2478	0.5099	2.3384	4.8327	92.72	26.36
15	552.283	3.3034	0.4941	2.2571	4.7475	93.04	224.09
16	571.546	3.4186	0.4629	2.0973	4.5722	93.66	248.34
17	581.868	3.4803	0.4469	2.0163	4.4790	93.97	127.86
18	652.188	3.9009	0.3503	1.5401	3.8637	95.70	85.27
19	667.495	3.9925	0.3319	1.4519	3.7351	96.01	55.02
20	678.944	4.0610	0.3188	1.3892	3.6403	96.22	84.63
21	935.780	5.5972	0.1238	0.5065	1.8952	98.91	59.42
22	3549.838	21.2327	0.0000	0.0000	0.0001	100.00	8.22
23	3635.416	21.7446	0.0000	0.0000	0.0001	100.00	13.42
24	3637.189	21.7552	0.0000	0.0000	0.0001	100.00	9.64
Total Vibrations		114.0534	17.5436	101.6125	126.8030		
Ideal Gas			2.4789				
Translation			3.7184	175.6596	12.4716		
Rotation			3.7184	123.3071	12.4716		
Totals			141.5127	400.5792	151.7462		

Vibrational(v) Corrections:

Temp. Correction Hv 141.5127
Entropy Correction (Hv-TSv) 22.0800

Figure S13. IR plot (Lorentzian line, 20 cm⁻¹ FWHH).



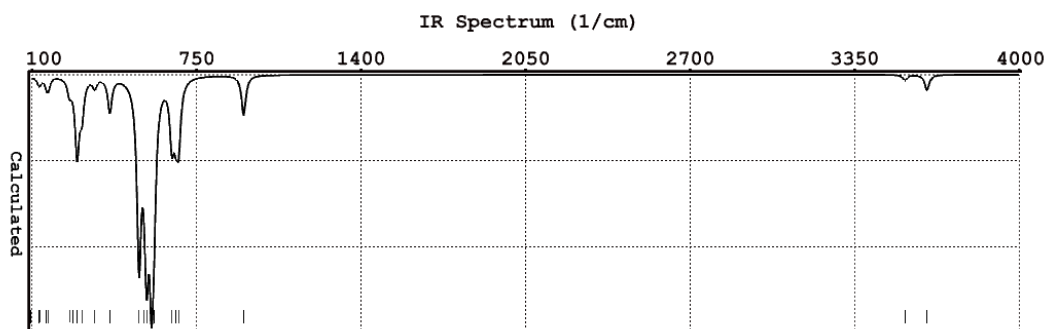
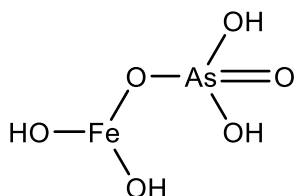


Figure S14. Optimised structure of Fe^{III}-O-As^V molecule (reported below) with coordinates given in mol2 format.



Method: UBP86
 Basis set: 6-31G(D)
 Number of shells: 47
 Number of basis functions: 162
 Multiplicity: 6

```
#
#       File Created by: Spartan '10 Export
#
```

```
@<TRIPOS>MOLECULE
M0001
12 11
SMALL
MULLIKEN_CHARGES
```

```
@<TRIPOS>ATOM
 1 As1  -1.453521455  -0.770058762  0.138146820  As 1 M0001  1.064460
 2 O2   -1.198949614  -2.054332047  1.346692664  O.3 1 M0001  -0.581093
 3 O3   -0.432061727  0.644609137  0.898977211  O.3 1 M0001  -0.690197
 4 O4   -0.249585000  -1.057202875  -1.057260452  O.3 1 M0001  -0.631309
 5 H5   -2.044914902  -2.123851621  1.847104281  H 1 M0001  0.434534
 6 H6   -0.944414291  1.475399275  0.758443719  H 1 M0001  0.455650
 7 Fe7   1.041058739  0.352839952  -0.674539758  Fe 1 M0001  1.122983
 8 H8    1.634460976  2.492419822  -1.705137897  H 1 M0001  0.421663
 9 O9    0.856836273  1.911550388  -1.578077302  O.3 1 M0001  -0.778964
10 O10   2.686761328  -0.101437992  -0.095313484  O.3 1 M0001  -0.769456
11 H11   2.935619719  -1.011507291  0.165778668  H 1 M0001  0.422909
12 O12  -3.005485311  -0.321757639  -0.117452698  O.2 1 M0001  -0.471181
```

```
@<TRIPOS>BOND
 1  1  2  1
 2  1  3  1
 3  1  4  1
 4  2  5  1
 5  3  6  1
 6  4  7  1
```

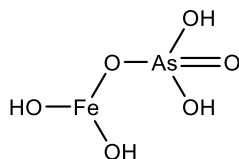
```

7  8  9  1
8 10 11  1
9 10  7  1
10 7  9  1
11 12  1  2

```

This Molecule has 0 Imaginary Frequencies
Zero point vibrational energy: 37.209 kcal/mol

Figure S15. Frequency calculation results.



Standard Thermodynamic quantities at 298.15 K and 1.00 atm

Modifying values for 8 low frequency terms

	Term cm-1	ZPE kJ/mol	Enthalpy kJ/mol	Entropy J/mol.K	Cv J/mol.K	% in Ground IR Int.	
1*	39.791	0.2380	1.2395	8.3144	8.2889	17.47	0.25
2*	66.644	0.3986	1.2395	8.3144	8.2431	27.50	2.94
3*	103.026	0.6162	1.2395	8.3144	8.1452	39.18	6.79
4*	122.426	0.7323	1.2395	8.3144	8.0767	44.61	2.45
5*	129.475	0.7744	1.2395	8.3144	8.0491	46.46	2.88
6*	187.442	1.1212	1.2395	8.3144	7.7700	59.53	6.11
7*	202.352	1.2103	1.2395	8.3144	7.6841	62.34	0.75
8*	212.198	1.2692	1.2395	8.3144	7.6244	64.08	21.01
9	270.293	1.6167	1.2041	6.6706	7.2295	72.87	37.18
10	294.305	1.7603	1.1219	6.0629	7.0473	75.83	22.54
11	307.607	1.8399	1.0784	5.7536	6.9422	77.34	33.69
12	313.623	1.8759	1.0591	5.6197	6.8938	77.99	79.37
13	325.407	1.9464	1.0222	5.3671	6.7976	79.20	57.14
14	370.872	2.2183	0.8895	4.5027	6.4099	83.30	163.98
15	499.920	2.9902	0.5885	2.7544	5.2307	91.04	128.48
16	518.240	3.0998	0.5539	2.5692	5.0609	91.80	132.41
17	592.064	3.5413	0.4316	1.9393	4.3876	94.26	10.44
18	596.904	3.5703	0.4245	1.9037	4.3445	94.39	210.42
19	634.252	3.7937	0.3730	1.6499	4.0170	95.31	161.62
20	667.489	3.9925	0.3319	1.4519	3.7352	96.01	45.11
21	682.299	4.0811	0.3150	1.3713	3.6128	96.28	104.40
22	718.755	4.2991	0.2766	1.1909	3.3210	96.88	22.42
23	765.340	4.5777	0.2337	0.9934	2.9687	97.51	156.62
24	932.391	5.5769	0.1254	0.5134	1.9133	98.89	37.80
25	967.503	5.7870	0.1096	0.4461	1.7329	99.06	116.52
26	1047.402	6.2649	0.0805	0.3231	1.3728	99.36	119.23
27	3575.029	21.3834	0.0000	0.0000	0.0001	100.00	77.32
28	3579.708	21.4114	0.0000	0.0000	0.0001	100.00	80.04
29	3652.070	21.8442	0.0000	0.0000	0.0001	100.00	88.38
30	3653.407	21.8522	0.0000	0.0000	0.0001	100.00	49.19

Total Vibrations 155.6834 20.1350 117.5984 146.8997

Ideal Gas	2.4789		
Translation	3.7184	176.6137	12.4716
Rotation	3.7184	125.7321	12.4716

Totals		185.7342	171.8429

Vibrational(v) Corrections:
Temp. Correction Hv 185.7342
Entropy Correction (Hv-Tsv) 60.5278

Figure S16. IR plot (Lorentzian line, 20 cm⁻¹ FWHH).

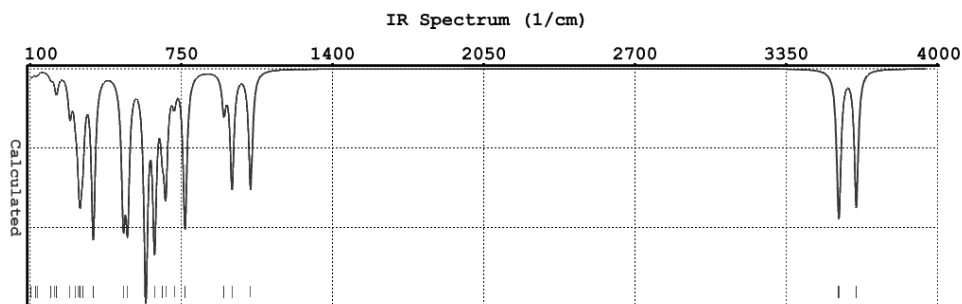
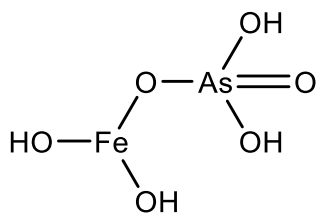
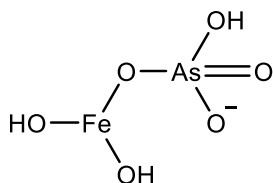


Figure S17. Optimised structure of Fe^{III}-O-As^V molecule (reported below) with coordinates given in mol2 format.



Method: UBP86
 Basis set: 6-31+G*
 Number of shells: 52
 Number of basis functions: 188
 Charge : -1
 Multiplicity: 6

 # File Created by: Spartan '10 Export
 #

@<TRIPOS>MOLECULE
 M0001
 11 10
 SMALL
 MULLIKEN_CHARGES

@<TRIPOS>ATOM

1	As1	-1.481593563	-0.454638446	0.333525911	As	1	M0001	1.185152
2	O2	-1.033191922	-1.877594369	1.407023298	O.3	1	M0001	-0.769935
3	O3	-0.531425285	0.897222894	0.939875975	O	1	M0001	-0.705387
4	O4	-0.517496722	-0.657885039	-1.124450169	O.3	1	M0001	-0.706844
5	H5	-1.917570747	-2.220298277	1.669005001	H	1	M0001	0.445845
6	Fe6	0.769412670	0.744697564	-0.552407020	Fe	1	M0001	1.218616
7	H7	1.980267638	2.440086570	-1.821536026	H	1	M0001	0.429392
8	O8	1.040727389	2.220848629	-1.652434917	O.3	1	M0001	-0.934198
9	O9	2.422748026	0.052151373	-0.032384576	O.3	1	M0001	-0.973163
10	H10	2.411061644	-0.739476959	0.544364665	H	1	M0001	0.441017
11	O11	-3.142939181	-0.405113887	0.289417911	O.2	1	M0001	-0.630496

@<TRIPOS>BOND

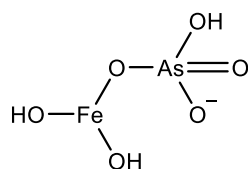
```

1 1 2 1
2 1 3 1
3 1 4 1
4 2 5 1
5 4 6 1
6 7 8 1
7 9 10 1
8 9 6 1
9 6 8 1
10 11 1 2

```

This Molecule has 0 Imaginary Frequencies
Zero point vibrational energy: 29.573 kcal/mol

Figure S18. Frequency calculation results.



Standard Thermodynamic quantities at 298.15 K and 1.00 atm

Modifying values for 9 low frequency terms

Term	cm-1	ZPE kJ/mol	Enthalpy kJ/mol	Entropy J/mol.K	Cv J/mol.K	% in Ground IR Int.
1*	48.092	0.2877	1.2395	8.3144	8.2772	20.71 0.18
2*	67.550	0.4040	1.2395	8.3144	8.2412	27.82 8.31
3*	124.104	0.7423	1.2395	8.3144	8.0703	45.06 1.27
4*	125.793	0.7524	1.2395	8.3144	8.0637	45.50 6.67
5*	136.734	0.8179	1.2395	8.3144	8.0192	48.31 4.01
6*	167.615	1.0026	1.2395	8.3144	7.8756	55.46 4.36
7*	178.346	1.0667	1.2395	8.3144	7.8197	57.71 18.32
8*	225.434	1.3484	1.2395	8.0123	7.5408	66.31 30.80
9*	247.295	1.4792	1.2395	7.3210	7.3942	69.68 154.35
10	264.377	1.5813	1.2251	6.8311	7.2728	72.08 66.80
11	291.333	1.7426	1.1318	6.1345	7.0704	75.49 9.45
12	304.412	1.8208	1.0887	5.8263	6.9677	76.98 44.97
13	325.561	1.9473	1.0217	5.3639	6.7963	79.22 33.66
14	419.990	2.5121	0.7625	3.7321	5.9697	86.82 38.02
15	522.998	3.1282	0.5452	2.5231	5.0169	91.98 228.68
16	567.822	3.3963	0.4688	2.1273	4.6059	93.54 131.49
17	583.372	3.4893	0.4446	2.0047	4.4655	94.01 309.82
18	591.805	3.5398	0.4320	1.9412	4.3900	94.25 44.46
19	665.346	3.9796	0.3345	1.4640	3.7530	95.97 71.32
20	673.125	4.0262	0.3254	1.4207	3.6884	96.12 133.52
21	674.699	4.0356	0.3236	1.4121	3.6753	96.15 81.80
22	711.517	4.2558	0.2838	1.2248	3.3778	96.77 81.99
23	882.498	5.2785	0.1514	0.6263	2.1940	98.59 156.38
24	1017.915	6.0885	0.0902	0.3641	1.4978	99.26 103.04
25	3587.598	21.4586	0.0000	0.0000	0.0001	100.00 28.37
26	3639.463	21.7688	0.0000	0.0000	0.0001	100.00 24.12
27	3641.939	21.7836	0.0000	0.0000	0.0001	100.00 19.21

Total Vibrations	123.7341	19.7845	116.5304	142.0434		
Ideal Gas		2.4789				
Translation		3.7184	176.5592	12.4716		
Rotation		3.7184	125.2777	12.4716		

Totals		153.4344	418.3673	166.9866		

Ideal Gas		2.4789				
Translation		3.7184	176.5592	12.4716		
Rotation		3.7184	125.2777	12.4716		

Totals		153.4344	418.3673	166.9866		

Vibrational(v) Corrections:
Temp. Correction Hv 153.4344
Entropy Correction (Hv-TSv) 28.6982

Figure S19. IR plot (Lorentzian line, 20 cm⁻¹ FWHH).

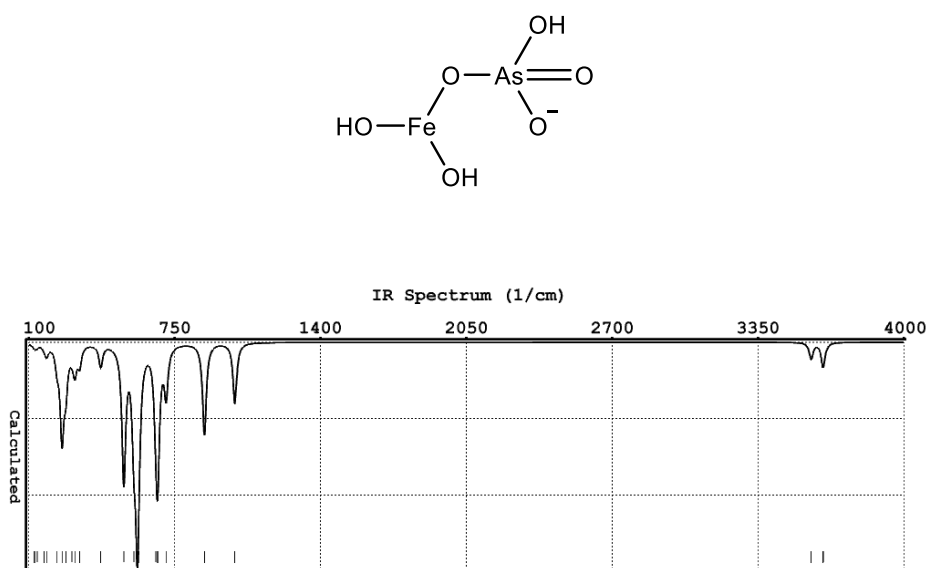
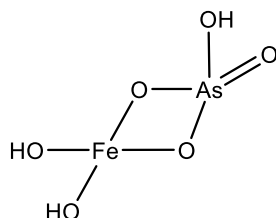


Figure S20. Optimised structure of Fe^{III}-O-As^V molecule (reported below) with coordinates given in mol2 format.



Method: UBP86
 Basis set: 6-31G(D)
 Number of shells: 45
 Number of basis functions: 160
 Charge : +1
 Multiplicity: 6

 # File Created by: Spartan '10 Export
 #

@<TRIPOS>MOLECULE
 M0001
 11 11
 SMALL
 MULLIKEN_CHARGES

@<TRIPOS>ATOM

1	As1	-1.346373268	-0.759868730	0.403047082	As	1	M0001	1.176180
2	O2	-1.481159735	-1.392109140	2.022562730	O.3	1	M0001	-0.502015
3	O3	-0.953497762	0.963611259	0.295030313	O.3	1	M0001	-0.471532
4	O4	0.267144539	-1.145313672	-0.176289325	O.3	1	M0001	-0.546336
5	H5	-2.428514933	-1.563582799	2.259263926	H	1	M0001	0.488049

```

6 Fe6 0.763675604 0.667434127 -0.461301791 Fe 1 M0001 1.280308
7 H7 2.015314759 2.681789546 -0.902517635 H 1 M0001 0.493322
8 O8 1.116658813 2.363102021 -0.637154781 O.3 1 M0001 -0.588795
9 O9 2.317630743 0.103482043 -1.054122456 O.3 1 M0001 -0.597836
10 H10 2.422134429 -0.877877255 -1.144839621 H 1 M0001 0.487738
11 O11 -2.693013138 -1.040667349 -0.603678442 O.2 1 M0001 -0.219084

```

@<TRIPOS>BOND

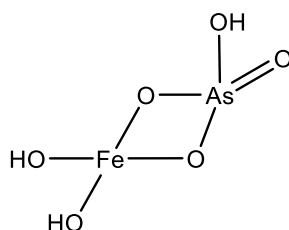
```

1 1 2 1
2 1 3 1
3 1 4 1
4 2 5 1
5 4 6 1
6 7 8 1
7 9 10 1
8 9 6 1
9 6 8 1
10 11 1 2
11 3 6 1

```

This Molecule has 0 Imaginary Frequencies
Zero point vibrational energy: 30.188 kcal/mol

Figure S21. Frequency calculation results.



Standard Thermodynamic quantities at 298.15 K and 1.00 atm

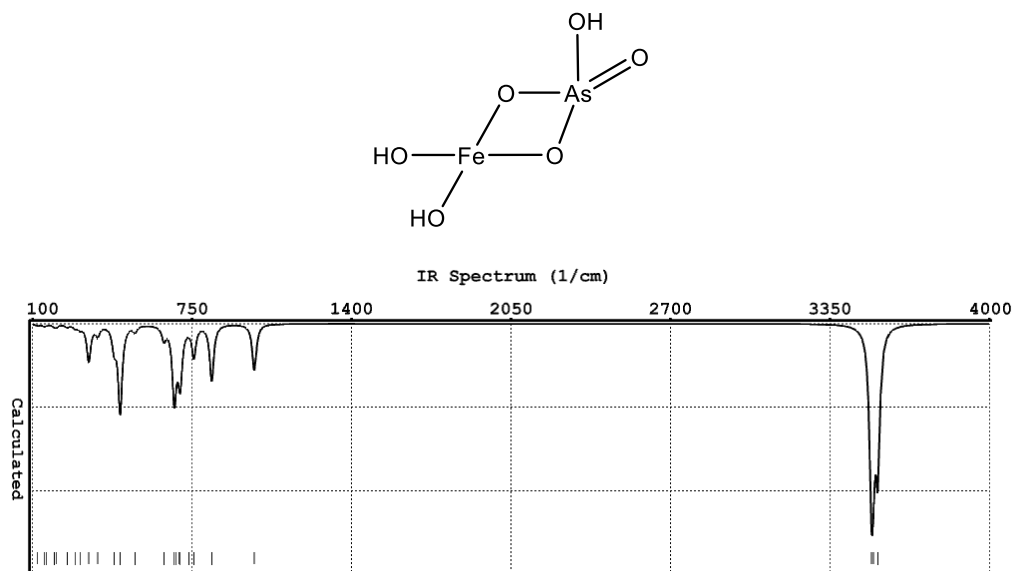
Modifying values for 8 low frequency terms

	Term cm-1	ZPE kJ/mol	Enthalpy kJ/mol	Entropy J/mol.K	Cv J/mol.K	% in Ground	IR Int.
1*	37.923	0.2268	1.2395	8.3144	8.2912	16.72	1.37
2*	58.961	0.3527	1.2395	8.3144	8.2585	24.76	3.82
3*	120.226	0.7191	1.2395	8.3144	8.0851	44.02	4.36
4*	146.123	0.8740	1.2395	8.3144	7.9783	50.60	4.41
5*	153.858	0.9203	1.2395	8.3144	7.9428	52.41	2.60
6*	187.779	1.1232	1.2395	8.3144	7.7681	59.59	5.70
7*	197.623	1.1820	1.2395	8.3144	7.7119	61.47	6.96
8*	241.321	1.4434	1.2395	7.5023	7.4352	68.79	7.30
9	272.104	1.6275	1.1978	6.6224	7.2161	73.10	8.45
10	292.158	1.7475	1.1291	6.1145	7.0640	75.58	11.16
11	328.172	1.9629	1.0137	5.3097	6.7747	79.48	104.57
12	364.464	2.1800	0.9073	4.6149	6.4659	82.77	28.86
13	431.672	2.5820	0.7346	3.5698	5.8627	87.55	60.57
14	456.269	2.7291	0.6788	3.2511	5.6359	88.94	251.20
15	516.618	3.0901	0.5569	2.5850	5.0759	91.73	18.64
16	634.416	3.7947	0.3728	1.6489	4.0156	95.32	38.52
17	677.064	4.0497	0.3209	1.3993	3.6558	96.19	208.86
18	684.964	4.0970	0.3120	1.3573	3.5910	96.33	5.77
19	694.475	4.1539	0.3017	1.3083	3.5138	96.50	16.13
20	701.271	4.1945	0.2944	1.2743	3.4592	96.61	151.56
21	736.334	4.4043	0.2596	1.1122	3.1852	97.14	3.23
22	756.764	4.5265	0.2411	1.0272	3.0318	97.41	87.93
23	829.529	4.9617	0.1846	0.7723	2.5241	98.17	162.14
24	1003.234	6.0007	0.0955	0.3863	1.5635	99.21	134.52
25	3519.796	21.0531	0.0000	0.0000	0.0001	100.00	408.78
26	3527.755	21.1007	0.0000	0.0000	0.0001	100.00	217.56
27	3545.724	21.2081	0.0000	0.0000	0.0001	100.00	377.54
---	-----	-----	-----	-----	-----	-----	-----
Total Vibrations		126.3053	18.5164	108.0568	136.1068		

Ideal Gas	2.4789		
Translation	3.7184	176.5592	12.4716
Rotation	3.7184	124.7743	12.4716
-----	-----	-----	-----
Totals	154.7374	409.3903	161.0500

Vibrational(v) Corrections:			
Temp. Correction	Hv	154.7374	
Entropy Correction	(Hv-TSv)	32.6777	

Figure S22. IR plot (Lorentzian line, 20 cm⁻¹ FWHH).



Morphological, magnetic and structural characterisation of the SAMN@As complexes

The morphology of SAMNs and SAMN@As complexes, as well as their elemental composition, was analysed by transmission electron microscopy coupled to energy-dispersive X-ray spectroscopy (TEM-EDS), as shown in Figure S23a,c. Samples were characterised by nanoparticles forming aggregates, exhibiting a spherical shape and size ranging from 10 to 20 nm. Chemical analysis by EDS confirmed the effective adsorption of As on both SAMN@As complexes (Figure S1 b,c for As^V and As^{III} complexes, respectively). Noteworthy, no change in shape or visible degradation of SAMNs were observed after arsenic adsorption, and excellent colloidal stability without visible agglomeration was maintained.

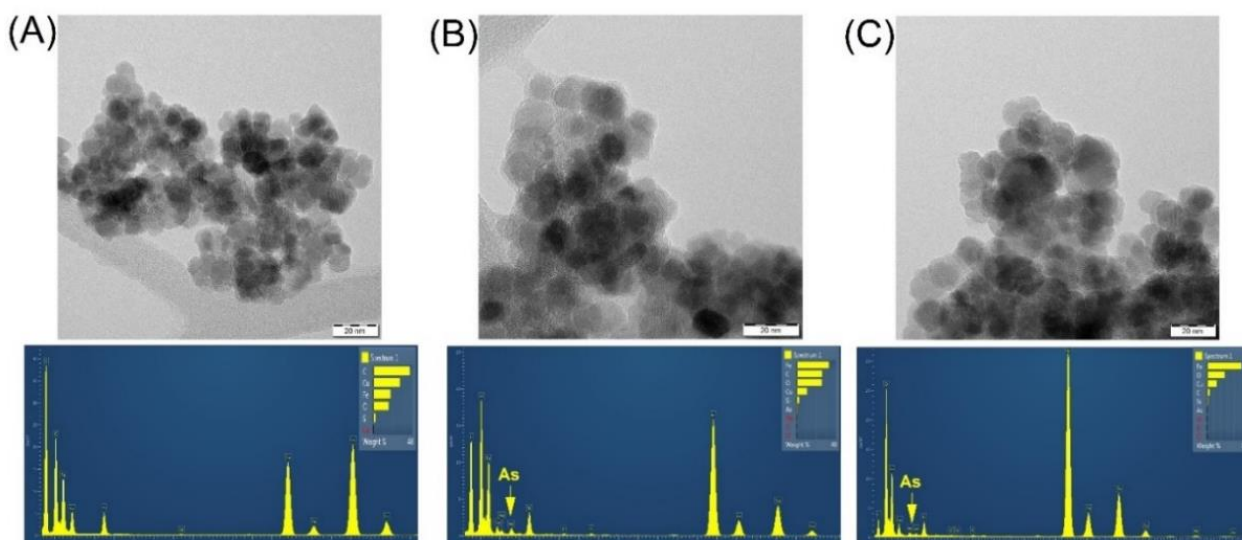


Figure S23. Representative TEM image naked SAMN, SAMN@As^{III} and SAMN@As^V complexes. A) SAMN; B) SAMN@As^{III} complex; C) SAMN@As^V complex. The EDS chemical analysis of the nanoparticles is reported under each TEM image showing the presence of arsenic adsorbed on SAMN surface.

Table S5. Parameters of the hysteresis loops of all samples, measured at temperature of 5 K and 300 K, where M_{max+} is a maximum magnetization at (50 kOe), M_{max-} is a maximum magnetization at -50 kOe, H_{C+} is a positive coercivity, H_{C-} is a negative coercivity, M_{R+} is a positive remnant magnetization and M_{R-} is a negative remnant magnetization.

Sample	T	M_{max+} (50 kOe)	M_{max-} (-50 kOe)	H_{C+}	H_{C-}	M_{R+}	M_{R-}
	(K)	(emu/g)	(emu/g)	(Oe)	(Oe)	(emu/g)	(emu/g)
SAMN@As ^{III}	5	72.32	-72.31	209.70	-278.05	19.51	-16.40
	300	60.20	-60.03	29.50	-26.40	1.89	-1.78
SAMN@As ^V	5	69.38	-69.35	200.97	-239.80	17.78	-15.29
	300	59.51	-59.58	20.39	-24.27	2.64	-2.11

Table S6. Values of the ^{57}Fe Mössbauer hyperfine parameters, derived from the least-square fitting of the room-temperature ^{57}Fe Mössbauer spectrum of the SAMN@As^{III} and SAMN@As^V sample. δ represent the isomer shift, ΔE_Q is the quadrupole splitting, B_{hf} is the hyperfine magnetic field, and RA is the spectral area of individual spectral components identified upon spectrum fitting. *Average value of B_{hf} derived from B_{hf} -distribution.

Sample	Component	$\delta \pm 0.01$ (mm/s)	$\Delta E_Q \pm 0.01$ (mm/s)	$B_{\text{hf}} \pm 0.3$ (T)	RA ± 1 (%)	Assignment
SAMN@As ^{III}	Sextet	0.31	0.00	42.1*	100	$\gamma\text{-Fe}_2\text{O}_3$ (Fe^{3+})
SAMN@As ^V	Sextet	0.32	0.00	41.6*	100	$\gamma\text{-Fe}_2\text{O}_3$ (Fe^{3+})

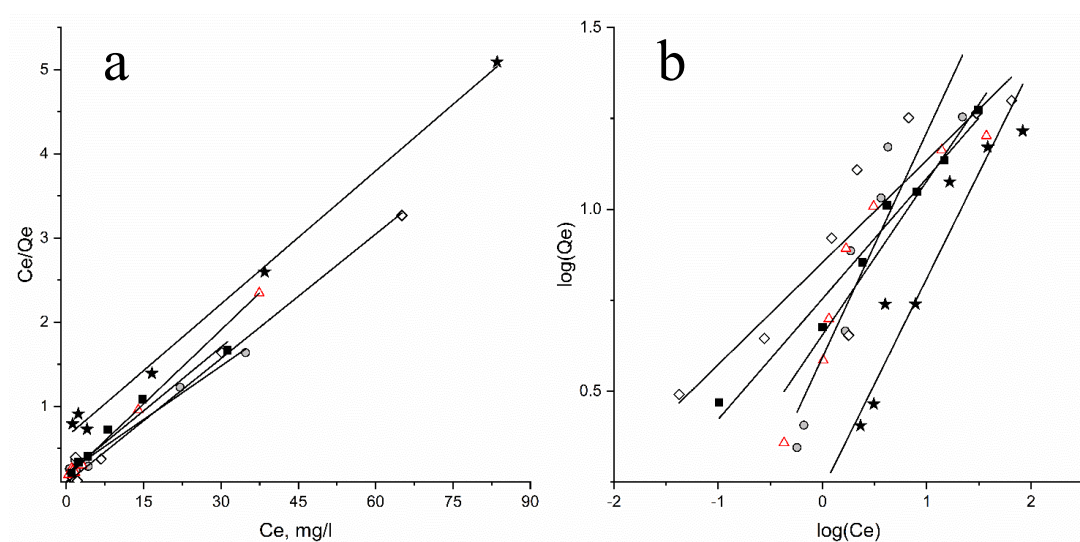


Figure S24. Linear plot of (a) Langmuir, (b) Freundlich isotherm models for As^{III} adsorption onto SAMNs. pH = 3 (black square), pH = 6 (grey circles), pH = 8 (rhombus), pH = 10 (red triangle), pH = 11 (black star).

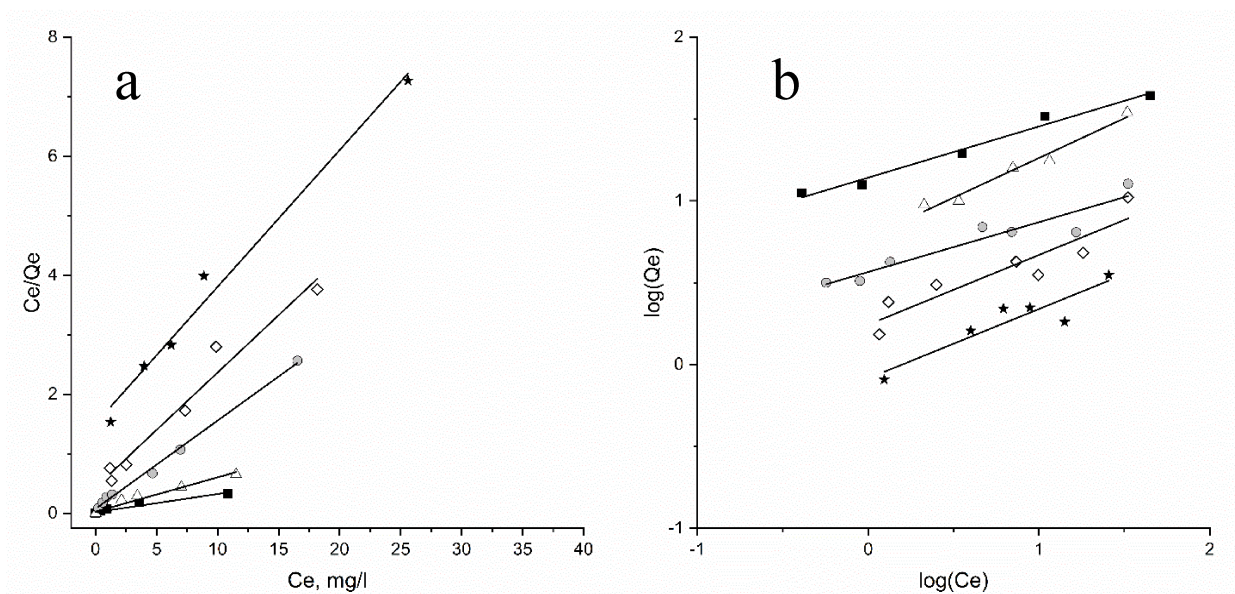


Figure S25. Linear plot of (a) Langmuir, (b) Freundlich isotherm models for As^V adsorption onto SAMNs. pH = 3 (black square), pH = 6 (grey circles), pH = 8 (rhombus), pH = 10 (red triangle), pH = 11 (black star).

Table S7. Linearised Isotherm models constants and correlation coefficients for As^V adsorption onto SAMNs.

pH	Langmuir ($C_e/q_e = 1/(q_m K_L) + C_e/q_m$)			pH	Freundlich ($\log q_e = \log K_F + (1/n)\log C_e$)		
	K_L (L mg ⁻¹)	q_m (mg/g)	R^2		K_F	$1/n$	R^2
3.0	0.56	32.52	0.94	3.0	13.90	0.31	0.98
5.0	0.48	17.33	0.97	6.0	6.85	0.48	0.97
6.0	0.53	6.75	0.99	8.0	3.68	0.30	0.89
8.0	2.27	5.19	0.96	10.0	1.75	0.43	0.85
11.0	6.56	4.35	0.99	11.0	0.82	0.42	0.85

Table S8. Linearised Isotherm models constants and correlation coefficients for As^{III} adsorption onto SAMNs.

pH	Langmuir ($C_e/q_e = 1/(q_m K_L) + C_e/q_m$)			Freundlich ($\log q_e = \log K_F + (1/n)\log C_e$)		
	K_L (L mg ⁻¹)	q_m (mg/g)	R ²	K_F	1/n	R ²
3.0	3.82	19.84	0.96	5.68	0.33	0.97
6.0	4.92	23.60	0.99	3.92	0.62	0.86
8.0	1.85	20.30	0.99	7.15	0.28	0.81
10.0	2.61	17.09	0.99	4.52	0.42	0.86
11.0	12.09	18.99	0.99	1.70	0.58	0.92

Table S9. The atomic fraction of C, O, Fe^{III} and As species of SAMNs and SAMN@As complexes obtained by XPS measurements.

Sample	C 1s	O 1s	Fe 2p	As 3d
SAMN	51.4 at. %	36.1 at. %	12.5 at. %	XXXXX
	32.61 w. %	30.51 w. %	36.88 w. %	XXXXX
SAMN@As ^{III}	35.2 at. %	45.6 at. %	18.4 at. %	0.8 at. %
	18.88 w. %	32.57 w. %	45.88 w. %	2.68 w. %
SAMN@As ^V	14.23 at. %	52.35 at. %	31.63 at. %	1.34 at. %
	5.94 w. %	29.13 w. %	61.43 w. %	3.49 w. %

7.3 Paper: Biologically safe colloidal suspensions of naked iron oxide nanoparticles for *in situ* antibiotic suppression

Colloids and Surfaces B: Biointerfaces 181 (2019) 102–111



Contents lists available at ScienceDirect

Colloids and Surfaces B: Biointerfaces

journal homepage: www.elsevier.com/locate/colsurfb



Biologically safe colloidal suspensions of naked iron oxide nanoparticles for *in situ* antibiotic suppression



Massimiliano Magro^{a,b}, Davide Baratella^a, Simone Molinari^c, Andrea Venerando^a, Gabriella Salviulo^c, Giulia Chemello^d, Ike Olivotto^d, Giorgio Zoppellaro^b, Juri Ugolotti^b, Claudia Aparicio^b, Jiri Tucek^b, Anna P. Fifi^e, Giuseppe Radaelli^d, Radek Zboril^b, Fabio Vianello^{a,*}

^a Department of Comparative Biomedicine and Food Science, University of Padua, Viale dell'Università, Legnaro, Agripolis, 35020, Italy

^b Regional Centre of Advanced Technologies and Materials, Palacky University in Olomouc, Štechtitelů, Olomouc, 78371, Czech Republic

^c Department of Geosciences, University of Padua, via Gradenigo 6, Padova, 35131, Italy

^d Department of Life and Environmental Sciences, Marche Polytechnic University, via Brece Bianche, Ancona, 60131, Italy

^e BioTecnologie BT S.r.l., Agrifood Technology Park of Umbria, Frazione Pantalla, Pantalla, 06059, Italy

ARTICLE INFO

Keywords:

Antibiotic
Oxytetracycline
Iron oxide nanoparticles
Drug suppression
Colloidal suspension

ABSTRACT

A category of naked maghemite nanoparticles ($\gamma\text{-Fe}_2\text{O}_3$), named surface active maghemite nanoparticles (SAMNs), is characterized by biological safety, high water colloidal stability and a surface chemistry permitting the binding of ligands. In the present study, the interaction between SAMNs and an antibiotic displaying chelating properties (oxytetracycline, OxyTC) was extensively structurally and magnetically characterized. OxyTC emerged as an ideal probe for providing insights into the colloidal properties of SAMNs. At the same time, SAMNs turned out as an elective tool for water remediation from OxyTC. Therefore, a dilute colloidal suspension of SAMNs was used for the removal of OxyTC in large volume tanks where, to simulate a real *in situ* application, a population of zebrafish (*Danio rerio*) was introduced. Interestingly, SAMNs led to the complete removal of the drug without any sign of toxicity for the animal model. Moreover, OxyTC immobilized on SAMNs surface resulted safe for sensitive *Escherichia coli* bacteria strain. Thus, SAMNs were able to recover the drug and to suppress its antibiotic activity envisaging their feasibility as competitive option for water remediation from OxyTC in more nature related scenarios. The present contribution stimulates the use of novel smart colloidal materials to cope with complex environmental issues.

1. Introduction

Water pollution from antibiotics is one of the most prominent environmental concern due to their massive and durable presence in the ecosystems and their bulky use [1]. Indeed, the magnitude of the worldwide use of antibiotics for human and veterinary medicine easily overcomes 100,000 tons per year [2], and most of these compounds are very stable in the environment, exerting their activity for long periods, thus granting their effects over time [3]. However, substantial differences exist among antibiotics with respect to their biological impact and, while some substances, such as penicillins, undergo rapid

degradation, some others, such as fluoroquinolones (e.g. ciprofloxacin), macrolides (e.g. tylosin) and tetracyclines, are considerably persistent, spreading wide and accumulating in high concentrations [4–6]. Oxytetracycline (OxyTC) is widely used as antibiotic and growth promoter in animal farming [7]. This drug is categorized as an emerging environmental contaminant due to its high solubility in water and elimination by treated animals through feces and urine. Systems for OxyTC remediation were already reported and its removal efficiency in current wastewater treatment plants can range from 12% [8] to 80% [9]. Among different remediation strategies, the use of granular activated carbon was almost discarded due to the difficulties of regeneration and

Abbreviations: DMSO, Dimethyl sulfoxide; EDS, electron dispersive spectroscopy; EGA, evolved gas analysis; FTIR, Fourier transform infrared spectroscopy; HAADF-STEM, high-angle annular dark-field scanning transmission electron microscopy; HPLC-MS, high-performance liquid chromatography–mass spectrometry HRTEM high-resolution transmission electron microscope; SAMNs, iron oxide nanoparticles; OxyTC, oxytetracycline; PEG, poly ethylene glycol; Q-TOF, quadrupole time of flight; RMSD, root mean square deviation; SQUID, superconducting quantum interference device; TGA, thermal gravimetric analysis; TRIS, tris(hydroxymethyl) aminomethane; XRPD, x-ray powder diffraction

* Correspondence author at: Department of Comparative Biomedicine and Food Science, University of Padua, Viale dell'Università, Legnaro, Agripolis, 35020, Italy.
E-mail address: fabio.vianello@unipd.it (F. Vianello).

<https://doi.org/10.1016/j.colsurfb.2019.05.036>

Received 13 March 2019; Received in revised form 14 May 2019; Accepted 15 May 2019

Available online 17 May 2019

0927-7765/© 2019 Elsevier B.V. All rights reserved.

the high costs [10]; aluminum oxide was also unsuitable as structural alterations occurs upon tetracycline adsorption [11]. Finally, aiming at the molecular degradation due to the scarce tolerance of tetracycline to light, direct photolysis was widely applied [12–14]. Alternatively, electrochemical oxidation was employed [15,16]. However, the main disadvantage of reported methods relies on the difficulty of application for *in-situ* remediation.

Magnetic separation strategies by nanomaterials represent desirable alternative or complementing methods for the removal of organic pollutants because nanoparticles have been demonstrated to be rapid, inexpensive, and effective tools for water purification tasks [17–20]. As a general concept, separation technologies based on magnetic particles offer the advantage of eliminating absorbed toxic compounds by the simple application of an external magnetic field. Among magnetic materials, iron oxide nanoparticles represent the gold standard. Different iron oxides, such as goethite, hematite [21] and magnetite [22], were recognized as efficient sorption systems for OxyTC due to their surface complexation chemistry. Nevertheless, despite the promising possibility offered by the thermodynamically favorable complexation by the above mentioned strong chelating agents, only rare efforts have been dedicated to the use of unmodified iron oxide nanoparticles for water remediation from OxyTC, to date [22,23]. This is not surprising as the preparation of stable colloidal suspensions of metal oxides remains an ambitious challenge for preparative nanotechnology [24]. Indeed, most iron oxide nanoparticles present scarce or absent colloidal stability and can be used exclusively upon modification with surface stabilizers. Surface modifications of nanosized iron oxides are commonly constituted of polymeric shells (i.e. dextran, polyvinyl-alcohol, polyethylene-glycol) [25], thin layers of inorganic metals (e.g. gold), nonmetals (e.g. carbon), or oxides (e.g. SiO₂) [26] or surfactants [27]. Alternatively, the surface of nanomaterials can be coated by organic shells exposing iron chelating functionalities, such as phosphate, carboxylate or catechol groups [28,29]. A different strategy for the treatment of water containing organic pollutants is given by magnetic separation developed by core-shell nanostructures and nanocomposites containing iron oxide nanoparticles as sorbents [30].

It has to be noted that the processes used for the surface modification of nanoparticles are often troublesome, time-consuming and expensive, with low yields limiting their massive applications. Furthermore, nanoparticle coatings reduce the average magnetic moment of the material by introducing a diamagnetic shell on the final product [31,32]. All these aspects should be considered for the evaluation of the competitiveness of magnetic nanoparticles for bulk water remediation.

The current study investigates on the sorption of OxyTC by synthetic maghemite nanoparticles, named SAMNs (Surface Active Maghemite Nanoparticles) and on their applicability in water remediation. SAMNs belong to an emerging category of pristine iron oxide nanomaterials, which found applications in different fields, such as recoverable catalysts [33].

Interestingly, OxyTC represented an ideal molecular probe to gather insights on the surface chemistry of SAMNs and to study their ligand binding proclivity and unique colloidal behavior. In this view, the availability and reactivity of under-coordinated Fe(III) sites at the boundary with solvent explain both SAMN affinity for OxyTC as well as their high colloidal stability, which is actually an essential requirement for water remediation processes.

2. Materials and methods

2.1. Materials

Iron(III) chloride hexahydrate (97%), sodium borohydride (NaBH₄), ammonium hydroxide solution (35% in water), dimethyl sulfoxide (DMSO) and oxytetracycline (OxyTC) were of analytical grade and were used as received from Aldrich (Sigma-Aldrich, Italy).

A series of Nd-Fe-B magnets (N35, 263–287 kJ/m³ BH, 1200 m T flux density by Powermagnet – Germany) was used for the nanoparticles control (magnetic driving and magnetic separation).

2.2. Synthesis of surface active magnetic nanoparticles

A typical synthesis of nanoparticles was already described [35] and can be summarized as follows: FeCl₃·6H₂O (10.0 g, 37 mmol) was dissolved in MilliQ grade water (800 mL) under vigorous stirring at room temperature. NaBH₄ solution (2 g, 53 mmol) in ammonia (3.5%, 100 mL, 4.86 mol mol⁻¹ Fe) was quickly added to the mixture. Soon after the reduction reaction occurrence, the temperature of the system was increased to 100 °C and kept constant for 2 h. Then, the material was cooled at room temperature and aged in water, as prepared, for other 24 h. This product was separated by imposition of an external magnet and washed several times with water. This material can be transformed into a red brown powder (final synthesis product) by drying and curing at 400 °C for 2 h. The resulting nanopowder showed a magnetic response upon exposure to a magnetic field. The final mass of product was 2.0 g (12.5 mmol) of Fe₂O₃ and a yield of 68% was calculated. The nanoparticulated resulting material resulted constituted of stoichiometric maghemite (γ-Fe₂O₃) with a mean diameter (d_{avg}) of 11 ± 2 nm, which can lead to the formation, upon ultrasound application in water (Bransonic 221, 48 kHz, 50 W, Emerson Electric Co., Ferguson, MO, USA) of a stable colloidal suspension, without any organic or inorganic coating or derivatization. The surface of these bare maghemite nanoparticles shows peculiar binding properties and can be reversibly derivatized with selected organic molecules. We called these bare nanoparticles as Surface Active Maghemite Nanoparticles (SAMNs).

2.3. Binding of oxytetracycline (OxyTC) to SAMNs

The binding of oxytetracycline to SAMNs occurred by self-assembly in water and was carried out at constant SAMN concentration (1.0 g L⁻¹) as a function of the concentration of OxyTC in the 5–100 mg L⁻¹ range, and at constant antibiotic concentration (20 mg L⁻¹) as a function of SAMN concentration in the range comprised between 0.1 and 2 g L⁻¹. The binding was followed by measuring the concentration of unbound OxyTC in water by spectrophotometry after the magnetic removal of SAMNs.

2.4. Instrumentation

2.4.1. Optical characterization by FT-IR and UV–vis spectroscopy

Fourier transform infrared (FT-IR) spectra of the dried nanoparticle samples (SAMNs and SAMN@OxyTC) were recorded using an IRAffinity-1S spectrometer (Shimadzu Corp., Kyoto, Japan) with diamond ATR analyzer and equipped with LabSolutions IR software (Shimadzu Corp., Kyoto, Japan). The scanning range was comprised between 500 and 4000 cm⁻¹ with a resolution of 4 cm⁻¹. Optical spectroscopy analysis were performed in 1 cm quartz cuvettes on a Cary 60 spectrophotometer (Varian Inc., Palo Alto, CA, U.S.A.).

2.4.2. Size-distribution and zeta-potentials

Size-distribution and zeta-potentials of SAMNs and SAMN@OxyTC were collected in water at pH 7.0 using a Zetasizer Nano particle analyser ZEN3600 (Malvern Instruments, UK) at 22 °C. Experiments were made in triplicate. Statistical analysis on the size-distribution was carried out using the LogNormal-function

2.4.3. Magnetization measurements by superconducting quantum interference device

Magnetization measurements were collected using a superconducting quantum interference device (SQUID, MPMS XL-7, Quantum Design, USA). Hysteresis loops were recorded at the

temperature of 300 K and 5 K and in a range of externally applied magnetic field comprised from -5 to $+5$ T. The zero-field-cooled (ZFC) and field-cooled (FC) magnetization curves analysis were carried out in the temperature ranging from 5 to 300 K.

2.4.4. Thermal gravimetric analysis (TGA)

Thermal gravimetric analysis (TGA) with evolved gas analysis (EGA) focused on $m/z = 18$ Da and $m/z = 44$ Da was carried out on a Netzsch STA 449C Jupiter instrument with an adapted quadrupole mass spectrometer QMS 403C Aëolos. Measurements were performed in an open α -Al₂O₃ crucible in synthetic air ($100 \text{ cm}^3 \text{ min}^{-1}$). A temperature program from 40 to 800 °C with $5 \text{ }^\circ\text{C min}^{-1}$ heating rate was used. Before each experiment, the crucibles were heated to 1340 °C and then cooled to room temperature.

2.4.5. X-ray powder diffraction (XRPD)

X-ray powder diffraction (XRPD) pattern for the SAMN@OxyTC sample was acquired at room temperature on X'Pert PRO (PANalytical, The Netherlands) instrument in Bragg-Brentano geometry with iron-filtered Co-K α radiation (40 kV, 40 mA, $\lambda = 0.1789 \text{ nm}$), equipped with an X'Celerator detector. The powdered sample was placed onto a rotating zero-background Si slide, the angular range was set as $2\theta = 3\text{--}85^\circ$, with a step size of 0.017° and scan speed of $0.0061^\circ \text{ s}^{-1}$. The identification of the crystalline phases in the experimental XRPD pattern was obtained using the X'Pert High Score Plus software.

2.4.6. Determination of OxyTC by HPLC-MS

OxyTC was determined by reversed-phase Zorbax Eclipse XDB C18 column ($4.6 \times 150 \text{ mm}$, $5 \mu\text{m}$) mounted on Agilent 1100 series HPLC system equipped with Chemstation software. The detection of the antibiotic was obtained by monitoring the signal at 360 nm in 0.8 mL min^{-1} mobile phase flow, containing 15:85 (V/V) acidified acetonitrile (0.1% phosphoric acid) and acidified water (1% phosphoric acid) filtered through a $0.45 \mu\text{m}$ nylon filter and degassed by ultra-sonication, at 25 °C. The quantitation was accomplished by using an analytical calibration curve built in the OxyTC range $20\text{--}250 \mu\text{g L}^{-1}$.

2.4.7. Animals and housing

Four hundred female zebrafish (*Danio rerio*), AB strain, were kept in four 100 L tanks equipped with biological, mechanical and UV filtration systems (Panaque, Italy) at 28 °C and subjected to a 12L:12D photoperiod. Ammonia and nitrite levels were constantly maintained below 0.01 mg L^{-1} . Water temperature, dissolved oxygen, pH, ammonia and nitrite levels were monitored daily. All procedures involving animals were conducted in compliance with Italian legislation on experimental animals and received the formal approval from the Italian Health Ministry's department of Veterinary Public Health and from the ethics committee of Università Politecnica delle Marche (Authorization N 640/2015-PR). Optimal rearing conditions were used throughout the study.

2.4.8. Fish exposure to OxyTC and SAMN@OxyTC

At the beginning of the experiments, fishes were randomly distributed in 100 L tanks and treated as follows for 28 days: Group A: control. Three 100 L tanks with 50 fish each; Group B: Three 100 L tanks added with OxyTC (4 mg L^{-1}) and SAMNs (100 mg L^{-1}) with 50 fish each. Each week $3 \times 50 \text{ mL}$ water samples were collected from the 6 tanks in order to evaluate OxyTC concentrations during the experiment.

2.4.9. Exposure of Escherichia coli (E. coli)

ATCC 25922 were inoculated in LB medium and incubated at 37 °C under agitation. The broth-culture was diluted at an optical density of $1 \times 10^8 \text{ CFU mL}^{-1}$ and used to test the following conditions: A) control for strain growth; B) 4 mg L^{-1} OxyTC; C) 2 mg L^{-1} OxyTC; D) 100 mg L^{-1} SAMNs; E) 50 mg L^{-1} SAMNs; F) 100 mg L^{-1} SAMN@

OxyTC; G) 50 mg L^{-1} SAMN@OxyTC. After 3 and 18 h incubation at 37 °C under shaking, serial dilutions (10^4 , 10^5 , 10^6 and 10^7) of each sample were plated on LB agar and CFU mL^{-1} were counted after overnight incubation at 37 °C. Each experiment was performed in triplicate.

3. Results

3.1. Characterization of SAMNs and of the SAMN@OxyTC complex in solution

In the current study, synthetic maghemite nanoparticles, named SAMNs (surface active maghemite nanoparticles) were applied [34,36,37]. SAMNs display high stability as colloidal suspensions in water without any superficial modification or coating derivatization, conversely to the other already described maghemite nanoparticles. Indeed, they show a significantly positive zeta potential at neutral pH ($\zeta = +38.7 \pm 8.7 \text{ mV}$) [36], likely a consequence of a strong interaction with water molecules acting as coordinating ligands for iron(III) sites on the nanoparticle surface as observed in the case of hydrous ferric oxides [38]. Differently, common maghemite nanomaterials at neutral pH approach the value of zero-charge, providing an explanation for their very low colloidal stability [39]. It should be considered that Patel and colleagues classified aqueous suspensions of nanoparticles as highly unstable, relatively stable, moderately stable and highly stable, with respect to the following zeta-potential (ζ) ranges: $0\text{--}\pm 10 \text{ mV}$, $\pm 10\text{--}\pm 20 \text{ mV}$ and $\pm 20\text{--}\pm 30 \text{ mV}$ and $< \pm 30 \text{ mV}$, respectively [40]. Thus, according to this scale, SAMNs suspensions can be considered as highly stable, while reported maghemite nanoparticles can be considered as unstable in water.

In order to provide an intuitive and plausible explanation of this behavior, a study on the colloidal stability of SAMNs was carried out in water and in dimethyl sulfoxide (DMSO). The latter is known to be, at the same time, a solvent and a surface stabilizer via metal ion co-ordination [41,42]. Hence, the optical spectra of colloidal suspensions of naked iron oxide nanoparticles were acquired in water and in DMSO (see Fig. 1a). The extinction coefficient of SAMNs, calculated at maximum absorbance (400 nm) in the two solvents in the range $10\text{--}100 \text{ mg L}^{-1}$ were slightly different and resulted $10.0 (\pm 0.3) \times 10^3 \text{ L mg}^{-1} \text{ cm}^{-1}$ and $17.2 (\pm 1.0) \times 10^3 \text{ L mg}^{-1} \text{ cm}^{-1}$ in water and DMSO, respectively. Thus, the dispersibility of SAMNs was assessed in the two solvents by measuring the absorbance at 400 nm as a function of nanoparticle concentration ($10\text{--}200 \text{ mg L}^{-1}$). Noteworthy, at concentrations higher than 100 mg L^{-1} , colloidal suspensions of naked SAMNs resulted more stable in DMSO than in water (see Fig. 1a, inset). Hence, the nanoparticle-solvent interactions were significantly more intense in the case of DMSO, which actually displays metal chelating properties. This simple approach confirms that iron(III) chemistry governs the colloidal properties of SAMNs. On these basis, the occurrence of an extensive coordination by water molecules on SAMN surface explains the positive value of ζ , involving positively charged $\text{OH}_2^{+0.5}$ groups, recalling the surface behavior of hydrous ferric oxide [38]. Furthermore, Rea and colleagues discriminated between labile and non-labile surface hydroxyl sites on ferrihydrites as the manifestation of different iron sites proclivity to participate at the interaction with chelating compounds [43]. Accordingly, under-coordinated iron(III) on SAMN surface are stabilized by water molecules, which can be easily substituted by other chelating molecules via ligand exchange mechanism.

3.2. The binding of oxytetracycline (OxyTC) on SAMNs

Oxytetracycline (OxyTC) was used as molecular probe to investigate the surface chemistry of SAMNs. Tetracyclines (TC) are considered strong chelating agents [44,45] and their coordination chemistry with iron(III) has been extensively investigated [46]. In particular, the

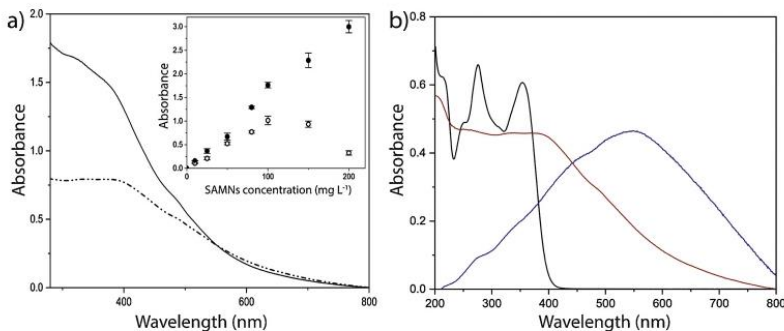


Fig. 1. Panel a) show the optical spectra of colloidal suspensions of SAMNs (100 mg L^{-1}) in water (dashed line) and in DMSO (straight line). Inset: dispersibility of iron oxide nanoparticles in water (open circles) and DMSO (black circle). Panel b) show the optical spectra of unmodified SAMNs (red), OxyTC (black) and of the SAMN@OxyTC complex (blue) in water.

stability constants of iron-TC complexes are the highest among a wide spectrum of metal ions with various oxidation states [47]. The biologically active tetracycline derivatives display several functional moieties available for complexation [48] and it is believed that their pharmacokinetic properties are correlated with this great proclivity to chelate metal ions [49].

A description of OxyTC adsorption on iron oxides, even in the absence of favorable electrostatic conditions, was provided in literature [50], outlining the surface complexation as the dominant mechanism. Indeed, the OxyTC adsorption was interpreted in terms of chelation between the divalent anion of the drug and the oxide surface [21].

The interaction between SAMNs and OxyTC was firstly studied by measuring the ζ value of the SAMN@OxyTC complex. The incubation with 20.0 mg L^{-1} OxyTC in the presence of 100 mg L^{-1} SAMNs (see next paragraph), at pH 7.0, was accompanied by a substantial reduction of the ζ value of the nanoparticles to $+6.7 \pm 2.3 \text{ mV}$ (conductivity $0.0146 \text{ mS cm}^{-1}$ in water at 22°C) [51], witnessing the immobilization of the antibiotic and confirming a ligand exchange mechanism, namely the substitution of water molecules with a polydentate chelating compound (OxyTC) on SAMN surface.

In order to appreciate the tendency of the SAMN-OxyTC system to evolve into a nanohybrid, the binding process was studied as a function of antibiotic as well as of nanoparticle concentrations. For this purpose, the response of SAMNs at a magnetic field was used for the recovery of the bound drug from the aqueous milieu and, unless otherwise indicated, the residual antibiotic concentration in solution was estimated by UV-vis spectroscopy. In Fig. 1b, the optical spectrum of OxyTC in water is reported.

The optical spectrum of OxyTC shows two absorption bands at 275 nm and 355 nm, and, aiming at the assessment of the unbound drug, two calibration curves were built. The calculated extinction coefficients of OxyTC in water were: $\epsilon_{275\text{nm}} = 12.9 \times 10^3 \text{ M}^{-1} \text{ cm}^{-1}$ and $\epsilon_{355\text{nm}} = 11.0 \times 10^3 \text{ M}^{-1} \text{ cm}^{-1}$. Moreover, the stability of OxyTC (20 mg L^{-1}) in water was checked, and after 15 days, under our experimental conditions, OxyTC degradation was estimated to be below 15%.

The binding phenomenon of OxyTC on SAMNs was studied at constant SAMN concentration (1 g L^{-1}) as a function of the concentration of OxyTC in the $5\text{--}100 \text{ mg L}^{-1}$ range, by building an adsorption isotherm (see Fig. 2a). The equilibrium between the OxyTC adsorbed on the nanoparticle surface (Q , expressed in mg OxyTC g^{-1} SAMN) and the antibiotic in solution (C_e , expressed in mg OxyTC L^{-1}) was studied according to the Langmuir model [52]. The analysis was carried out on the assumption that each binding site on nanoparticle surface acts independently of other sites [53]. In order to establish the maximum binding capacity, the Langmuir equation was applied in the form:

$$\frac{1}{Q} = \frac{1}{Q_{\max}} + \frac{1}{Q_{\max}K_L C_e}$$

where Q_{\max} is the surface concentration of bound substance at full monolayer coverage and K_L is the apparent stability constant. Q_{\max} and K_L were determined from the slope and the intercept of the linear plot $1/Q$ vs. $1/C_e$ (see Fig. 2a, inset).

As shown in Fig. 2a, the binding of OxyTC to SAMNs, depicted by plotting Q values vs. the concentration in solution of the drug, followed exponential curve rising to a maximum value ($R^2 > 0.98$), indicating that at high OxyTC concentrations the surface of nanoparticles was saturated. This suggests the completion of a monolayer formation at the Q_{\max} value. Moreover, OxyTC binding to SAMNs fits the Langmuir model ($R^2 > 0.99$), and Q_{\max} and K_L values resulted 30 mg g^{-1} and 485 mL mg^{-1} (Fig. 2a, inset). It is worth to note that the calculated stability constant, K_L , is one the highest ever reported for OxyTC binding on an iron oxide [22]. The stability of the binding is a fundamental prerequisite the applicability of materials for water remediation. In this regard, in order to provide a deeper insight into the interaction between OxyTC and SAMNs, as well as to further validate the stability of the binding, OxyTC releasing experiments were carried out.

Efforts to release the antibiotic from SAMN surface were performed using absolute ethanol and $0.5 \text{ M NH}_4\text{OH}$, which represent conditions already used for the releasing of organic molecules from these iron oxide nanoparticles, and resulted unsuccessful [54,55]. A partial OxyTC release was observed after increasing NH_4OH concentration to 2 M , combined with a prolonged overnight incubation. Intriguingly, this partial release resulted dependent on the concentrations of SAMNs and OxyTC used for the formation of the complex. For instance, when the complex formation was obtained employing 1 g L^{-1} SAMN and 5 mg L^{-1} OxyTC, the release in $2 \text{ M NH}_4\text{OH}$ was below 40%. Hence, the binding of OxyTC on SAMNs was studied at constant antibiotic concentration (20 mg L^{-1}) and in the presence of nanoparticles in the concentration range comprised between 0.1 and 2 g L^{-1} . The self-assembly of the complex was observed in the whole SAMN concentration range, as witnessed by the progressive decrease of soluble OxyTC. The complete disappearance of the OxyTC in solution was accomplished at 2 g L^{-1} SAMNs. Noteworthy, the amount of bound OxyTC normalized for SAMN concentration (Q , expressed as OxyTC to SAMN mass ratio, in mg g^{-1}) decreased with the nanoparticle concentration roughly following an exponential trend (see Fig. 2b). The maximum amount of OxyTC on SAMNs surface, calculated at the lowest SAMN concentration (100 mg L^{-1}), was 65 mg g^{-1} SAMN. The concentration value of 100 mg L^{-1} SAMN is the maximum of the nanoparticle dispersibility observed in water (see Fig. 1a, previous paragraph). At this concentration, we observed the maximum available SAMN surface exposed to the solvent, and, as consequence, the maximum antibiotic to SAMNs mass ratio. At higher SAMN concentrations, OxyTC binding tends to decrease due to nanoparticle clustering leading to a reduction of the available surface. In this view, according to the maximum amount of bound OxyTC and to the total surface area of SAMNs obtained by Brunauer-Emmett-Teller (BET) analysis [54], the surface density of the

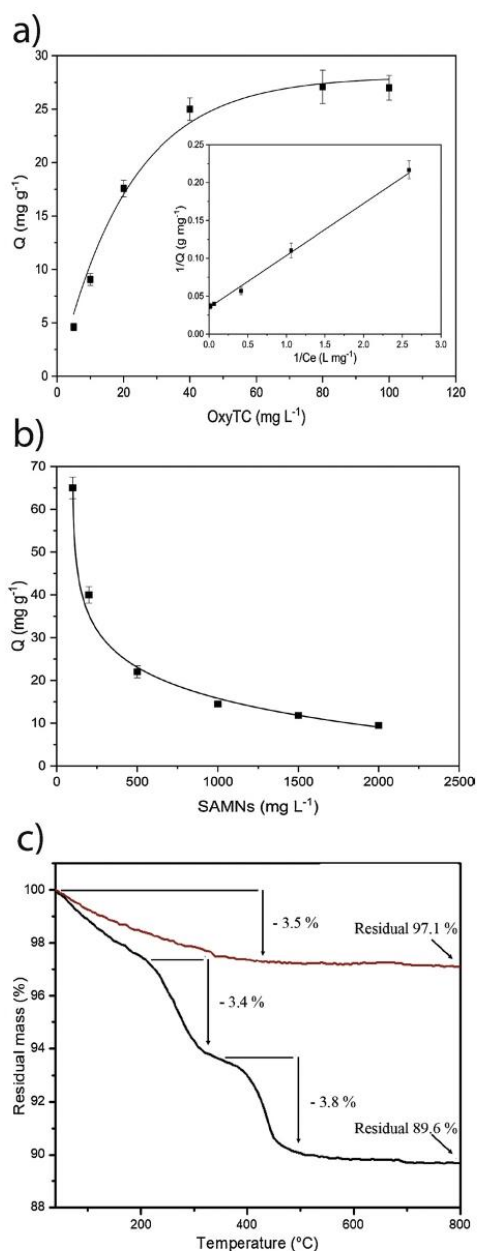


Fig. 2. Panel a) show the adsorption isotherm of the binding of OxyTC on SAMNs. Q , expressed in mg OxyTC g^{-1} SAMN, represents the amount of OxyTC adsorbed on the SAMN surface and C_e , expressed in mg OxyTC L^{-1} , is the antibiotic concentration in solution. **Inset:** linearization of the Langmuir isotherm. Panel b) show the binding of OxyTC on SAMNs at constant antibiotic concentration (20 mg L^{-1}) as a function of the concentration of SAMNs. Panel c) shows the thermogravimetric (TGA) analysis of the SAMN@OxyTC complex. Neat iron oxide nanoparticles (SAMN, red line) are compared to SAMN@OxyTC (black line).

antibiotic on SAMN was calculated and corresponded to about 2 molecules nm^{-2} . Taking into account that the distribution of iron(III) sites on SAMNs can be schematized as a square grid with a side length of $0.39 \pm 0.09 \text{ nm}$ [36,56,57], whose nodes are occupied by iron(III) sites, the calculated value of OxyTC surface density reflected the saturation of all the available binding sites on the SAMN surface, considering that the antibiotic is anchored via binuclear surface complexation (see hereafter). This, according to OxyTC structure (see below), led to monolayer on SAMN surface with a close packed geometry.

The organic phase in the SAMN@OxyTC complex under the above reported conditions was estimated by thermal gravimetric analysis (TGA) in comparison with naked SAMNs, evidencing a total weight loss at $800 \text{ }^{\circ}\text{C}$ of 2.9% for SAMNs and 10.4% for the oxytetracycline loaded material (Fig. 2c). Upon increasing the temperature from 40 to ca. $200 \text{ }^{\circ}\text{C}$, a similar weight loss was recorded for both SAMNs and SAMN@OxyTC, which can be attributed to the release of adsorbed water. This was substantiated by evolved gas analysis (EGA), in which the production of a gas at $m/z = 18 \text{ Da}$ was observed. A weight loss was observed for SAMN@OxyTC at about $250 \text{ }^{\circ}\text{C}$ (3.4%) and $450 \text{ }^{\circ}\text{C}$ (3.8%). EGA measurements showed the involvement of H_2O at $m/z = 18$ and CO_2 at $m/z = 44 \text{ Da}$. Thus, the thermal assays of SAMN@OxyTC estimated a total amount of the organic component of about 7.0%, in good very agreement with the estimate by UV–vis spectroscopy [51].

The SAMN@OxyTC complex was characterized by high resolution transmission electron microscopy (HR-TEM) as reported in Fig. 3a, revealing the formation of a core-shell structure. The organic layer thickness ($\sim 2 \text{ nm}$) was compatible with the size of an OxyTC molecule bound onto the SAMN surface, further confirming the formation of an organic layer. The STEM-HAADF image (Fig. 3b) complemented by electron dispersive spectroscopy (EDS) (Fig. 3g) with chemical mapping of SAMN@OxyTC further showed the distribution of elemental oxygen (Fig. 3e), iron (Fig. 3d), carbon (Fig. 3c), iron (Fig. 3d) and the elemental overlay of FeC (Fig. 3f). The retention of the superparamagnetic properties in SAMN@OxyTC nanoparticles, $T_{\text{irreversible}}$ of 241 K with blocking temperature T_b of 140 K, has been observed by recording the variation of the magnetic properties (magnetic moment, M) vs temperature (T) in field-cooled (FC) and zero-field-cooled experiments (H_{ex} of 1000 Oe applied field). The resulting traces are shown in Fig. 3i (M of 29.9 emu/g at 5 K in FC and M of 24.6 emu/g at 5 K in ZFC).

The size of the SAMN@OxyTC complex, in comparison with naked SAMNs, was determined by dynamic light scattering: the size distribution plot and the statistical analysis by Log-normal functions are given in Fig. 3h. The hydrodynamic size of nanoparticles increased substantially from naked SAMNs ($d_{\text{mean}} = 114.9 \pm 0.95 \text{ nm}$) to SAMN@OxyTC ($d_{\text{mean}} = 239.9 \pm 2.34 \text{ nm}$).

In the nano-sized domain, the crystal truncation at the boundary with solvent forces the surface atoms to adjust their coordination environment and generate dangling bonds, which promote ligand adsorption. Ideally, the surface restoration of nanostructured highly crystalline metal oxides displaying colloidal stability and size below 20 nm, can be testified by the modification of their UV–vis spectrum [58]. In this view, SAMNs, composed of maghemite characterized by proper size and colloidal stability, represent an exemplary paradigm for this theory, and optical spectroscopy was already used to investigate the surface re-organization in the presence of several ligands [54,55,59]. As reported in Fig. 1b, UV–vis spectrum of SAMNs shows a wide band with a maximum at about 400 nm. Differently, the spectrum of the SAMN@OxyTC complex was characterized by a peak at 550 nm and (see Fig. 1b, blue line). The observed shift and change in the absorption envelope (shape) of SAMN spectrum upon OxyTC binding was observed with other biomolecules following their interaction with the nanoparticle surface in analogy with previous reported results [54,55,59].

The basic skeleton of tetracyclines is characterized by a fused 4 carbocyclic linear structure (see inset of Fig. 4a, inset b), exposing a

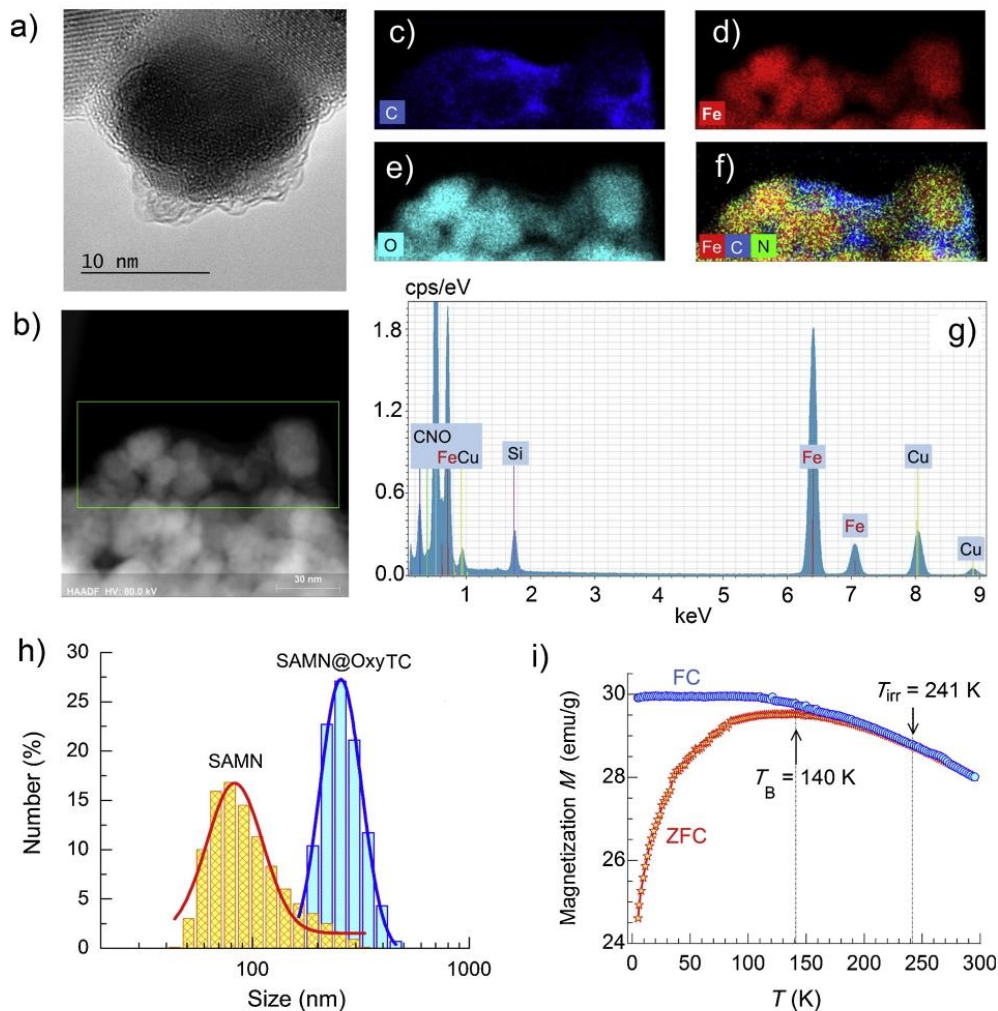


Fig. 3. Panel a) show the high-resolution transmission electron microscopy (HR-TEM) image of the SAMN@OxyTC complex. Panel b) show the STEM-HAADF image and panel g) the Electron dispersive spectroscopy (EDS) analysis (green-rectangle in panel b). The elemental distributions images are given for carbon in panel c), iron in panel d), oxygen in panel e), and the elemental overlay of FeC in panel f). Panel h) shows the DLS analysis performed in water at room temperature for bare SAMN (orange) and SAMN@OxyTC complex (blue) expressed in the form of Number (%) versus hydrodynamic size (d, nm). Panel i) shows the FC-ZFC magnetic responses (H_{ex} of 1000 Oe) of the SAMN@OxyTC complex.

variety of functional groups. In particular, the features responsible of the antibiotic activity include the (α) stereochemical configurations at the 4a, 12a (A–B ring junction), a dimethylamino group in position 4, and the keto-enol system (positions 11, 12, and 12a) in proximity to the phenolic D ring [60]. Hence, aiming to shed light into the chemical groups involved into the binding with SAMNs, FT-IR was employed as an informative technique. Clear differences emerged from the superimposition of vibrational profiles of bare iron oxide nanoparticles and SAMN@OxyTC (Fig. 4a). Besides the presence of the strong typical vibrations of iron-oxide (Fe–O) around 530 cm^{-1} , which highlights the integrity of the iron oxide nanoparticle in the nanohybrid, an additional cluster of sharp signals appeared in the $1000\text{--}1250\text{ cm}^{-1}$ region of the SAMN@OxyTC spectrum (marked at 1020 cm^{-1} , 1120 cm^{-1} and 1240 cm^{-1} in the Fig. 4a, inset a). These represent the signatures of the C–H/C–OH and C–C ring twisting components of the antibiotic

backbone. Nevertheless, the most characteristic tetracycline signals, which occurred in the wavelength region from $1200\text{ to }1800\text{ cm}^{-1}$, were not observable in the SAMN@OxyTC vibrational spectrum. This can be ascribed to the participation of both A and BCD chelating moieties to the coordination of iron(III) sites on SAMN surface. The phenomenon behind such an alteration of OxyTC infrared profile, was already described for ferric oxyhydroxide and correlated to a binding mechanism named binuclear surface complexation; namely, a multiple point binding involving both A and BCD rings of OxyTC and two iron (III) sites [38,61,62].

It should be considered that OxyTC, due to the extensively commented chelating activity, is often responsible for the degradation of metal oxides, via a process known as “ligand promoted dissolution” [38]. This chemical reactivity actually frustrates the attempts of using metal oxides for removing OxyTC from the environment [11].

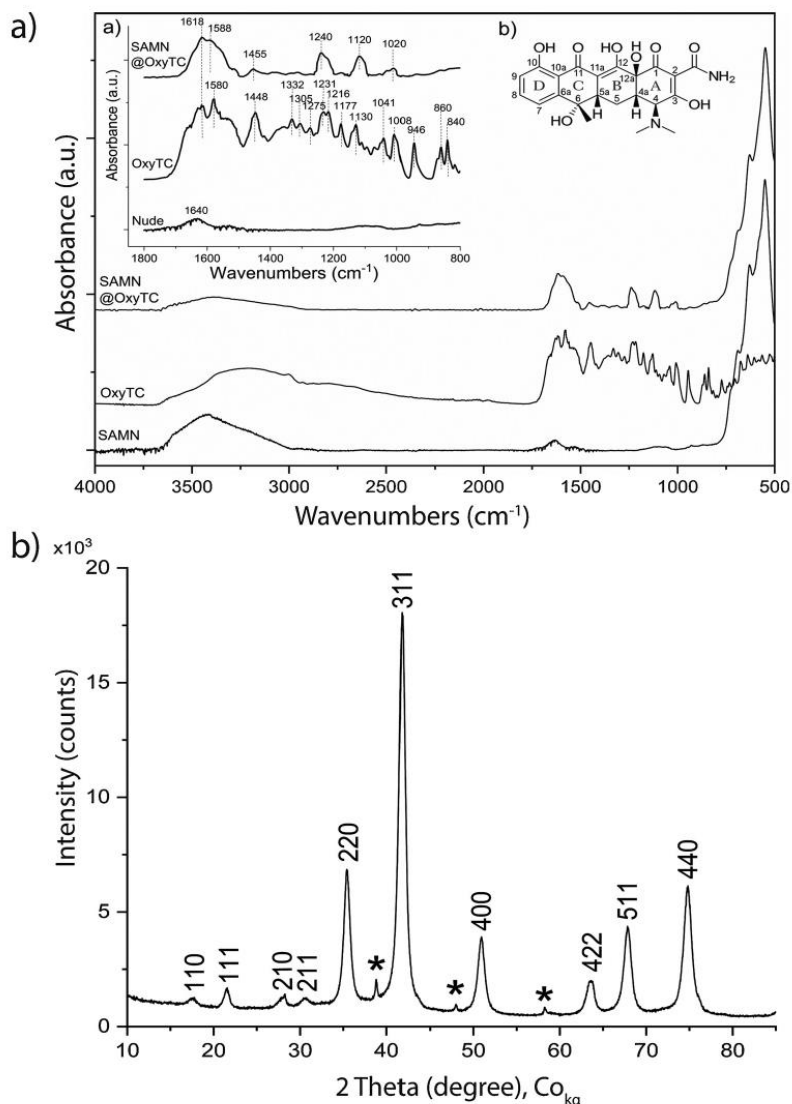


Fig. 4. Panel a) show the FT-IR spectrum of the SAMN@OxyTC complex. Inset: a) differences between naked SAMNs and SAMN@OxyTC in the region 800–1800 cm⁻¹; b) structure of the OxyTC molecule. Panel b) shows the X-Ray Powder Diffraction Pattern (CoK α radiation) of SAMN@OxyTC complex. The numbers are the Miller indices for maghemite (bold). The hematite contribution (*) is found below 5% w/w.

Therefore, in order to evidence any structural alteration of SAMNs upon OxyTC binding and long incubation in water, X-ray powder diffraction (XRPD) was also acquired before and after OxyTC binding, followed by 30 days storage in water. XRPD analysis showed that the SAMN@OxyTC complex remained composed by the maghemite-phase (see Fig. 4b). Therefore, this characterization demonstrated the robustness of SAMNs upon interaction with OxyTC and long-term storage.

From the above reported measurements, it can be concluded that SAMNs effectively and strongly bind OxyTC by the formation of a metal-chelating complex (binuclear surface complexation) with the surface exposed iron(III) sites. Their crystalline structure was preserved upon OxyTC binding and their highest loading capacity coincided with

their highest dispersibility value in water (100 mg L⁻¹). Furthermore, OxyTC emerged as useful tool for characterizing the surface chemistry of SAMNs, envisaging an analogy with the behavior of hydrous oxides.

3.3. Evaluation of the applicability of SAMNs for water remediation

The introduction of nanomaterials in the environment could lead adverse effects on higher organisms [63]. Thus, the applicability of SAMNs for the sequestration of OxyTC was tested in large volume tanks (100 L) in the absence and in the presence of zebrafish (*Danio rerio*, 50 fishes) as animal model. The concentration of soluble OxyTC (4 mg L⁻¹) in water was monitored by HPLC-MS as described in Methods over 28

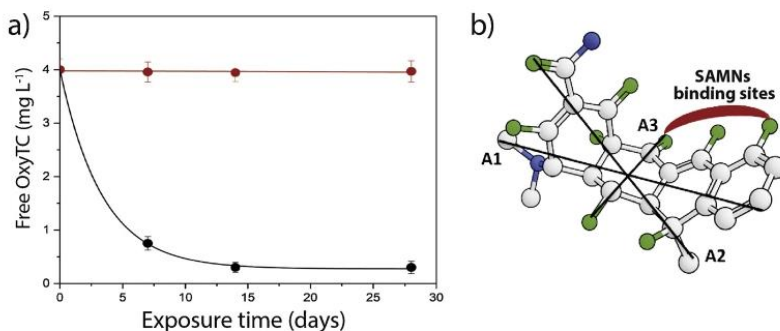


Fig. 5. Panel a) show the tridimensional structure of the oxytetracycline molecule with the representation of three different spatial axes. Panel b) show the Sequestration of OxyTC by iron oxide nanoparticles in water. Red: OxyTC concentration in water; Black: OxyTC concentration in the presence of 100 mg L^{-1} iron oxide nanoparticles. Panel c) show the Growth of *E. coli* in LB medium after 3 and 18 h of incubation at 37°C .

days (Fig. 5a) in the presence of 100 mg L^{-1} SAMNs. The latter represents an unusual value for water remediation tasks, namely a nanoparticle concentration two orders of magnitude lower than reported studies [19]. At the same time, the concentration of OxyTC was selected as a typical drug dosage for the application in fish farming.

The mere introduction of SAMNs in the farming water determined a progressive reduction of the concentration of soluble OxyTC, leading to an antibiotic concentration below the limit of instrumental detection after 14 days, and demonstrating the ability of these bare iron oxide nanoparticles in zeroing OxyTC in aquatic environment (Fig. 5a). The drug concentration decreased following an exponential decay and the corresponding half-life in solution was about 3 days. Furthermore, no sign of toxic effect was evidenced in comparison with a population of zebrafish used as control. Moreover, the fate and the potential ecotoxic effects of SAMN@OxyTC were studied in terms of their environmental risks.

Bacteria play a key role in aquatic ecosystems, where they degrade and uptake carbon from the DOC pool, and their biomass forms the basis of the aquatic food web; in addition, several bacteria species are involved in element cycles that represents the starting point for living aquatic organisms. However, bacterial communities are sensitive to disturbances, and alterations in community productivity and abundance may deeply affect the whole ecosystem [64].

At date, data on ecotoxicity of synthetic nanoparticles and especially on metal oxide ones, except nanoTiO₂, are rare [65,69]. As water is an essential compartment in ecosystems and is the main route for pollutant migration, the data on fate of synthetic nanoparticles as well as their potential ecotoxic effects are essential for evaluation of the environmental risks of nanotechnologies [59–63].

SAMNs aroused interest as competitive options for biotechnological issues, hence their cytotoxicity was extensively investigated *in vitro* on eukaryotic cells, such as HeLa cells [71], mesenchymal stromal cells (MSCs) from rat and human [72], mesenchymal stem cells from horse peripheral blood [36] and on prokaryotic cells, such as *Salmonella typhimurium* [37] and *Pseudomonas fluorescens* [73].

In the present study, SAMNs were applied for evaluating the effect of microorganisms upon interaction with an antibiotic (OxyTC), and *E. coli* ATCC 25922 was used as oxytetracycline sensitive strain model. Microorganism growth was tested in the presence of different concentrations of OxyTC, iron oxide nanoparticles and SAMN@OxyTC. Table 1 shows the growth of *E. coli* under different conditions after 3 and 18 h incubation at 37°C . In particular, *E. coli* cultures were treated with OxyTC (2 and 4 mg mL^{-1}) and iron oxide nanoparticles (50 and 100 mg mL^{-1}). As expected, OxyTC completely suppressed *E. coli* growth. Conversely, as previously described for other iron oxide nanoparticles [67], SAMNs did not inhibit the growth of the microorganism. Moreover, no interference on *E. coli* growth was observed when OxyTC was immobilized on SAMN surface, evidencing that the antibiotic binding was accompanied by the loss of the toxicity toward

Table 1
Growth of *E. coli* in LB medium after 3 and 18 h of incubation at 37°C .

Group	Experimental condition	Growth (CFU mL ⁻¹) of <i>E. coli</i> after incubation	
		3 h	18 h
A	control	1.3×10^8	2.5×10^9
B	4 mg L^{-1} OxyTC	0	0
C	2 mg L^{-1} OxyTC	0	0
D	100 mg L^{-1} iron oxide nanoparticles	3.0×10^7	1.0×10^9
E	50 mg L^{-1} iron oxide nanoparticles	7.4×10^7	2.2×10^9
F	100 mg L^{-1} SAMN@OxyTC	1.6×10^8	1.7×10^9
G	50 mg L^{-1} SAMN@OxyTC	2.0×10^8	2.0×10^8

the bacteria. This further substantiated the applicability of SAMNs for OxyTC water remediation, where the absence of SAMN@OxyTC cytotoxicity can be attributed to the high stability of the complex. In addition, SAMN porosity can provide useful insights on the OxyTC adsorption phenomenon and, more specifically, on the drug masking from the interaction with the biological interfaces.

According to Horváth-Kawazoe (HK) method, using N₂ adsorption measurements at 77 K, SAMNs can be considered a porous material with a pore diameter spanning from 2.0 to 0.6 nm. [55].

Taking into account OxyTC geometry, three spatial dimensions can be depicted and considered as the molecule length, height and width (A1, A2 and A3 axes in Fig. 5b) measuring 1.1, 0.9 and 0.5 nm respectively. Considering the adsorbate molecule rotating around the A1 axis and parallel to the pore wall, with the planar BCD chromophore pointing to the deep of the cavity and the non-reactive dimethylamino side pointing outside the pore, it is possible to conclude that even for the pores of smallest size, nanoparticle porosity is suitable for hosting the drug. Furthermore, a distinct value of Van der Waals (VDW) volume can be assessed by the conformational analysis, as evidenced by negligible differences within a set of twelve possible drug conformers ($\sigma = 4.4 \cdot 10^{-3} \text{ nm}^3$). Hence, the theoretical mass ratio of OxyTC entrapped on nanoparticle pores, was calculated considering the antibiotic (VDW) average volume (0.4 nm^3) and nanoparticle cumulative pore volume ($24 \times 10^{18} \text{ nm}^3 \text{ g}^{-1}$ SAMN). The value resulted of 46.4 mg g^{-1} SAMN, in agreement with the surface amount of OxyTC at the full monolayer coverage calculated according to Langmuir isotherm model as well as assessed by thermal gravimetric analysis (TGA). These findings suggest that nanoparticle porosity can entrap the antibiotic, providing a protection for microorganisms.

4. Conclusions

Iron oxide nanomaterials represent an interesting option for environmental remediation tasks. Nevertheless, the use of massive

amounts of nanoparticles seems to be a common, unavoidable drawback behind their promising applicability. In particular, the employment of these attracting nanomaterials could become a paradox for two main reasons: firstly, the syntheses of nanomaterials could involve consumption of organic solvents, high costs, and a heavy impact on the environment. Secondly, and most importantly, even in the case of biologically safe nanoparticles, their high concentrations combined to their scarce stability in water make them lethal due to their mere physical impact on aquatic organisms [68]. Therefore, in real world scenarios large-scale exploitation of nanoparticles is a matter of concern as it could represent itself a source of direct or indirect hazard. Herein, a colloidal, multifaceted nanomaterial was presented and successfully applied *in vitro* and in an *in-situ* simulation for the suppression of the antibiotic activity of OxyTC.

Indeed, a suspension of 100 mg L^{-1} SAMN was able to capture the drug in large, not agitated tanks in the presence of zebrafish with no sign of adverse outcome on the animal model. Moreover, the docking of OxyTC on SAMN surface induces the loss of the drug efficacy as substantiated by the absence of lethality on sensitive bacterial strains (*Escherichia coli*), and the drug emerged as elective probe for SAMN surface, whose chemistry recalls hydroxous ferric oxides. Finally, due to the preserved structural features, even OxyTC degradation products are supposed to follow the same fate of the native drug [75], and studies are in progress.

The present contribution highlights the importance of understanding the nanoparticle colloidal and surface properties in the view of their interplay with the biological counterparts, as well as envisages competitive tools applicable in real world scenarios.

Fundings

Authors gratefully acknowledge CARIPARO Foundation, Italy, and the excellence department project of the Italian Ministry of Education, University and research (MIUR) "Centro di Eccellenza per la Salute degli Animali Acquatici – ECCE AQUA" for the support. Moreover, authors gratefully acknowledge the support of the Nanomaterials and Nanotechnologies for Environment Protection and Sustainable Future (NanoEnviCz, LM2015073) and the project LO1305 of the Ministry of Education, Youth and Sports of the Czech Republic. Finally, authors would like to thank Biotecnologie BT S.r.l. for supporting a GC PhD.

Ethics

Experiments on animals were carried out in accordance with the EU Directive 2010/63/EU, and were authorized by the Italian Health Ministry's department of Veterinary Public Health and from the ethics committee of Università Politecnica delle Marche (Authorization N 640/2015-PR).

Declarations of interest

None.

References

- R. Coyne, P. Smith, C. Moriarty, The fate of oxytetracycline in the marine environment of a salmon cage farm, *Mar. Environ. Heal. Ser.* (2001).
- R. Wise, Antimicrobial resistance: priorities for action, *J. Antimicrob. Chemother.* 49 (2002) 585–586, <https://doi.org/10.1093/jac/49.4.585>.
- A. De La Torre, I. Iglesias, M. Carballo, P. Ramírez, M.J. Muñoz, An approach for mapping the vulnerability of European Union soils to antibiotic contamination, *Sci. Total Environ.* 414 (2012) 672–679, <https://doi.org/10.1016/j.scitotenv.2011.10.032>.
- P.A. Blackwell, A.B.A. Boxall, P. Kay, H. Noble, Evaluation of a lower tier exposure assessment model for veterinary medicines, *J. Agric. Food Chem.* 53 (2005) 2192–2201, <https://doi.org/10.1021/jf049527b>.
- J.S. Lin, H.Y. Pan, S.M. Liu, H.T. Lai, Effects of light and microbial activity on the degradation of two fluoroquinolone antibiotics in pond water and sediment, *J. Environ. Sci. Heal. Part B Pestic. Food Contam. Agric. Wastes.* 45 (2010) 456–465, <https://doi.org/10.1080/03601231003800222>.
- G. Hamscher, S. Sczesny, H. Höper, H. Nau, Determination of persistent tetracycline residues in soil fertilized with liquid manure by high-performance liquid chromatography with electrospray ionization tandem mass spectrometry, *Anal. Chem.* 74 (2002) 1509–1518, <https://doi.org/10.1021/ac015588m>.
- K. Holmström, S. Gräslund, A. Wahlström, S. Pongshompoo, B.E. Bengtsson, N. Kautsky, Antibiotic use in shrimp farming and implications for environmental impacts and human health, *Int. J. Food Sci. Technol.* 38 (2003) 255–266, <https://doi.org/10.1046/j.1365-2621.2003.00671.x>.
- A.L. Spongberg, J.D. Witter, Pharmaceutical compounds in the wastewater process stream in Northwest Ohio, *Sci. Total Environ.* 397 (2008) 148–157, <https://doi.org/10.1016/j.scitotenv.2008.02.042>.
- K.G. Karthikeyan, M.T. Meyer, Occurrence of antibiotics in wastewater treatment facilities in Wisconsin, USA, *Sci. Total Environ.* 361 (2006) 196–207, <https://doi.org/10.1016/j.scitotenv.2005.06.030>.
- R. Crisafulli, M.A.L. Milhome, R.M. Cavalcante, E.R. Silveira, D. De Keukeleire, R.F. Nascimento, Removal of some polycyclic aromatic hydrocarbons from petrochemical wastewater using low-cost adsorbents of natural origin, *Bioresour. Technol.* 99 (2008) 4515–4519, <https://doi.org/10.1016/j.biortech.2007.08.041>.
- W.-R. Chen, C.-H. Huang, Adsorption and transformation of tetracycline antibiotics with aluminum oxide, *Chemosphere.* 79 (2010) 779–785, <https://doi.org/10.1016/j.chemosphere.2010.03.020>.
- Y. Chen, H. Li, Z. Wang, T. Tao, D. Wei, C. Hu, Photolysis of Chlorotetracycline in aqueous solution: kinetics, toxicity and products, *J. Environ. Sci. China (China)* 24 (2012) 254–260, [https://doi.org/10.1016/S1001-0742\(11\)160775-4](https://doi.org/10.1016/S1001-0742(11)160775-4).
- S. Jiao, S. Zheng, D. Yin, L. Wang, L. Chen, Aqueous oxytetracycline degradation and the toxicity change of degradation compounds in photoradiation process, *J. Environ. Sci. China (China)* 20 (2008) 806–813, [https://doi.org/10.1016/S1001-0742\(08\)62130-0](https://doi.org/10.1016/S1001-0742(08)62130-0).
- S. Jiao, S. Zheng, D. Yin, L. Wang, L. Chen, Aqueous photolysis of tetracycline and toxicity of photolytic products to luminescent bacteria, *Chemosphere.* 73 (2008) 377–382, <https://doi.org/10.1016/j.chemosphere.2008.05.042>.
- A. Rossi, V.A. Alves, L.A. Da Silva, M.A. Oliveira, D.O.S. Assis, F.A. Santos, R.R.S. De Miranda, Electrooxidation and inhibition of the antibacterial activity of oxytetracycline hydrochloride using a RuO₂ electrode, *J. Appl. Electrochem.* 39 (2009) 329–337, <https://doi.org/10.1007/s10800-008-9676-2>.
- M. Miyata, I. Ihara, G. Yoshid, K. Toyod, K. Umetsu, Electrochemical oxidation of tetracycline antibiotics using a Ti/IrO₂ anode for wastewater treatment of animal husbandry, *Water Sci. Technol.* 63 (2011) 456–461, <https://doi.org/10.2166/wst.2011.243>.
- S.C.N. Tang, L.M.C. Lo, Magnetic nanoparticles: essential factors for sustainable environmental applications, *Water Res.* 47 (2013) 2613–2632, <https://doi.org/10.1016/j.watres.2013.02.039>.
- P. Plachtová, Z. Medřiková, R. Zbořil, J. Tuček, R.S. Varma, B. Maršálek, Iron and iron oxide nanoparticles synthesized with green tea extract: differences in ecotoxicological profile and ability to degrade malachite green, *ACS Sustain. Chem. Eng.* 6 (2018) 8679–8687, <https://doi.org/10.1021/acssuschemeng.8b00986>.
- Z. Markova, P. Novak, J. Kaslik, P. Plachtova, M. Brazdova, D. Jancula, K.M. Siskova, L. Machala, B. Marsalek, R. Zboril, R. Varma, Iron(II,III)-polyphenol complex nanoparticles derived from green tea with remarkable ecotoxicological impact, *ACS Sustain. Chem. Eng.* 2 (2014) 1674–1680, <https://doi.org/10.1021/sc5001435>.
- S.K. Mwilu, E. Siska, R.B.N. Baig, R.S. Varma, E. Heithmar, K.R. Rogers, Separation and measurement of silver nanoparticles and silver ions using magnetic particles, *Sci. Total Environ.* 472 (2014) 316–323, <https://doi.org/10.1016/j.scitotenv.2013.10.077>.
- R.A. Figueroa, A.A. Mackay, Sorption of oxytetracycline to iron oxides and iron oxide-rich soils, *Environ. Sci. Technol.* 39 (2005) 6664–6671, <https://doi.org/10.1021/es048044l>.
- S. Rakshit, D. Sarkar, E. Elzinga, P. Punamiya, R. Datta, Surface Complexation of Oxytetracycline by Magnetite: Effect of Solution Properties, 13 (2014), <https://doi.org/10.2136/vzj2013.08.0147>.
- I. Ihara, K. Toyoda, N. Beneragama, K. Umetsu, Magnetic separation of antibiotics by electrochemical magnetic seeding, *J. Phys. Conf. Ser.* 156 (2009), <https://doi.org/10.1088/1742-6596/156/1/012034>.
- L. Xiao, J. Li, D.F. Brougham, E.K. Fox, N. Feliu, A. Bushmelev, A. Schmidt, N. Mertens, F. Kiessling, M. Valldor, B. Fadeel, S. Mathur, Water-soluble superparamagnetic magnetite nanoparticles with biocompatible coating for enhanced magnetic resonance imaging, *ACS Nano* 5 (2011) 6315–6324, <https://doi.org/10.1021/nn201348s>.
- A.K. Gupta, M. Gupta, Synthesis and surface engineering of iron oxide nanoparticles for biomedical applications, *Biomaterials.* 26 (2005) 3995–4021, <https://doi.org/10.1016/j.biomaterials.2004.10.012>.
- W. Wu, Q. He, C. Jiang, Magnetic iron oxide nanoparticles: synthesis and surface functionalization strategies, *Nanoscale Res. Lett.* 3 (2008) 397–415, <https://doi.org/10.1007/s11671-008-9174-9>.
- L.H. Reddy, J.L. Arias, J. Nicolas, P. Couvreur, Magnetic nanoparticles: design and characterization, toxicity and biocompatibility, pharmaceutical and biomedical applications, *Chem. Rev.* 112 (2012) 5818–5878, <https://doi.org/10.1021/cr300068p>.
- D. Portet, B. Denizot, E. Rump, J.-J. Lejeune, P. Jallet, Nonpolymeric coatings of iron oxide colloids for biological use as magnetic resonance imaging contrast agents, *J. Colloid Interface Sci.* 238 (2001) 37–42, <https://doi.org/10.1006/jcis.2001.7500>.
- D.I. Kreller, G. Gibson, W. Novak, G.W. Van Loon, J.H. Horton, Competitive adsorption of phosphate and carboxylate with natural organic matter on hydrous iron

- oxides as investigated by chemical force microscopy, *Colloids Surfaces A Physicochem. Eng. Asp.* 212 (2003) 249–264, [https://doi.org/10.1016/S0927-7757\(02\)00325-4](https://doi.org/10.1016/S0927-7757(02)00325-4).
- [30] A.M. Gutierrez, T.D. Dziubla, J.Z. Hilt, Recent advances on iron oxide magnetic nanoparticles as sorbents of organic pollutants in water and wastewater treatment, *Rev. Environ. Health* 32 (2017) 111–117, <https://doi.org/10.1515/reveh-2016-0063>.
- [31] D.L.J. Thorek, A.K. Chen, J. Czupryna, A. Tsourkas, Superparamagnetic iron oxide nanoparticle probes for molecular imaging, *Ann. Biomed. Eng.* 34 (2006) 23–38, <https://doi.org/10.1007/s10439-005-9002-7>.
- [32] M.E. Mackay, A. Tuteja, P.M. Duxbury, C.J. Hawker, B. Van Horn, Z. Guan, G. Chen, R.S. Krishnan, General strategies for nanoparticle dispersion, *Science* 311 (2006), <https://doi.org/10.1126/science.1122225> 1740 LP–1743.
- [33] R. Hudson, Y. Feng, R.S. Varma, A. Moores, Bare magnetic nanoparticles: sustainable synthesis and applications in catalytic organic transformations, *Green Chem.* 16 (2014) 4493–4505, <https://doi.org/10.1039/c4gc00418c>.
- [34] M. Magro, L. Nodari, U. Russo, G. Valle, F. Vianello, Maghemite Nanoparticles and Method for Preparing Thereof, (2012) <https://www.google.com/patents/WO2012010200A1?cl=en>.
- [35] M. Magro, G. Sinigaglia, L. Nodari, J. Tucek, K. Polakova, Z. Marusak, S. Cardillo, G. Salviulo, U. Russo, R. Stevanato, R. Zboril, F. Vianello, Charge binding of rhodamine derivative to OH⁻ stabilized nanomaghemite: universal nanocarrier for construction of magnetofluorescent biosensors, *Acta Biomater.* 8 (2012) 2068–2076, <https://doi.org/10.1016/j.actbio.2012.02.005>.
- [36] M. Magro, T. Martinello, E. Bonaiuto, C. Gomiero, D. Baratella, G. Zoppellaro, G. Cozza, M. Patrino, R. Zboril, F. Vianello, Covalently bound DNA on naked iron oxide nanoparticles: intelligent colloidal nano-vector for cell transfection, *Biochim. Biophys. Acta Gen. Subj.* 1861 (2017) 2802–2810, <https://doi.org/10.1016/j.bbagen.2017.07.025>.
- [37] M. Magro, S. Domeneghetti, D. Baratella, P. Jakubec, G. Salviulo, E. Bonaiuto, P. Venier, O. Malina, J. Tucek, V. Ranc, G. Zoppellaro, R. Zboril, F. Vianello, Colloidal surface active maghemite nanoparticles for biologically safe Cr^{VI} remediation: from core-shell nanostructures to pilot plant development, *Chem. A Eur. J.* 22 (2016) 14219–14226, <https://doi.org/10.1002/chem.201600544>.
- [38] C. Gu, K.G. Karthikeyan, Interaction of tetracycline with aluminum and iron hydroxides, *Environ. Sci. Technol.* 39 (2005) 2660–2667, <https://doi.org/10.1021/es048603a>.
- [39] I.T. Lucas, S. Durand-Vidal, E. Dubois, J. Chevalier, P. Turq, Surface charge density of maghemite nanoparticles: role of electrostatics in the proton exchange, *J. Phys. Chem. C* 111 (2007) 18568–18576, <https://doi.org/10.1021/jp0743119>.
- [40] V.R. Patel, Y.K. Agrawal, Nanosuspension: an approach to enhance solubility of drugs, *J. Adv. Pharm. Technol. Res.* 2 (2011) 81–87, <https://doi.org/10.4103/2231-4040.82950>.
- [41] D.W. Meek, D.K. Straub, R.S. Drago, Transition metal ion complexes of dimethyl sulfoxide, *J. Am. Chem. Soc.* 82 (1960) 6013–6016, <https://doi.org/10.1021/ja01508a012>.
- [42] J.N. Duggan, M.J. Bozack, C.B. Roberts, The synthesis and arrested oxidation of amorphous cobalt nanoparticles using DMSO as a functional solvent, *J. Nanopart. Res.* 15 (2013) 2089, <https://doi.org/10.1007/s11051-013-2089-0>.
- [43] B.A. Rea, J.A. Davis, G.A. Waychunas, Studies of the reactivity of the ferrihydrite surface by iron isotopic exchange and Mössbauer spectroscopy, *Clays Clay Miner.* 42 (1994) 23–34, <https://doi.org/10.1346/CCMN.1994.0420104>.
- [44] I. Chopra, P.M. Hawkey, M. Hinton, Tetracyclines, molecular and clinical aspects, *J. Antimicrob. Chemother.* 29 (1992) 245–277, <https://doi.org/10.1093/jac/29.3.245>.
- [45] R.K. H. Blackwood, J.H. Boothe, I. Chopra, B.A. Cunha, J.J. Goodman, R.H. Gustafson, J.J. Hlavka, Z. V.Z., J.S. Kiser, W. Rogalski, The tetracyclines, in: J.J. Hlavka, J.H. Boothe (Eds.), *Handbook of Experimental Pharmacology*, Vol. 78 1985, <https://doi.org/10.1007/978-3-642-70304-1>.
- [46] A. Albert, C.W. Rees, Avidity of the tetracyclines for the cations of metals, *Nature* 177 (1956) 433–434, <https://doi.org/10.1038/177433a0>.
- [47] K.G.A. El Wahed, M. Ayad, R. El Sheikh, Potentiometric study of tetracycline and oxytetracycline with some metal ions of biological interest, *Anal. Lett.* 17 (1984) 413–422, <https://doi.org/10.1080/00032718408069087>.
- [48] K.H. Jogun, J.J. Stezowski, Chemical-structural properties of tetracycline derivatives. 2. Coordination and conformational aspects of oxytetracycline metal ion complexation, *J. Am. Chem. Soc.* 98 (1976) 6018–6026, <https://doi.org/10.1021/ja00435a040>.
- [49] H.A. Duarte, S. Carvalho, E.B. Paniago, A.M. Simas, Importance of tautomers in the chemical behavior of tetracyclines, *J. Pharm. Sci.* 88 (1999) 111–120, <https://doi.org/10.1021/js980181r>.
- [50] A.J. Carrasquillo, G.L. Bruland, A.A. Mackay, D. Vasudevan, Sorption of ciprofloxacin and oxytetracycline zwitterions to soils and soil minerals: influence of compound structure, *Environ. Sci. Technol.* 42 (2008) 7634–7642, <https://doi.org/10.1021/es801277y>.
- [51] M. Magro, D. Baratella, E. Bonaiuto, J. de Almeida Roger, G. Chemello, S. Pasquaroli, L. Mancini, I. Olivotto, G. Zoppellaro, J. Ugolotti, C. Aparicio, A.P. Fifi, G. Cozza, G. Miotto, G. Radaelli, D. Bertotto, R. Zboril, F. Vianello, Stealth iron oxide nanoparticles for organotrophic drug targeting, *Biomacromolecules* 20 (2019) 1375–1384, <https://doi.org/10.1021/acs.biomac.8b01750>.
- [52] I. Langmuir, The adsorption of gases on plane surfaces of glass, mica and platinum, *J. Am. Chem. Soc.* 60 (1918) 467–475, <https://doi.org/10.1021/ja02242a004>.
- [53] J. Yang, C.P. Swaminathan, Y. Huang, R. Guan, S. Cho, M.C. Kieke, D.M. Kranz, R.A. Mariuzza, E.J. Sundberg, Dissecting cooperative and additive binding energetics in the affinity maturation pathway of a protein-Protein interface, *J. Biol. Chem.* 278 (2003) 50412–50421 <http://www.jbc.org/content/278/50/50412.abstract>.
- [54] M. Magro, D. Baratella, G. Salviulo, K. Polakova, G. Zoppellaro, J. Tucek, J. Kaslik, R. Zboril, F. Vianello, Core-shell hybrid nanomaterial based on prussian blue and surface active maghemite nanoparticles as stable electrocatalyst, *Biosens. Bioelectron.* 52 (2014) 159–165, <https://doi.org/10.1016/j.bios.2013.08.052>.
- [55] M. Magro, D. Baratella, P. Jakubec, G. Zoppellaro, J. Tucek, C. Aparicio, R. Venerando, G. Sartori, F. Francescato, F. Mion, N. Gabellini, R. Zboril, F. Vianello, Triggering mechanism for DNA electrical conductivity: reversible Electron transfer between DNA and iron oxide nanoparticles, *Adv. Funct. Mater.* 25 (2015) 1822–1831, <https://doi.org/10.1002/adfm.201404372>.
- [56] E. Bonaiuto, M. Magro, D. Baratella, P. Jakubec, E. Sconcerle, M. Terzo, G. Miotto, A. MacOne, E. Agostinelli, S. Fasolato, R. Venerando, G. Salviulo, O. Malina, R. Zboril, F. Vianello, Ternary hybrid γ -Fe₂O₃/CrVI/Amine oxidase nanostructure for electrochemical sensing: application for polyamine detection in tumor tissue, *Chem. A Eur. J.* 22 (2016) 6846–6852, <https://doi.org/10.1002/chem.201600156>.
- [57] M. Magro, M. Zaccarin, G. Miotto, L. Da Dalt, D. Baratella, P. Farselli, G. Gabai, F. Vianello, Analysis of hard protein corona composition on selective iron oxide nanoparticles by MALDI-TOF mass spectrometry: identification and amplification of a hidden mastitis biomarker in milk proteome, *Anal. Bioanal. Chem.* 410 (2018) 2949–2959, <https://doi.org/10.1007/s00216-018-0976-z>.
- [58] T. Rajh, L.X. Chen, K. Lukas, T. Liu, M.C. Thurnauer, D.M. Tiede, Surface restructuring of nanoparticles: an efficient route for ligand–Metal oxide crosstalk, *J. Phys. Chem. B* 106 (2002) 10543–10552, <https://doi.org/10.1021/jp021235v>.
- [59] M. Magro, A. Faralli, D. Baratella, I. Bertipaglia, S. Giannetti, G. Salviulo, R. Zboril, F. Vianello, Avidin functionalized maghemite nanoparticles and their application for recombinant human Biotinyl-SERCA purification, *Langmuir* 28 (2012) 15392–15401, <https://doi.org/10.1021/la303148u>.
- [60] I. Chopra, M. Roberts, Tetracycline antibiotics: mode of action, applications, molecular biology, and epidemiology of bacterial resistance, *Microbiol. Mol. Biol. Rev.* 65 (2001) 232–260, <https://doi.org/10.1128/MMBR.65.2.232-260.2001>.
- [61] M.O. Schmitt, S. Schneider, Spectroscopic investigation of complexation between various tetracyclines and Mg²⁺ or Ca²⁺, *PhysChemComm.* 3 (2000) 42–55, <https://doi.org/10.1039/B005722N>.
- [62] E. Tanis, K. Hanna, E. Emmanuel, Experimental and modeling studies of sorption of tetracycline onto iron oxides-coated quartz, *Colloids Surfaces A Physicochem. Int. J. Pavement Eng. Asp. Technol.* 327 (2008) 57–63, <https://doi.org/10.1016/j.colsurfa.2008.06.013>.
- [63] A.D. Dwivedi, S.P. Dubey, M. Sillanpää, Y.N. Kwon, C. Lee, R.S. Varma, Fate of engineered nanoparticles: implications in the environment, *Coord. Chem. Rev.* 287 (2015) 64–78, <https://doi.org/10.1016/j.ccr.2014.12.014>.
- [64] A. Shade, H. Peter, S. Allison, D. Baho, M. Berga, H. Buergermann, D. Huber, S. Langenheder, J. Lennon, J. Martiny, K. Matulich, T. Schmidt, J. Handelsman, Fundamentals of microbial community resistance and resilience, *Front. Microbiol.* 3 (2012) 417, <https://doi.org/10.3389/fmicb.2012.00417>.
- [65] V.K. Sharma, Aggregation and toxicity of titanium dioxide nanoparticles in aquatic environment—a review, *J. Environ. Sci. Heal. Part A Toxic/Hazardous Subst. Environ. Eng.* 44 (2009) 1485–1495, <https://doi.org/10.1080/10934520903263231>.
- [66] B. Nowack, The behavior and effects of nanoparticles in the environment, *Environ. Pollut.* 157 (2009) 1063–1064, <https://doi.org/10.1016/j.envpol.2008.12.019>.
- [67] B. Nowack, T.D. Bucheli, Occurrence, behavior and effects of nanoparticles in the environment, *Environ. Pollut.* 150 (2007) 5–22, <https://doi.org/10.1016/j.envpol.2007.06.006>.
- [68] V.K. Sharma, J. Filip, R. Zboril, R.S. Varma, Natural inorganic nanoparticles-formation, fate, and toxicity in the environment, *Chem. Soc. Rev.* 44 (2015) 8410–8423, <https://doi.org/10.1039/c5cs00236b>.
- [69] R. Venerando, G. Miotto, M. Magro, M. Dallan, D. Baratella, E. Bonaiuto, R. Zboril, F. Vianello, Magnetic nanoparticles with covalently bound self-assembled protein Corona for advanced biomedical applications, *J. Phys. Chem. C* 117 (2013) 20320–20331, <https://doi.org/10.1021/jp4068137>.
- [70] J. Skopalik, K. Polakova, M. Havrdova, I. Justan, M. Magro, D. Milde, L. Knopfova, J. Smarda, H. Polakova, E. Gabrielova, F. Vianello, J. Michalek, R. Zboril, Mesenchymal stromal cell labeling by new uncoated superparamagnetic maghemite nanoparticles in comparison with commercial Resovist—an initial in vitro study, *Int. J. Nanomedicine* 9 (2014) 5355–5372, <https://doi.org/10.2147/IJN.S66986>.
- [71] M. Magro, L. Fasolato, E. Bonaiuto, N.A. Andreani, D. Baratella, V. Corraducci, G. Miotto, B. Cardazzo, F. Vianello, Enlightening mineral iron sensing in *Pseudomonas fluorescens* by surface active maghemite nanoparticles: involvement of the OprF porin, *Biochim. Biophys. Acta - Gen. Subj.* 1860 (2016) 2202–2210, <https://doi.org/10.1016/j.bbagen.2016.05.007>.
- [72] B. Halling-Sørensen, G. Sengeløv, J. Tjørnelund, Toxicity of tetracyclines and tetracycline degradation products to environmentally relevant bacteria, including selected tetracycline-resistant bacteria, *Arch. Environ. Contam. Toxicol.* 42 (2002) 263–271, <https://doi.org/10.1007/s00244-001-0017-2>.

8. References

Adeleye, A. S., Conway, J. R., Garner, K., Huang, Y., Su, Y., & Keller, A. A. (2016). Engineered nanomaterials for water treatment and remediation: costs, benefits, and applicability. *Chemical Engineering Journal*, 286, 640-662.

Ajmal, M., Rao, R. A., Ahmad, R., Ahmad, J., & Rao, L. A. (2001). Removal and recovery of heavy metals from electroplating wastewater by using Kyanite as an adsorbent. *Journal of Hazardous Materials*, 87(1-3), 127-137.

Akyuz, S., Akyuz, T., Basaran, S., Kocabas, I., Gulec, A., Cesmeli, H., & Ucar, B. (2009). FT-IR and EDXRF analysis of wall paintings of ancient Ainos Hagia Sophia Church. *Journal of Molecular Structure*, 924, 400-403.

Ali, A., Hira Zafar, M. Z., ul Haq, I., Phull, A. R., Ali, J. S., & Hussain, A. (2016). Synthesis, characterization, applications, and challenges of iron oxide nanoparticles. *Nanotechnology, science and applications*, 9, 49.

American Public Health Association, 1975, Water pollution control federation, Standard Methods for the examination of water and wastewater: Washington D.C., USA, American Public Health Association Publisher.

Amstaetter, K., Borch, T., Larese-Casanova, P., & Kappler, A. (2009). Redox transformation of arsenic by Fe (II)-activated goethite (α -FeOOH). *Environmental science & technology*, 44(1), 102-108.

An, B., Liang, Q., & Zhao, D. (2011). Removal of arsenic (V) from spent ion exchange brine using a new class of starch-bridged magnetite nanoparticles. *Water research*, 45(5), 1961-1972.

Angelone, M., Cremisini, C., Piscopo, V., Proposito, M., & Spaziani, F. (2009). Influence of hydrostratigraphy and structural setting on the arsenic occurrence in groundwater of the Cimino-Vico volcanic area (central Italy). *Hydrogeology Journal*, 17(4), 901-914.

Anjum, M., Miandad, R., Waqas, M., Gehany, F., & Barakat, M. A. (2016). Remediation of wastewater using various nano-materials. *Arabian Journal of Chemistry*.

Antony, M. P., Tathavadkar, V. D., Calvert, C. C., & Jha, A. (2001). The soda-ash roasting of chromite ore processing residue for the reclamation of chromium. *Metallurgical and Materials transactions B*, 32(6), 987-995.

Argo, D. G. (1972). Heavy Metal Removal in Wastewater Treatment Processes: Part I. *Water and sewage works*, 119, 62-65.

Aronniemi, M., Sainio, J., & Lahtinen, J. (2005). Chemical state quantification of iron and chromium oxides using XPS: the effect of the background subtraction method. *Surface Science*, 578(1-3), 108-123.

Auffan, M., Rose, J., Bottero, J. Y., Lowry, G. V., Jolivet, J. P., & Wiesner, M. R. (2009). Towards a definition of inorganic nanoparticles from an environmental, health and safety perspective. *Nature nanotechnology*, 4(10), 634.

Auffan, M., Rose, J., Proux, O., Borschneck, D., Masion, A., Chaurand, P., Hazemann, J.L., Chaneac, C., Jolivet, J.P., Wiesner, M.R., Van Geen, A. & Bottero J.Y. (2008). Enhanced adsorption of arsenic onto maghemites nanoparticles: As (III) as a probe of the surface structure and heterogeneity. *Langmuir*, 24(7), 3215-3222.

- Badruddoza, A. Z. M., Shawon, Z. B. Z., Rahman, M. T., Hao, K. W., Hidajat, K., & Uddin, M. S. (2013). Ionically modified magnetic nanomaterials for arsenic and chromium removal from water. *Chemical engineering journal*, 225, 607-615.
- Ball, J. W., & Nordstrom, D. K. (1998). Critical evaluation and selection of standard state thermodynamic properties for chromium metal and its aqueous ions, hydrolysis species, oxides, and hydroxides. *Journal of Chemical & Engineering Data*, 43(6), 895-918.
- Bandhu, A., Mukherjee, S., Acharya, S., Modak, S., Brahma, S. K., Das, D., & Chakrabarti, P. K. (2009). Dynamic magnetic behaviour and Mössbauer effect measurements of magnetite nanoparticles prepared by a new technique in the co-precipitation method. *Solid State Communications*, 149(41-42), 1790-1794.
- Baral, S. S., Das, S. N., & Rath, P. (2006). Hexavalent chromium removal from aqueous solution by adsorption on treated sawdust. *Biochemical Engineering Journal*, 31(3), 216-222.
- Baratella, D., Magro, M., Sinigaglia, G., Zboril, R., Salviulo, G., & Vianello, F. (2013). A glucose biosensor based on surface active maghemite nanoparticles. *Biosensors and Bioelectronics*, 45, 13-18.
- Barquist, K., & Larsen, S. C. (2010). Chromate adsorption on bifunctional, magnetic zeolite composites. *Microporous and Mesoporous Materials*, 130(1-3), 197-202.
- Bartlett, R. J., & James, B. R. (1988). Mobility and bioavailability of chromium in soils. *Chromium in the natural and human environments*, 20, 571.
- Belin, T., Millot, N., Bovet, N., & Gailhanou, M. (2007). In situ and time resolved study of the γ/α -Fe₂O₃ transition in nanometric particles. *Journal of Solid State Chemistry*, 180(8), 2377-2385.
- Bertolotto, R. M., Tortarolo, B., Frignani, M., Bellucci, L. G., Albanese, S., Cuneo, C., Alvarado-Aguilar, D., Picca, M.R. & Gollo, E. (2005). Heavy metals in surficial coastal sediments of the Ligurian Sea. *Marine Pollution Bulletin*, 50(3), 348.
- Biesinger, M. C., Payne, B. P., Grosvenor, A. P., Lau, L. W., Gerson, A. R., & Smart, R. S. C. (2011). Resolving surface chemical states in XPS analysis of first row transition metals, oxides and hydroxides: Cr, Mn, Fe, Co and Ni. *Applied Surface Science*, 257(7), 2717-2730.
- Biryukov, Y. P., Bubnova, R. S., Filatov, S. K., & Goncharov, A. G. (2016). Synthesis and thermal behavior of Fe₃O₂ (BO₄) oxoborate. *Glass Physics and Chemistry*, 42(2), 202-206.
- Boecher, T., Tinjum, J. M., & XU, H. (2012). Quantification of mineralogical and amorphous species in chromium ore processing residue. *Journal of Residuals Science & Technology*, 9(4), 131-141.
- Bonaiuto, E., Magro, M., Baratella, D., Jakubec, P., Sconcerle, E., Terzo, M., Miotto, G., Macone, A., Agostinelli, E., Fasolato, S., Venerando, R., Salviulo, G., Malina, O., Zboril, R., & Vianello, F. (2016). Ternary Hybrid γ -Fe₂O₃/CrVI/Amine Oxidase Nanostructure for Electrochemical Sensing: Application for Polyamine Detection in Tumor Tissue. *Chemistry—A European Journal*, 22(20), 6846-6852.
- Bönnemann, H., Brijoux, W., Brinkmann, R., Fretzen, R., Jousen, T., Köppler, R., Korall, B., Neiteler, P., & Richter, J. (1994). Preparation, characterization, and application of fine metal particles and metal colloids using hydrotriorganoborates. *Journal of molecular catalysis*, 86(1-3), 129-177.
- Boyer, C., Whittaker, M. R., Bulmus, V., Liu, J., & Davis, T. P. (2010). The design and utility of polymer-stabilized iron-oxide nanoparticles for nanomedicine applications. *NPG Asia Materials*, 2(1), 23.

- Brito, F., Ascanio, J., Mateo, S., Hernandez, C., Araujo, L., Gili, P., Martin-Zarza, P., Dominguez, S., & Mederos, A. (1997). Equilibria of chromate (VI) species in acid medium and ab initio studies of these species. *Polyhedron*, 16(21), 3835-3846.
- Brown, P. A., Gill, S. A., & Allen, S. J. (2000). Metal removal from wastewater using peat. *Water research*, 34(16), 3907-3916.
- Burgess, W. G., Hoque, M. A., Michael, H. A., Voss, C. I., Breit, G. N., & Ahmed, K. M. (2010). Vulnerability of deep groundwater in the Bengal Aquifer System to contamination by arsenic. *Nature Geoscience*, 3(2), 83.
- Çam, İ., & Timuçin, M. (2004). Chemical Synthesis of Iron Borate (Fe₃BO₆). II. *Uluslar Arası Bor Sempozyumu, Eskişehir/TÜRKİYE*, 195.
- Cao, C. Y., Qu, J., Yan, W. S., Zhu, J. F., Wu, Z. Y., & Song, W. G. (2012). Low-cost synthesis of flowerlike α -Fe₂O₃ nanostructures for heavy metal ion removal: adsorption property and mechanism. *Langmuir*, 28(9), 4573-4579.
- Carlin, D. J., Naujokas, M. F., Bradham, K. D., Cowden, J., Heacock, M., Henry, H. F., Lee, J.S., Thomas, D.J., Thompson, C., Tokar, E.J, Waalkes, M. P., Birnbaum, L.S., & Suk, W.A. (2015). Arsenic and environmental health: state of the science and future research opportunities. *Environmental health perspectives*, 124(7), 890-899.
- Carraro, A., Fabbri, P., Giaretta, A., Peruzzo, L., Tateo, F., & Tellini, F. (2013). Arsenic anomalies in shallow Venetian Plain (Northeast Italy) groundwater. *Environmental earth sciences*, 70(7), 3067-3084.
- Carraro, A., Fabbri, P., Giaretta, A., Peruzzo, L., Tateo, F., & Tellini, F. (2015). Effects of redox conditions on the control of arsenic mobility in shallow alluvial aquifers on the Venetian Plain (Italy). *Science of the Total Environment*, 532, 581-594.
- Catalano, J. G., Park, C., Fenter, P., & Zhang, Z. (2008). Simultaneous inner-and outer-sphere arsenate adsorption on corundum and hematite. *Geochimica et Cosmochimica Acta*, 72(8), 1986-2004.
- Chakraborti, D., Das, B., & Murrill, M. T. (2010). Examining India's groundwater quality management. *Environmental Science and Technology*, 45(1), 27-33
- Chen, Y. H., & Li, F. A. (2010). Kinetic study on removal of copper (II) using goethite and hematite nano-photocatalysts. *Journal of Colloid and Interface Science*, 347(2), 277-281.
- Chen, W., Parette, R., Zou, J., Cannon, F. S., & Dempsey, B. A. (2007). Arsenic removal by iron-modified activated carbon. *Water research*, 41(9), 1851-1858.
- Chmielarz, L., Kuśtrowski, P., Rafalska-Łasocha, A., & Dziembaj, R. (2002). Influence of Cu, Co and Ni cations incorporated in brucite-type layers on thermal behaviour of hydrotalcites and reducibility of the derived mixed oxide systems. *Thermochimica Acta*, 395(1-2), 225-236.
- Cho, K. J., Keener, T. C., & Khang, S. J. (2008). A study on the conversion of trona to sodium bicarbonate. *Powder Technology*, 184(1), 58-63.
- Chowdhury, U. K., Biswas, B. K., Chowdhury, T. R., Samanta, G., Mandal, B. K., Basu, G. C., Chanda, C.R., Lodh, D., Saha, K.C., Mukherjee, S.K., Roy, S., Kabir, S., Quamruzzaman, Q., & Chakraborti, D. (2000). Groundwater arsenic contamination in Bangladesh and West Bengal, India. *Environmental health perspectives*, 108(5), 393-397.

Chowdhury, S. R., & Yanful, E. K. (2010). Arsenic and chromium removal by mixed magnetite–maghemite nanoparticles and the effect of phosphate on removal. *Journal of Environmental Management*, 91(11), 2238-2247.

Chowdhury, S. R., Yanful, E. K., & Pratt, A. R. (2011). Arsenic removal from aqueous solutions by mixed magnetite–maghemite nanoparticles. *Environmental Earth Sciences*, 64(2), 411-423.

Chrysochoou, M., & Dermatas, D. (2007). Application of the Rietveld method to assess chromium (VI) speciation in chromite ore processing residue. *Journal of hazardous materials*, 141(2), 370-377.

Chrysochoou, M., & Dermatas, D. (2006). Evaluation of ettringite and hydrocalumite formation for heavy metal immobilization: literature review and experimental study. *Journal of hazardous materials*, 136(1), 20-33.

Chrysochoou, M., Dermatas, D., Grubb, D. G., Moon, D. H., & Christodoulatos, C. (2009). Importance of mineralogy in the geoenvironmental characterization and treatment of chromite ore processing residue. *Journal of geotechnical and geoenvironmental engineering*, 136(3), 510-521.

Chrysochoou, M., Fakra, S. C., Marcus, M. A., Moon, D. H., & Dermatas, D. (2009). Microstructural analyses of Cr (VI) speciation in chromite ore processing residue (COPR). *Environmental science & technology*, 43(14), 5461-5466.

Cloete, T. E., De Kwaadsteniet, M., & Botes, M. (Eds.). (2010). *Nanotechnology in water treatment applications*. Horizon Scientific Press.

Collier, N. C. (2016). Transition and decomposition temperatures of cement phases—a collection of thermal analysis data. *Ceramics-Silikaty*, 60(4).

Consani, S., Ianni, M. C., Dinelli, E., Capello, M., Cutroneo, L., & Carbone, C. (2019). Assessment of metal distribution in different Fe precipitates related to Acid Mine Drainage through two sequential extraction procedures. *Journal of Geochemical Exploration*, 196, 247-258.

Cornell, R. M., & Schwertmann, U. (2003). *The iron oxides: structure, properties, reactions, occurrences and uses*. John Wiley & Sons.

Cundy, A. B., Hopkinson, L., & Whitby, R. L. (2008). Use of iron-based technologies in contaminated land and groundwater remediation: A review. *Science of the total environment*, 400(1-3), 42-51.

Cushnie Jr, G. C. (1985). Electroplating wastewater pollution control technology.

D.Lgs 152/2006 Decreto Legislativo n.152 del 3 aprile (2006) Norme in materia ambientale.

Davies, J. M., Easton, D. F., & Bidstrup, P. L. (1991). Mortality from respiratory cancer and other causes in United Kingdom chromate production workers. *Occupational and Environmental Medicine*, 48(5), 299-313.

Davies, J. E. D., & Long, D. A. (1971). Solid-state vibrational spectroscopy. Part II. The vibrational spectra of some chromates and dichromates. *Journal of the Chemical Society A: Inorganic, Physical, Theoretical*, 1275-1280.

Davis, C. M., & Vincent, J. B. (1997). Chromium in carbohydrate and lipid metabolism. *JBIC Journal of Biological Inorganic Chemistry*, 2(6), 675-679.

Dermatas, D., Bonaparte, R., Chrysochoou, M., & Moon, D. H. (2006). Chromite Ore Processing Residue (COPR): Hazardous contaminated soil or solid waste?. In *Contaminated Sediments: Evaluation and Remediation Techniques*. ASTM International.

- Di, Z. C., Ding, J., Peng, X. J., Li, Y. H., Luan, Z. K., & Liang, J. (2006). Chromium adsorption by aligned carbon nanotubes supported ceria nanoparticles. *Chemosphere*, 62(5), 861-865.
- Diehl, R., & Friedrich, F. (1976). Growth of bulk single crystals of the weak ferromagnet Fe₃BO₆ by a vapor phase reaction. *Journal of Crystal Growth*, 36(2), 263-266.
- Driehaus, W., Jekel, M., & Hildebrandt, U. (1998). Granular ferric hydroxide—a new adsorbent for the removal of arsenic from natural water. *Journal of Water Supply: Research and Technology-Aqua*, 47(1), 30-35.
- Duggan, J. N., Bozack, M. J., & Roberts, C. B. (2013). The synthesis and arrested oxidation of amorphous cobalt nanoparticles using DMSO as a functional solvent. *Journal of nanoparticle research*, 15(11), 2089.
- Ekmekyapar, A., Erşahan, H., & Yapıcı, S. (1996). Nonisothermal decomposition kinetics of trona. *Industrial & engineering chemistry research*, 35(1), 258-262.
- Elzinga, E. J., & Cirmo, A. (2010). Application of sequential extractions and X-ray absorption spectroscopy to determine the speciation of chromium in Northern New Jersey marsh soils developed in chromite ore processing residue (COPR). *Journal of hazardous materials*, 183(1-3), 145-154.
- Ennas, G., Musinu, A. N. N. A., Piccaluga, G., Zedda, D., Gatteschi, D., Sangregorio, C., ... & Spano, G. (1998). Characterization of iron oxide nanoparticles in an Fe₂O₃-SiO₂ composite prepared by a sol-gel method. *Chemistry of Materials*, 10(2), 495-502.
- Esteller, M. V., Domínguez-Mariani, E., Garrido, S. E., & Avilés, M. (2015). Groundwater pollution by arsenic and other toxic elements in an abandoned silver mine, Mexico. *Environmental earth sciences*, 74(4), 2893-2906.
- Estelrich, J., Escribano, E., Queralt, J., & Busquets, M. (2015). Iron oxide nanoparticles for magnetically-guided and magnetically-responsive drug delivery. *International journal of molecular sciences*, 16(4), 8070-8101.
- Evanko, C. R., & Dzombak, D. A. (1997). *Remediation of metals-contaminated soils and groundwater*. Pittsburg,, USA: Ground-water remediation technologies analysis center.
- Farmer, J. G., Paterson, E., Bewley, R. J. F., Geelhoed, J. S., Hillier, S., Meeussen, J. C. L., Lumsdon, D.G., Thomas, R.P. & Graham, M. C. (2006). The implications of integrated assessment and modelling studies for the future remediation of chromite ore processing residue disposal sites. *Science of the Total Environment*, 360(1-3), 90-97.
- Farmer, J. G., Thomas, R. P., Graham, M. C., Geelhoed, J. S., Lumsdon, D. G., & Paterson, E. (2002). Chromium speciation and fractionation in ground and surface waters in the vicinity of chromite ore processing residue disposal sites. *Journal of Environmental Monitoring*, 4(2), 235-243.
- Fendorf, S., Michael, H. A., & van Geen, A. (2010). Spatial and temporal variations of groundwater arsenic in South and Southeast Asia. *Science*, 328(5982), 1123-1127.
- Feng, L., Cao, M., Ma, X., Zhu, Y., & Hu, C. (2012). Superparamagnetic high-surface-area Fe₃O₄ nanoparticles as adsorbents for arsenic removal. *Journal of hazardous materials*, 217, 439-446.
- Filgueiras, A. V., Lavilla, I., & Bendicho, C. (2002). Chemical sequential extraction for metal partitioning in environmental solid samples. *Journal of Environmental Monitoring*, 4(6), 823-857.

- Freundlich, H. (1907). Über die adsorption in lösungen. *Zeitschrift für physikalische Chemie*, 57(1), 385-470.
- Frost, R. L. (2004). Raman microscopy of selected chromate minerals. *Journal of Raman Spectroscopy*, 35(2), 153-158.
- Fu, F., Dionysiou, D. D., & Liu, H. (2014). The use of zero-valent iron for groundwater remediation and wastewater treatment: a review. *Journal of hazardous materials*, 267, 194-205.
- Fu, R., Yang, Y., Xu, Z., Zhang, X., Guo, X., & Bi, D. (2015). The removal of chromium (VI) and lead (II) from groundwater using sepiolite-supported nanoscale zero-valent iron (S-NZVI). *Chemosphere*, 138, 726-734.
- Gao, X., Root, R. A., Farrell, J., Ela, W., & Chorover, J. (2013). Effect of silicic acid on arsenate and arsenite retention mechanisms on 6-L ferrihydrite: A spectroscopic and batch adsorption approach. *Applied Geochemistry*, 38, 110-120.
- Gao, L., & Zhang, Q. (2001). Effects of amorphous contents and particle size on the photocatalytic properties of TiO₂ nanoparticles. *Scripta materialia*, 44(8-9), 1195-1198.
- García-Salgado, S., García-Casillas, D., Quijano-Nieto, M. A., & Bonilla-Simón, M. M. (2012). Arsenic and heavy metal uptake and accumulation in native plant species from soils polluted by mining activities. *Water, Air, & Soil Pollution*, 223(2), 559-572.
- Gärtner, R. S., & Witkamp, G. J. (2002). Wet calcining of trona (sodium sesquicarbonate) and bicarbonate in a mixed solvent. *Journal of crystal growth*, 237, 2199-2204.
- Gazeau, F., Shilov, V., Bacri, J. C., Dubois, E., Gendron, F., Perzynski, R., Raikher, Y.L. & Stepanov, V. I. (1999). Magnetic resonance of nanoparticles in a ferrofluid: evidence of thermofluctuational effects. *Journal of magnetism and magnetic materials*, 202(2-3), 535-546.
- Geelhoed, J. S., Meeussen, J. C., Hillier, S., Lumsdon, D. G., Thomas, R. P., Farmer, J. G., & Paterson, E. (2002). Identification and geochemical modeling of processes controlling leaching of Cr (VI) and other major elements from chromite ore processing residue. *Geochimica et Cosmochimica Acta*, 66(22), 3927-3942.
- Geelhoed, J. S., Meeussen, J. C., Roe, M. J., Hillier, S., Thomas, R. P., Farmer, J. G., & Paterson, E. (2003). Chromium remediation or release? Effect of iron (II) sulfate addition on chromium (VI) leaching from columns of chromite ore processing residue. *Environmental science & technology*, 37(14), 3206-3213.
- Gheju, M. (2011). Hexavalent chromium reduction with zero-valent iron (ZVI) in aquatic systems. *Water, Air, & Soil Pollution*, 222(1-4), 103-148.
- Gimenez, J., Martinez, M., de Pablo, J., Rovira, M., & Duro, L. (2007). Arsenic sorption onto natural hematite, magnetite, and goethite. *Journal of hazardous materials*, 141(3), 575-580.
- Giraldo, L., Erto, A., & Moreno-Piraján, J. C. (2013). Magnetite nanoparticles for removal of heavy metals from aqueous solutions: synthesis and characterization. *Adsorption*, 19(2-4), 465-474.
- Gnanaprakash, G., Ayyappan, S., Jayakumar, T., Philip, J., & Raj, B. (2006). Magnetic nanoparticles with enhanced γ -Fe₂O₃ to α -Fe₂O₃ phase transition temperature. *Nanotechnology*, 17(23), 5851.
- Goldberg, S., & Johnston, C. T. (2001). Mechanisms of arsenic adsorption on amorphous oxides evaluated using macroscopic measurements, vibrational spectroscopy, and surface complexation modeling. *Journal of colloid and Interface Science*, 234(1), 204-216.

- Goto, S., Suenaga, K., Kado, T., & Fukuhara, M. (1995). Calcium silicate carbonation products. *Journal of the American Ceramic Society*, 78(11), 2867-2872.
- Farmer, J. G., Graham, M. C., Thomas, R. P., Licona-Manzur, C., Licona-Manzur, C., Paterson, E., Campbell, C.D., Geelhoed, J.S., Lumsdon, D.G., Meeussen, J.C.L., Roe, M. J., Conner, A., Fallick, A.E. & Bewley, R.J.F. (1999). Assessment and modelling of the environmental chemistry and potential for remediative treatment of chromium-contaminated land. *Environmental Geochemistry and Health*, 21(4), 331-337.
- Grossl, P. R., Sparks, D. L., & Ainsworth, C. C. (1994). Rapid kinetics of Cu (II) adsorption/desorption on goethite. *Environmental science & technology*, 28(8), 1422-1429.
- Gu, C., & Karthikeyan, K. G. (2005). Interaction of tetracycline with aluminum and iron hydrous oxides. *Environmental Science & Technology*, 39(8), 2660-2667.
- Gunasekaran, S., Anbalagan, G., & Pandi, S. (2006). Raman and infrared spectra of carbonates of calcite structure. *Journal of Raman Spectroscopy: An International Journal for Original Work in all Aspects of Raman Spectroscopy, Including Higher Order Processes, and also Brillouin and Rayleigh Scattering*, 37(9), 892-899.
- Gunatilake, S. K. (2015). Methods of removing heavy metals from industrial wastewater. *Methods*, 1(1), 14.
- Gupta, A. K., & Gupta, M. (2005). Synthesis and surface engineering of iron oxide nanoparticles for biomedical applications. *biomaterials*, 26(18), 3995-4021.
- Gutierrez, A. M., Dziubla, T. D., & Hilt, J. Z. (2017). Recent advances on iron oxide magnetic nanoparticles as sorbents of organic pollutants in water and wastewater treatment. *Reviews on environmental health*, 32(1-2), 111-117.
- Hamilton, A., & Menzies, R. I. (2010). Raman spectra of mirabilite, Na₂SO₄· 10H₂O and the rediscovered metastable heptahydrate, Na₂SO₄· 7H₂O. *Journal of Raman Spectroscopy*, 41(9), 1014-1020.
- Hausmann, M. R. (1990). *Engineering principles of ground modification*.
- Heiligtag, F. J., & Niederberger, M. (2013). The fascinating world of nanoparticle research. *Materials Today*, 16(7-8), 262-271.
- Hillier, S., Lumsdon, D. G., Brydson, R., & Paterson, E. (2007). Hydrogarnet: A host phase for Cr (VI) in chromite ore processing residue (COPR) and other high pH wastes. *Environmental science & technology*, 41(6), 1921-1927.
- Hillier, S., Roe, M. J., Geelhoed, J. S., Fraser, A. R., Farmer, J. G., & Paterson, E. (2003). Role of quantitative mineralogical analysis in the investigation of sites contaminated by chromite ore processing residue. *Science of the Total Environment*, 308(1-3), 195-210.
- Ho, Y. S., Ng, J. C. Y., & McKay, G. (2000). Kinetics of pollutant sorption by biosorbents. *Separation and purification methods*, 29(2), 189-232.
- Hola, K., Markova, Z., Zoppellaro, G., Tucek, J., & Zboril, R. (2015). Tailored functionalization of iron oxide nanoparticles for MRI, drug delivery, magnetic separation and immobilization of biosubstances. *Biotechnology advances*, 33(6), 1162-1176.
- Holmes, A. L., Wise, S. S., & Wise Sr, J. P. (2008). Carcinogenicity of hexavalent chromium. *Indian journal of medical research*.

- Hong, M. Y., Lee, D., & Kim, H. S. (2005). Kinetic and Equilibrium Binding Analysis of Protein–Ligand Interactions at Poly (amidoamine) Dendrimer Monolayers. *Analytical chemistry*, 77(22), 7326-7334.
- Hu, J., Chen, G., & Lo, I. M. (2005). Removal and recovery of Cr (VI) from wastewater by maghemite nanoparticles. *Water research*, 39(18), 4528-4536.
- Hu, J., Chen, G., & Lo, I. M. (2006). Selective removal of heavy metals from industrial wastewater using maghemite nanoparticle: performance and mechanisms. *Journal of environmental engineering*, 132(7), 709-715.
- Hu, J., Lo, I. M., & Chen, G. (2007). Performance and mechanism of chromate (VI) adsorption by δ -FeOOH-coated maghemite (γ -Fe₂O₃) nanoparticles. *Separation and Purification Technology*, 58(1), 76-82.
- Hu, J., Lo, I. M. C., & Chen, G. (2004). Removal of Cr (VI) by magnetite. *Water Science and Technology*, 50(12), 139-146.
- Hu, H., Wang, Z., & Pan, L. (2010). Synthesis of monodisperse Fe₃O₄@ silica core–shell microspheres and their application for removal of heavy metal ions from water. *Journal of Alloys and Compounds*, 492(1-2), 656-661.
- Hua, M., Zhang, S., Pan, B., Zhang, W., Lv, L., & Zhang, Q. (2012). Heavy metal removal from water/wastewater by nanosized metal oxides: a review. *Journal of hazardous materials*, 211, 317-331.
- Huang, C. K., & Kerr, P. F. (1960). Infrared study of the carbonate minerals. *American Mineralogist: Journal of Earth and Planetary Materials*, 45(3-4), 311-324.
- Huang, C. P., & Wu, M. H. (1977). The removal of chromium (VI) from dilute aqueous solution by activated carbon. *Water Research*, 11(8), 673-679.
- James, B. R. (1994). Hexavalent chromium solubility and reduction in alkaline soils enriched with chromite ore processing residue. *Journal of Environmental Quality*, 23(2), 227-233.
- James, B. R. (1996). Peer reviewed: the challenge of remediating chromium-contaminated soil. *Environmental Science & Technology*, 30(6), 248A-251A.
- James, B. R., & Bartlett, R. J. (1983). Behavior of Chromium in Soils: VII. Adsorption and Reduction of Hexavalent Forms 1. *Journal of Environmental Quality*, 12(2), 177-181.
- James, B. R., & Bartlett, R. J. (1984). Plant-Soil Interactions of Chromium 1. *Journal of Environmental Quality*, 13(1), 67-70.
- Jiang, J. Q., Ashekuzzaman, S., Jiang, A., Sharifuzzaman, S., & Chowdhury, S. (2013). Arsenic contaminated groundwater and its treatment options in Bangladesh. *International journal of environmental research and public health*, 10(1), 18-46.
- Jobby, R., Jha, P., Yadav, A. K., & Desai, N. (2018). Biosorption and biotransformation of hexavalent chromium [Cr (VI)]: a comprehensive review. *Chemosphere*, 207, 255-266.
- Kachkachi, H., Ezzir, A., Noguez, M., & Tronc, E. (2000). Surface effects in nanoparticles: application to maghemite-Fe O. *The European Physical Journal B*, 14(4), 681-689.
- Von der Kammer, F., Ottofuelling, S., & Hofmann, T. (2010). Assessment of the physico-chemical behavior of titanium dioxide nanoparticles in aquatic environments using multi-dimensional parameter testing. *Environmental Pollution*, 158(12), 3472-3481.
- Kanel, S. R., Manning, B., Charlet, L., & Choi, H. (2005). Removal of arsenic (III) from groundwater by nanoscale zero-valent iron. *Environmental science & technology*, 39(5), 1291-1298.

Kanematsu, M., Young, T. M., Fukushi, K., Green, P. G., & Darby, J. L. (2013). Arsenic (III, V) adsorption on a goethite-based adsorbent in the presence of major co-existing ions: modeling competitive adsorption consistent with spectroscopic and molecular evidence. *Geochimica et Cosmochimica Acta*, *106*, 404-428.

Karpushenkov, S. A., Shchukin, G. L., Belanovich, A. L., Savenko, V. P., & Kulak, A. I. (2010). Plasma electrolytic ceramic-like aluminum oxide coatings on iron. *Journal of applied electrochemistry*, *40*(2), 365-374.

Kim, Y., Kim, C., Choi, I., Rengaraj, S., & Yi, J. (2004). Arsenic removal using mesoporous alumina prepared via a templating method. *Environmental science & technology*, *38*(3), 924-931.

Kimbrough, D. E., Cohen, Y., Winer, A. M., Creelman, L., & Mabuni, C. (1999). A critical assessment of chromium in the environment. *Critical reviews in environmental science and technology*, *29*(1), 1-46.

Kongsricharoen, N., & Polprasert, C. (1995). Electrochemical precipitation of chromium (Cr⁶⁺) from an electroplating wastewater. *Water Science and Technology*, *31*(9), 109-117.

Kotaś, J., & Stasicka, Z. (2000). Chromium occurrence in the environment and methods of its speciation. *Environmental pollution*, *107*(3), 263-283.

Krajnc, M., Štupar, J., & Miličev, S. (1995). Characterization of chromium and copper complexes with fulvic acids isolated from soils in Slovenia. *Science of the total environment*, *159*(1), 23-31.

Lagergren, S. K. (1898). About the theory of so-called adsorption of soluble substances. *Sven. Vetenskapsakad. Handlingar*, *24*, 1-39.

Langmuir, I. (1918). The adsorption of gases on plane surfaces of glass, mica and platinum. *Journal of the American Chemical society*, *40*(9), 1361-1403.

Lenglet, M., & Hochu, F. (1997). Correlation between ionic-covalent parameters and infrared spectroscopic data in II-III transition metal spinel-type oxides. *Materials Research Bulletin*, *32*(7), 863-872.

Li, Y., Cundy, A. B., Feng, J., Fu, H., Wang, X., & Liu, Y. (2017). Remediation of hexavalent chromium contamination in chromite ore processing residue by sodium dithionite and sodium phosphate addition and its mechanism. *Journal of environmental management*, *192*, 100-106.

Li, X. Q., & Zhang, W. X. (2006). Iron nanoparticles: The core-shell structure and unique properties for Ni (II) sequestration. *Langmuir*, *22*(10), 4638-4642.

Liang, C. P., Wang, S. W., Kao, Y. H., & Chen, J. S. (2016). Health risk assessment of groundwater arsenic pollution in southern Taiwan. *Environmental geochemistry and health*, *38*(6), 1271-1281.

Lin, S., Lu, D., & Liu, Z. (2012). Removal of arsenic contaminants with magnetic γ -Fe₂O₃ nanoparticles. *Chemical Engineering Journal*, *211*, 46-52.

Lin, J., & Wang, L. (2009). Comparison between linear and non-linear forms of pseudo-first-order and pseudo-second-order adsorption kinetic models for the removal of methylene blue by activated carbon. *Frontiers of Environmental Science & Engineering in China*, *3*(3), 320-324.

Liu, R., Liu, J. F., Zhang, L. Q., Sun, J. F., & Jiang, G. B. (2016). Low temperature synthesized ultrathin γ -Fe₂O₃ nanosheets show similar adsorption behaviour for As (iii) and As (v). *Journal of Materials Chemistry A*, *4*(20), 7606-7614.

Lofrano, G., Libralato, G., & Brown, J. (2017). *Nanotechnologies for Environmental Remediation*. Springer International Publishing.

Scrivener, K., Snellings, R., & Lothenbach, B. (Eds.). (2018). *A practical guide to microstructural analysis of cementitious materials*. Crc Press.

Lu, P., & Zhu, C. (2011). Arsenic Eh–pH diagrams at 25 C and 1 bar. *Environmental Earth Sciences*, 62(8), 1673-1683.

Lucas, I. T., Durand-Vidal, S., Dubois, E., Chevalet, J., & Turq, P. (2007). Surface charge density of maghemite nanoparticles: role of electrostatics in the proton exchange. *The Journal of Physical Chemistry C*, 111(50), 18568-18576.

Machala, L., Tucek, J., & Zboril, R. (2011). Polymorphous transformations of nanometric iron (III) oxide: a review. *Chemistry of Materials*, 23(14), 3255-3272.

Machala, L., Zboril, R., & Gedanken, A. (2007). Amorphous iron (III) oxide a review. *The Journal of Physical Chemistry B*, 111(16), 4003-4018.

Mackay, M. E., Tuteja, A., Duxbury, P. M., Hawker, C. J., Van Horn, B., Guan, Z., Chen, G., & Krishnan, R. S. (2006). General strategies for nanoparticle dispersion. *Science*, 311(5768), 1740-1743.

Maglione, G., & Carn, M. (1975). Spectres infrarouges des minéraux salins et des silicates néoformés dans le bassin Tchadien. *Cahier ORSTOM série géologie*, 7(1), 3-9.

Magro, M., Baratella, D., Bonaiuto, E., de A Roger, J., & Vianello, F. (2018). New perspectives on biomedical applications of iron oxide nanoparticles. *Current medicinal chemistry*, 25(4), 540-555.

Magro, M., Baratella, D., Bonaiuto, E., de Almeida Roger, J., Chemello, G., Pasquaroli, S., Mancini, L., Olivotto, I., Zoppellaro, G., Ugolotti, J., Aparicio, C., Fifi, A.P., Cozza, G., Miotto, G., Radaelli, G., Bertotto, D., Zboril, R., & Vianello, F., (2019). Stealth iron oxide nanoparticles for organotropic drug targeting. *Biomacromolecules*, 20(3), 1375-1384.

Magro, M., Baratella, D., Jakubec, P., Zoppellaro, G., Tucek, J., Aparicio, C., Venerando, R., Sartori, G., Francescato, F., Mion, F., Gabellini, N., Zboril, R., and Vianello, F., (2015). Triggering Mechanism for DNA Electrical Conductivity: Reversible Electron Transfer between DNA and Iron Oxide Nanoparticles. *Advanced Functional Materials*, 25(12), 1822-1831.

Magro, M., Baratella, D., Pianca, N., Toninello, A., Grancara, S., Zboril, R., & Vianello, F. (2013). Electrochemical determination of hydrogen peroxide production by isolated mitochondria: a novel nanocomposite carbon–maghemite nanoparticle electrode. *Sensors and Actuators B: Chemical*, 176, 315-322.

Magro, M., Baratella, D., Salviulo, G., Polakova, K., Zoppellaro, G., Tucek, J., Kaslik, J., Zboril, R., and Vianello, F., (2014). Core–shell hybrid nanomaterial based on prussian blue and surface active maghemite nanoparticles as stable electrocatalyst. *Biosensors and Bioelectronics*, 52, 159-165.

Magro, M., Domeneghetti, S., Baratella, D., Jakubec, P., Salviulo, G., Bonaiuto, E., Venier, P., Malina, O., Tuček, J., Ranc, V., Zoppellaro, G., Zbořil, R., and Vianello, F. (2016). Colloidal Surface Active Maghemite Nanoparticles for Biologically Safe CrVI Remediation: from Core-Shell Nanostructures to Pilot Plant Development. *Chemistry–A European Journal*, 22(40), 14219-14226.

Magro, M., Faralli, A., Baratella, D., Bertipaglia, I., Giannetti, S., Salviulo, G., Zboril, R., & Vianello, F. (2012). Avidin functionalized maghemite nanoparticles and their application for recombinant human biotinyl-SERCA purification. *Langmuir*, 28(43), 15392-15401.

Magro, M., De Liguoro, M., Franzago, E., Baratella, D., & Vianello, F. (2018). The surface reactivity of iron oxide nanoparticles as a potential hazard for aquatic environments: A study on *Daphnia magna* adults and embryos. *Scientific reports*, 8(1), 13017.

Magro, M., Martinello, T., Bonaiuto, E., Gomiero, C., Baratella, D., Zoppellaro, G., Cozza, G., Patruno, M., Zboril, R., & Vianello, F. (2017). Covalently bound DNA on naked iron oxide nanoparticles: intelligent colloidal nano-vector for cell transfection. *Biochimica et Biophysica Acta (BBA)-General Subjects*, 1861(11), 2802-2810.

Magro, M., Moritz, D.E., Bonaiuto, E., Baratella, D., Terzo, M., Jakubec, P., Malina, O., Čépe, K., Aragao, G.M.F. de, Zboril, R., & Vianello, F. (2016). Citrinin mycotoxin recognition and removal by naked magnetic nanoparticles. *Food chemistry*, 203, 505-512.

Russo, U., Nodari, L., Vianello, F., Magro, M., & Valle, G. (2015). *U.S. Patent No. 8,980,218*. Washington, DC: U.S. Patent and Trademark Office.

Magro, M., Sinigaglia, G., Nodari, L., Tucek, J., Polakova, K., Marusak, Z., Cardillo, S., Salviulo, G., Russo, U., Stevanato, R., Zboril, R., & Vianello, F. (2012). Charge binding of rhodamine derivative to OH-stabilized nanomagnetite: universal nanocarrier for construction of magnetofluorescent biosensors. *Acta biomaterialia*, 8(6), 2068-2076.

Magro, M., Zaccarin, M., Miotto, G., Da Dalt, L., Baratella, D., Fariselli, P., Gabai, G., & Vianello, F. (2018). Analysis of hard protein corona composition on selective iron oxide nanoparticles by MALDI-TOF mass spectrometry: identification and amplification of a hidden mastitis biomarker in milk proteome. *Analytical and bioanalytical chemistry*, 410(12), 2949-2959.

Mak, M. S., Rao, P., & Lo, I. M. (2009). Effects of hardness and alkalinity on the removal of arsenic (V) from humic acid-deficient and humic acid-rich groundwater by zero-valent iron. *Water research*, 43(17), 4296-4304.

Manceau, A., & Charlet, L. (1994). The mechanism of selenate adsorption on goethite and hydrous ferric oxide. *Journal of Colloid and Interface Science*, 168(1), 87-93.

Manning, B. A., Fendorf, S. E., & Goldberg, S. (1998). Surface structures and stability of arsenic (III) on goethite: spectroscopic evidence for inner-sphere complexes. *Environmental science & technology*, 32(16), 2383-2388.

Martin, J. E., Herzing, A. A., Yan, W., Li, X. Q., Koel, B. E., Kiely, C. J., & Zhang, W. X. (2008). Determination of the oxide layer thickness in core-shell zerovalent iron nanoparticles. *Langmuir*, 24(8), 4329-4334.

Matern, K., Kletti, H., & Mansfeldt, T. (2016). Chemical and mineralogical characterization of chromite ore processing residue from two recent Indian disposal sites. *Chemosphere*, 155, 188-195.

Matern, K., Weigand, H., Singh, A., & Mansfeldt, T. (2017). Environmental status of groundwater affected by chromite ore processing residue (COPR) dumpsites during pre-monsoon and monsoon seasons. *Environmental Science and Pollution Research*, 24(4), 3582-3592.

Meek, D. W., Straub, D. K., & Drago, R. S. (1960). Transition metal ion complexes of dimethyl sulfoxide. *Journal of the American Chemical Society*, 82(23), 6013-6016.

Meyers, P. H., Cronin, F. R., & Nice Jr, C. (1963). Experimental approach in the use and magnetic control of metallic iron particles in the lymphatic and vascular system of dogs as a contrast and isotropic agent. *Am. J. Roentgenol., Radium Therapy Nucl. Med.*, 90.

Miller, F. A., & Wilkins, C. H. (1952). Infrared spectra and characteristic frequencies of inorganic ions. *Analytical chemistry*, 24(8), 1253-1294.

Mirbagheri, S. A., & Hosseini, S. N. (2005). Pilot plant investigation on petrochemical wastewater treatment for the removal of copper and chromium with the objective of reuse. *Desalination*, 171(1), 85-93.

Mitra, P., Sarkar, D., Chakrabarti, S., & Dutta, B. K. (2011). Reduction of hexavalent chromium with zero-valent iron: batch kinetic studies and rate model. *Chemical Engineering Journal*, 171(1), 54-60.

Mohan, D., & Pittman Jr, C. U. (2007). Arsenic removal from water/wastewater using adsorbents—a critical review. *Journal of hazardous materials*, 142(1-2), 1-53.

Mohapatra, D., Mishra, D., Chaudhury, G. R., & Das, R. P. (2007). Arsenic (V) adsorption mechanism using kaolinite, montmorillonite and illite from aqueous medium. *Journal of Environmental Science and Health, Part A*, 42(4), 463-469.

Molinari, A., Guadagnini, L., Marcaccio, M., Straface, S., Sanchez-Vila, X., & Guadagnini, A. (2013). Arsenic release from deep natural solid matrices under experimentally controlled redox conditions. *Science of the Total Environment*, 444, 231-240.

Monico, L., Janssens, K., Cotte, M., Sorace, L., Vanmeert, F., Brunetti, B. G., & Miliani, C. (2016). Chromium speciation methods and infrared spectroscopy for studying the chemical reactivity of lead chromate-based pigments in oil medium. *Microchemical Journal*, 124, 272-282.

Moon, D. H., Wazne, M., Jagupilla, S. C., Christodoulatos, C., Kim, M. G., & Koutsospyros, A. (2008). Particle size and pH effects on remediation of chromite ore processing residue using calcium polysulfide (CaS₅). *Science of the total environment*, 399(1-3), 2-10.

Mugnai, C., Bertolotto, R. M., Gaino, F., Tiberiade, C., Bellucci, L. G., Giuliani, S., ... & Galazzo, D. (2010). History and trends of sediment contamination by heavy metals within and close to a marine area of national interest: the Ligurian Sea off Cogoleto-Stoppani (Genoa, Italy). *Water, Air, & Soil Pollution*, 211(1-4), 69-77.

Müller, K., Ciminelli, V. S., Dantas, M. S. S., & Willscher, S. (2010). A comparative study of As (III) and As (V) in aqueous solutions and adsorbed on iron oxy-hydroxides by Raman spectroscopy. *Water Research*, 44(19), 5660-5672.

Multari, C., Miola, M., Laviano, F., Gerbaldo, R., Pezzotti, G., Debellis, D., & Verné, E. (2019). Magnetoplasmonic nanoparticles for photothermal therapy. *Nanotechnology*, 30(25), 255705.

Muthukrishnan, M., & Guha, B. K. (2008). Effect of pH on rejection of hexavalent chromium by nanofiltration. *Desalination*, 219(1-3), 171-178.

Namduri, H., & Nasrazadani, S. (2008). Quantitative analysis of iron oxides using Fourier transform infrared spectrophotometry. *Corrosion Science*, 50(9), 2493-2497.

Naujokas, M. F., Anderson, B., Ahsan, H., Aposhian, H. V., Graziano, J. H., Thompson, C., & Suk, W. A. (2013). The broad scope of health effects from chronic arsenic exposure: update on a worldwide public health problem. *Environmental health perspectives*, 121(3), 295-302.

- Navoni, J. A., De Pietri, D., Olmos, V., Gimenez, C., Mitre, G. B., De Titto, E., & Lepori, E. V. (2014). Human health risk assessment with spatial analysis: study of a population chronically exposed to arsenic through drinking water from Argentina. *Science of the Total Environment*, 499, 166-174.
- Nguyen, C. M., Bang, S., Cho, J., & Kim, K. W. (2009). Performance and mechanism of arsenic removal from water by a nanofiltration membrane. *Desalination*, 245(1-3), 82-94.
- Nickens, K. P., Patierno, S. R., & Ceryak, S. (2010). Chromium genotoxicity: a double-edged sword. *Chemico-biological interactions*, 188(2), 276-288.
- Nikolaidis, N. P., Dobbs, G. M., & Lackovic, J. A. (2003). Arsenic removal by zero-valent iron: field, laboratory and modeling studies. *Water research*, 37(6), 1417-1425.
- Nogués, J., & Schuller, I. K. (1999). Exchange bias. *Journal of Magnetism and Magnetic Materials*, 192(2), 203-232.
- Nordstrom, D. K., Majzlan, J., & Königsberger, E. (2014). Thermodynamic properties for arsenic minerals and aqueous species. *Reviews in Mineralogy and Geochemistry*, 79(1), 217-255.
- Nurmi, J. T., Tratnyek, P. G., Sarathy, V., Baer, D. R., Amonette, J. E., Pecher, K., Wang, C., Linehan, J.C., Matson, D.W., Penn, R.L., & Driessen, M. D. (2005). Characterization and properties of metallic iron nanoparticles: spectroscopy, electrochemistry, and kinetics. *Environmental science & technology*, 39(5), 1221-1230.
- O'Bannon III, E., BEavErs, C. M., & Willlams, Q. (2014). Trona at extreme conditions: A pollutant-sequestering material at high pressures and low temperatures. *American Mineralogist*, 99(10), 1973-1984.
- Ona-Nguema, G., Morin, G., Juillot, F., Calas, G., & Brown, G. E. (2005). EXAFS analysis of arsenite adsorption onto two-line ferrihydrite, hematite, goethite, and lepidocrocite. *Environmental science & technology*, 39(23), 9147-9155.
- Oze, C., Bird, D. K., & Fendorf, S. (2007). Genesis of hexavalent chromium from natural sources in soil and groundwater. *Proceedings of the National Academy of Sciences*, 104(16), 6544-6549.
- Ozer, D., & Icten, O. Solution Combustion Synthesis of Iron Oxyborate (Fe₃BO₆). *Journal of the Turkish Chemical Society, Section A: Chemistry*, 6(2), 97-102.
- Palmer, C. D. (2000). Precipitates in a Cr (VI)-contaminated concrete. *Environmental science & technology*, 34(19), 4185-4192.
- Patel, V. R., & Agrawal, Y. K. (2011). Nanosuspension: An approach to enhance solubility of drugs. *Journal of advanced pharmaceutical technology & research*, 2(2), 81.
- Paulukat, C., Døssing, L. N., Mondal, S. K., Voegelin, A. R., & Frei, R. (2015). Oxidative release of chromium from Archean ultramafic rocks, its transport and environmental impact—A Cr isotope perspective on the Sukinda valley ore district (Orissa, India). *Applied Geochemistry*, 59, 125-138.
- Peak, D., Luther III, G. W., & Sparks, D. L. (2003). ATR-FTIR spectroscopic studies of boric acid adsorption on hydrous ferric oxide. *Geochimica et Cosmochimica Acta*, 67(14), 2551-2560.
- Pechova, A., & Pavlata, L. (2007). Chromium as an essential nutrient: a review. *VETERINARNI MEDICINA-PRAHA*, 52(1), 1.
- Pena, M., Meng, X., Korfiatis, G. P., & Jing, C. (2006). Adsorption mechanism of arsenic on nanocrystalline titanium dioxide. *Environmental Science & Technology*, 40(4), 1257-1262.

Petala, E., Dimos, K., Douvalis, A., Bakas, T., Tucek, J., Zbořil, R., & Karakassides, M. A. (2013). Nanoscale zero-valent iron supported on mesoporous silica: characterization and reactivity for Cr (VI) removal from aqueous solution. *Journal of hazardous materials*, 261, 295-306.

Petros, R. A., & DeSimone, J. M. (2010). Strategies in the design of nanoparticles for therapeutic applications. *Nature reviews Drug discovery*, 9(8), 615.

Pettine, M., & Millero, F. J. (1990). Chromium speciation in seawater: The probable role of hydrogen peroxide. *Limnology and Oceanography*, 35(3), 730-736.

Pfeiffer, C., Rehbock, C., Hühn, D., Carrillo-Carrion, C., de Aberasturi, D. J., Merk, V., Barcikowski, S., & Parak, W. J. (2014). Interaction of colloidal nanoparticles with their local environment: the (ionic) nanoenvironment around nanoparticles is different from bulk and determines the physico-chemical properties of the nanoparticles. *Journal of The Royal Society Interface*, 11(96), 20130931.

Pillay, K., Cukrowska, E. M., & Coville, N. J. (2009). Multi-walled carbon nanotubes as adsorbents for the removal of parts per billion levels of hexavalent chromium from aqueous solution. *Journal of hazardous materials*, 166(2-3), 1067-1075.

Pisarchick, M. L., & Thompson, N. L. (1990). Binding of a monoclonal antibody and its Fab fragment to supported phospholipid monolayers measured by total internal reflection fluorescence microscopy. *Biophysical journal*, 58(5), 1235-1249.

Pollard, S. J. T., Fowler, G. D., Sollars, C. J., & Perry, R. (1992). Low-cost adsorbents for waste and wastewater treatment: a review. *Science of the Total Environment*, 116(1-2), 31-52.

Pueyo, M., Rauret, G., Lück, D., Yli-Halla, M., Muntau, H., Quevauviller, P., & López-Sánchez, J. F. (2001). Certification of the extractable contents of Cd, Cr, Cu, Ni, Pb and Zn in a freshwater sediment following a collaboratively tested and optimised three-step sequential extraction procedure. *Journal of Environmental Monitoring*, 3(2), 243-250.

Qu, X., Alvarez, P. J., & Li, Q. (2013). Applications of nanotechnology in water and wastewater treatment. *Water research*, 47(12), 3931-3946.

Rai, D., Eary, L. E., & Zachara, J. M. (1989). Environmental chemistry of chromium. *Science of the Total Environment*, 86(1-2), 15-23.

Rai, D., Sass, B. M., & Moore, D. A. (1987). Chromium (III) hydrolysis constants and solubility of chromium (III) hydroxide. *Inorganic Chemistry*, 26(3), 345-349.

Ramos, M. A., Yan, W., Li, X. Q., Koel, B. E., & Zhang, W. X. (2009). Simultaneous oxidation and reduction of arsenic by zero-valent iron nanoparticles: understanding the significance of the core-shell structure. *The Journal of Physical Chemistry C*, 113(33), 14591-14594.

Ratnaik, R. N. (2003). Acute and chronic arsenic toxicity. *Postgraduate medical journal*, 79(933), 391-396.

Rauret, G., Lopez-Sanchez, J. F., Sahuquillo, A., Rubio, R., Davidson, C., Ure, A., & Quevauviller, P. (1999). Improvement of the BCR three step sequential extraction procedure prior to the certification of new sediment and soil reference materials. *Journal of Environmental Monitoring*, 1(1), 57-61.

Reddy, L. H., Arias, J. L., Nicolas, J., & Couvreur, P. (2012). Magnetic nanoparticles: design and characterization, toxicity and biocompatibility, pharmaceutical and biomedical applications. *Chemical reviews*, 112(11), 5818-5878.

Reddy, B. J., & Frost, R. L. (2005). Spectroscopic characterization of chromite from the Moa-Baracoa ophiolitic massif, Cuba. *Spectrochimica Acta Part A: Molecular and Biomolecular Spectroscopy*, 61(8), 1721-1728.

Ren, X., Chen, C., Nagatsu, M., & Wang, X. (2011). Carbon nanotubes as adsorbents in environmental pollution management: a review. *Chemical Engineering Journal*, 170(2-3), 395-410.

Rengaraj, S., Yeon, K. H., & Moon, S. H. (2001). Removal of chromium from water and wastewater by ion exchange resins. *Journal of hazardous materials*, 87(1-3), 273-287.

Richard, F. C., & Bourg, A. C. (1991). Aqueous geochemistry of chromium: a review. *Water research*, 25(7), 807-816.

Rowell, J. L. C., Gaubicher, J., & Nazar, L. F. (2001). A new class of materials for lithium-ion batteries: iron (III) borates. *Journal of power sources*, 97, 254-257.

Sahuquillo, A., Lopez-Sanchez, J. F., Rubio, R., Rauret, G., Thomas, R. P., Davidson, C. M., & Ure, A. M. (1999). Use of a certified reference material for extractable trace metals to assess sources of uncertainty in the BCR three-stage sequential extraction procedure. *Analytica Chimica Acta*, 382(3), 317-327.

Saito, S., Tsugeno, M., Koto, D., Mori, Y., Yoshioka, Y., Nohara, S., & Murase, K. (2012). Impact of surface coating and particle size on the uptake of small and ultrasmall superparamagnetic iron oxide nanoparticles by macrophages. *International journal of nanomedicine*, 7, 5415.

Santhosh, C., Velmurugan, V., Jacob, G., Jeong, S. K., Grace, A. N., & Bhatnagar, A. (2016). Role of nanomaterials in water treatment applications: a review. *Chemical Engineering Journal*, 306, 1116-1137.

Santillán, J. M., Muñetón Arboleda, D., Coral, D. F., Fernández van Raap, M. B., Muraca, D., Schinca, D. C., & Scaffardi, L. B. (2017). Optical and magnetic properties of Fe nanoparticles fabricated by femtosecond laser ablation in organic and inorganic solvents. *ChemPhysChem*, 18(9), 1192-1209.

Sardar, R., Park, J. W., & Shumaker-Parry, J. S. (2007). Polymer-induced synthesis of stable gold and silver nanoparticles and subsequent ligand exchange in water. *Langmuir*, 23(23), 11883-11889.

Sasaki, K., Nakano, H., Wilopo, W., Miura, Y., & Hirajima, T. (2009). Sorption and speciation of arsenic by zero-valent iron. *Colloids and Surfaces A: Physicochemical and Engineering Aspects*, 347(1-3), 8-17.

Scheinost, A. C., Kretzschmar, R., Pfister, S., & Roberts, D. R. (2002). Combining selective sequential extractions, X-ray absorption spectroscopy, and principal component analysis for quantitative zinc speciation in soil. *Environmental science & technology*, 36(23), 5021-5028.

Schellenberger, E. A., Bogdanov Jr, A., Högemann, D., Tait, J., Weissleder, R., & Josephson, L. (2002). Annexin V-CLIO: a nanoparticle for detecting apoptosis by MRI. *Molecular imaging*, 1(2), 15353500200202103.

Schillinger, U., Brill, T., Rudolph, C., Huth, S., Gersting, S., Krötz, F., Hirschberger, J., Bergemann, C., & Plank, C. (2005). Advances in magnetofection—magnetically guided nucleic acid delivery. *Journal of Magnetism and Magnetic Materials*, 293(1), 501-508.

Sharma, Y. C., Srivastava, V., Singh, V. K., Kaul, S. N., & Weng, C. H. (2009). Nano-adsorbents for the removal of metallic pollutants from water and wastewater. *Environmental technology*, 30(6), 583-609.

- Shi, L., Zhang, X., and Chen, Z., 2011, Removal of chromium (VI) from wastewater using bentonite-supported nanoscale zero-valent iron: *Water research*, v. 45, p. 886–892.
- Singh, R., Singh, S., Parihar, P., Singh, V. P., & Prasad, S. M. (2015). Arsenic contamination, consequences and remediation techniques: a review. *Ecotoxicology and environmental safety*, 112, 247-270.
- Sinigaglia, G., Magro, M., Miotto, G., Cardillo, S., Agostinelli, E., Zboril, R., Bidollari, E., & Vianello, F. (2012). Catalytically active bovine serum amine oxidase bound to fluorescent and magnetically drivable nanoparticles. *International journal of nanomedicine*, 7, 2249.
- Smedley, P. L., & Kinniburgh, D. G. (2002). A review of the source, behaviour and distribution of arsenic in natural waters. *Applied geochemistry*, 17(5), 517-568.
- Smedley, P. L., & Kinniburgh, D. G. (2013). Arsenic in groundwater and the environment. In *Essentials of medical geology* (pp. 279-310). Springer, Dordrecht.
- Smith, E. R. G., Naidu, R., & Alston, A. M. (1998). *Arsenic in the soil environment* (Doctoral dissertation, Academic Press).
- Altundoğan, H. S., Altundoğan, S., Tümen, F., & Bildik, M. (2000). Arsenic removal from aqueous solutions by adsorption on red mud. *Waste Management*, 20(8), 761-767.
- Sorg, T. J., Chen, A. S., & Wang, L. (2014). Arsenic species in drinking water wells in the USA with high arsenic concentrations. *Water research*, 48, 156-169.
- Sowers, T. D., Harrington, J. M., Polizzotto, M. L., & Duckworth, O. W. (2017). Sorption of arsenic to biogenic iron (oxyhydr) oxides produced in circumneutral environments. *Geochimica et Cosmochimica Acta*, 198, 194-207.
- Su, C., & Suarez, D. L. (1995). Coordination of adsorbed boron: A FTIR spectroscopic study. *Environmental science & technology*, 29(2), 302-311.
- Sudhakar, C., Anil Kumar, A., Bhui, R. G., Sen Gupta, S., Natarajan, G., & Pradeep, T. (2018). Species-Specific Uptake of Arsenic on Confined Metastable 2-Line Ferrihydrite: A Combined Raman-X-Ray Photoelectron Spectroscopy Investigation of the Adsorption Mechanism. *ACS Sustainable Chemistry & Engineering*, 6(8), 9990-10000.
- Sun, H., Brocato, J., & Costa, M. (2015). Oral chromium exposure and toxicity. *Current environmental health reports*, 2(3), 295-303.
- Tesh, S. J., & Scott, T. B. (2014). Nano-composites for water remediation: A review. *Advanced Materials*, 26(35), 6056-6068.
- Tessier, A., Campbell, P. G., & Bisson, M. (1979). Sequential extraction procedure for the speciation of particulate trace metals. *Analytical chemistry*, 51(7), 844-851.
- Thorek, D. L., Chen, A. K., Czupryna, J., & Tsourkas, A. (2006). Superparamagnetic iron oxide nanoparticle probes for molecular imaging. *Annals of biomedical engineering*, 34(1), 23-38.
- Tiravanti, G., Petruzzelli, D., & Passino, R. (1997). Pretreatment of tannery wastewaters by an ion exchange process for Cr (III) removal and recovery. *Water Science and Technology*, 36(2-3), 197-207.
- Tuček, J., Pucek, R., Kolařík, J., Zoppellaro, G., Petr, M., Filip, J., Sharma, V.K., & Zbořil, R. (2017). Zero-valent iron nanoparticles reduce arsenites and arsenates to As (0) firmly embedded in Core–Shell

superstructure: Challenging strategy of arsenic treatment under anoxic conditions. *ACS Sustainable Chemistry & Engineering*, 5(4), 3027-3038.

Tuček, J., Zboril, R., & Petridis, D. (2006). Maghemite nanoparticles by view of Mössbauer spectroscopy. *Journal of nanoscience and nanotechnology*, 6(4), 926-947.

Tufano, K. J., & Fendorf, S. (2008). Confounding impacts of iron reduction on arsenic retention. *Environmental Science & Technology*, 42(13), 4777-4783.

Turabik, M., & Simsek, U. B. (2017). Effect of synthesis parameters on the particle size of the zero valent iron particles. *Inorganic and Nano-Metal Chemistry*, 47(7), 1033-1043.

Tuutijärvi, T., Lu, J., Sillanpää, M., & Chen, G. (2009). As (V) adsorption on maghemite nanoparticles. *Journal of Hazardous Materials*, 166(2-3), 1415-1420.

Tuutijärvi, T., Repo, E., Vahala, R., Sillanpää, M., & Chen, G. (2012). Effect of competing anions on arsenate adsorption onto maghemite nanoparticles. *Chinese Journal of Chemical Engineering*, 20(3), 505-514.

United States. Environmental Protection Agency. (1990). *Environmental Pollution Control Alternatives: drinking water treatment for small communities*. EPA Center for Environmental Research Information.

Ungaro, F., Ragazzi, F., Cappellin, R., & Giandon, P. (2008). Arsenic concentration in the soils of the Brenta Plain (Northern Italy): mapping the probability of exceeding contamination thresholds. *Journal of Geochemical Exploration*, 96(2-3), 117-131.

Ure, A. M., Quevauviller, P. H., Muntau, H., & Griepink, B. (1993). Speciation of heavy metals in soils and sediments. An account of the improvement and harmonization of extraction techniques undertaken under the auspices of the BCR of the Commission of the European Communities. *International journal of environmental analytical chemistry*, 51(1-4), 135-151.

Vadahanambi, S., Lee, S. H., Kim, W. J., & Oh, I. K. (2013). Arsenic removal from contaminated water using three-dimensional graphene-carbon nanotube-iron oxide nanostructures. *Environmental science & technology*, 47(18), 10510-10517.

Venerando, R., Miotto, G., Magro, M., Dallan, M., Baratella, D., Bonaiuto, E., Zboril, R., & Vianello, F. (2013). Magnetic nanoparticles with covalently bound self-assembled protein corona for advanced biomedical applications. *The Journal of Physical Chemistry C*, 117(39), 20320-20331.

Wang, J., & Chen, C. (2009). Biosorbents for heavy metals removal and their future. *Biotechnology advances*, 27(2), 195-226.

Wang, J., Huang, Y., E David, A., Chertok, B., Zhang, L., Yu, F., & C Yang, V. (2012). Magnetic nanoparticles for MRI of brain tumours. *Current pharmaceutical biotechnology*, 13(12), 2403-2416.

Wang, S., & Mulligan, C. N. (2006). Occurrence of arsenic contamination in Canada: sources, behavior and distribution. *Science of the total Environment*, 366(2-3), 701-721.

Wang, S. D., Scrivener, K. L., & Pratt, P. L. (1994). Factors affecting the strength of alkali-activated slag. *Cement and concrete research*, 24(6), 1033-1043.

Wang, T., Liu, Y., Wang, J., Wang, X., Liu, B., & Wang, Y. (2019). In-situ remediation of hexavalent chromium contaminated groundwater and saturated soil using stabilized iron sulfide nanoparticles. *Journal of environmental management*, 231, 679-686.

- J Wang, Y. X., Xuan, S., Port, M., & Idee, J. M. (2013). Recent advances in superparamagnetic iron oxide nanoparticles for cellular imaging and targeted therapy research. *Current pharmaceutical design*, 19(37), 6575-6593.
- Wazne, M., Jagupilla, S. C., Moon, D. H., Christodoulatos, C., & Koutsospyros, A. (2008). Leaching mechanisms of Cr (VI) from chromite ore processing residue. *Journal of environmental quality*, 37(6), 2125-2134.
- Welch, A. H., Westjohn, D. B., Helsel, D. R., & Wanty, R. B. (2000). Arsenic in ground water of the United States: occurrence and geochemistry. *Groundwater*, 38(4), 589-604.
- Weng, C. H., Huang, C. P., Allen, H. E., Cheng, A. D., & Sanders, P. F. (1994). Chromium leaching behavior in soil derived from chromite ore processing waste. *Science of the total environment*, 154(1), 71-86.
- Weng, C. H., Huang, C. P., & Sanders, P. F. (2001). Effect of pH on Cr (VI) leaching from soil enriched in chromite ore processing residue. *Environmental Geochemistry and Health*, 23(3), 207-211.
- White, K., Detherage, T., Verellen, M., Tully, J., & Krekeler, M. P. (2014). An investigation of lead chromate (crocoite-PbCrO₄) and other inorganic pigments in aged traffic paint samples from Hamilton, Ohio: implications for lead in the environment. *Environmental earth sciences*, 71(8), 3517-3528.
- WHO, 2017, Guidelines for drinking-water quality: Fourth edition incorporating the first addendum
- WHO 2011, Guidelines for Drinking-Water Quality, 4th edition. *WHO chronicle*, 38(4), 104-108.
- Wiesner, M. R., Lowry, G. V., Jones, K. L., Hochella, Jr, M. F., Di Giulio, R. T., Casman, E., & Bernhardt, E. S. (2009). Decreasing uncertainties in assessing environmental exposure, risk, and ecological implications of nanomaterials.
- Wilkie, J. A., & Hering, J. G. (1996). Adsorption of arsenic onto hydrous ferric oxide: effects of adsorbate/adsorbent ratios and co-occurring solutes. *Colloids and Surfaces A: Physicochemical and Engineering Aspects*, 107, 97-110.
- Wilkie, J. A., & Hering, J. G. (1998). Rapid oxidation of geothermal arsenic (III) in streamwaters of the eastern Sierra Nevada. *Environmental science & technology*, 32(5), 657-662.
- World Health Organization, 2003, Chromium in Drinking-water.
- Wu, L., Mendoza-Garcia, A., Li, Q., & Sun, S. (2016). Organic phase syntheses of magnetic nanoparticles and their applications. *Chemical reviews*, 116(18), 10473-10512.
- Wu, W., Wu, Z., Yu, T., Jiang, C., & Kim, W. S. (2015). Recent progress on magnetic iron oxide nanoparticles: synthesis, surface functional strategies and biomedical applications. *Science and technology of advanced materials*, 16(2), 023501.
- Wunderbaldinger, P., Josephson, L., & Weissleder, R. (2002). Crosslinked iron oxides (CLIO): a new platform for the development of targeted MR contrast agents. *Academic radiology*, 9(2), S304-S306.
- Xia, L., Akiyama, E., Frankel, G., & McCreery, R. (2000). Storage and release of soluble hexavalent chromium from chromate conversion coatings equilibrium aspects of Cr VI concentration. *Journal of The Electrochemical Society*, 147(7), 2556-2562.
- Xu, P., Zeng, G.M., Huang, D.L., Feng, C.L., Hu, S., Zhao, M.H., Lai, C., Wei, Z., Huang, C., Xie, G.X., & Liu, Z. F. (2012). Use of iron oxide nanomaterials in wastewater treatment: a review. *Science of the Total Environment*, 424, 1-10.

Yan, W., Ramos, M.A. V, Koel, B.E., & Zhang, W.X., (2010). Multi-tiered distributions of arsenic in iron nanoparticles: observation of dual redox functionality enabled by a core–shell structure. *Chemical communications*, 46(37), 6995-6997.

Yang, J., Swaminathan, C.P., Huang, Y., Guan, R., Cho, S., Kieke, M.C., Kranz, D.M., Mariuzza, R.A., & Sundberg, E. J. (2003). Dissecting cooperative and additive binding energetics in the affinity maturation pathway of a protein-protein interface. *Journal of Biological Chemistry*, 278(50), 50412-50421.

Yean, S., Cong, L., Yavuz, C.T., Mayo, J.T., Yu, W.W., Kan, A.T., Colvin, V.L., & Tomson, M. B. (2005). Effect of magnetite particle size on adsorption and desorption of arsenite and arsenate. *Journal of Materials Research*, 20(12), 3255-3264.

Zhang, W. X. (2003). Nanoscale iron particles for environmental remediation: an overview. *Journal of nanoparticle Research*, 5(3-4), 323-332.

Zhang, L., Qin, X., Tang, J., Liu, W., & Yang, H. (2017). Review of arsenic geochemical characteristics and its significance on arsenic pollution studies in karst groundwater, Southwest China. *Applied geochemistry*, 77, 80-88.

Zhang, Q., Xu, R., Xu, P., Chen, R., He, Q., Zhong, J., & Gu, X. (2014). Performance study of ZrO₂ ceramic micro-filtration membranes used in pretreatment of DMF wastewater. *Desalination*, 346, 1-8.

Zhang, Y., Yang, M., & Huang, X. (2003). Arsenic (V) removal with a Ce (IV)-doped iron oxide adsorbent. *Chemosphere*, 51(9), 945-952.